Nuclear Electric Propulsion with Low Enriched Uranium

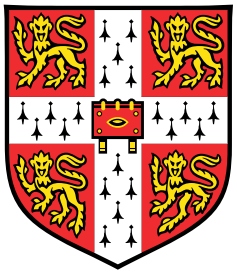

Nathaniel Read

Department of Engineering
University of Cambridge

This dissertation is submitted for the degree of
Doctor of Philosophy

Darwin College

January 2020

For Issy and Alice

Declaration

I hereby declare that except where specific reference is made to the work of others, the contents of this dissertation are original and have not been submitted in whole or in part for consideration for any other degree or qualification in this, or any other university. This dissertation is my own work and contains nothing which is the outcome of work done in collaboration with others, except as specified in the text and Acknowledgements. This dissertation contains fewer than 65,000 words including appendices, bibliography, footnotes, tables and equations and has fewer than 150 figures.

Nathaniel Read
January 2020

Nuclear Electric Propulsion with Low Enriched Uranium

Nathaniel Read

Most space missions have used monopropellant or fuel-oxidiser propulsion systems to provide the required delta-v for orbital transfers and other in-space manoeuvres. Electric propulsion offers an alternative means of providing thrust that makes much more economical use of propellant due to its very high specific impulse. For higher payload missions, especially for travelling to Jupiter and beyond, the only technology capable of supplying the high levels of power required with a reasonable mass and size in the medium term is nuclear fission. However, most proposed space fission systems' designs have opted for the technically desirable but politically problematic fuel choice of highly enriched uranium (HEU).

Using low enriched uranium (LEU, 20% ^{235}U by mass) avoids many of the security costs and public perception issues associated with HEU but has implications for the power system design. The core will require more fuel and/or a moderator, increasing its size and mass. The use of a hydrogenous moderator also reduces allowable core temperatures and brings a reduction in thermodynamic efficiency.

The impact on overall system mass of choosing an LEU over a HEU fuel is examined in the context of a prismatic, gas-cooled reactor using a tri-structural isotropic (TRISO) fuel form, in conjunction with a direct Brayton conversion system producing an electrical power of 1MW. This is a closely coupled system with many potential trade-offs. A deterministic neutronics route is established within WIMS allowing fast analysis of many possible core designs. Core thermal limits are assessed using a finite element method within a thermal hydraulics solver. Models are constructed for estimating the mass of the power conversion system components: turbomachinery, alternator, recuperator and waste heat radiator. A surrogate function optimisation method is adopted to seek minimum mass power system designs in the cases of LEU and HEU fuels in order to make a fair comparison between them.

A zirconium hydride moderator is found to be sub-optimal for an LEU system, with a larger but higher-temperature graphite-based core leading to an overall 40% lighter power system. This sytem was found to have a mass 50% greater than the best HEU-based system. It was confirmed that a 40g/mol helium-xenon working fluid is preferable to pure helium. The design space search revealed that diverse systems with significant differences in the allocation of mass across components can have similar overall masses.

Acknowledgements

I am extremely grateful to my supervisor, Dr Eugene Shwageraus, for his constant guidance and whose interest and knowledge in seemingly all aspects of nuclear energy continues to impress.

I am also very grateful to the National Nuclear Laboratory and the Engineering and Physical Sciences Research Council who provided the vital funding for this project through the ICO CDT programme, whose administrators I also thank for organising many enjoyable events and trips.

Many thanks to the support staff at the ANSWERS Software Service, in particular Dr Ben Lindley whose knowledge of the many subtleties of WIMS was invaluable.

I thank all the members of the Nuclear Energy Group, who are always available to answer questions and make for a vibrant and enjoyable place to work. Having an office that one looks forward to arriving in should never be taken for granted.

Thank you to my family and my in-laws for their constant support, encouragement and interest in my research.

Finally, I thank my wife and best friend Isabel for her enthusiasm for my decision to return to academia and for her endless patience.

Table of contents

List of figures

List of tables

Chapter 1

Introduction

1.1 Electric propulsion

All space missions require some means of propulsion. The most familiar of these is the chemical rocket, used throughout the space age for the first and most dramatic stage of any mission, the launch from the Earth's surface into Low Earth Orbit (LEO). For the launch phase, the chemical rocket is likely to maintain its status as the dominant technology for some time due to its ability to provide the enormous amounts of thrust required. However, once in LEO, other technologies can be preferable. Electric propulsion is one such technology that is now relatively mature. It is regularly used for station keeping (maintaining a desired orbit) and orbit modification by satellites. The first demonstration of electric propulsion used as the primary means of in-space propulsion was Deep Space 1 [91]. This was followed by the Dawn mission, which explored the asteroid belt objects Ceres and Vesta [92]. These missions both used ion thrusters, the most common form of electric propulsion technology. In these systems a gas (usually an inert gas) is ionized and the positive ions accelerated towards the exhaust by an electrostatic field. At the exhaust the removed electrons are recombined with the ions so that the resulting neutrally-charged atoms cease to interact with the electrostatic field and travel freely into space.

The most attractive feature of electric propulsion systems is that their exhaust velocities are generally extremely high. To understand why this is important, one must look to the Tsiolkovsky rocket equation [117]. For a vehicle which accelerates by expelling some of its mass, the total change in its velocity (commonly referred to as 'delta-v') is given by:

$$\Delta v = v_{\mathrm{e}} \ln \frac{m_0}{m_{\mathrm{f}}} \tag{1.1}$$

where v_e is the exhaust velocity and m_0 and m_f are the initial and final masses of the vehicle. It is clear from this equation that the higher the exhaust velocity, the smaller the proportion of the vehicle's initial mass that will be composed of propellant.

There is a quantity related to the exhaust velocity known as the *specific impulse*, I_{sp}, which has the units of seconds. This commonly-used measure is defined as the impulse (the change in momentum) provided for each unit weight of propellant expelled. Cold gas thrusters used for small manoeuvres such as orientation changing have an I_{sp} of between 30s and 70s. Solid and liquid rockets can achieve up to around 340s. Electric propulsion, however, can achieve in excess of 3,000s [117].

The ion thruster used on the Dawn spacecraft produced a maximum thrust of just 90mN. This is the main downside of adopting electric propulsion. Whilst they use propellant very efficiently, they produce relatively small absolute thrusts, requiring very long burn times. For example, Dawn spent 85% of the time between LEO and its Mars fly-by thrusting, a total of 270 days. Burn times using chemical rockets are normally on the order of seconds or minutes and most of the travel time is spent coasting. The high I_{sp} of Dawn's propulsion system allowed for a higher delta-v budget than would be achievable with conventional propulsion systems. The mission involved a rendezvous and orbital capture by a low-mass object (rather than just a fly-by), requiring a large deceleration and associated delta-v cost [92].

It is hoped that electric propulsion could be used in the future for delivering larger payloads to destinations such as Mars and the Jovian moons, and potentially returning. The power required will therefore increase accordingly. However, obtaining this power using solar panels, as did Dawn, becomes less attractive as the required power levels increase. This is particularly relevant when considering missions to Jupiter or beyond; Jupiter is around five times further from the Sun than Earth, so the solar flux falls to around 4% of what is available in LEO. Therefore, nuclear power is considered to be an excellent candidate as a source of power for electric propulsion. The other clear advantage of electric propulsion is that in periods where the propulsion system is not active, such as in the orbit of a body of interest, the power system is then available for other purposes, such as for powering scientific instrumentation and communication systems.

1.1.1 European ambitions

The MEGAHIT (Megawatt Highly Efficient Technologies for Space Power and Propulsion Systems for Long-duration Exploration Missions) was a project funded by the European Commission which sought to create a roadmap for achieving megawatt level nuclear electric propulsion. Its summary report states that "very ambitious missions to the outer solar system, like sample return from moons of giant planets or manned Mars exploration, are

challenges that are difficult, if not impossible, to undertake with current propulsion means" [32]. It took as a reference spacecraft a flagship of more than 30m in length, with a radiator area of 1,000m^2 and a mass of 40 metric tons, powered by a nuclear reactor producing more than 1MW$_e$. This project was followed by DEMOCRITOS which sought to identify the prototyping and demonstration projects that related to the overall goal of achieving high-powered nuclear electric propulsion.

A number of potential missions that such a system would be suited to were identified by MEGAHIT and DEMOCRITOS:

- Near Earth object deflection: Rendezvous with an approaching threat such as an asteroid in order to change its trajectory, thereby reducing the risk of collision with Earth.
- Robotic exploration: The spacecraft would open a new class of exploration mission whereby samples are returned to Earth from as far as away the Jovian moons.
- Space tug: General purpose transport for removal of orbital debris or moving cargo between LEO and either the Moon or Mars.
- Manned Mars missions: The system would be less reliant than conventional propulsion on infrequent launch windows relating to low-energy orbital transfers to Mars and would reduce the transit time, thereby minimising the exposure of astronauts to cosmic radiation.

In addition to these space applications, it should also be noted that there is an increasing interest in the use of similarly sized reactors (so called "micro" reactors) on Earth for remote locations, mining installations and military bases among others. Whilst these operating environments are very different to space, any research or development of such systems has the potential to inform the design of terrestrial systems.

1.2 Nuclear power in space

1.2.1 Radioisotope thermoelectric generators

Nuclear power sources have powered many space missions in the form of radioisotope thermoelectric generators (RTGs). These rely on the heat generated by radioactive decay of a suitable isotope. This heat is then converted into electricity using a thermocouple. However, the specific power of such systems is relatively low. The most recently used system, the

Fig. 1.1 Multi-Mission Radioisotope Thermal Generator (MMRTG) undergoing vibration testing at Idaho National Labs.[1]

multi-mission RTG (MMRTG) which formed the power source for the *Curiosity* Mars rover, had a total power of 2,000W_{th} and 125W_e (a conversion efficiency of around 6%). This system is shown in Figure 1.1. The specific power of the MMRTG is 357kg/kW_e [49]. A specific power of this order is unlikely to be suitable for higher power systems. For example, the dry (excluding propellant) mass of the entire Prometheus spacecraft (see subsequent section) was specified to be no greater than 25,000kg [118]. Meeting its 250kW_e power requirement using the MMRTG's specific power of 357kg/kW_e would result in a mass of around 90,000kg for the power system alone.

Efforts are being made to improve the efficiency of radioisotope power sources, for example by moving to dynamic conversion in the form of Stirling engines, rather than the static conversion of thermocouples [18]. However, even if the hoped-for efficiency of 25% is achieved, the quantity of a suitable isotope required for megawatt-level power is likely to be prohibitive. The most favoured isotope for space missions has been Pu-238 which has a half-life of 87.7 years. The production of this isotope is an expensive process, requiring the neutron irradiation of separated Np-237 in a suitable reactor. Indeed, justifications for pursuing more efficient conversion technologies, such as Stirling engines, have tended to place as much importance on reducing the consumption of valuable Pu-238 as on reducing the mass of the system.

[1] Image distributed under Creative Commons 2.0 Licence

There are other isotopes which could potentially replace Pu-238 for RTG-like systems, notably Am-241 [83]. This has a half-life around four times longer (and therefore roughly a quarter of the specific power output) and has a higher level of gamma emission but could be produced more cheaply. Broadly speaking, the search for alternatives to Pu-238 is motivated by cost reduction and availability rather than performance, so one can rule out the possibility of such alternatives making high-power systems more feasible.

Electric propulsion for orbital transfers using radioisotope power sources in conjunction with efficient Stirling conversion has been proposed [95]. However, this is intended as a solution for low mass, low power missions such as *Dawn* whose thrusters used 2.6kW at maximum throttle [92]. Scaling RTGs to the megawatt power level is not expected to be feasible, if only due the scarcity of Pu-238. Decay-based heat sources provide a determined specific thermal power (unlike fission sources); therefore one can readily estimate the minimum mass of an RTG system. The 4.8kg of fresh Pu-238 within the MMRTG unit [21] produced 2,000W_{th}. If we assume a conversion efficiency of 25%, then for the 1MW_e system we would require a 4MW_{th} Pu-238 source, which would have a mass of 9,600kg. It is estimated that one 10MW research reactor could produce around 6kg per year at a cost of between 1.6 and 4.3 million US dollars per kilogram [49]. Scaling RTGs up to the megawatt level therefore seems unfeasible. To provide power of a megawatt and beyond, one must turn to nuclear fission.

1.2.2 Soviet space reactors

The former Soviet Union launched over 30 fission reactors into orbit, providing power for its Radar Ocean Reconnaissance Satellites (RORSATs). The first Soviet design was the Romashka reactor. This was a fast spectrum reactor using uranium carbide fuel with an enrichment of 90%. The layout is reminiscent of an RTG, with heat being conducted passively to thermoelectric elements arranged around the core and waste heat being dissipated by radial fins. This reactor produced 28.2kW_{th} but only 0.45kW_e and was never actually flown. The next Soviet design, the Bouk reactor, was launched in 32 RORSATs between 1966 and 1988. It was another fast spectrum reactor using highly enriched uranium, but used a uranium-molybdenum alloy as the fuel form. Passive heat conduction was replaced with active cooling using two loops of sodium-potassium eutectic coolant. One loop transferred heat from the core to the hot side of the thermoelectric converters and one from the cold side of the converters to the waste heat radiator which formed the cylindrical case of the nuclear power module. This improved conversion efficiency from 1.6% in the Romashka to 2.5% in the Bouk [101].

The RORSAT programme gained more attention than its sponsors might have desired when Kosmos-954 re-entered the atmosphere in 1978 and scattered debris, including the fragmented reactor, in a line across northern Canada. The RORSAT had two emergency safety procedures. The first was to boost the satellite from its standard orbit of around 260km into a 'burial' orbit of at least 850km. The backup system was designed to eject the U-Mo fuel elements such that they would disintegrate more effectively in the atmosphere and not reach the surface in any harmful concentration. There appears to be some disagreement in the literature over whether both systems failed or if the backup system was only introduced for subsequent launches in response to the Kosmos-954 incident [13, 101, 121]. This is not entirely surprising given the level of secrecy surrounding the Soviet space reactor programme.

The third and final Soviet design to reach orbit was the Topaz-1 reactor, with two known launches in 1987. This was a step change in reactor design from the Bouk and Romashka reactors. Thermionic conversion was adopted, facilitated by 'thermionic fuel elements' which are integrated pins containing both the uranium dioxide fuel pellets (90% enriched) and the thermionic emitters and collectors. Topaz operated with a thermal spectrum, moderated by zirconium hydride discs. This allowed a lower fuel loading of 11.5kg compared to 25-30kg in the Bouk reactor. Thermionic conversion provided an efficiency of around 4% for a total electric power of up to 7kW_e [101].

1.2.3 US space reactors

SNAP

The United States has only launched one nuclear reactor into orbit, the SNAP-10A in 1965. This was a thermal spectrum reactor using uranium-zirconium-hydride fuel. A sodium-potassium eutectic coolant transferred heat from the Hastelloy-clad fuel elements to thermoelectric converter panels which were arranged on a conical 'apron' such that they radiated waste heat directly to space. This arrangement had an efficiency of 1.25%, producing 500W_e from 40kW_{th}. Unfortunately the failure of an electronic component caused the reactor to shut down after 43 hours of operation [53].

The wider SNAP programme produced two related space reactor designs, SNAP-2 and SNAP-8, which replaced the thermoelectric conversion system with mercury Rankine (two-phase) dynamic conversion. These were designed to produce 55kW_e and 600kW_e respectively. These designs never progressed beyond ground testing as the space reactor programme in the US was terminated in 1973 [112, 101]

Rover/NERVA

A great deal of effort was put into a related technology, nuclear thermal rockets (NTRs), in the Rover and NERVA programmes which ran from 1955 to 1973. An NTR produces thrust directly by using a nuclear core to heat hydrogen to above 2,000K which then passes through a supersonic nozzle [35]. This can result in higher I_{sp} values than are available from conventional chemical rockets, although not as high as in electric propulsion. Such a system would likely operate in a 'burn and coast' manner for orbital transfers as for chemical systems. NTRs are still considered to be a viable technology and they remain an active area of research. One drawback that NTRs have is that ground tests of the sort that were carried out during the Rover and NERVA programmes, where exhaust gas is simply vented into the atmosphere, are no longer likely to be politically acceptable. Therefore, a means of either collecting and scrubbing the exhaust gas or venting into an appropriate geological formation is required [50]. Nuclear electric propulsion does not suffer from this drawback, since both the power and propulsion systems can be safely and separately tested on Earth without these extra facilities.

SP-100

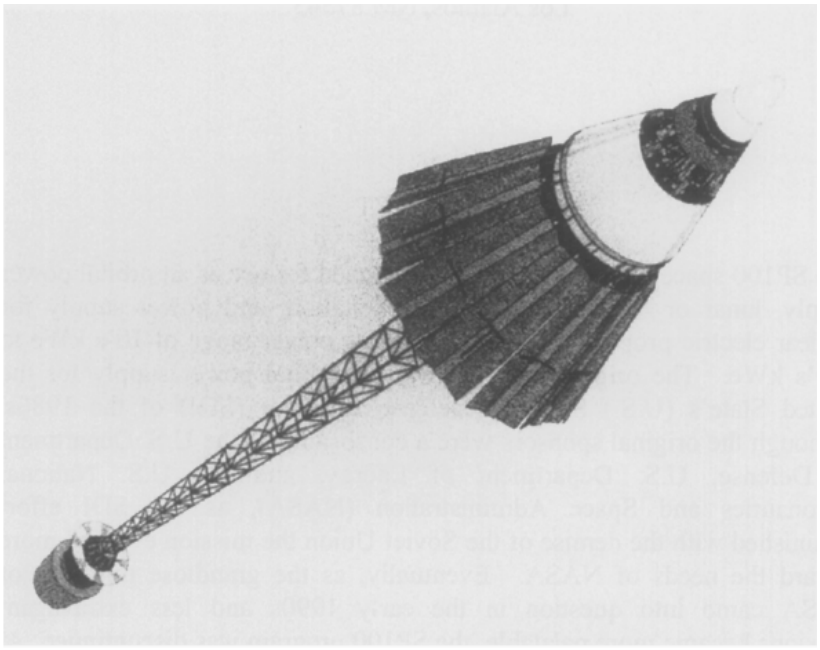

Fig. 1.2 SP-100 nuclear power system including payload boom. The reactor sits at the top right of the image. The shuttlecock-shaped structure is the waste-heat radiator [25]

The SP-100 reactor system was intended to be a highly flexible and scalable system. The project began under the Strategic Defence Initiative and had a number of potential military applications including surveillance, communications and 'force application'. The system was also expected to be usable for civil missions either in LEO or in conjunction with electric propulsion for lunar, Mars or outer solar system exploration. The power output was expected to be in the range 10kW$_e$ to 1,000kW$_e$ [113].

The design which was selected for further development was a fast-spectrum, liquid lithium-cooled reactor using uranium nitride fuel. The core outlet temperature of the coolant was intended to be 1,375K. Waste heat was rejected via heat pipe radiators mounted on a conical apron below the core, as shown in Figure 1.2. The generic design had a thermal power of 2,400kW$_{th}$ and an electrical power of 100kW$_e$, although the design which had been advanced to the most detailed level was a smaller 20-40kW$_e$ system which, under the threat of possible programme cancellation, was seen to be deployable sooner. Ultimately the SP-100 project was cancelled in 1994 after around $1 billion had been invested in design and development [25].

Prometheus

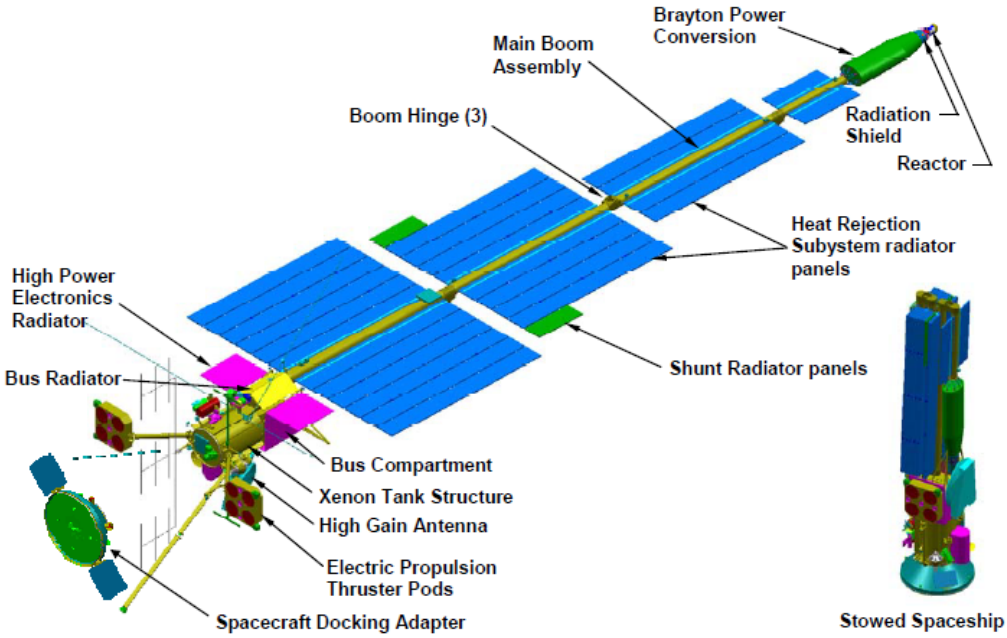

Fig. 1.3 Entire Prometheus spacecraft design [80]

Beginning in 2002, the Prometheus project pursued the most ambitious space reactor design to date. Initially the project was known as the Jupiter Icy Moons Orbiter (JIMO)

which specified the development of "a Deep Space Vehicle for outer solar system robotic exploration missions that combines a safe, reliable Space Nuclear Reactor with electric propulsion" [80]. The target mission was a tour of the Jovian moons Callisto, Ganymede and Europa with a scientific payload of at least 1,500kg. Later in the project it was assumed that the vehicle would be more general purpose and should be suitable for a number of different missions, including travelling to Saturn and its moons, Neptune and its moons and even a rendezvous with Kuiper belt objects. The power output of the reactor system was to be around 200kW$_e$ [80].

The Naval Reactors Prime Contractor Team tasked with the design of the reactor module concluded that there were five combinations of reactor type and energy conversion type that were worth considering in detail [118]:

- Gas-cooled reactor with direct cycle Brayton conversion[2]
- A heat pipe-cooled reactor with Brayton conversion
- A liquid lithium-cooled reactor with Brayton conversion
- A liquid lithium-cooled reactor with thermoelectric conversion (this was the choice for the previous SP-100 project)
- A lower temperature liquid metal-cooled (sodium, potassium or a eutectic of both) reactor with Stirling engine conversion

Of these five, the first option, a direct cycle gas-cooled Brayton system, was seen to have the fewest hurdles to development and was therefore chosen as the design to pursue further. However, in 2005 the Prometheus project was cancelled. The spacecraft design as it existed at the termination of the project is shown in Figure 1.3. The work of the Naval Reactors Prime Contractor Team is documented in a series of reports and letters, some of which are classified. Unfortunately the particular report which contains the detailed cost-benefit analysis for each of the reactor systems listed above and the rationale for ultimately choosing the first option remains unobtainable.

The choice between gas coolant and liquid metals is a complex one. Liquid metals are obviously far more effective at removing heat from a reactor than gases but have a number of drawbacks, not least the requirement to thaw the coolant during startup. In the available documentation, it is noted that "even low temperature liquid metal systems require special facilities for liquid metal processing, purification, and safe testing" [5]. The same document

[2] 'Direct cycle' refers to a system in which the reactor coolant is also the working fluid of the Brayton system with no intermediate heat exchanger

also notes that "trade studies performed on potential electric power distribution systems show a clear preference for Brayton cycle energy conversion when compared to thermoelectrics or Stirling. This advantage is due to the inherent ability of Brayton converters to produce high frequency AC power which is simpler to convert and distribute over long distances." Clearly there are a large number of factors which influence a project such as Prometheus in its choice of one system over another, and some of these will change with time as technologies develop. This can be seen in the fact that, just two decades earlier, the SP-100 project opted for liquid lithium coolant in conjunction with thermoelectric conversion. Therefore one should be cautious in assuming that the ultimate choice of any particular project is the best candidate at other times and other power levels.

kiloPower

The ongoing kiloPower project aims to produce a small fission power system that is scalable from 1 to 10kW$_e$, for use both in space and on the surface of Mars. It has a number of fairly novel design features. The fuel form consists of a monolithic block of uranium molybdenum alloy, composed of 7% molybdenum and 93% highly enriched uranium (HEU) by weight. The core is surrounded by a further monolithic block of beryllium oxide. The control system is relatively simple, using a single control rod which runs along the centre of the fuel block, rather than the more common arrangement of rotating control drums within the reflector [40]. Some redundancy would appear to have been sacrificed here, since one might expect that the loss of control of one control drum might not be critical fault, whereas loss of control of the single control rod clearly would be.

Heat removal is achieved with sodium heat pipes which surround the core, connected to a Stirling cycle conversion system. The heat pipes transfer heat in a two-phase process, using the heat from the reactor to vaporise the liquid sodium, which then travels to the cooler end of the heat pipe, where the sodium condenses, releasing its latent heat. The liquid sodium is transported along a wick back to the hot end of the pipe. Lower temperature heat pipes using water as the working fluid are also used to thermally connect the cold side of the Stirling converters to the waste heat radiators. Heat pipes have some attractive features in a space reactor context. They are simple and robust, having no moving parts. They are entirely passive, requiring no external power source to operate, reducing the parasitic losses within the system and simplifying the startup procedure [40]. Testing of the heat pipe and Stirling systems using an electrically heated, depleted uranium core has already taken place.

The progress shown in the kiloPower project suggests that in the power level of 1-10kW$_e$ a monolithic uranium alloy block cooled with heat pipes is a strong candidate system. However, further investigation would be required to determine whether this class of system

is scalable by two orders of magnitude to the $1MW_e$ level. It is interesting that, in the Prometheus project's shortlist of five reactor types given above, heat pipes were included in one possible design but in conjunction with a Brayton conversion system. The Stirling cycle was only considered in the context of the 'lower temperature' liquid metal-cooled reactor. This suggests that previous investigations have identified the Brayton cycle as preferable to the Stirling cycle at higher temperatures, even though it requires the inclusion of a gas heat exchanger.

1.3 Objectives and motivation

It is notable that most of the historically used or proposed space fission systems have in common the use of HEU fuel. From a reactor design perspective it is the ideal fuel for such an application, allowing for a highly compact, low mass source of heat that can sustain criticality without the need for a moderator. However, there are some less technical considerations that make its use less desirable. The use of HEU, considered as weapons-grade, raises understandable concerns. Even with the recent rapid expansion of private sector launch services, space exploration remains a largely publicly funded endeavour. Association with weapons-grade material, even if sufficient precautions have been taken, risks reducing the public's willingness to support such missions. The development and transportation of the fuel form must occur under the highest levels of security which also contributes to the cost of the mission.

An alternative fuel could be low enriched uranium (LEU), here defined to be less than 20% enriched. It is reasonable to assume that this will bring with it a penalty in terms of the system mass. For the core alone, it would be expected that the core will require more fuel and/or moderator. The use of a moderator such as zirconium hydride will likely reduce the achievable core outlet temperature, reducing the thermodynamic efficiency of the energy conversion system. LEU is a much less contentious material, being used widely in civilian research reactors, and is proposed for some Generation IV power reactor designs. As well as alleviating the cost and perception issues mentioned above, it also allows more collaboration between space agencies and academia in developing space fission systems. Recently, NASA announced [79] that it will fund research into an LEU-fuelled nuclear thermal rocket. It notes the reduced cost of security as an advantage, with handling regulations for LEU being broadly in line with those that apply to a university research reactor. It also notes that this allows closer collaboration with industry and academia. Another key driver is political acceptability: the public support required for space exploration is likely to be weakened if it requires the production of weapons-grade material or is perceived to be a proliferation risk.

Weighing the technical disadvantages against the political advantages of choosing an LEU system is a difficult task and not one undertaken here. But whoever is required to make such a comparison will benefit from knowing what the technical disadvantages actually are. This project aims to address one aspect of the technical disadvantage, attempting to quantify the increase in the mass of the power system.

A recent white paper on the subject of an LEU variant of kiloPower [87] considers how the current design might be adapted and the impact on the overall mass of the power unit, as well as providing a useful summary of the political and economic benefits of a switch to LEU from the perspective of NASA. It was found that, for a $1kW_e$ system, the LEU system might increase in mass by between 130% and 220%, but for a 10kW system the increase was around 60% to 74%.

The central objective of this project is to investigate the technical disadvantages, principally the system mass, of choosing to use LEU (meaning here 20% enriched, sometimes called 'high-assay LEU' or HALEU) as a fuel instead of HEU (assumed to be 93% enriched) in a space reactor with a power output of $1MW_e$. This reactor is intended to provide power over a period equivalent to seven years at full power to an in-space electric propulsion system as per the DEMOCRITOS specification.

It is important, therefore, to understand the technical drawbacks of adopting LEU such that they can be weighed against these non-technical considerations. Whether an LEU or HEU system is ultimately adopted will depend on the territory and the political environment. For example, the USA has chosen to use HEU for its Mars surface system kiloPower [40]. However, the USA has historic stockpiles of HEU and the necessary facilities and institutions to handle it. The situation would be very different in a European context in which multiple states, some of which are not nuclear weapons states, must collaborate.

There are a number of areas that could be investigated where a change in the fuel choice from HEU to LEU (and the assumed accompanying change from a fast to thermal spectrum system) could have a significant impact. Some examples are:

- **Core mass:** It is reasonable to expect that using LEU instead of HEU will require either significantly more fuel or the addition of a moderator. It is conceivable that the addition of a moderator, even though it improves neutronic efficiency, might overall lead to an increase in the mass of the core

- **Core volume:** The additional fuel and/or moderator will also increase the volume of the core. This in itself would be a slight disadvantage since launch vehicles have a limited internal volume. The main implication of a larger core is that the shield, typically a high mass component, may need to be larger to accommodate the larger

core. However, thermal spectrum reactors would be expected to release fewer of the high energy neutrons that are most relevant for assessing material damage, which might reduce the required shield thickness. In addition, the lower leakage of thermal reactors should make them less sensitive to changes in aspect ratio. This could make a long, thin, core more feasible for a thermal reactor than for a fast reactor, thus reducing the required cross-sectional area of the shield.

- **Long term reactivity control:** The move from a HEU fast spectrum system to a LEU thermal spectrum system is likely to have significant implications for reactivity control. Broadly speaking, thermal spectrum systems tend have a higher initial reactivity that is often dampened with burnable neutron absorbers that deplete over time.

- **Launch/crash safety:** For any reactor system which is flown, a variety of impact scenarios must be considered. Immersion in water or wet sand are usually considered, as well as compaction of the core. The main aim is to avoid core criticality in all scenarios.

- **Materials compatibility**: Some materials will be incompatible with fast or thermal spectrum systems. For example, tantalum is often used in refractory alloys but is unsuitable for thermal spectrum systems due to its very high absorption cross section at low energies.

- **Overall system mass**: Although the core mass is a relevant factor, this should not be considered in isolation. Minimising the mass of the power system as a whole is the more important goal. Changes in the core design can influence the wider system. For example, if the introduction of a hydrogen-bearing moderator necessitates a lower core outlet temperature, this will reduce the thermodynamic efficiency of the power conversion system.

1.3.1 Thesis scope

Attempting to address every area of investigation in the above list (which is itself not exhaustive) would be too large a scope for this project. Therefore, the focus will be on the impact of the fuel choice on the mass of the overall nuclear power system. In order to make a fair comparison between systems using either LEU or HEU, it will be necessary to find the minimum mass system in each case. This is not a trivial task and constitutes the majority of the work in this project. The reason for the complexity is the large number of trade-offs that exist within the system. One example that is applicable to any variety of space nuclear power

system is the balance between reactor power output and the waste heat radiator. Having a larger, more massive, waste heat radiator will improve the thermodynamic efficiency of the conversion system, thereby reducing the thermal power required from the reactor (and therefore its size and mass).

It is also necessary to reduce the scope of possible power system designs. As the previous discussion of historic space nuclear power systems reveals, there is an impressively wide range of plausible (as well as almost-plausible) designs. The fuel in the reactor could be arranged in traditional pins, a dispersed particulate fuel in a graphite block, or in a monolithic metallic alloy. Heat might be removed from the core using heat pipes, a pumped liquid metal or noble gas. This heat might be converted into electricity using static conversion technologies such as thermoelectrics or in-core thermionics, or dynamic conversion technologies such as a noble gas Brayton cycle, metal vapour Rankine cycle, or a Stirling engine. Attempting to determine which of these, or which combination of these, is the most suitable for either fuel type would also present too large a scope.

In order to create a tractable problem, one class of nuclear power system is chosen - a gas-cooled reactor in conjunction with a direct Brayton cycle conversion system. The 'direct' refers to the fact that coolant flows from the reactor to the turbine rather than transferring heat to a separate working fluid via a heat exchanger. Such appears to be the system of choice in the Prometheus project, the most relevant historic undertaking due to its identical intended mission (electric propulsion) and high intended power level.

Chapter 2

Tungsten cermet reactor

The first stage of the investigation is limited to consideration of the reactor core and how its mass might be affected by a change from LEU to HEU fuel. This analysis covers two main areas of interest:

- **Neutronic analysis**: The core is required to produce power for the required amount of time. As mentioned in the Introduction, this is assumed to be the equivalent of seven years producing $1MW_e$, to enable a variety of mission types. In order to produce power during this period, the reactor must remain critical, that is, continue to sustain the nuclear chain reaction. Neutronic analysis refers to those methods that assess whether the core is critical or not and determine the core power distribution.
- **Thermal hydraulic analysis**: As discussed in the Introduction, this project focusses on a gas-cooled reactor. It is necessary to model the flow of heat from the fuel, where it is produced, into the coolant. This will allow the determination of the temperature of the coolant at different points in the core, as well as the temperatures of the materials in the core which must not be allowed to breach specified limits.

An overall computational framework is therefore required to find core designs that are of minimal mass but which satisfy the above neutronic and thermal hydraulic constraints. Once minimum mass cores are obtained for the HEU and LEU cases, they can be compared to arrive at the mass penalty of LEU fuel.

2.1 Core material choices

In order to construct this computational framework, an initial set of core material choices is required. Once the framework is in place, the analysis could then, in principle, be extended

to other material choices. The first candidate fuel material to be considered is tungsten cermet. This fuel material is a composite material of tungsten metal and a ceramic such as uranium dioxide. Pioneering work was done during the "710" High-Temperature Gas Reactor programme, which investigated this fuel form for use both in a power reactor and a nuclear thermal rocket application [38].

In this programme the hexagonal tungsten cermet fuel elements were formed by hot isostatic pressing and sintering, followed by diamond drilling of the coolant channels. This pressing method was found to result in some undesirable grain growth which is detrimental to the effectiveness of the sintering stage. The high temperatures used in the pressing phase were found to result in the formation of non-cermet regions. An alternative manufacturing process, spark plasma sintering, has been developed, which uses lower temperatures and thereby alleviates some of these fabrication issues [84]. It is noted by Husemeyer [51] that natural tungsten is not likely to be optimal for use in a thermal spectrum reactor. Tungsten occurs in five natural isotopes, with the most abundant, W-184, having the lowest absorption cross section in the thermal region. The tungsten used is therefore assumed to be artificially enriched from its natural fractional abundance of 30.64% to 95%.

As in the 710 programme, the fuel elements are hexagonal with circular channels through which the helium coolant will flow. However, the dimensions of these elements and their coolant channels are not assumed to be the same as those used in the rocket application. The coolant temperature of the hydrogen coolant/propellant found in an NTR application can exceed 2,500K [35], which is likely to be higher than the turbomachinery of a Brayton conversion system could tolerate. For example, in order to use currently available technology, the Prometheus project opted for a coolant outlet temperature of 1,150K [118]. Therefore, one might expect that the coolant channels will occupy a smaller proportion of the element's cross-sectional area, whilst conforming to the same maximum fuel temperature limit.

In the 710 programme a variety of refractory metal claddings were considered for the interior of the coolant channels and the outer surface of the fuel elements [38]. In the context of a thermal rocket, Husemeyer [51] additionally considered a 50μm plasma spray of tungsten on the interior and exterior surfaces of the fuel elements. This level of detail is not considered in the modelling undertaken so cladding is ignored; however, the fact that a 50μm layer of tungsten is sufficient is reassuring that this simplification does not introduce significant error into the modelling.

For the HEU fast reactor core, these fuel elements are arranged in a hexagonal array and surrounded by a reflector. For the LEU cores, moderation is introduced by substituting moderating elements for fuel assemblies in some positions. There are many possible ways of arranging the moderating elements within the core; here four possible ways have been

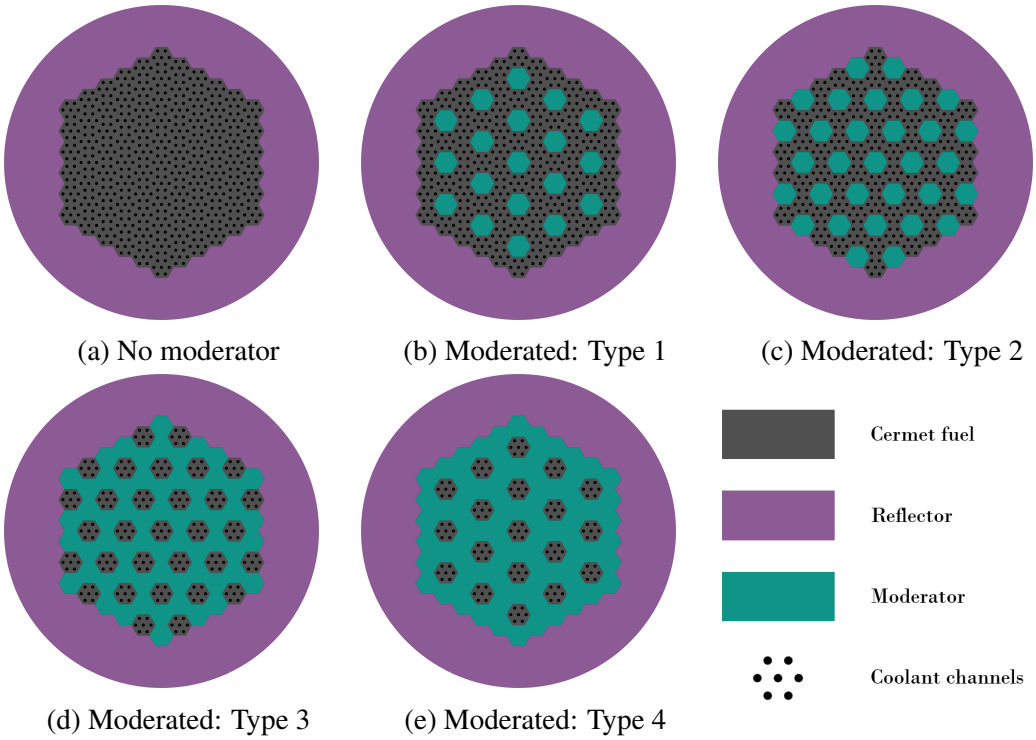

Fig. 2.1 Example reactor cores showing the five possible core patterns. All have five rings of hexagonal elements and one ring of coolant channels per element

selected which provide a relatively uniform distribution. These patterns are a subset of those considered in the investigation of LEU-fuelled NTRs of Husemeyer [51]. The four moderated patterns and the one non-moderated pattern used are shown in Figure 2.1. Type 1 has one moderator element for every three fuel elements (in the limit of a large core) and Type 2 has one moderator for every two fuel elements. Types 3 and 4 are inversions of Types 2 and 1, respectively, such that the level of moderation increases as one progresses from Types 1 to 4.

The height of each core is determined by maintaining a fixed aspect ratio, that is, the ratio of core radius to core height. In a subsequent stage of the project, different core aspect ratios could be investigated, with an interest in the relative effect on LEU thermal reactors as compared to HEU fast reactors. As mentioned previously, it is expected that thermal spectrum reactors will be more amenable to elongation, since fast reactors generally have higher leakage of neutrons. This occurs because neutrons have a longer mean free path in a fast reactor, in turn caused by the generally smaller nuclear cross sections at higher energies. The change in aspect ratio will then have an impact on the thermal hydraulic performance of the core and the shielding requirements, which could be investigated. At this stage, an arbitrary choice must made in order to demonstrate the functionality of the calculation routine. A reasonable choice is the ratio which gives the minimum leakage. The choice is a

ratio of radius to height of $R/H = 0.5413$. Under a simple one energy group analysis of a homogeneous cylindrical reactor, this is the value which minimises the geometrical buckling, which is given by [63]:

$$B_g^2 = \left(\frac{\pi}{H}\right)^2 + \left(\frac{2.405}{R}\right)^2 \tag{2.1}$$

The buckling is a reasonable proxy for the neutron leakage so this should be approximately the minimum leakage geometry. This is a sensible starting point from which to make departures to other less neutronically favourable aspect ratios but which might have positive impacts in other respects. For example, shortening the coolant channels by choosing a flatter core design would decrease the overall pressure drop and, for a given pumping power, would allow the channels to be narrowed.

2.1.1 Moderator and reflector choice

Later in the investigation, one possible area of exploration is the consideration and testing of different choices of moderator and reflector materials. For this initial modelling, one choice is made in order to demonstrate the successful execution of the overall calculation routine.

The initial choice made for the moderator is zirconium hydride, with the moderation being provided by the hydrogen contained within it. One concern which was expressed in the Prometheus project was the ability of any hydrogen-based moderator to retain its hydrogen to a sufficient extent at elevated temperatures over long operation times [118]. In this initial modelling, the moderator is assumed to sit in monolithic blocks within the core lattice; requirements for cooling the moderator are considered later in the investigation. The reflector is initially chosen to be beryllium oxide, as used in the kiloPower project.

2.2 Thermal hydraulic model

The thermal hydraulic analysis focusses on the hottest coolant channel in the reactor, which is determined with reference to the fission power distribution calculated by Serpent. It is a finite element model written in MATLAB which considers the heat transferred from the cermet fuel to the helium coolant over small intervals along the coolant channel. For each small interval, there is a thin slice of fuel which is assumed, in the steady state, to deposit all of its heating power into the associated thin slice of coolant flowing along the coolant channel. This is in turn based on the assumption that the conduction of heat axially along the fuel can be neglected. The change in temperature, $\mathrm{d}T_\mathrm{c}$, of the bulk coolant within the small

element dz is given by [63]:

$$\mathrm{d}T_\mathrm{c} = \frac{q'}{\dot{m}c_\mathrm{p}}\,\mathrm{d}z \tag{2.2}$$

where q' is the linear heating rate, $\dot{m}$ is the coolant mass flow rate and c_p is the specific heat capacity at constant pressure. In order to calculate the temperature of the channel wall, one must then consider the effectiveness of heat transfer between the wall and the bulk coolant, which is captured by the heat transfer coefficient, h. The rate of heat flow from the channel wall, which is at a temperature T_wall, to the bulk coolant, which is at a temperature T_c, is given by [63]:

$$q = hA(T_\mathrm{wall} - T_\mathrm{c}) \tag{2.3}$$

where A is the area of the channel wall in the thin element being considered.

The value of the heat transfer coefficient can be calculated using the Dittus-Boelter equation. For a long, straight, circular tube with a gas flowing through it the heat transfer coefficient is given by [63]:

$$h = 0.023\frac{k}{D_e}\mathrm{Re}^{0.8}\mathrm{Pr}^{0.4} \tag{2.4}$$

where k is the thermal conductivity of the fluid, D_e is the diameter of the coolant channel, Re is the Reynolds number and Pr is the Prandtl number. With the ability to calculate the coolant channel wall temperature one can then proceed to determine the temperature within the cermet. This is described in the following section.

In order to check the thermal hydraulic model has been implemented correctly, a simplistic representation for the reactor power distribution is used so that it can be compared against an analytical solution. For this analysis, an example core is chosen which is composed of five rings of fuel elements with seven coolant channels per fuel element. The core is assumed to have a total power of $4\mathrm{MW_{th}}$ with a flat radial power distribution, so the single coolant channel has a total power output of $6{,}279\mathrm{W_{th}}$ associated with it. The power along the coolant channel is assumed to obey a simple cosine relation:

$$q' = q'_\mathrm{max}\cos\left(\frac{\pi z}{H}\right) \tag{2.5}$$

Here, H is the height of the fuel elements. Often in such a model this parameter is not the actual length but includes an 'extrapolation distance' to account for the fact that the neutron flux at the boundary is not in fact zero. However, including the extrapolation distance would not add anything to this basic check on the functionality of the thermal hydraulic model.

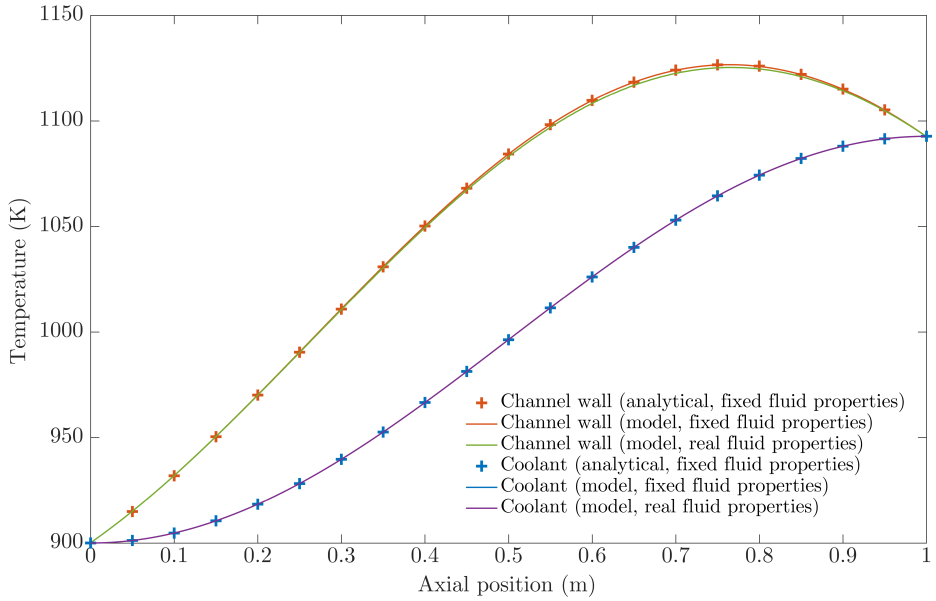

Fig. 2.2 Coolant and channel wall temperatures calculated by thermal hydraulic model and reference analytical solution

For a coolant channel with the power shape described by Equation 2.5, it can be shown [63] that the temperature of the bulk coolant obeys:

$$T_{\text{coolant}} = T_{\text{inlet}} + \frac{q'_{\text{max}} H}{\pi \dot{m} c_{\text{p}}} \left[1 + \sin\left(\frac{\pi z}{H}\right)\right] \tag{2.6}$$

Here c_{p} is assumed, along with all other fluid properties, to be constant. It can also be shown that the temperature of the channel wall is given by:

$$T_{\text{wall}} = T_{\text{inlet}} + \frac{q'_{\text{max}} H}{\pi w c_{\text{p}}} \left[1 + \sin\left(\frac{\pi z}{H}\right)\right] + \frac{q'_{\text{max}}}{h C_{\text{c}}} \left[1 + \cos\left(\frac{\pi z}{H}\right)\right] \tag{2.7}$$

where h is the heat transfer coefficient from Equation 2.4 (assumed to be constant) and C_{c} is the channel circumference.

Figure 2.2 shows the coolant and channel wall temperatures as calculated by the thermal hydraulic model and using the analytical reference solution. Two sets of results are shown for the thermal hydraulic model: one set is based on fixed fluid properties (such as viscosity and thermal conductivity) based on the values that apply at the inlet temperature of 900K and the other set uses temperature-dependent data. This data was taken from the National Institute of Standards and Technology Chemistry WebBook [81] and is used for the subsequent modelling outside of this verification exercise.

An assumption is required for the power distribution within the reactor. In the radial direction, the approach taken here is to establish, for a critical core, the power shape provided by Serpent for each moderator pattern. A 'peaking factor' is produced which is the ratio of the power output of the highest power fuel element to the average fuel element power. This is then assumed to be constant for other size cores of the same moderator pattern. The peaking factor is then assumed to apply to the hottest channel in the core. In reality, the power is likely to vary across the fuel element. This will be investigated at the next stage of the project and the power profile of the hottest channel can be refined.

In the axial direction, a simple assumption is made that the power is cosine shaped, as per Equation 2.5. This is somewhat conservative as this simple assumption implies that the power at the top and bottom faces of the reactor is zero, which is obviously not the case in the reality. Therefore, the peak power in the centre of the reactor is assumed to be higher than would actually be the case, leading to a higher estimation of peak fuel temperature. In a later stage of the modelling, power information will be taken directly from the neutronics solver, removing the need for an explicit power shape assumption.

The other quantity which is calculated by the thermal hydraulic model is what is referred to here as the 'pumping power'. It should be noted that here this refers to the power associated with pumping coolant through the reactor, not to the total power of the Brayton cycle compressor. Specifically, if the pressure drop between the inlet and outlet plena is Δp, then the pumping power is calculated as [106]:

$$\text{Pumping power} = \frac{\dot{m}}{\rho}\Delta p \tag{2.8}$$

The pressure drop associated with frictional losses is calculated within each of the small intervals $\mathrm{d}z$ in the thermal hydraulic model using [106]:

$$\Delta p_{\text{friction}} = \frac{1}{2}\rho v^2 f \frac{\mathrm{d}z}{D} \tag{2.9}$$

where ρ is the density, v is the velocity, D is the channel diameter and f is the friction factor. For turbulent flow in the range $3 \times 10^4 < \mathrm{Re} < 10^6$ one can use the McAdams relation to calculate the friction factor [106]:

$$f = 0.184\mathrm{Re}^{-0.20} \tag{2.10}$$

In addition to the frictional losses, account is taken of the 'shock losses' associated with the entry of the coolant from the cool plenum into the channels and the exit from the channels

into the hot plenum. The total shock loss is given by [106]:

$$\Delta p_{\text{shock}} = \frac{1}{2}(K_c + K_e)\rho v^2 \tag{2.11}$$

where K_c and K_e are the compression and expansion loss coefficients. In the limit of the plenum being much larger than the channel, $K_c \approx 0.5$ and $K_e \approx 1$ [106].

2.3 Fuel temperature model

One of the limits which the core design must not breach is the maximum temperature in the fuel cermet. In order to determine the maximum temperature within the reactor it is necessary to model the temperature distribution within the fuel elements. First, the thermal conductivity of the fuel cermet must be established.

2.3.1 Thermal conductivity

In the absence of experimental data on the thermal conductivity of this material, a model must be relied on which combines the thermal conductivities of the constituent materials whose thermal conductivities are known. Husemeyer [51] found that the theoretical model which produced the most conservative (that is, lowest) values of the thermal conductivity was the implicit Bruggeman model [15]. For high volume filler fractions, the Bruggeman model is also considered to be the most appropriate of the classical 'effective medium theories' [86, 33]. In this model, the composite material is assumed to be composed of a continuous medium of one constituent containing dispersed spheres of the other constituent. For a continuous material with a thermal conductivity of k_1 containing a volume fraction χ of dispersed material with a thermal conductivity of k_2, the effective thermal conductivity of the composite material is given by k_e satisfying:

$$\left(\frac{k_2 - k_\text{e}}{k_2 - k_1}\right)^3 \frac{k_1}{k_\text{e}} = (1-\chi)^3 \tag{2.12}$$

The thermal conductivity of tungsten at different temperatures was taken from experimental data [48]. The thermal conductivity of uranium dioxide is based on an empirically derived formula [60]:

$$k = \frac{100}{7.5408 + 17.692t + 3.6142t^2} + \frac{6400}{t^{5/2}} \exp\left(\frac{-16.35}{t}\right) \tag{2.13}$$

where t is $T/1000$ and T is the temperature in Kelvin (K). Equation 2.12 is solved numerically for k_e in one degree temperature increments. The values obtained are shown in Figure 2.3

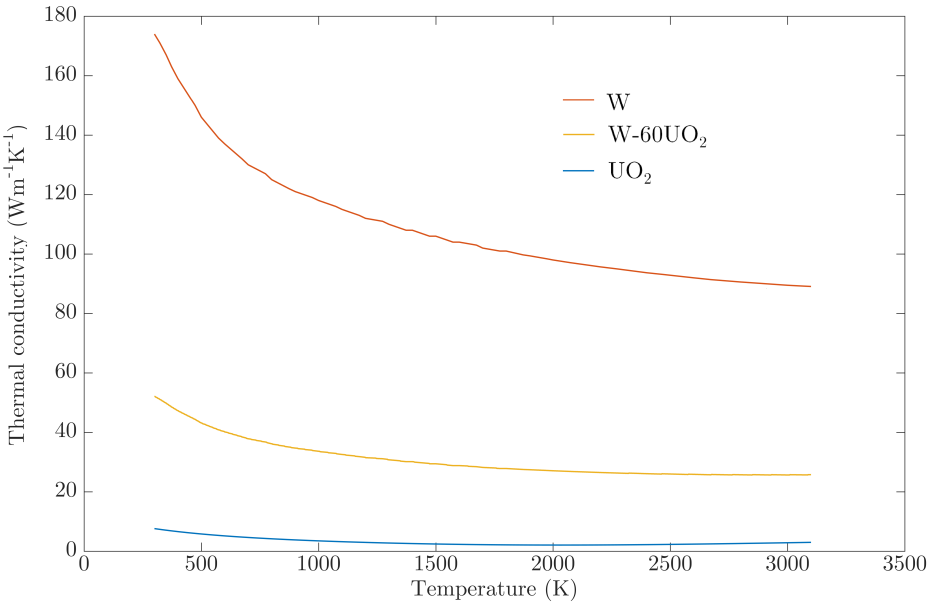

Fig. 2.3 Thermal conductivity of W-60UO$_2$ and its constituent materials

2.3.2 Heat transfer modelling

The temperature distribution within the cermet fuel element would ideally be determined using a two-dimensional finite element model which fully represents the hexagonal geometry. This is in contrast to the more familiar fuel pin arrangement where the radial temperature distribution is readily recognisable as a one-dimensional problem. However, it is possible to construct an approximate model of the hexagonal fuel element which results in a one-dimensional problem that is far more easily solved than the full two-dimensional treatment [106]. This method assumes that the hexagonal unit cell of a coolant channel can be approximated as circular with an 'equivalent annulus' which has the same area of fuel as in the hexagonal unit cell, as shown in Figure 2.4. For a hexagonal array of channels with pitch P the radius of the equivalent annulus is given by:

$$R_{EA} = P\sqrt{\frac{\sqrt{3}}{2\pi}} \tag{2.14}$$

It is assumed that the highest fuel temperature will occur at the point that is equidistant from (but between) neighbouring coolant channels. Therefore one assumes an adiabatic

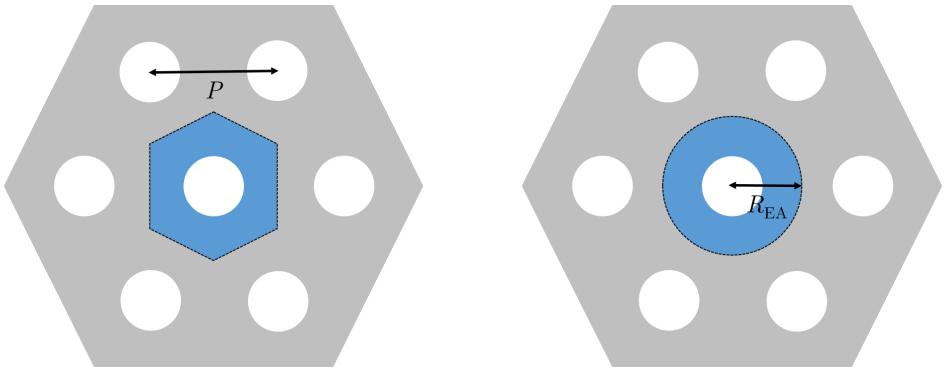

(a) Unit cell for central coolant channel for a pitch of P

(b) Equivalent fuel annulus with a radius of R_{EA}

Fig. 2.4 Approximation of hexagonal unit cell by equivalent annulus

boundary condition at the outer radius of the equivalent annulus. The boundary condition at the inside of the annulus is the channel wall temperature which is provided by the thermal hydraulic model described above. The annulus is divided up into ten sub-regions which are solved for individually so that the temperature dependence of the thermal conductivity is taken into account. One begins with the one-dimensional steady-state heat conduction equation in the radial direction [106]:

$$\frac{1}{r}\frac{\mathrm{d}}{\mathrm{d}r}\left(kr\frac{\mathrm{d}T}{\mathrm{d}r}\right)+q'''=0 \tag{2.15}$$

We also note that we have the following boundary conditions:

- The innermost radius is the channel wall whose temperature is given by Equation 2.3.
- The outermost radius is where the highest temperature in the cermet will occur so the temperature gradient will be zero.
- At the boundary between two zones the temperature and its gradient must be equal.

Equation 2.15 is then solved subject to these boundary conditions and one arrives at the following relation for the temperature at a point r_{n+1} based on the temperature at a more inner point r_n:

$$T_{n+1}=T_n+\frac{q'''}{4k_n}\left(r_n^2-r_{n+1}^2-2r_N^2\ln\frac{r_n}{r_{n+1}}\right) \tag{2.16}$$

where r_N is the outermost radius, where the maximum temperature is found (the outer radius of the equivalent annulus).

There is a potential shortcoming of this approach (in addition to its approximate nature) that should be noted at this stage. The hottest channel may not actually be surrounded by

other coolant channels in a hexagonal array - it may be at the edge or corner of a fuel element. In a moderated core, the fuel element may be completely surrounded by moderator and the outermost regions of the fuel element will see the highest thermal neutron flux. If the hottest coolant channel is indeed at the edge of a fuel element, a more sophisticated heat transfer model would be required since the region surrounding the channel is not radially symmetric. One would also need to consider the conduction of heat into the neighbouring moderator. The work of Husemeyer [51] showed that it can indeed be the case that the hottest point in the fuel occurs near the edge of the fuel element. The method currently used would therefore underestimate the peak fuel temperature.

There is a similar potential problem in the un-moderated core where fuel elements are adjacent to each other. At the interface between two fuel elements one can see that the nearest coolant channels are not in fact in a hexagonal arrangement but form the corners of a square. If the hottest point in the fuel occurs at the interface, finding the temperature of this point would require incorporating this square, rather than hexagonal, geometry. One would also need to make an assumption about how well heat conducts across the gap between fuel elements, perhaps including the effect of any outer cladding that may be added to the fuel elements. These various shortcomings of the one-dimensional heat conduction model are addressed at a later stage in the investigation.

2.4 Neutronic analysis

The initial tool chosen for neutronic analysis in this investigation is the Monte Carlo code Serpent [65]. The main advantage of Monte Carlo codes is that they are able to handle arbitrary geometries with ease and do not require consideration of how the various assumptions and approximations of deterministic methods might interact with a particular geometry. However, this comes at the cost of the considerably longer run-times that are required to reduce the associated statistical uncertainties to an acceptable level. This issue is compounded by the need to carry out burnup calculations to determine the reactivity at end of life, which multiplies the run-time by at least the number of burnup steps taken, compared to an analysis of just the fresh core. This long run-time can become prohibitively long when used in a context such as this, where many core designs might need to be analysed, even if an efficient search algorithm is employed to minimise the number of runs required. In the next chapter, the use of an alternative, deterministic, method is presented.

The input for Serpent consists of a single text file. Since various core configurations will be explored, it is appropriate to automate the process of producing these input files. In addition, the in-built macros within Serpent which simplify the input cater more for

the common geometry of cylindrical fuel pins immersed in coolant. The geometry of the tungsten cermet reactor considered here is fairly unusual and the input file is correspondingly more complex and cumbersome, making automation more attractive. To this end, code was produced in MATLAB which produces the input file based on a few input parameters which describe the core. These are:

- Coolant channel radius
- Number of rings of coolant channels per fuel element
- Radius (centre-to-flat) of the fuel/moderator elements
- Number of rings of fuel/moderator elements
- Reflector thickness
- Height of the core
- Moderator pattern (see Figure 2.1)
- Fuel enrichment level (93% or 20%)

2.5 Calculation routine: *coreFinder*

The overall structure of the calculation routine, which is referred to as *coreFinder*, is shown in Figure 2.5. This routine, for a given choice of fuel (HEU or LEU) and moderator pattern (see Figure 2.1), determines the core geometries that are both critical and satisfy the three specified limits of maximum fuel temperature, maximum coolant outlet temperature and maximum pumping power.

The calculation begins with two rings of fuel/moderator elements, plus the centre element (a total of 19). The first stage of the calculation is the thermal hydraulic analysis which determines the minimum coolant channel size which still satisfies the limits of maximum fuel temperature, maximum coolant outlet temperature and maximum pumping power. The exact method used to determine the minimum channel size for a given number of coolant channels is described in the following section. This process is carried out assuming one, two, three, four or five rings of coolant channels per fuel element. The configuration which has the lowest overall coolant flow area (and therefore the most fuel per fuel element) is selected. If it is the case that there is no combination of channel size and number of channels that satisfies the prescribed constraints, this means that the core is essentially too small and it is impossible to effectively remove the heat produced by it. Therefore, there is no point in

proceeding to the neutronics analysis stage. The core is increased in size by adding another ring of coolant/moderator elements such that the specific power is reduced.

If this is *not* the case, then the core is a suitable size from a thermal hydraulic perspective. The next stage is the neutronic analysis. The aim is to establish if there is a reflector thickness between the minimum and maximum that are allowable (these are fixed inputs) which makes this core critical. First, the minimum reflector case is run. If the core is critical with the minimum allowable reflector, then from a neutronic perspective there is no point in adding more fuel to the core, so this is the largest core that needs to be considered. If the core is not critical with the minimum reflector, the maximum thickness reflector is considered. If the core is *not* critical with this maximum reflector, then there is insufficient fuel in the core and the core size is increased by adding another ring of fuel/moderator elements.

If the current core *is* (at least) critical with the maximum reflector, then this means that there is some reflector size between the minimum and maximum that makes the core exactly critical, and is considered a suitable core size. The *coreFinder* routine then iteratively searches for this minimum size using the secant method. In order to reduce the considerable run-time of Serpent, variable fidelity is used in the secant search. The number of neutrons per cycle is fixed at 4,000 and the number of inactive cycles is fixed at 100. The maximum number of active cycles used, when convergence on k_{eff} is within 5,000pcm, is 300. This gives a statistical uncertainty in k_{eff} of around 100pcm at each burnup step. The number of burnup steps is kept fixed at 19 steps, with small initial steps to establish the saturated concentrations of various important fission products and a main step length of 184 days. The statistical error in k_{eff} at the end of life cannot be estimated without an ensemble of runs with different random number seeds. However, it can be seen from the progress of the secant searches that the chosen neutron population combined with a convergence criterion of 1,000pcm seems to correspond to finding the ideal reflector size to within around 1cm, which is adequate for this initial study.

Once the minimum reflector thickness has been found, the result is stored and another ring of assemblies is added to the core. At some point the code inevitably halts due to finding a large core that only requires the minimum reflector for criticality. The suitable cores that are found can then be compared in terms of overall mass, with the lowest mass being considered the most favourable.

This entire process can then be repeated for a different moderator pattern (Type 1, Type 2 etc.) or for a different choice of HEU or LEU fuel. For each run, one optimal core is produced. Five runs are carried out, one for the HEU fast reactor and one for each of the four moderator patterns using LEU fuel.

The geometry parameters that are variable within the calculation are the number of rings of coolant channels in each fuel element, the radius of the coolant channels, the number of fuel/moderator elements in the core and the reflector thickness. The other parameters and assumptions used are, with frequent reference to the 710 programme [38]:

- **Element diameter:** Initially this is chosen to remain constant at 4cm across the flats of the hexagon. During the 710 programme cermet elements were made with a diameter of approximately 3.6cm, so it is reasonable to assume that such an element could be fabricated. The size of the element could, of course, be allowed to vary; however, this adds a further layer of complexity to the process of finding suitable core geometries and a corresponding increase in calculation time. Once the WIMS code is implemented as the main neutronics tool it was envisioned that allowing for a further degree of freedom would be feasible.

- **Minimum channel size:** A lower limit must be placed on the size of the coolant channel based on what can be machined. The smallest channel radius produced during the 710 programme was 0.046cm, so the lower limit here is set at 0.05cm which one can be confident is achievable in practice.

- **Maximum channel size:** Clearly the coolant channels must not actually touch, but before this limit is reached the thickness of the fuel cermet between the channels will become very thin. A minimum allowable thickness must be set. A thin wall between coolant channels may create a weak area that is susceptible to damage; however, it is not clear how thin a wall is unacceptable. The thinnest wall seen in the 710 programme was 0.15cm so the same limit is taken here.

- **Number of coolant channels:** Initially the code is allowed to test assemblies with between one and five rings of coolant channels, again in line with the minimum and maximum considered in the 710 programme; however, if the code selects for the maximum allowable number of channels, the maximum could be increased for subsequent runs. There is no obvious reason why an arbitrary number of channels can not be produced, within the limits of the minimum channel size.

- **Reflector thickness:** The ‘thickness’ of the radial reflector is measured from the outermost point of the core to the edge of the reflector, where it is thinnest. Since the core is approximately hexagonal and the reflector is cylindrical, the ‘thickness’ stated in this way can give the impression of there being less reflector material than there actually is. The axial reflectors are the same thickness as that stated. Of course, in principle, the radial and axial reflector sizes could be allowed to vary independently.

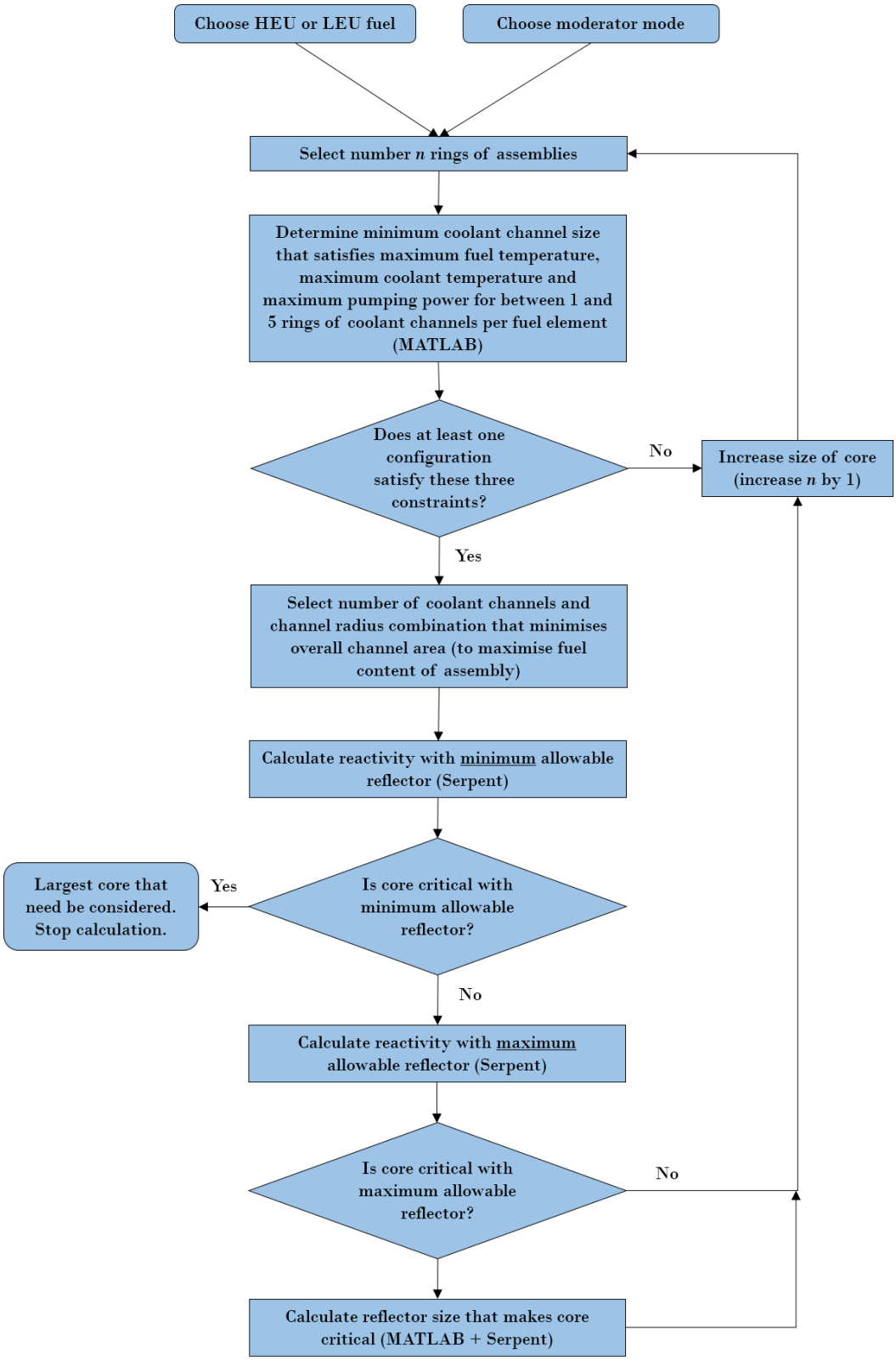

Fig. 2.5 Calculation structure for *coreFinder*

The minimum allowable thickness is zero, although this still leaves thin sections between the corners of the core. The maximum thickness has been set at 50cm. This is somewhat arbitrary, but could, of course, be increased if *coreFinder* selects for the maximum allowable value.

- **Maximum allowable coolant outlet temperature:** From a purely thermodynamic perspective one would like this to be as high as possible to achieve a high conversion efficiency. However, this must be compatible with both the reactor core and the conversion system. If a direct Brayton system is assumed for conversion, the maximum tolerable temperature of suitable turbine systems will impose a limit. The Prometheus project [118] adopted a coolant temperature limit of 1,150K in order to be able to use "conventional materials for the plant and energy conversion system and reduce pressure loading on the fuel element cladding". The 710 programme considered for its reference reactor a coolant outlet temperature of 1,170K. Other studies adopt coolant temperatures of above 1,300K [23, 22]. The more ambitious assumption of 1,300K is adopted here.

- **Coolant inlet temperature:** The inlet temperature depends on the size and number of turbine stages, the number (if any) of recuperator stages and the size and efficiency of the radiators. The choice of these systems and their impact on conversion efficiency must be weighed against their mass in a full-system analysis which is not carried out at this stage. For a space power system it is reasonable to suppose that a temperature drop of 400K is feasible [72, 119] giving a core inlet temperature of 900K.

- **Pumping power:** If we assume a direct Brayton system, the pumping is provided by the compressor. At this initial stage the pumping power is assumed to be limited to 10% of the thermal power (4MW) giving a maximum pumping power of 0.4MW. The approach taken is to allow any pumping power up to this limit and to reduce the coolant flow area as far as possible before breaching material limits. Currently no credit is given to cores that use less than the maximum pumping power, although this only occurs when the coolant flow area is restricted by the minimum channel size. Once models are established for the remainder of the power system in Chapter 4 the impact of the pressure loss in the core is accounted for more explicitly.

- **Working pressure:** At this stage, the analysis will be carried out at 3MPa (as per the 710 reactor). The working pressure has implications for the entire power system through its effects on fluid properties, as well as impacting the required thickness, and therefore mass, of the core pressure vessel and piping.

- **Maximum fuel temperature:** The constituent materials of the fuel cermet both have very high melting temperatures. Uranium dioxide melts at 3,120K [34] and pure tungsten at 3,695K [66]. However, one would expect that some undesirable phenomena such as cracking may occur before the onset of melting. During the 710 programme, some investigation was carried out on the heat tolerance of cermet fuel elements. An element composed of W-60UO_2, as is considered here, was held at a temperature of 1,566K for 5,000 hours. This sample was found to still have a continuous bond with its cladding and contained no cracking. Therefore, for this stage of the investigation, the maximum allowable fuel temperature is set at 1,500K.

2.6 Finding the minimum channel area

As shown in Figure 2.5, the calculation routine seeks to find the smallest possible core by minimising the total area of the fuel element that is occupied by coolant channels. The method by which it does this explained with reference to Figure 2.6.

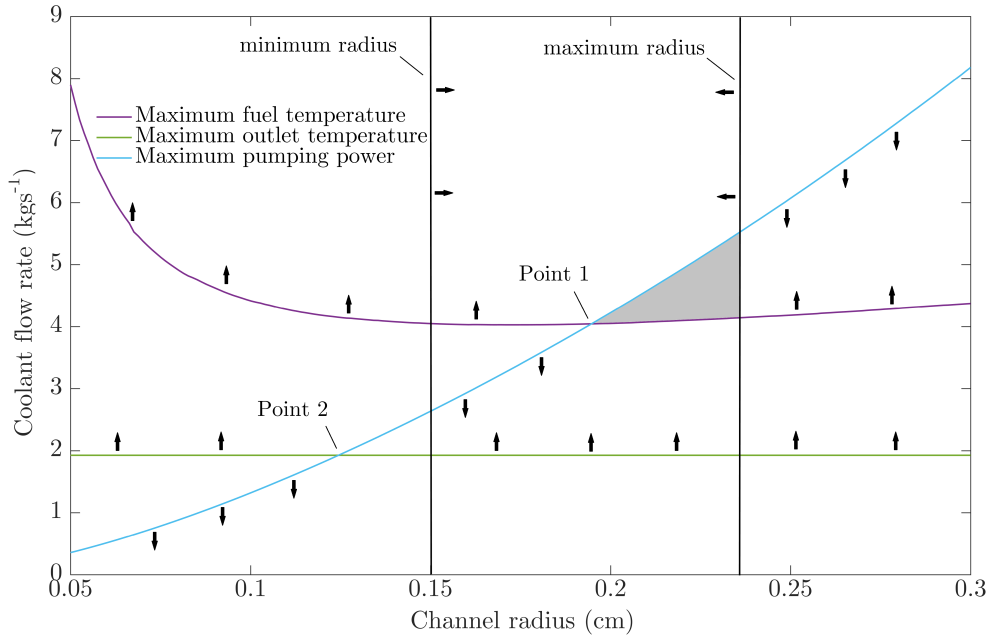

Fig. 2.6 Coolant flow rates which result in reaching the maximum pumping power, fuel temperature and outlet temperature limits. The shaded area indicates where all limits are satisfied. This is the area below the maximum pumping power (blue) but above the pumping powers which breach the fuel or outlet temperature limits (purple and green) and between the minimum and maximum machinable channel radii. The smallest permissible channel radius is given by the higher of Points 1 and 2 (in this case, Point 1)

This graph shows, for a fixed number of coolant channels, the total coolant flow rates at each channel radius which breach the pumping power (a maximum flow rate) and the fuel and outlet temperature limits (minimum flow rates). Along with the minimum and maximum allowable channel radii (as described above) these curves describe an allowable area. The goal then is to find the minimum channel radius that falls within this zone. Rather than searching through all possible channel radii, the code solves numerically using the secant method to find the intersection of the lines describing the maximum pumping power and each of the fuel and outlet temperature limits. These are shown as Point 1 and Point 2 in Figure 2.6. Whichever of these has the higher channel radius is the solution giving the minimum allowable channel radius. In the case that the solution lies below the overall allowable minimum, the code returns this as the solution and gives the required pumping power. If the solution is above the overall maximum channel radius, then this particular geometry is rejected.

One can see that the curve for the maximum fuel temperature is U-shaped. This is because, as the channel radius increases, the volume of fuel in each element is reduced so the volumetric heat rate must increase accordingly to satisfy the fixed total power. Eventually this increase in volumetric power is sufficient to offset the increase in the area of the coolant channel wall and the decrease in distance from the hottest point to the coolant channels.

2.7 Reactor power shape

To accurately model the thermal hydraulics of a reactor core, information is required about the power distribution within it. This is ordinarily provided by a neutronics code such as Serpent. Further, reactor analysis ideally reflects the impact of temperature changes on the core neutronics, since nuclear cross sections are temperature-dependent. Therefore, 'coupled' analysis is often carried out where information flows in both directions between neutronic and thermal hydraulic codes. One implication of this coupled approach is that several executions of each code are typically required to converge their respective solutions. Since this initial stage uses a Monte Carlo neutronic analysis, where calculation time is already significant, a simpler approach is taken. First, the *coreFinder* routine is run assuming a flat power shape for the thermal hydraulics analysis and finds minimum mass cores that are simply critical with a fresh core. The neutronics calculation also assumes a flat temperature profile across the core. For each of the five core types (fast reactor and moderated Types 1 to 4, see Figure 2.1) the 'peaking factor' is determined. This is simply the ratio of the power of the hottest fuel element to the average power. This peaking factor is then assumed to apply to all core designs of that moderator type. The details of the core designs that result from this analysis

are shown in Table 2.1. The power shape for each of these cores is shown in Figure 2.7, along with the corresponding peaking factor calculated.

Table 2.1 Critical at start of life cores found by *coreFinder* assuming a radially flat power shape.

	Fast reactor	**Type 1**	**Type 2**	**Type 3**	**Type 4**
Fuel	HEU	LEU	LEU	LEU	LEU
Fuel elements	37	90	60	19	19
Moderator elements	0	37	31	42	42
Total elements	37	127	91	61	61
Coolant channels per element	19	7	7	37	37
Coolant channel radius (mm)	1.7	1.6	2.3	1.5	1.5
Reflector thickness (cm)	4.8	7.3	9.6	7.6	7.7
Overall diameter (cm)	37.7	66.5	63.2	51.2	51.4
Cermet mass (kg)	174	865	465	107	107
Moderator mass (kg)	0	147	104	116	116
Reflector mass (kg)	81	412	420	221	225
Total mass (kg)	255	1,424	990	444	447

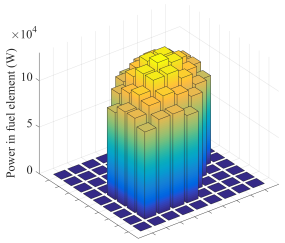

(a) No moderator
Peaking factor = 1.20

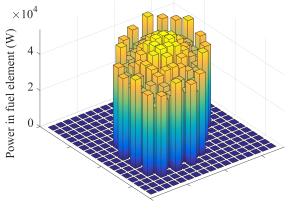

(b) Moderator Type 1
Peaking factor = 1.21

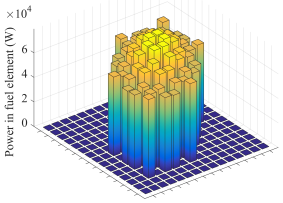

(c) Moderator Type 2
Peaking factor = 1.19

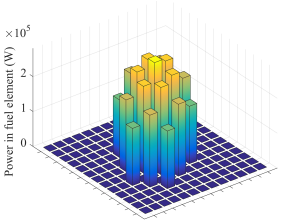

(d) Moderator Type 3
Peaking factor = 1.33

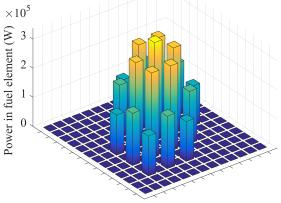

(e) Moderator Type 4
Peaking factor = 1.60

Fig. 2.7 The per-fuel element power distribution for each of the initially critical cores

2.8 Results

Running the *coreFinder* routine for the five core types considered gives a minimum mass core in each case that satisfies the thermal, pumping power and reactivity limits imposed. The details of these core designs are shown in Table 2.2. These results provide an initial indication of the impact of choosing LEU fuel over HEU, for the simplest case of just considering the core mass as the measure of value. The lowest mass LEU core uses the Type 3 core design, with a mass of 2,235kg, compared to the HEU fast reactor design which has a mass of 543kg. The LEU 'penalty', then, would in this case be an increase in core mass by a factor of approximately four.

By inspecting the results in Table 2.2 it can be seen which of the imposed limits have been met in each design. The first thing one notices is that the imposed minimum channel radius is frequently encountered. In these cases, *coreFinder* is indifferent to which of the other limits is met, so these results are not hugely informative except that they identify the current minimum channel radius as being restrictive. In cases where the minimum channel radius has not been chosen, two of the other three limits (fuel temperature, outlet temperature, pumping power) are met. This is as expected, which can be seen by referring to Figure 2.6. It can also be seen that cores with relatively few fuel assemblies (such as the third HEU fast reactor design) are restricted by the maximum fuel temperature, because the fixed total thermal power of 4MW is spread over a smaller amount of fuel, resulting in a high power density. For core designs with more fuel assemblies, the first limit reached is that of the maximum coolant outlet temperature. As mentioned previously, no credit is given in this algorithm for using less than the maximum allowable pumping power, so it will always maximise the pumping power in order to minimise the coolant flow area. Once the power conversion system is included in the modelling, this simplistic approach to the pumping power can be revised.

Table 2.2 Final output of *coreFinder*. Minimum mass cores that remain critical at end of seven year life (EOL) and satisfy thermal, pumping power and manufacturing limits. Shaded cells indicate where these limits have been met.

Reactor type	Fuel	Core rings	Coolant channels per element	Channel radius (mm)	Max fuel temp. (K)	Outlet temp. (K)	Pumping power (kW)	Reflector thickness (cm)	k_{eff} @ EOL	Fuel mass (kg)	Moderator mass (kg)	Reflector mass (kg)	**Total mass (kg)**
Fast	HEU	3	37	1.50	1500	1222	178	12.7	1.0016	154	0	1,422	**1,576**
Fast	HEU	4	19	1.50	1500	1255	236	1.1	1.0014	363	0	180	**543**
Fast	HEU	5	7	2.06	1497	1175	400	0.0	1.1632	683	0	153	**836**
Type 1	LEU	6	7	1.93	1497	1226	400	27.1	1.0035	805	352	11,699	**12,856**
Type 1	LEU	7	7	1.51	1462	1300	400	13.9	1.0022	1,396	406	5,337	**7,139**
Type 1	LEU	8	7	1.50	1417	1300	330	5.1	1.0008	1,870	758	2,301	**4,928**
Type 1	LEU	9	7	1.50	1379	1300	210	0.4	1.0014	2,813	847	926	**4,586**
Type 1	LEU	10	7	1.50	1360	1300	180	0.0	1.0473	3,552	1,397	1,063	**6,012**
Type 2	LEU	6	7	2.00	1497	1216	400	21.5	1.0032	748	409	7,944	**9,101**
Type 2	LEU	7	7	1.58	1482	1300	400	8.4	1.0003	1,201	603	2,905	**4,710**
Type 2	LEU	8	7	1.50	1423	1300	367	1.7	1.0032	1,726	907	1,105	**3,738**
Type 2	LEU	9	7	1.50	1387	1300	267	0.0	1.0366	2,411	1,264	787	**4,462**
Type 3	LEU	6	19	1.63	1497	1296	400	13.9	1.0009	362	799	4,173	**5,333**
Type 3	LEU	7	19	1.51	1432	1300	400	0.2	1.0008	544	1,250	440	**2,235**
Type 3	LEU	8	7	2.21	1499	1255	400	0.0	1.0995	837	1,790	564	**3,191**
Type 4	LEU	6	37	1.50	1441	1301	363	50.0	0.9992	285	856	37,030	**38,171**
Type 4	LEU	7	19	2.01	1500	1284	400	27.8	1.0005	335	1,448	14,693	**16,476**
Type 4	LEU	8	19	1.66	1417	1297	400	0.0	1.0508	668	1,939	564	**3,171**

2.9 Summary

An initial investigation into the mass of a $4MW_{th}$ reactor core was carried out with a single choice of core materials. This aimed to quantify the impact on the core mass of choosing an LEU over a HEU fuel. A simple scheme *coreFinder* was created to search for minimum mass core designs from four possible choices of moderator amount and layout and one unmoderated design. The output of this was the finding that the uplift in core mass caused by choosing LEU was approximately a factor of four increase. The thermal hydraulic analysis was fairly rudimentary, considering only a single coolant channel in order to determine the maximum fuel temperature, neglecting the likely lower limit imposed by the moderator. It did, however, provide valuable experience in generating arbitrary core designs as needed within Serpent. It was also a valuable exercise in determining a scheme to search for a minimum mass core, taking into account the prescribed constraints of fuel temperature, pumping power, outlet temperature and core reactivity.

2.10 Next steps

The analysis up to this point focussed on one choice of core materials: a tungsten cermet fuel with a zirconium hydride moderator and a beryllium oxide reflector. It also considers the reactor core in isolation, without reference to the wider power system. Before moving on to consider other possible core materials and incorporating the mass of the conversion system, it is clear that the Monte Carlo neutronics code Serpent has a run-time that is unsuitably long for this type of investigation, which necessarily involves analysis of a large number of different core designs. One of the next areas of development is therefore the adoption of a faster deterministic neutronics analysis tool. Additionally, the analysis so far has used a fairly simple 1-D approximation of heat transfer within the fuel block and considers only the hottest coolant channel in the reactor. Perhaps more importantly, the temperature limits of the moderator, which may be more restrictive than those of the fuel, have not been considered. These limitations will be addressed in the next chapter.

Chapter 3

TRISO core design

3.1 Deterministic neutronics modelling

As mentioned at the close of the previous chapter, the most obvious next area of development is the replacement of Serpent as the main neutronics tool with a deterministic tool to gain a significant improvement in calculation speed. The tool chosen is the WIMS modular reactor physics code [68]. In its traditional application, WIMS is used to carry out 'lattice physics' calculations. This refers to the analysis of assemblies of fuel pins, typically arranged in square or hexagonal lattices, or in annular clusters. The output of this analysis would be average effective cross section data for that assembly (or rather, a horizontal slice of an assembly) which could then be used in a full-core calculation in a code such as PANTHER [69]. In more recent years, with the addition of various new modules, WIMS has itself become suitable for carrying out full-core calculations.

Before proceeding, it is worth covering the basic theory behind the various methods used in WIMS and other deterministic neutronics tools.

3.1.1 The neutron transport equation

If the density of neutrons with position $\mathbf{r}$, travelling in a direction $\boldsymbol{\Omega}$ with energy E at time t is $N(\boldsymbol{r},\boldsymbol{\Omega},t,E)$ and they have a speed of v, then we can define the neutron flux as:

$$\psi(\boldsymbol{r},\boldsymbol{\Omega},t,E) = vN(\boldsymbol{r},\boldsymbol{\Omega},t,E) \tag{3.1}$$

This is often referred to as the angular flux. Integrating this quantity over all angles results in the useful direction independent or scalar flux:

$$\int_{4\pi} \psi(\boldsymbol{r},\boldsymbol{\Omega},t,E)d\boldsymbol{\Omega} = \phi(\boldsymbol{r},t,E) \tag{3.2}$$

The scalar flux is a somewhat mathematical construct that might be best understood as the link between two more physical quantities: the reaction rate per unit volume and the macroscopic cross section for that reaction, labelled as reaction i:

$$R_i(r,t) = \int_0^\infty \phi(\boldsymbol{r},t,E)\Sigma_i(E)dE \tag{3.3}$$

By considering a differential control volume and the conservation of neutrons within it and in the absence of external sources [12], one can arrive at the steady-state form of the neutron transport equation:

$$\begin{aligned} &\boldsymbol{\Omega}\cdot\boldsymbol{\nabla}\psi(\boldsymbol{r},\boldsymbol{\Omega},E) + \Sigma_t\psi(\boldsymbol{r},\boldsymbol{\Omega},E) \\ &= \frac{\chi_{\text{eff}}(\boldsymbol{r},E)}{4\pi k_{\text{eff}}}\int_0^\infty\int_{4\pi} \nu(E')\Sigma_f(\boldsymbol{r},E')\psi(\boldsymbol{r},\boldsymbol{\Omega}',E')dE'd\Omega' \\ &\quad + \int_0^\infty\int_{4\pi} \Sigma_s(\boldsymbol{r},\boldsymbol{\Omega}'\rightarrow\boldsymbol{\Omega},E'\rightarrow E)\psi(\boldsymbol{r},\boldsymbol{\Omega}',E')dE'd\Omega' \end{aligned} \tag{3.4}$$

The left hand side of this equation accounts for removals from the angular flux at $\boldsymbol{r}$ with direction $\boldsymbol{\Omega}$ and energy E and the right hand side to contributions to it. The first term accounts for streaming of neutrons out of the control volume. The second term accounts for all interactions between neutrons and matter, using the 'total' cross section, including scattering to new angles and energies or being absorbed. The first term on the right hand side is the fission term. Fissions from all possible energies E' are summed, with each fission resulting in the production of $\nu(E')$ neutrons. The probability density function $\chi_{\text{eff}}(\boldsymbol{r},E)$ accounts for the energy distribution of neutrons produced by fission. The final term accounts for neutrons being scattered from all angles and energies to an angle $\boldsymbol{\Omega}$ and energy E. Finally, time independence is enforced by the inclusion of the k-eigenvalue in the fission term, which we can identify as the familiar multiplication factor k_{eff}.

3.1.2 The P_N approximation

The neutron transport equation is not generally solvable for most problems in the form shown in Equation 3.4. One helpful simplification is to express the angular flux and the differential scattering cross sections as a functional expansion. In the P_N method, Legendre polynomials

are used. The first Legendre polynomials are:

$$\begin{aligned} P_0(\mu) &= 1 \\ P_1(\mu) &= \mu \\ P_2(\mu) &= \tfrac{1}{2}(3\mu^2 - 1) \\ P_3(\mu) &= \tfrac{1}{2}(5\mu^2 - 3\mu) \end{aligned} \tag{3.5}$$

Higher order polynomials can be generated using the following recursion relation:

$$(2n+1)\mu P_n(\mu) = (n+1)P_{n+1}(\mu) + nP_{n-1}(\mu) \tag{3.6}$$

One feature of the Legendre polynomials is that they are orthogonal:

$$\int_{-1}^{1} P_m(\mu)P_n(\mu)d\mu = \frac{2\delta_{mn}}{2n+1} \tag{3.7}$$

where the Kronecker delta δmn is equal to 1 when $m = n$ and zero otherwise.

For ease of understanding, the following derivation [99] applies to the case of an infinite slab such that the spatial variability of the flux is along one dimension only, but a similar procedure can be carried out in spherical and cylindrical coordinates. First, the angular flux is approximated by expanding its angular dependence using the first $N+1$ Legendre polynomials:

$$\psi(x,\mu) = \sum_{n=0}^{N} \frac{2n+1}{2}\phi_n(x)P_n(\mu) \tag{3.8}$$

Note that μ is now defined as $\mu = cos\theta$. We also define μ_0 as the cosine of the angle θ_0 between the original direction θ' and the new direction after a scattering event θ. Now, the differential scattering cross section can also be defined in terms of a series of Legendre polynomials:

$$\Sigma_s(x,\mu_0) = \sum_{n=0}^{N} \frac{2n+1}{2}\Sigma_{sn}(x)P_n(\mu_0) \tag{3.9}$$

These can then be substituted into the one-dimensional (plus angle) version of the neutron transport equation. After some manipulation, including invoking the orthogonality of the Legendre polynomials, one arrives at the $N+1$ P_N equations. Note that the fission term is not explicit and appears within the source term $S(x,\mu)$ which then becomes the $S_n(x)$ terms

below:

$$\frac{d\phi_1(x)}{dx} + (\Sigma_t - \Sigma_{s0})\phi_0(x) = S_0(x) \quad , \quad n = 0 \tag{3.10}$$

$$\frac{n+1}{2n+1}\frac{d\phi_{n+1}(x)}{dx} + \frac{n}{2n+1}\frac{d\phi_{n-1}(x)}{dx} + (\Sigma_t - \Sigma_{sn})\phi_n(x) = S_n(x) \quad , \quad n = 1...N \tag{3.11}$$

This set of $N+1$ equations has $N+2$ unknowns. This problem can be resolved by assuming the $d\phi_{N+1}/dx$ term in the final equation is zero, thus removing one unknown and closing the equations.

3.1.3 Diffusion theory

Using a series expansion is most useful when truncating it is expected to result in a reasonable approximation. Taking just the first two equations and closing them by assuming that $d\phi_2/dx = 0$ produces the P_1 equations [99]:

$$\frac{d\phi_1}{dx} + (\Sigma_t - \Sigma_{s0})\phi_0 = S_0 \tag{3.12}$$

$$\frac{1}{3}\frac{d\phi_0}{dx} + (\Sigma_t - \Sigma_{s1})\phi_1 = S_1 \tag{3.13}$$

Integrating the scattering cross section expansion (Equation 3.9) over all angles (or equivalently, all cosines μ), one sees that the zeroth moment $\Sigma_{s0} = \Sigma_s$, the total scattering cross section. Additionally, $\Sigma_{s1} = \overline{\mu}_0\Sigma_s$, where $\overline{\mu}_0$ is the mean cosine of the scattering angle. If we make the additional assumption that the neutron source is isotropic ($S_1 = 0$), the second P_1 equation results in Fick's Law, giving the neutron current as the gradient of the scalar flux:

$$\phi_1(x) \equiv J(x) = -\frac{1}{3(\Sigma_t - \overline{\mu}_0\Sigma_s)}\frac{d\phi_0}{dx} \tag{3.14}$$

When substituted into the first P_1 equation, we arrive at the neutron diffusion equation:

$$-\frac{d}{dx}\left[D_0(x)\frac{d\phi_0(x)}{dx}\right] + (\Sigma_t - \Sigma_s)\phi_0(x) = S_0(x) \tag{3.15}$$

where we define the diffusion coefficient and transport cross sections as:

$$D_0 \equiv \frac{1}{3(\Sigma_t - \overline{\mu}_0\Sigma_s)} \equiv \frac{1}{3\Sigma_{\text{tr}}} \tag{3.16}$$

Diffusion is a very commonly used technique in the analysis of nuclear reactors. For most thermal spectrum power reactors, the assumptions made in the diffusion approximation are

suitable. These are that the neutron flux has at most a linearly anisotropic angular dependence and that the neutron source has no significant linearly anisotropic component. Away from strong absorbers or material interfaces these are usually reasonable assumptions in power reactors.

3.1.4 Simplified P_3 (SP_3) method

The method shown above to reach the diffusion equation can be extended to higher moments, using gradients of the even-order moments of the flux to eliminate odd-order moments of the flux in the odd-order equations. Taking one step beyond diffusion to the P_3 equations and again assuming isotropic scattering and isotropic sources, we first make a change of variables to simplify the resulting equations [99]:

$$\begin{aligned} F_0 &= 2\phi_2 + \phi_0 \\ F_1 &= \phi_2 \end{aligned} \tag{3.17}$$

The four initial P_3 equations are then reduced to two coupled diffusion equations:

$$\begin{aligned} -\frac{d}{dx}\left(D_0\frac{dF_0}{dx}\right) + (\Sigma_t - \Sigma_{s0})F_0 &= S_0 + 2(\Sigma_t - \Sigma_{s0})F_1 \\ -\frac{d}{dx}\left(D_1\frac{dF_1}{dx}\right) + \left[\frac{5}{3}(\Sigma_t - \Sigma_{s2}) + \frac{4}{3}(\Sigma_t - \Sigma_{s0)}\right]F_1 &= -\frac{2}{3}S_0 + \frac{2}{3}(\Sigma_t - \Sigma_{s0})F_0 \end{aligned} \tag{3.18}$$

Unlike diffusion, developing the P_3 equations in three dimensions does not result in an easily solvable set of equations. One approximation [39] that has seen implementation [11] is to simply take the above equations, which are developed for a one-dimensional slab geometry, and replace the differentials dx with the three-dimensional $\boldsymbol{\nabla}$ operator.

3.1.5 Collision probability method

The collision probability is another method that has historically been used extensively for reactor analysis. In more recent years it has been largely superseded by the Method of Characteristics (MoC) for many problems, but will be briefly described as it is the basis of some WIMS modules that will be made use of in this project.

First, the concept of an optical path length is introduced, defined as:

$$\alpha(\boldsymbol{r}', \boldsymbol{r}) \equiv \left| \int_{\boldsymbol{r}'}^{\boldsymbol{r}} \Sigma_t(R) dR \right| \tag{3.19}$$

This quantifies the likelihood that a neutron travelling from $\boldsymbol{r}'$ to $\boldsymbol{r}$ through a medium with total cross section Σ_t will undergo an interaction. Applied to the simplest case of a point isotropic neutron source of strength S_0, it can be used to calculate the flux at a distance from the source [99]:

$$\psi(R) = \frac{S_0 e^{-\alpha(\boldsymbol{r}',\boldsymbol{r})}}{4\pi|\boldsymbol{r}-\boldsymbol{r}'|^2} = \frac{S_0 e^{-\alpha(R,0)}}{4\pi R^2} \tag{3.20}$$

This concept can then be extended to a many-region problem. For each pair of regions i and j, within which we assume flat fluxes and cross sections, we can calculate a first-flight transmission probability $T^{j\to i}$:

$$T^{j\to i} \equiv \frac{1}{V_i}\int_{V_i} d\boldsymbol{r}_i \int_{V_j} d\boldsymbol{r}_j \frac{e^{-\alpha(\boldsymbol{r}_i,\boldsymbol{r}_j)}}{4\pi|\boldsymbol{r}-\boldsymbol{r}'|^2} \tag{3.21}$$

These can be calculated by considering many tracks of different angles through the geometry to produce an estimate of each $T^{j\to i}$. The fluxes in different regions can then be related by the following relation, resulting in a solvable problem:

$$\phi_i = \sum_j T^{j\to i}\left[(\Sigma_{sj} + \nu\Sigma_{fj})\phi_j + S_{0_j}\right] \tag{3.22}$$

3.1.6 Method of Characteristics

The neutron transport equation can be transformed into a much more tractable form by considering neutron flight paths along specified directions [6]. First, we re-write the full steady-state transport equation but with a simpler representation, where all possible contributions to $\psi(\boldsymbol{r},\boldsymbol{\Omega},E)$ are gathered into a single neutron source $Q(\boldsymbol{r},\boldsymbol{\Omega},E)$, giving:

$$\boldsymbol{\Omega}\cdot\boldsymbol{\nabla}\psi(\boldsymbol{r},\boldsymbol{\Omega},E) + \Sigma_t(\boldsymbol{r},E)\psi(\boldsymbol{r},\boldsymbol{\Omega},E) = Q(\boldsymbol{r},\boldsymbol{\Omega},E) \tag{3.23}$$

A change of variables is made, referring to every point $\boldsymbol{r}$ using a matching reference point $\boldsymbol{r}_0'$ and angular direction vector $\boldsymbol{\Omega}'$, so that $\boldsymbol{r} = \boldsymbol{r}_0' + s\boldsymbol{\Omega}'$. The neutron transport equation now takes the form:

$$\boldsymbol{\Omega}\cdot\boldsymbol{\nabla}\psi(\boldsymbol{r}_0+s\boldsymbol{\Omega},\boldsymbol{\Omega},E) + \Sigma_t(\boldsymbol{r}_0+s\boldsymbol{\Omega},E)\psi(\boldsymbol{r}_0+s\boldsymbol{\Omega},\boldsymbol{\Omega},E) = Q(\boldsymbol{r}_0+s\boldsymbol{\Omega},\boldsymbol{\Omega},E) \tag{3.24}$$

Now, differentiating with respect to s along a particular direction results in the characteristic form of the neutron transport equation:

$$\frac{d}{ds}\psi(\boldsymbol{r}_0+s\boldsymbol{\Omega},\boldsymbol{\Omega},E)+\Sigma_t(\boldsymbol{r}_0+s\boldsymbol{\Omega},E)\psi(\boldsymbol{r}_0+s\boldsymbol{\Omega},\boldsymbol{\Omega},E)=Q(\boldsymbol{r}_0+s\boldsymbol{\Omega},\boldsymbol{\Omega},E) \tag{3.25}$$

To simplify, we assume the dependence of s on $\boldsymbol{r_0}$ and $\boldsymbol{\Omega}$, simply writing $\boldsymbol{r_0}+s\boldsymbol{\Omega}$ as s. The characteristic equation then takes the form:

$$\frac{d}{ds}\psi(s,\boldsymbol{\Omega},E)+\Sigma_t(s,E)\psi(s,\boldsymbol{\Omega},E)=Q(s,\boldsymbol{\Omega},E) \tag{3.26}$$

This differential equation is of a standard type that is solvable with an integrating factor:

$$I=\exp\left(-\int_0^s ds'\Sigma_t(s',E)\right) \tag{3.27}$$

Using this, we find the solution for the flux along a particular track:

$$\psi(s,\boldsymbol{\Omega},E)=\psi(\boldsymbol{r}_0,\boldsymbol{\Omega},E)e^{-\int_0^s ds'\Sigma_t(s',E)}+\int_0^s ds''Q(s'',\boldsymbol{\Omega},E)e^{-\int_{s''}^s ds'\Sigma_t(s',E)} \tag{3.28}$$

In practice, many sets of parallel tracks are overlaid on the geometry at many different angles. The geometry is discretised into mesh cells with assumed flat fluxes and cross sections within them. Each mesh cell then contributes to the above integrals as tracks cross them. In practice, the MoC method is normally only used in two-dimensional problems due to the high computational cost (including memory usage) of a fully three-dimensional treatment, unless the problem is very small.

3.2 Modelling tungsten-based core in WIMS

Within WIMS there are a number of different possible methods of producing the required quantities of end-of-life criticality and power distribution. A number of steps are generally required in a fully deterministic neutronics model before the final full-core calculation can be carried out. These steps generally involve calculations at a small scale (such as a single fuel pin) with detailed geometry and fine energy group structure. The purpose of these intermediate calculations is to prepare cross section data for the final full-core calculation. Frequently these data will relate to simplified, homogenised geometry with fewer energy groups.

The first main step in this process when using WIMS is the ‘self-shielding’ calculation, often carried out at the level of a single fuel pin or an assembly of pins. Self-shielding is an

effect which occurs due to resonance absorption, relevant in the intermediate energy range of around 1eV to 100keV. In this energy range the neutrons are mainly absorbed in one of many peaks in the absorption cross section occurring at resonance energies [12]. For a simple system, such as a single fuel pin sitting in a moderating medium such as water, it is simple to see how the self-shielding effect occurs. For neutrons in an energy group which contains a resonance entering a fuel pin, neutrons near the resonance energy are far more likely to be absorbed than those that are not. They are therefore far less likely to reach the interior of the fuel pin, such that the energy spectrum of the neutrons will have a pronounced dip at the resonance energy which increases in magnitude moving from the pin periphery to its centre. The total amount of absorption by this particular resonance will therefore be overestimated if the effect on the flux shape is ignored. An adjustment to the group averaged cross section is therefore required. This adjustment is carried out by the HEAD module within WIMS, using equivalence theory. This well-established method has been widely used for decades in lattice codes but relies on a number of approximations that limit its applicability to simple geometries such as a simple pin cell, or a regular lattice of such pins.

Referring back to the four possible chequerboard layouts of fuel and moderator presented in the previous chapter, one can see that a single repeatable fuel-centred unit cell is not as immediately identifiable as with, say, the familiar rectangular lattice of fuel pins found in light water reactors. Nevertheless, one can initially just consider the Type 4 design which does have such an identifiable unit cell: a hexagonal fuel block surrounded by a hexagonal region of moderator. Hexagonal lattices are not unusual, being used in Russian VVER designs, so this in itself is not an issue when using HEAD or WIMS more generally, since common geometries are well catered for.

One alternative method of carrying out the self-shielding calculation within WIMS, instead of the equivalence treatment available in HEAD, is available in the WIMSECCO module, a WIMS-compatible version of the lattice code ECCO [93]. This is a European code developed specifically for modelling fast reactor assemblies. This is done using the collision probability method and a fine energy group structure of 1,968 groups. Not all nuclides are actually represented in the fine group library, just those that are generally important to reactor analysis. For less common or less important nuclides, ECCO refers to the standard WIMS 172 group library and simply maps the cross sections into the 1,968 group structure assuming they are flat in each of the 172 groups. Tungsten isotopes are in this latter group, about which more later.

WIMSECCO is often used in WIMS in fast reactor analysis. The reason for this is that the standard ‘XMAS 172’ energy group structure used in WIMS is intended principally for thermal spectrum systems, with only 31 groups in the fast (>0.18MeV) region. For more

accurate analysis of fast spectrum systems, ECCO carries out a two-dimensional analysis of fast-reactor fuel assemblies, which is then used to produce corrected cross sections in the 172 group structure for the next stage of the overall calculation. In fact, the documentation for WIMSECCO [2] suggests that it should give improved results compared to either the standard treatment in HEAD or even the sub-group method available via the PRES/RES route, without referring specifically to fast spectrum systems. It is therefore worth testing whether ECCO has improved performance against other methods for the present design, which contains an uncommon resonant absorber (tungsten) in large amounts with which HEAD may not cope well.

The success of the self-shielding calculation can be assessed by using the resulting adjusted cross sections to carry out a simple eigenvalue calculation. Reflective boundary conditions are applied to the hexagonal unit cell and k_{eff} calculated for this 'infinite' reactor.

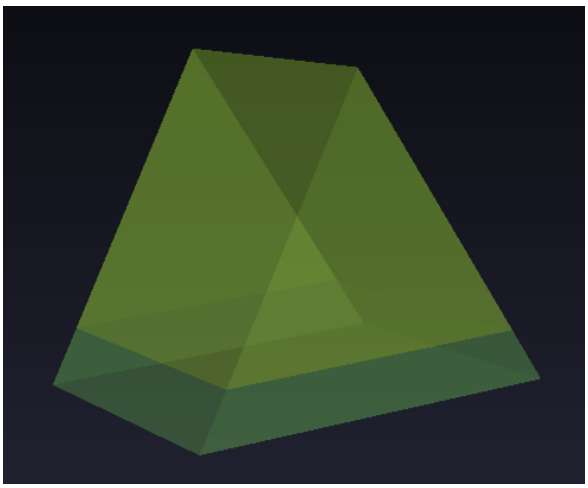

Fig. 3.1 60 degree segment in CACTUS3D with rotational symmetry used to create simple fuel-in-moderator hexagonal lattice

This can be achieved by passing the cross sections to the MoC solver, CACTUS3D. In fact, reflective boundary conditions with an overall hexagonal geometry are not possible in CACTUS3D, but a 60 degree segment with rotational symmetry achieves the same result. If the self-shielding calculation performs adequately, then reasonable agreement should be found with the equivalent calculation in Serpent. This test was carried out using the unit cell from a Type 4 design, which has a hexagonal block of tungsten cermet fuel of diameter 4cm surrounded by a concentric hexagon of zirconium hydride moderator of thickness 2cm. The results are shown in Table 3.1.

It is very clear from these results that the HEAD module alone can not be used for the tungsten cermet-based fuel. It is also interesting that, despite tungsten not being represented

Table 3.1 Comparison of k_{eff} for a unit cell to assess success of self-shielding calculation

Method	k_{eff}	Error vs Serpent (pcm)
Serpent	1.44406 ± 0.00029	-
WIMS (HEAD)	1.38825	5581
WIMS (ECCO)	1.43811	595

in the ECCO fine-group library, the effect of using ECCO is considerable. This is because, even though ECCO has no more information on tungsten cross sections than HEAD (both are using the standard 172 group library data), HEAD does not adjust the tungsten cross sections at all whilst ECCO does calculate an effective average cross section. This amounts to a very approximate self-shielding calculation. The magnitude of the effect of the ECCO calculation on the tungsten cross sections can be seen in Figure 3.2, where the absorption cross section is reduced in the resonance region. It should be recalled that the tungsten composition is assumed to be 95% enriched in the least absorbing isotope, W-184. There are also some minor differences in the calculated cross sections for other isotopes (most clearly in U-238) in the resonance region. This is not surprising given that fundamentally different methods are being used in HEAD and ECCO and also that ECCO accounts for the effect of tungsten on other isotopes and HEAD does not.

The k_{eff} results using cross sections from ECCO still differ from Serpent rather more than one might hope for such a simple pin-cell calculation, likely arising from the approximate nature of the treatment of tungsten. An error of 600pcm might be considered acceptable, depending on the performance of the final full-core calculation. Some time was invested in developing a computational route for modelling the entire core, but its performance was rendered largely irrelevant by the discovery that including burnup introduced a significant problem; burnup is, of course, an integral part of the neutronics model since its main purpose is to determine whether any given reactor design is critical at the end of its life.

3.2.1 Burnup calculations using ECCO

To explain this problem, it is first necessary to explain how WIMS is used in burnup calculations. Once the self-shielding calculation is carried out, the corrected cross sections for the nuclides present in the geometry can be passed to another module to calculate the neutron flux distribution in the full core, although often with some intermediate steps to homogenise the detailed geometry and reduce the number of energy groups. These full-core fluxes are then passed to the burnup module (called BURNUP in WIMS). In conjunction with

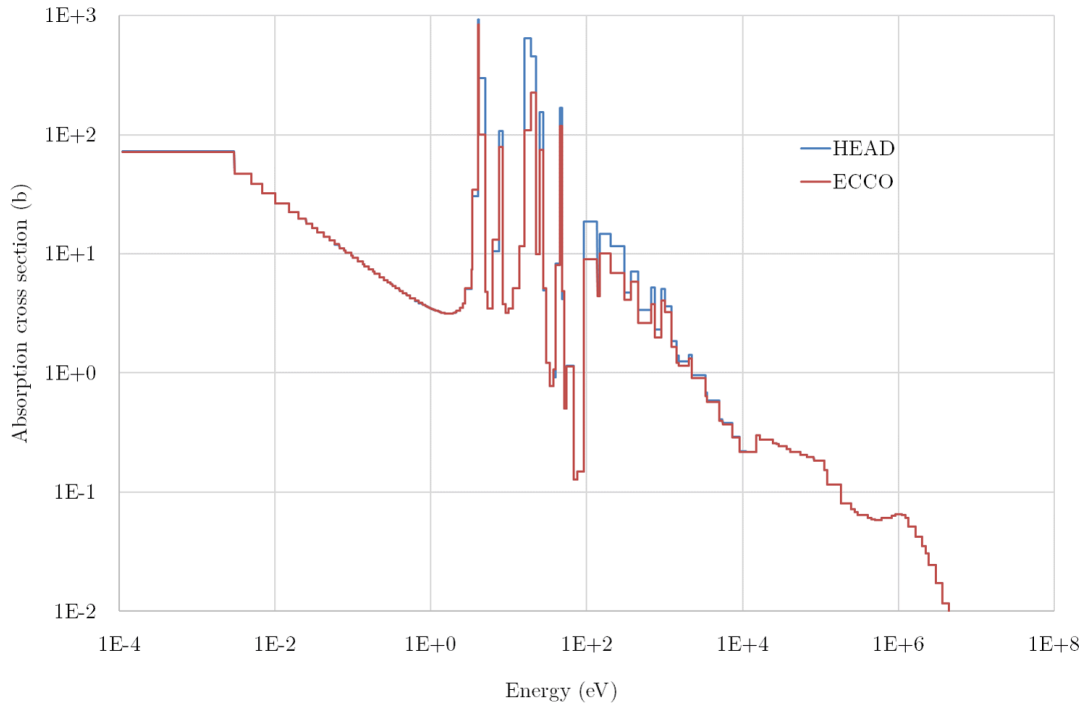

(a) Natural tungsten

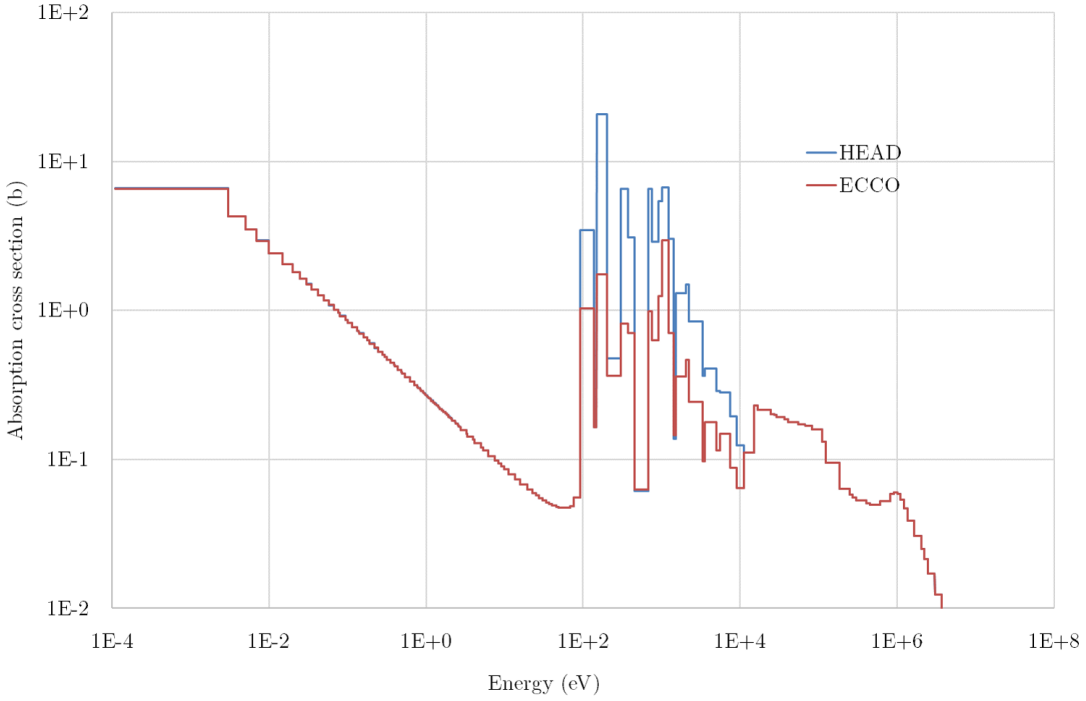

(b) W-184

Fig. 3.2 Absorption cross sections of natural tungsten and W-184 arising from HEAD and ECCO modules

a specified power and time step length, the burnup module calculates the change in isotopic compositions in the various materials. A number of processes are accounted for, principally the depletion of fissile materials, the accumulation of fission products and the capture of neutrons leading to the formation of new isotopes. Independent of the flux information, the decay of unstable isotopes is also accounted for. Once this new isotopic composition has been calculated, the overall calculation starts from the beginning with the new isotopic compositions. That is, the resonance self-shielding calculation is repeated at each burnup step.

For the results presented in Table 3.1, the cross sections for all nuclides present in the geometry are calculated either by HEAD or by ECCO in isolation. In a burnup calculation however, where a much larger number of nuclides are present, a different scheme is normally used. First, HEAD carries out its own shielding calculation for nuclides for which the relevant data is present. Then ECCO carries out a subsequent calculation but *only* for nuclides which are represented in the ECCO fine-group library. The resulting cross sections for these fine-group nuclides then overwrite those produced by HEAD, but leaving the coarse-group nuclide cross sections as being those produced by HEAD. The reason for this is that the execution time of ECCO increases with the number of nuclides present in the geometry; in a simple fresh-fuel eigenvalue calculation this might be a few tens of nuclides covering fuel, cladding, coolant and structural materials. After a burnup step, the fuel is populated with fission products, capture products and decay products, which is on the order of hundreds of nuclides. For most typical reactor designs, it is sufficient to include in the ECCO calculation only the most neutronically important common nuclides, which are represented in the ECCO fine-group library. Unfortunately, tungsten isotopes are not in this group and are therefore ignored by ECCO in a burnup calculation, reverting back to those produced by HEAD. The resulting k_{eff} results therefore also essentially revert to those produced in the HEAD-only calculation shown in Table 3.1 (before any burnup has actually taken place).

There is actually an option within ECCO which is not mentioned in the WIMS documentation[1] to include every nuclide present in the ECCO calculation. Unfortunately this leads to a significantly longer run-time, as shown in Table 3.2. This is not a commonly used function and is typically used for debugging or benchmarking purposes [3]. As discussed later, the self-shielding calculation will need to be carried out more than once in each burnup step, since different regions in the reactor experience different power levels and flux spectra. Multiplying the run-time for ECCO in its 'all-nuclides' mode by even a modest number

[1]The ANSWERS Software Service provided information on this functionality in private correspondence [3], invoked by including 'eccofp' as the final instruction in the ECCO input.

of burnup regions and burnup steps will lead to a significant run-time that is likely to be prohibitive in the context of assessing large numbers of core designs.

Table 3.2 Comparison of run-times for HEAD and ECCO

Case	Example run-time (seconds)
HEAD	0.1
ECCO: fine-group nuclides only	83
ECCO: all nuclides	510

In conclusion, the attempt to establish a methodology using the present version of WIMS (a development version of WIMS11) to carry out rapid analysis of a tungsten-cermet design was unsuccessful. Some possible avenues do remain in this area. For example, it is possible to manually manipulate cross sections by group and by nuclide. It has been suggested [67] that the tungsten cross sections produced by ECCO and HEAD could be compared and the ratio between them calculated for each energy group. It could then be assumed that this ratio persists throughout burnup. Then HEAD could be used in the main calculation but the cross sections for tungsten manually adjusted by the relevant ratio. Another remedy could come in the form of new cross section data: if the main WIMS library included "shieldable data", then HEAD should be able to adequately handle tungsten. There are plans to include this data in future WIMS data libraries [3]. These avenues were not explored further.

The aim of the overall project is not to assess the suitability of a tungsten-cermet fuel form per se, or indeed any specific fuel form, but to investigate how the use of higher or low-enriched uranium affects the system mass. There are many potential fuel form candidates. It was therefore decided to change the fuel form to another with better prospects for analysis within WIMS, since this should make possible the analysis of large numbers of reactor designs in a reasonable time. The form chosen is a particulate fuel in a graphite matrix.

3.3 TRISO fuel design

3.3.1 TRISO fuel

Tri-structural isotropic (TRISO) fuel particles are an alternative fuel form proposed for various reactor designs, generally with the aim of achieving high coolant temperatures and high burnup. These particles consist of a central spherical fuel kernel surrounded by four concentric spherical shells, as shown in Figure 3.3, and have an overall diameter of around 1mm.

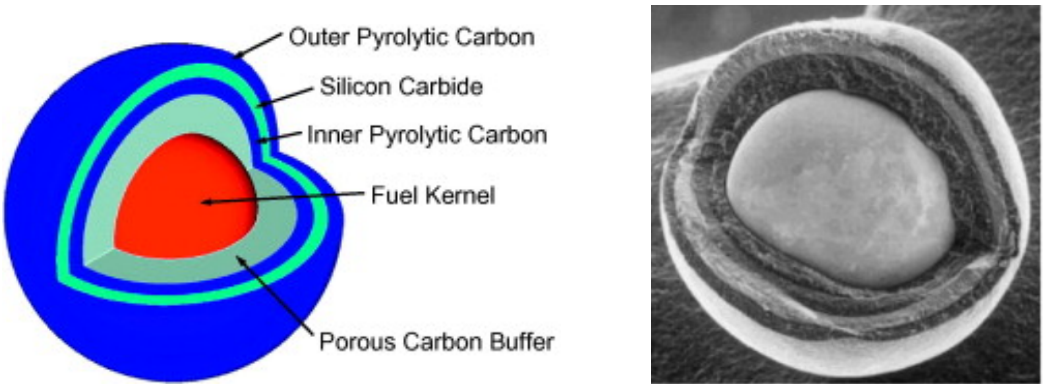

(a) Cutaway diagram

(b) Scanning electron microscope (SEM) image of deliberately cracked particle

Fig. 3.3 Constituent layers of TRISO particle [46]

The kernel is often composed of UO_2 (and is assumed to be so for this study) but it could also contain plutonium and/or transuranics or indeed take a non-oxide form such as a carbide or oxycarbide [89]. The first coating is a porous carbon buffer layer which is able to accommodate dimensional changes in the kernel resulting from burnup and fission gases which escape the kernel. Following this is a layer of dense pyrolytic carbon, then a layer of silicon carbide, followed by another layer of pyrolytic carbon. The silicon carbide layer is the main barrier preventing fission products leaving the particle by presenting a significant impediment to their diffusion. It also has sufficient strength to withstand foreseeable stresses, arising principally from fission gas pressure. The pyrolytic carbon layers either side of the silicon carbide protect it from chemical attack, with the inner layer also serving to protect the fuel kernel from the corrosive gases used in the process of deposition of the silicon carbide layer [89].

The particles can then be held in a graphite matrix to create an overall fuel form. The first demonstration of TRISO particles was in the UK's Dragon reactor [90]. There, the fuel particles were held in a hollow cylindrical graphite 'compact'. This was then surrounded by a further graphite sleeve to form a fuel rod. A similar approach using solid cylindrical compacts in a graphite sleeve is used in the Japanese High Temperature Test Reactor (HTTR) [96]. Alternatively, the compacts can be placed inside graphite blocks cooled by internal channels, for example in designs of Very High Temperature Reactors (VHTRs) [103].

Another early application of TRISO particles in Germany was a 'pebble bed' reactor called the AVR [43]. In this design, graphite spheres of approximately 6cm in diameter contain the TRISO particles. These pebbles then sit in a pressure vessel and are cooled by helium coolant. Pebbles can be removed from the bottom of the vessel and fresh (or recycled) pebbles added to the top, allowing for continuous refuelling.

A simplified geometry is considered for this study, which is shown in Figure 3.4.

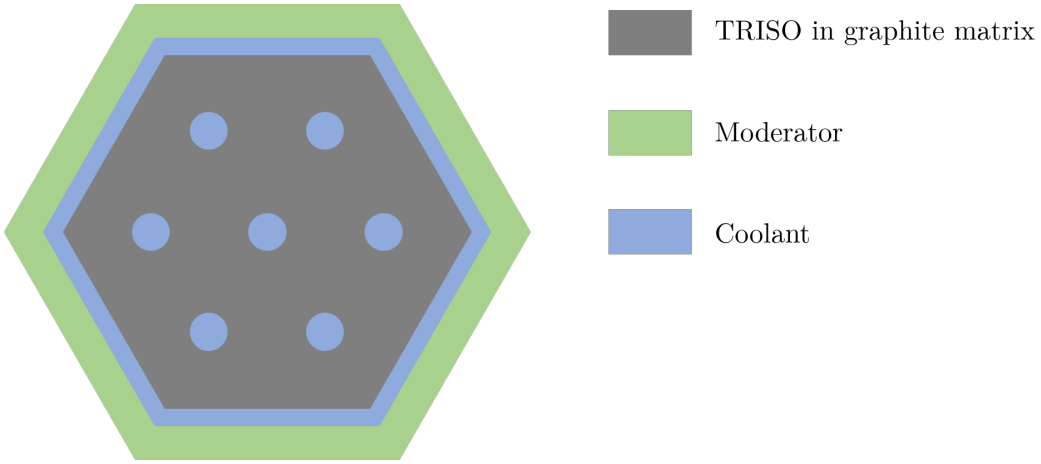

Fig. 3.4 Arrangement of fuel block, coolant and moderator

A TRISO-based space reactor has been recently proposed [28], targeting an electrical power output of 150 to 320kW$_e$, based on a terrestrial micro-reactor under development by the same company. There is limited information about this design, but it uses a prismatic fuel design, with hexagonal fuel blocks containing a large cylindrical moderator made of an unspecified hydride. Most interestingly, the fuel is LEU. Mass estimates are given of 4,000 to 5,500kg for the entire system, including shielding. This initial study suggests that TRISO is a reasonable candidate fuel form and will therefore be adopted in the core design used in the remainder of the study.

3.3.2 Fuel assembly design

A hexagonal fuel block is used as before, except, instead of being composed of tungsten cermet, it is composed of TRISO particles suspended in a graphite matrix. The TRISO particles are assumed to occupy 50% of the volume (the so-called 'packing fraction'). The packing fraction could, of course, be left as another variable in the design space exploration, but, broadly speaking, having more fissile material in the core is likely to be favoured over less. Changing the packing fraction will, of course, have an impact on the fuel to moderator ratio (considering graphite as a moderator) and the power density. These, however, can be varied by other means such as the amount of dedicated ZrH moderator and the overall core size and total thermal power. Therefore, the highest reasonable packing fraction is chosen and used as a fixed input. For spheres of equal size, the maximum packing fraction for settled randomly packed spheres is 62.5%. In fact, the current process of forming TRISO-graphite compacts might reduce the maximum achievable to around 48%. This is due to the fact that

particles are settled imperfectly under gravity before bonding and then the compact is only compressed in one direction in a die [78].

As before, the hexagonal fuel block has internal channels through which coolant flows. The fuelled region is assumed, as before, to extend to the walls of the channel. In reality, some sort of unfuelled region, such as a graphite cladding, would be required so that bare fuel kernels are not directly in contact with the coolant, since contamination in the primary circuit would be undesirable. Due to the increased complexity of the heat transfer modelling (discussed in Section 3.7) and in the interests of minimising the dimensionality of the design space, the number of channels is for now fixed at seven.

The major change in overall core geometry is the placement of the moderator. In the previous scheme, assembly positions were either occupied by a fuel block or a moderator block. In the new design, each assembly position is identical and contains a combined fuel and moderator assembly. The moderator sits as a wrapper around each fuel block, such that in the overall core the moderator sits interstitially between fuel blocks. One advantage of this is that the amount of moderator can be varied continuously, whereas in the previous scheme, only discrete choices of one chequerboard layout or another were available. Deterministic modelling of the core will also be simplified by the presence of an easily identifiable, fuel-centred, unit cell (one assembly), whereas for some of the moderator layouts seen in Chapter 2 this was not the case.

The final aspect of the fuel assembly design is the ring of coolant that separates the fuel block from the moderator, addressing the previously neglected issue of moderator cooling. If this gap were not present, the peak fuel temperature might be expected to occur at the periphery of the fuel block where the distance from the coolant channels is greatest. Having the moderator in direct contact with possibly the hottest part of the fuel block will make it much more likely that a given design will breach the allowed maximum moderator temperature. This maximum, at least in the case of zirconium hydride, will be lower than that allowable in the fuel. Even though the part of the moderator that faces the fuel block across the coolant gap will have the same temperature as the fuel block surface due to radiative equilibrium, the presence of the coolant means that the periphery of the fuel block can at least be cooled, reducing the temperature that the moderator sees. Additionally, the width of the internal coolant channels and the annular coolant gap will be allowed to vary independently of the size of the coolant channels, enabling significant variation in the proportion of coolant that flows through the interior of the fuel versus the periphery. A design might therefore be chosen that preferentially diverts coolant to the moderator to keep it below its maximum operating temperature. A more sophisticated solution to moderator cooling would be a two-pass coolant flow path such as that used in the British Advanced Gas-cooled Reactor

(AGR). There some incoming coolant is routed to the top of the core and sent first downward through the graphite bricks to cool them, before travelling upward through the core [82]. The design of the proposed Pylon space reactor [28] also uses a two-pass coolant path. Similarly, in the present design, the flow in the annular channel could be downward and in the internal circular coolant channels the flow could be upward. In this way, the coolest possible coolant (at the inlet) would encounter the moderator where is would otherwise be hottest. Modelling the temperature distribution in such a design would be more challenging and is left as an area of possible future investigation.

Finally, the assemblies are arranged in hexagonal rings, as before, such that the overall core shape is hexagonal. The reflector shape is changed though so that it is overall hexagonal rather than cylindrical; in the previous design, for thin reflectors the effective thickness of the reflector varied at different positions of the core, since the vertices protrude out towards the edge of the reflector.

3.4 Monte Carlo modelling

Before describing the main deterministic neutronics modelling methodology, a brief aside is required on the new considerations required for modelling a TRISO-based reactor design in a Monte Carlo model. While not functioning as the main neutronics tool, Serpent is retained for the purposes of assessing the performance of WIMS.

When modelling the tungsten cermet core it was assumed that the small scales over which tungsten and uranium dioxide were mixed (tens of micrometres) justified defining the cermet as a homogeneous mixture of the isotopic components. TRISO particles, whilst still small compared to a typical fuel pin in power reactors, are too large to ignore their heterogeneity. Three approaches are possible in a Monte Carlo model [64]:

- **Implicit model**: In this method, a random sampling method is used based on calculating the probability that any particular neutron track that traverses a fuelled region encounters a fuel particle. This is an approximate approach that is not recommended, especially at anything other than low packing fractions.

- **Lattice model**: Here the TRISO particles are represented fully in the geometry, but their placement is regular rather than random, being placed in an evenly spaced three-dimensional lattice.

- **Explicit model**: This is the most realistic representation of the particulate fuel, where exact particle coordinates are supplied to the Monte Carlo code, having been generated in a suitable manner.

The explicit model is the one adopted. Random particle coordinates can be generated in two ways using an in-built tool within Serpent. The standard algorithm takes a user-specified volume and randomly places spheres of the size of the particle within it. If an overlap with another sphere or the bounding surface is found, that placement is rejected. This algorithm is suitable for low packing fractions, but at packing fractions above around 30% the rate of particle rejection becomes very high and the process becomes unusably slow. The alternative is the 'grow and shake' algorithm [105] which first populates the space with the required number of particles to achieve the target packing fraction, but having negligible size and therefore no overlap. For each particle in turn the algorithm attempts a small increase in size and a small shift in its position, rejecting these moves if they result in an overlap. This algorithm might still take several hours to populate a 10cm cube at a packing fraction of 50% but one can be confident that it will converge. Due to this computational load, the core is not fully randomly populated with particles. A single cylindrical region is used so that a 4cm diameter (flat to flat) hexagonal fuel block can be filled over a height of 4cm and this populated volume is then reused for neighbouring areas. The resulting geometry within Serpent can be seen in Figure 3.5.

3.5 Modelling TRISO-based core in WIMS

As before, we begin with the consideration of a small unit cell within which a resonance self-shielding calculation can be carried out. This can not be done using HEAD alone since the three-dimensional doubly-heterogeneous fuel form (particles in a matrix, matrix within a moderator) is not a geometry that has an available equivalence treatment. Instead, the sub-group method is used. For this method, collision probabilities for the various materials within the unit cell (TRISO particle constituents, graphite matrix, moderator and coolant) are required in the sub-group energy structure. A module called PROCOL is used to generate collision probabilities for particulate fuels that are embedded in spherical, annular or slab geometries. An annular representation is most appropriate and is constructed by preserving the volumes of each material. The ring of six coolant channels that are arranged in a hexagon are smeared into a single thin annulus that also preserves their volume. This simplified geometry is shown in Figure 3.6.

With resonance-corrected cross sections in 172 energy groups in hand, we can proceed in the next stage towards a full-core calculation. Generally, one wishes to reduce both the number of energy groups and the level of detail in the geometry before carrying out a full-core calculation. A variety of routes could be taken to achieve this.

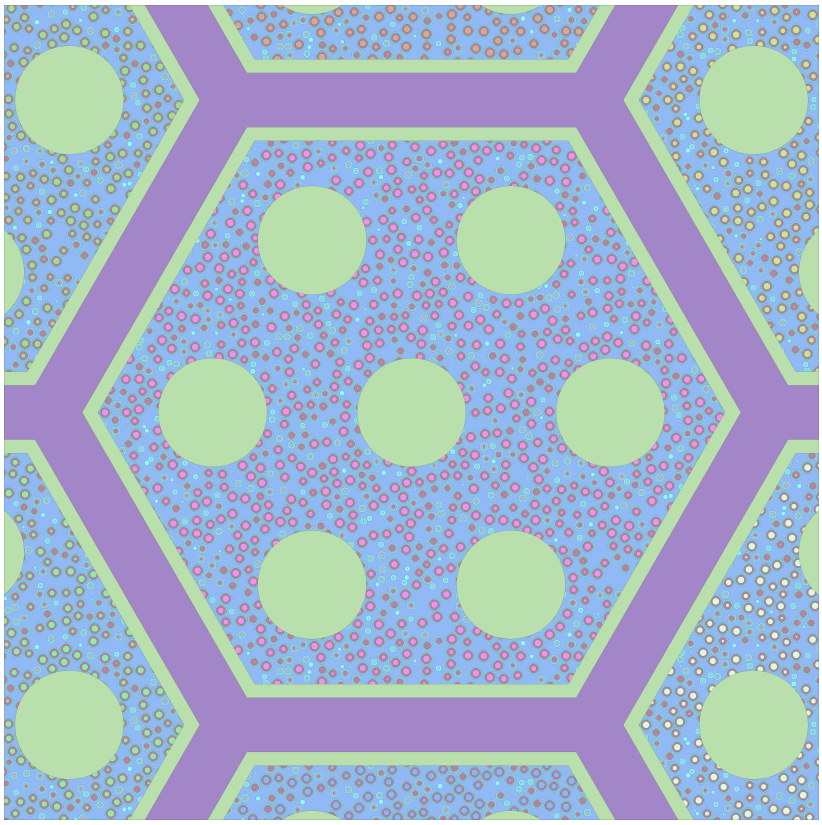

Fig. 3.5 Geometry of fuel assemblies in Serpent. The colour of fuel kernels differs between fuel assemblies due to being treated as different materials for burnup purposes.

3.5.1 Assembly-level calculations

First addressing the issue of homogenising materials, the simplest method is to smear materials together (using the module SMEAR) and form flux-weighted group-wise averaged cross sections. One option is to simply use the annular geometry given to PROCOL for the resonance treatment. In this method, a second execution of PROCOL generates collision densities in 172 groups (rather than in the sub-group energy structure), which can then be fed to the module PIP, which uses the collision probabilities to calculate a flux solution. This flux solution can then be used to homogenise materials in the assembly. Since PROCOL is the only module which can handle particulate fuel, the TRISO particles must be combined with the graphite matrix at this stage. This leaves just three distinct materials: the 'fuel', moderator and coolant. These could also be blended together using the same flux solution. An alternative which better reflects the real geometry is to represent the assembly in CACTUS3D (which permits almost any geometry) and use a flux solution from that to homogenise the remaining materials together. An intermediate solution, which avoids having to construct the detailed coolant channel geometry in CACTUS3D, is to smear together the fuel and neutronically

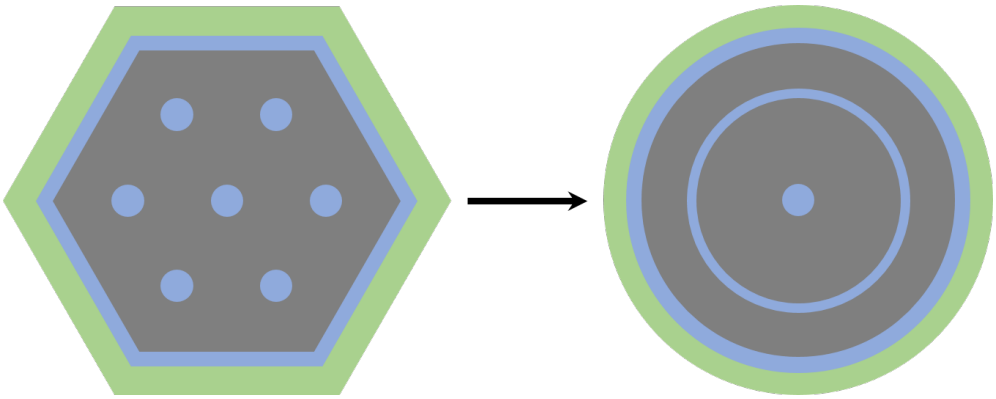

Fig. 3.6 Assembly and its approximate annular representation, based on preserving volumes, used for generating collision probabilities in PROCOL

unimportant gaseous coolant using the PROCOL geometry, then using CACTUS3D for the more important fuel and moderator homogenisation.

It is also possible at this stage, using flux solutions from either PROCOL or CACTUS3D, to reduce the energy group structure from 172 groups to fewer groups. Therefore it would be possible to produce a single homogenised material with cross sections in a few-group structure suitable for a rapid full-core analysis. Before proceeding to this final stage, another intermediate step could be incorporated.

3.5.2 Core-plane analysis

In the simple method just described, a single assembly was considered, which was assumed to be situated in an infinite lattice of identical assemblies. No allowance was made for the fact that different assemblies experience different environments, depending on their position in the core. The neutron energy spectrum in the centre of the core is likely to differ from that at the core periphery, next to the reflector, particularly if the reflector has moderating properties such as in the case of the beryllium reflector chosen for this study. In order to capture these differences, a two-dimensional core-plane analysis can be carried out. In this analysis, two materials are left separate: the fuel/coolant combination and the moderator. These simplified two-zone assemblies are then placed in a lattice, surrounded by a reflector, to create a two-dimensional model representing a horizontal slice through the core. An example geometry as modelled in CACTUS is shown in Figure 3.7. A flux solution is then produced for this geometry in the few-group structure. One additional material is required - a fictitious 'black' material at the periphery of the geometry. This is required because CACTUS can only use a reflective outer boundary condition. Applying a thin layer of (unphysically) dense boron ensures that the flux falls effectively to zero at the outer boundary, simulating a vacuum.

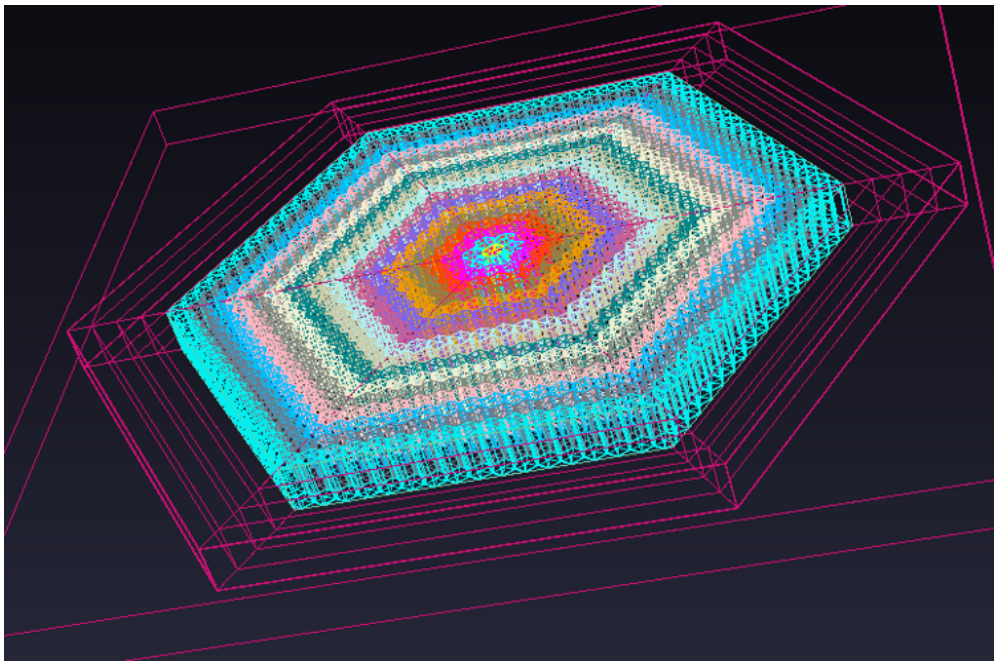

Fig. 3.7 Two-dimensional core slice in CACTUS3D

One additional input which is required for this calculation is the volume of each region in the geometry, since CACTUS can only calculate these itself for very simple geometries. It is possible to produce a stochastic estimate of region volumes using a track length estimator, but achieving low uncertainties, especially for small regions, requires a large number of tracks and a significant computation time. A separate routine in MATLAB was created to construct this list of volumes for all regions (generally in excess of 1,000 regions) in a format readable by CACTUS. Care is required here as the ordering of regions is not necessarily intuitive.

Using the flux solution calculated by CACTUS, the final material homogenisation of the assemblies can take place, but only within each core ring. Arguably one could also preserve the small difference that presumably exists between assemblies sitting on the corner of the hexagonal lattice and those along an edge. But, given that a cylindrical approximation is ultimately used for the full-core calculation (described later), it is appropriate to treat each hexagonal core ring as a single region and smear out any variation that may exist around that hexagon.

This intermediate calculation is expected to provide some improvement in the performance of the final full-core calculation, but its major shortcoming is that it does not allow for the influence of the axial reflectors, which will be assumed to be of the same thickness as the radial reflectors. One possible improvement would therefore would be to have another slice geometry, but with an axial reflector layer on top of it. This would, of course, be axially heterogeneous and therefore be a three- rather than two-dimensional problem, likely bringing

an increased computational burden. Some additional thought and experimentation would be required to determine the most appropriate geometry and whether the computational load is justified by increased performance in the final full-core calculation.

3.5.3 Reflector data preparation

Before the full-core calculation, or the core-plane analysis just described, can take place, cross section data for the reflector is required in the few-group structure. A suitable neutron flux is therefore required to carry out the energy group condensation. The process used to produce this data is as follows: first carry out the assembly-level material homogenisation and energy group condensation. Then, a simple one-dimensional MoC calculation is carried out in CACTUS, having materials from the core centre out to the reflector and terminating in another artificial black boundary material.

This simple one-dimensional calculation is designed to approximate the flux conditions experienced by the reflector at little computational cost. Further, in order to capture any significant differences from the interior to the exterior of the reflector (such as a softening of the spectrum due to a moderating reflector), the reflector is divided into five regions in which to condense the energy group structure. These five reflector regions are then kept distinct in the core-plane and/or the full-core calculation.

3.5.4 Full-core calculation

With cross sections for all core materials in the few-group structure in hand, it is now possible to carry out the full-core calculation, determining the flux throughout the core and its value of k_{eff}. Two possible approaches were explored and will now be described.

CACTUSOT

One possibility for the full-core analysis is to use a fully three-dimensional method of characteristics calculation. This is, in principle, possible with the established module CACTUS3D. There are two reasons why this might be undesirable. First, as mentioned earlier, CACTUS3D cannot accept a true vacuum boundary condition, requiring the use of artificial materials. When doing this is it recommended [2] that homogeneous acceleration is deactivated, likely carrying a penalty in calculation time. Second is the issue of tracking errors. The method used by CACTUS3D requires that the tracks that it draws through the geometry are reflected around the outer boundary and return to their starting point with a fine degree of tolerance. When a track fails to meet this tolerance, a tracking error occurs. This tends to occur more in

geometries with a high aspect ratio but is a somewhat unpredictable phenomenon. Using it as part of the main neutronics tool in a scheme which will ultimately assess perhaps hundreds or thousands of core designs of varying size and shape is likely to bring a risk of unpredictable crashing. More promising is a tool which was in development at the time of attempting

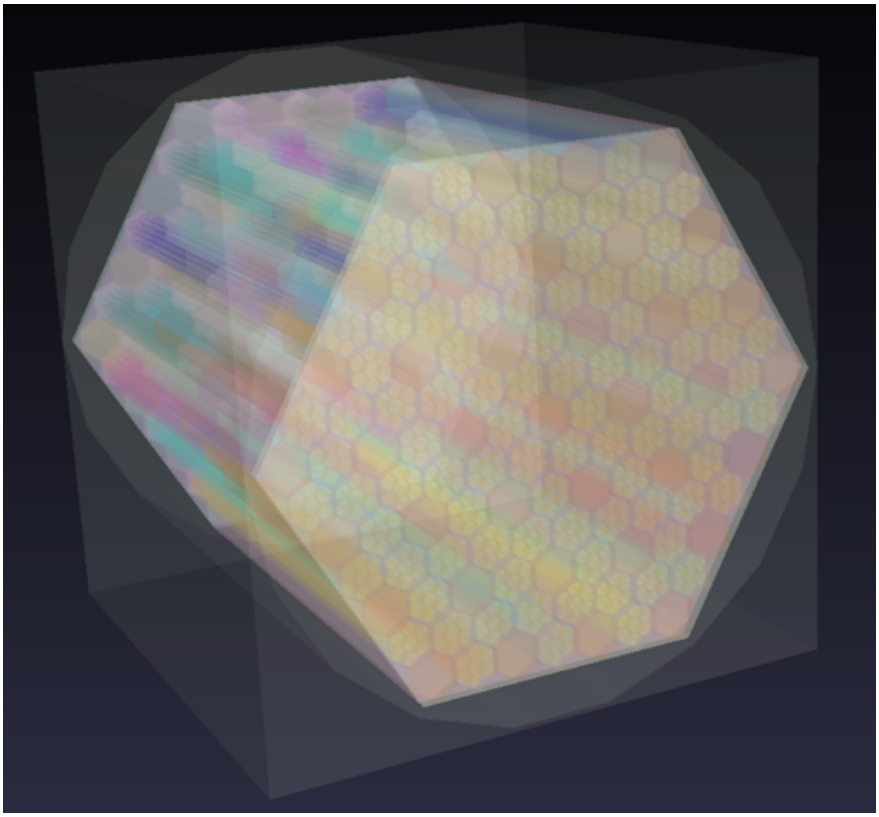

Fig. 3.8 Full-detail core in CACTUSOT

its utilisation: CACTUSOT. The 'OT' refers to 'once-through', referring to an alternative method of tracking in the MoC where tracks are not required to be reflected around the outer boundary. This results in a black boundary condition, obviating the need for any fictitious materials, and is intended principally for full-core calculations, as required here. An example core as modelled in CACTUSOT is shown in Figure 3.8. Removing the need for reflected tracks also improves the spatial coverage of the tracks. CACTUSOT has demonstrated good performance, for example against a sodium-cooled fast reactor benchmark [102]. Unlike in CACTUS3D, CACTUSOT is parallelisable, potentially leading to significant run-time improvements. Another attractive feature of this method is the almost arbitrary geometry allowed, in principle permitting a full-core calculation without any material homogenisation at all, although at the cost of increased calculation time and memory requirements.

Fully three-dimensional detailed analysis of entire cores using the MoC is still generally seen as a computationally expensive endeavour. For example, recent work [44] assessed the code OpenMOC against the BEAVRS pressurised water reactor benchmark. For an eigenvalue calculation (that is, without burnup), a calculation time of eight hours was required but using an impressive 92,480 CPU cores. However, the core under consideration in this study is significantly smaller and would be considered a 'micro-reactor' in terrestrial terminology. The level of accuracy and geometrical detail is also, of course, lower than would be required in a benchmarking exercise. It was therefore considered that CACTUSOT was a promising candidate tool for the full-core calculation.

Unfortunately, a number of problems arose in the attempt to implement CACTUSOT. With the version available at the time, the coarse-mesh finite difference (CMFD) acceleration method was unavailable. This method uses an overlaid coarse mesh and uses a low-order method (such as diffusion) to help converge the higher-order MoC solver. At the time of the investigation (and possibly still), CMFD was not available for geometries having hexagonal elements. For practical problems, CMFD is generally necessary to achieve reasonable convergence times [44] with reductions in calculation time reported in excess of a factor of 100 [98], albeit in the context of large light water reactors. The unavailability of this feature in CACTUSOT was unfortunately only realised after some investment had been made in developing code to produce the full reactor geometry in CACTUSOT for any choice of reactor design parameters. Initial investigations did confirm that even for moderate levels of geometrical detail, run-times were fairly long (of the order of one hour). Finally, some code instability was encountered when editing the number of tracks and track angles which was apparently due to a bug in the code as it existed at that time [4]. This is a risk inherent in using any developmental software over which one has no control. Due to these issues, CACTUSOT was not considered any further. Development of it will, of course, have continued and the computational infrastructure for generating core geometries for it already exists, leaving it as a potentially fruitful area of future investigation.

MERLIN

The MERLIN module allows the use of the diffusion and SP3 methods in a few simple geometry types. The first geometry type that is of interest is 'TRIZ', which has triangular/hexagonal geometry in the $x-y$ plane and extends this as a prism in the z direction. The reactor core has exactly this sort of geometry, being composed of hexagonal prisms arranged in a hexagon, and so this would appear a reasonable choice. Each hexagon in the lattice can have its six constituent equilateral triangles populated independently with different materials, which would facilitate the construction of the smooth hexagonal outer

boundary of the reflector. The other geometry type in MERLIN of interest is 'RZ', which is a cylindrical geometry, which can be used to approximate a core which is overall hexagonal. This geometry type only has two dimensions from a calculation point of view, providing some speed-up over the truly three-dimensional TRIZ geometry.

Ultimately the RZ geometry was chosen because of its increased flexibility in meshing. In the TRIZ geometry, any number of meshes is permitted in the z direction but, in the $x-y$ plane, the mesh is fixed as simply the six constituent triangles within the hexagon. For common larger reactor types which have hexagonal fuel assemblies, such as the VVER and many fast reactors, this mesh density is likely appropriate. For the designs considered here which potentially have relatively few assemblies, the size of the mesh is larger as a proportion of the overall core. For the RZ geometry, each material region in both the r and z directions can be subdivided into any number of meshes. This enables a study to be carried out to determine the number of meshes above which negligible changes in the flux solution occur. In the case of RZ geometry, this was found to be around ten meshes for each radial region for a typical ten-ring core, which is finer than the radial mesh detail in the equivalent TRIZ geometry.

3.6 Eigenvalue calculation performance

Suitable methods have been described for each step in the WIMS calculation: resonance self-shielding, material homogenisation, energy group condensation and full-core calculation. Two possible routes are tested, one incorporating the intermediate core-plane calculation with the aim of improving accuracy and the other without it. These will be referred to as the 'main' and 'quick' routes respectively. They are shown in flow chart form in Figure 3.9. The performance of the two WIMS routes will first be compared against Serpent for a basic eigenvalue calculation, using a fresh LEU core. Figure 3.10 shows a comparison of k_{eff} values calculated by WIMS and Serpent. As well as showing the main and quick routes in the six-group energy structure chosen, both are also shown using 172 groups to indicate how much fidelity is lost in the reduction in energy group structure. The first effect that can be seen is that, at the lowest levels of moderation, both the main and quick routes accumulate error to the same extent. As mentioned previously, the XMAS 172 energy group structure is optimised for the analysis of thermal spectrum systems, with relatively few groups in the fast region, which is why ECCO is generally used for fast reactors. It is therefore not surprising that performance is poorer in those cores with very little moderator and therefore harder spectra. It should be mentioned at this point that ECCO does not have the capability to handle particulate fuel; it might otherwise have alleviated this problem.

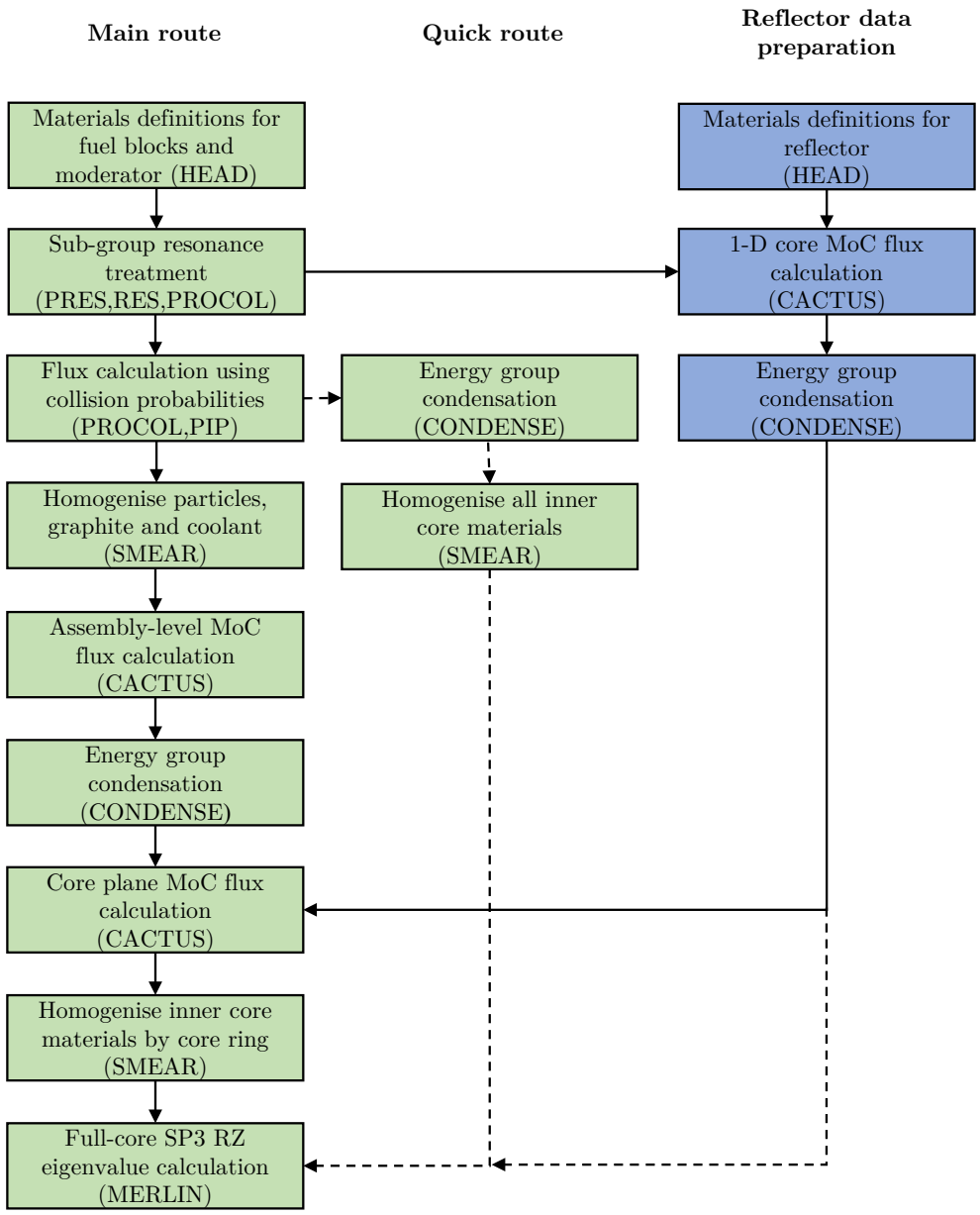

Fig. 3.9 Flow chart showing main and quick routes for eigenvalue calculation

Moving to higher levels of moderation, the error in the main route falls off and it performs well compared to Serpent. The additional error accumulated by condensing the energy spectrum with this method is around 500pcm. For the quick route, it can be seen that an additional source of error accumulates in heavily moderated systems. To recapitulate, the major difference between the main and quick WIMS routes is that, in the quick route, the final homogenisation of fuel with moderator is carried out using the energy spectrum of an infinite reactor. The main route, in comparison, uses a different spectrum for different core

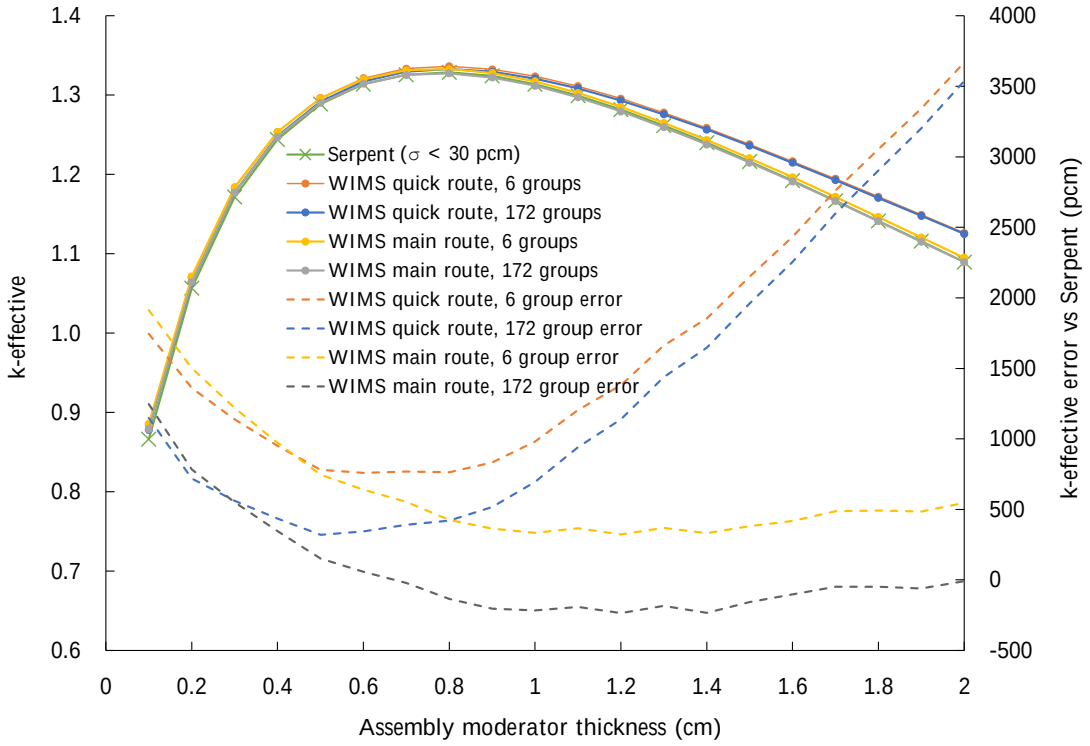

Fig. 3.10 k_{eff} calculated by WIMS and Serpent for 8-ring core with 8cm reflector for different amounts of moderation

radial positions, which captures (approximately, in two-dimensions) the effect of leakage from the core on the spectrum. Leakage is generally higher for higher energy groups, such that the spectrum at the core periphery is likely to be softer than at the core centre. For systems which have less moderation and a generally hard spectrum, the difference in spectra between the core centre and the core periphery would be less pronounced. Therefore using a method which ignores such spectral differences (the quick route) will suffer more from this effect at higher levels of moderation. This hypothesis is corroborated by the fact that, for the hardest spectrum systems, the main and quick routes give very similar values of k_{eff}, but both are affected equally by the previously mentioned shortcomings of using the 172-group structure for hard-spectrum systems.

The analysis presented so far is not sufficient to determine whether these tools are acceptable, since it is the core reactivity at the end of life, not the beginning of life, that determines whether a core design can be accepted. We must therefore now turn to the burnup calculation.

3.6.1 Burnup

The very broad approach to burnup in WIMS is as follows: One of the various modules that calculates flux solutions (PIP, CACTUS, MERLIN etc.) passes to the module BURNUP some very basic information. This consists of the material composition and the flux in each of the mesh cells that it has in its geometry. It is important to recognise that BURNUP does not 'know' what the geometry actually is; it merely possesses a series of numbered mesh cells and what they contain, but does not know how they relate to each other. The flux and material composition in each mesh cell is used, in combination with a user-supplied power and time-step length, to determine what the new material composition is at the end of the time step. This accounts for the depletion of fissile isotopes, the accumulation of fission products and capture products and the decay of radioactive isotopes. Some computationally cheap sub-steps are taken, which estimate the changes in the flux arising from the change in material composition, but treating each region in isolation since BURNUP does not know how different regions interact.

The new material compositions can then be passed back to the starting point of the calculation, HEAD, so that the full calculation route is followed and a new flux solution calculated, and so on. This loop is repeated for each burnup step. The first complication arises when any material homogenisation has taken place. Whilst BURNUP can, of course, be asked to calculate the change in composition of a homogenised mixture, it would not then necessarily be possible to separate out the updated composition into the original constituent materials. This is resolved by the UNSMEAR module which is invoked after the main flux solution is produced. This can take the original heterogeneous flux solution that was used to homogenise assembly-level detail and use it to 'unsmear' the flux found by the full-core solver for that region back into the heterogeneous solution. It is those unsmeared fluxes that can then be passed to BURNUP. This also applies to energy group condensation and its reversal. In the 'main' calculation route, three unsmear operations are required: first to translate the full-core solution onto the CACTUS core slice, then from the core slice onto the CACTUS assembly-level triangular unit cell, then from the triangular unit cell onto the annular PROCOL unit cell so that 172-group fluxes at the TRISO-particle level of detail are available. These detailed fluxes are then supplied to BURNUP to determine the composition changes at this required fine level of geometrical detail.

The power and neutron spectrum, of course, varies throughout the core and the effect of these differences is captured by having many separate burnable regions in which the composition changes are separately calculated. During the unsmearing process, the volumes of the donor regions must be manually calculated and supplied to the recipient geometry. For example, the flux information relating to a whole ring of assemblies might be translated onto

a single annular unit cell in PROCOL, but the power density used by BURNUP needs to be corrected for the disparity in volumes between the donor and recipient geometries.

Burnup and resonance treatment

The presence of new fission products and actinides that result from burnup needs to be accounted for in the resonance treatment at each burnup step, since many of the new nuclides are strong resonant absorbers. One approach to this in WIMS is to calculate the size of this effect but averaged over all burnable regions. The module DIFF takes an average of the fuel compositions across the geometry which can then be used to carry out a single resonance treatment calculation (such as with HEAD). The resulting corrected microscopic cross sections are then applied to the nuclide densities in the various burnable regions to calculate new macroscopic cross sections for each of them. This approach is reasonable when one does not expect large variations between burnable regions. One example geometry where this could be the case is if geometry being analysed is a fuel assembly from a large reactor containing separate pins. Assembly-level analysis is the traditional application of WIMS, being used to produce fully spatially homogenised few-group cross sections for each assembly, to be supplied to an external full-core solver such as PANTHER.

Carrying out full-core calculations in WIMS is more recent, so the standard 'averaging' approach using DIFF is likely to be inadequate. The alternative is to carry out a separate resonance treatment calculation for every burnable region. This approach also requires any assembly-level spatial homogenisation and energy group condensation to be repeated for each such region. The resulting calculation structure for the main route is shown in Figure 3.11.

Assigning burnable regions

In WIMS, the input/output of each module is a block of information in temporary memory called an interface, which contains data such as geometries, meshes, fluxes, cross sections and so on. The total number of interfaces is restricted to 99. Using the looping structure just described to carry out a self-shielding calculation uses a large number of interfaces due to the need to store a copy of the pre- and post-homogenisation/condensation versions of the assembly-level cross sections. In practice, this limits the number of burnable regions to around 40. One solution is to write interfaces to permanent memory and then clear them to make space as required, which allows an arbitrary number of burnable regions. It was found that adding the hard-disk reading and writing added around 20% to the calculation time for the quick route but yielded an insignificant improvement in the results, assuming that the

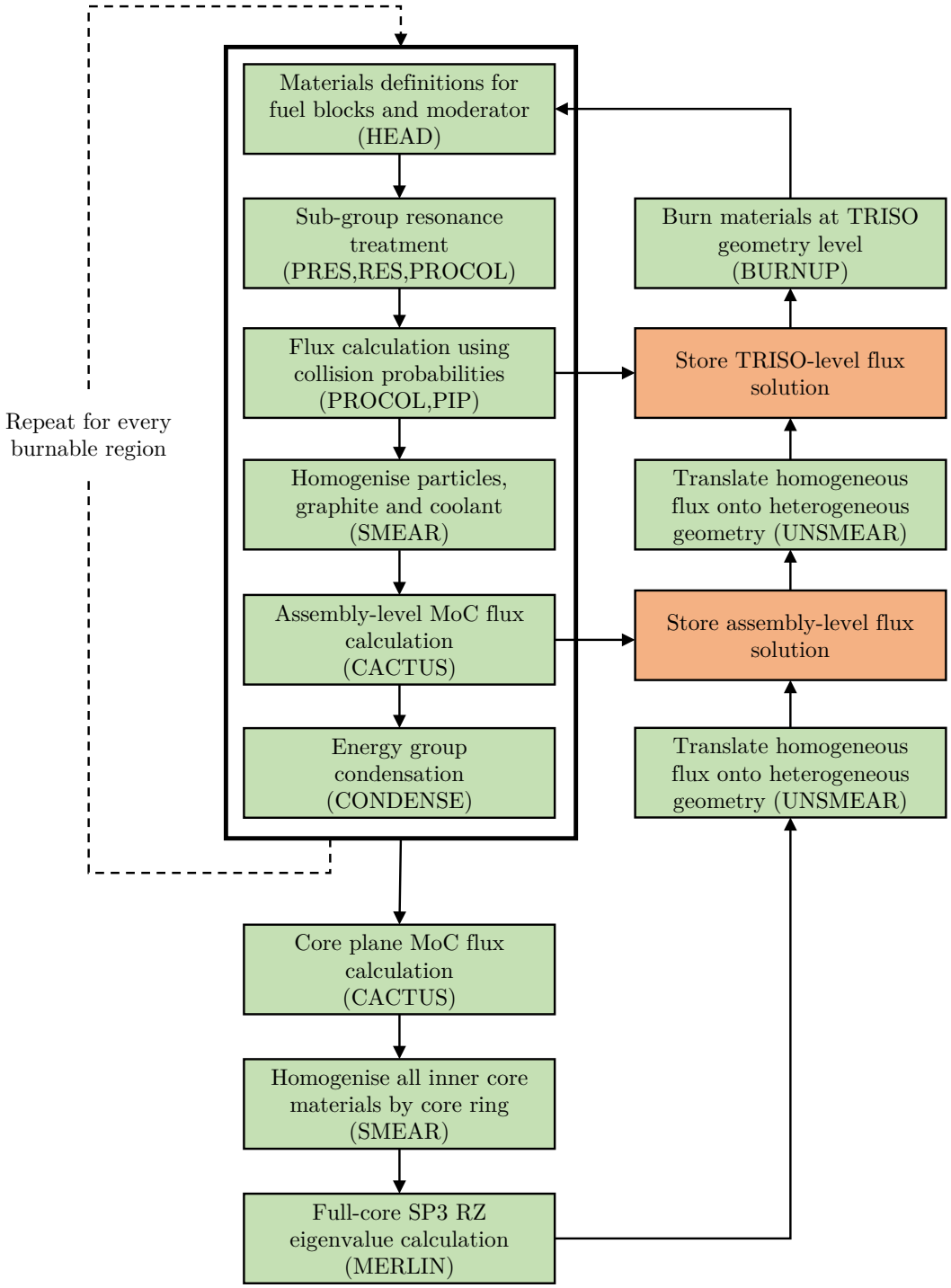

Fig. 3.11 Structure of burnup calculation for main route

unlimited space is used to double the number of burnable regions. Therefore, the number of burnable regions is limited to 40 in the interests of maximising calculation speed.

Another complication arises when considering how to apply axially variable burnup in the 'main' calculation route, specifically how it would interact with the core-plane calculation. This would require some additional procedures:

- Referring to Figure 3.11, in the 'upward' unsmearing process, the fluxes relating to each axial burnable layer would need to be extracted and manipulated for a separate unsmear operation onto the CACTUS core slice
- In the 'downward' process, some sort of averaging would need to take place over the axial burnable regions whilst keeping radial regions distinct, so that the CACTUS core-plane calculation is carried out using an average axial composition. Some investigation might be required to determine if a straight volume and flux weighting is sufficient to calculate the appropriate axial average composition.

A slightly simpler alternative to the above modifications would be to have a separate CACTUS core-plane calculation for each axial burnable region. Since this stage of the calculation often represents the majority of the computation time, increasing the number of times it is required to execute is undesirable given the high value placed on calculation speed. A decision was taken to freeze the development of the main route at this stage and only return to implement the above changes if it was felt that the quick route is inadequate.

Burnup calculation performance

In order to compare the relative burnup performance of the quick and main WIMS routes, calculations were first run using only a single axial burnable region and a separate burnable region for each ring of assemblies. For a fair comparison, a single axial region was also used in Serpent. The results are shown in Figure 3.12. As can be seen here, there appears to be little additional error accrued in the burnup process in WIMS, with end-of-life k_{eff} differing from the Serpent comparator to around the same extent as start-of-life k_{eff}. As before, very heavily moderated designs appear to present a problem for the quick route, resulting in an overestimation of end-of-life k_{eff}. This raises the concern that the search for the optimal reactor design might falsely select such a heavily moderated design due to the significant inbuilt bias in the neutronics analysis. It is more likely, given where the peak end-of-life k_{eff} occurs in Figure 3.12, that the very highest levels of moderation will not be selected as optimal, even with an overestimated value of k_{eff}. However, judgement must be reserved until the results of the optimisation process are examined in Chapter 5.

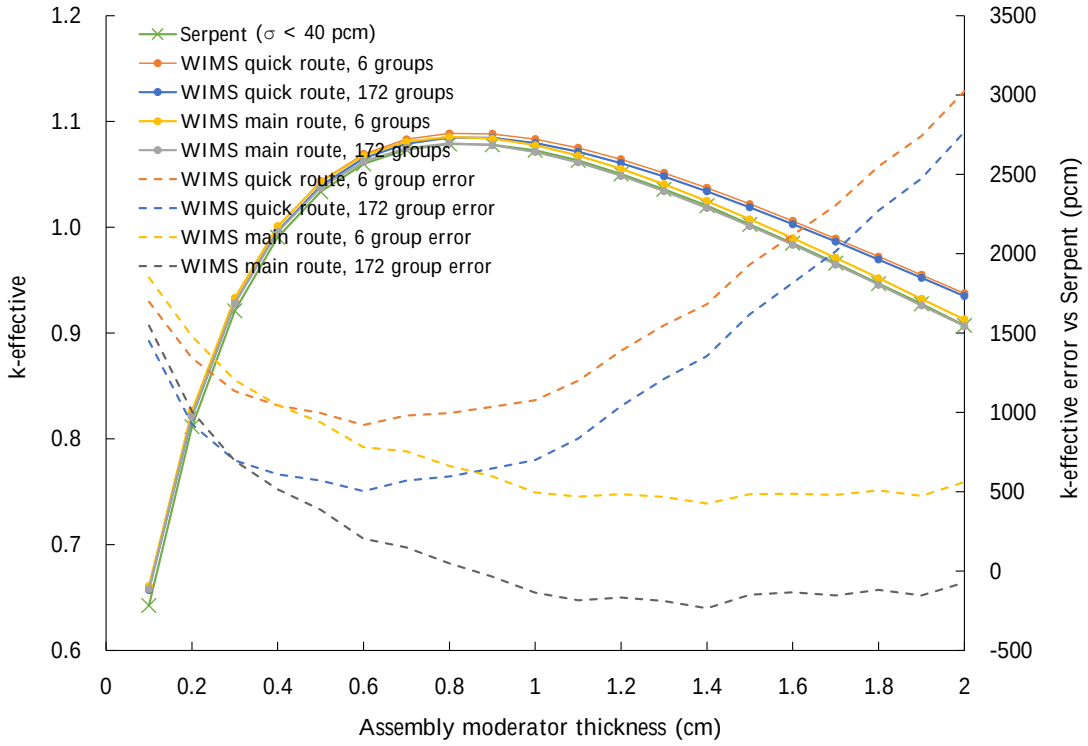

Fig. 3.12 k_{eff} at end of life (7 years at 4MW_{th}) calculated by WIMS and Serpent for 8-ring core with 8cm reflector for different amounts of moderation.

The results shown in Figure 3.12 relate to cores using LEU fuel and ZrH moderator. Designs using HEU and/or removing the ZrH moderator also need to be assessed. Table 3.3 compares end-of-life k_{eff} calculated by Serpent and WIMS for the same core but with no ZrH. The results are somewhat worse for HEU than LEU when using the few-group structure, accruing around 700pcm of additional error.

Finally, the computational cost of the various calculation methods is compared. The main comparison of interest here is between the two WIMS routes but Serpent run-times are also given, with the caveat that different machines are used for the two codes and Serpent was configured with an emphasis on accuracy rather than speed. WIMS runs are carried out using a single thread on an Intel Xeon E5 processor at 2.6GHz. Serpent runs are carried out using 32 threads on Cambridge University's CSD3 High Performance Computing system, with 100 inactive and 120 active cycles, each with 200,000 neutrons per cycle, over 20 burnup steps. Sample run-times for the example of a 0.4cm interstitial moderator core are shown in Table 3.4. What is clear from this is that using 172 energy groups carries a significant burden

Table 3.3 k_{eff} calculated by Serpent and WIMS for cores with no ZrH

Fuel	**Method**	k_{eff}	Error vs Serpent (pcm)
LEU	Serpent	0.44359 ± 0.00050	-
	WIMS main route (6 groups)	0.45886	1,528
	WIMS main route(172 groups)	0.46158	1,800
	WIMS quick route (6 groups)	0.45851	1,492
	WIMS quick route (172 groups)	0.46158	1,800
HEU	Serpent	0.88887 ± 0.00027	-
	WIMS main route (6 groups)	0.91120	2,233
	WIMS main route (172 groups)	0.89875	987
	WIMS quick route (6 groups)	0.91075	2,188
	WIMS quick route (172 groups)	0.89885	997

compared to the few-group structure, particularly in the CACTUS core-plane calculation (affecting the main route) but also in the MERLIN SP3 full-core calculation (affecting both).

Table 3.4 Comparison of run-times for two WIMS routes and Serpent

Method	**Calculation time (thread minutes)**
WIMS main route (6 groups)	20
WIMS main route (172 groups)	784
WIMS quick route (6 groups)	7
WIMS quick route (172 groups)	228
Serpent	9,856

3.7 Thermal hydraulic model

The initial analysis of the reactor core's thermal hydraulics described in Chapter 2 was limited in three main respects: it only considered the hottest channel in the reactor, the 1-D model of heat conduction in the fuel was fairly simplistic, and the temperature in the moderator was not considered. A revised model is required to improve these aspects whilst, of course, taking account of the new core layout with interstitial moderator between every fuel block.

The flow of coolant through this new geometry is more complicated due to the introduction of a hexagonal-annular flow channel between the fuel block and moderator. In the previous model, the coolant was only able to flow through one of many identical circular channels. It was therefore reasonable to assume that the coolant mass flow rate was very approximately equal in all channels. However, it would be a very poor assumption that the

flow rate in the annular channel is equal to the flow in one of the circular coolant channels. Indeed, since the width of the annular coolant channel will be allowed to vary independently from circular channel diameters, the relative flow rates could vary considerably across different designs. Therefore the temperature distribution across the fuel block could also vary considerably, depending on the proportion of the heat generated in the fuel that is ultimately carried away by coolant within the circular channels or the annular channel. Unfortunately there is no obvious analytical approximation, such as the 1-D model used previously, for the heat conduction problem of the whole coolant block being cooled differentially. Therefore the more computationally intensive route of finite element analysis is used.

3.7.1 Finite element heat conduction analysis

It is possible to set up a finite element analysis within MATLAB, helping to keep as much as possible of the overall computational framework within one platform. The geometry of the problem as represented within MATLAB and the mesh used are shown in Figure 3.13. The generation of the geometry is relatively simple, requiring the specification of a hexagon and seven circles and the way in which they bound the single domain, which is assumed to have uniform properties and heat generation rate. One complication is that for circle-type geometries, the assignment of edge labels is somewhat unpredictable. As can be seen in Figure 3.13a, some of the channels have four edge segments and others five. A separate subroutine is therefore required to ensure that boundary conditions are correctly specified for each channel. For this stage of the analysis, the previously available freedom in the number of channels has been removed and designs will be restricted to having seven coolant channels.

For this type of geometry the only available meshing method is an unstructured mesh, with only a single parameter to specify, the maximum allowable mesh size. The modelling is two-dimensional, invoking the commonly used assumption that axial heat conduction within the fuel is small compared to the transfer of heat radially into the coolant. This modelling is carried out for the fuel block only; the moderator has a much simpler geometry, being in a hexagonal ring around the fuel block (separated by the annular coolant ring) and is therefore more amenable to an analytical approximation. Two example results from this model are shown in Figure 3.14, showing the effect of changing the relative cooling rates of the interior and annular coolant channels.

The finite element model requires as inputs the internal heat generation rate and the boundary conditions at the interfaces with the coolant. The internal heat generation rate is taken as a constant across the fuel block in each two-dimensional slice, but the actual value of this is derived from the outputs of the neutronics model, as explained earlier. The

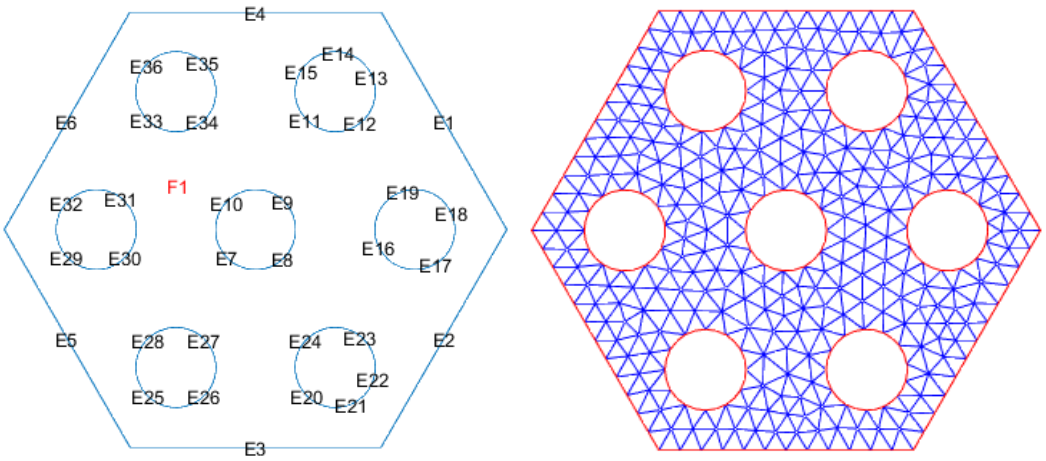

(a) Geometry of finite element model showing domain and edge labels

(b) Example mesh with maximum cell size of 0.2cm

Fig. 3.13 Finite element model geometry used in MATLAB for 4cm diameter fuel block

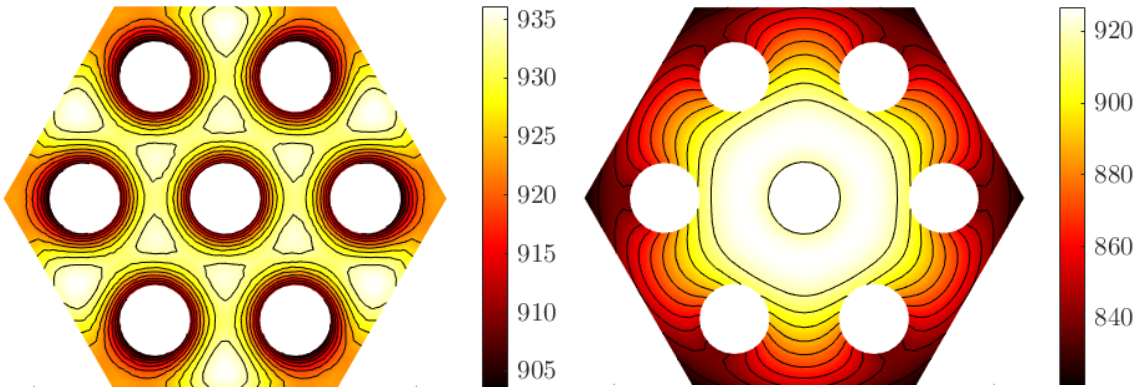

(a) Little cooling from annular channel

(b) Significant cooling from annular channel

Fig. 3.14 Example results from finite element heat conduction model, showing temperature in Kelvin (K)

boundary conditions can be specified as being for convective heat transfer, such that only the heat transfer coefficient and bulk coolant temperature need be specified for each surface. To calculate the heat transfer coefficient for the interior channels, the approach used in the previous chapter is retained (the Dittus-Boelter correlation for circular channels). For the annular channel, this approach is not obviously applicable. The applicability of various correlations for the convective heat transfer coefficient in annular channels was examined experimentally in [26]. It was found that for channels where the ratio of the outer and inner radii was less than 2.5, Dittus-Boelter is still a suitable correlation. It is reasonable to expect that much lower values of this ratio will appear in this study. Finally, the hydraulic diameter of an annular coolant channel can be taken as the difference between the diameters of the inner and outer surfaces.

Meshing

Since a large number of core designs will be assessed in an optimisation scheme, a high level of importance is placed on calculation speed. Some measures can be taken to improve speed which do not impact accuracy. One example of this is keeping the detailed solution of each finite element model solution to use in the next axial layer. Since the solutions for the temperature distributions of neighbouring axial layers are fairly similar this results in a reduction in calculation time of around 50% for the finite element model calculation, from around four seconds to around two seconds. Some measures, however, can only buy increased calculation speed with the loss of some accuracy. Two such parameters are the density of the finite element mesh, and the number of axial layers in the thermal hydraulic model. The effect of varying these parameters on the calculated maximum fuel and moderator temperatures is shown in Figure 3.15. As can be seen there, halving the size of the finite element model meshes has a very small effect on the temperatures of interest, while approximately doubling the calculation time. A maximum mesh size of 0.2cm is therefore chosen. The results are more sensitive to the number of axial layers used, whilst the calculation time is straightforwardly linear in the number of axial layers. Figure 3.15 shows the variation of the maximum calculated fuel and moderator temperatures with the number of axial layers. These results seem to converge between 200 and 500 axial layers. An error of around 5K is perfectly acceptable for these purposes, so 100 layers were used for all subsequent calculations.

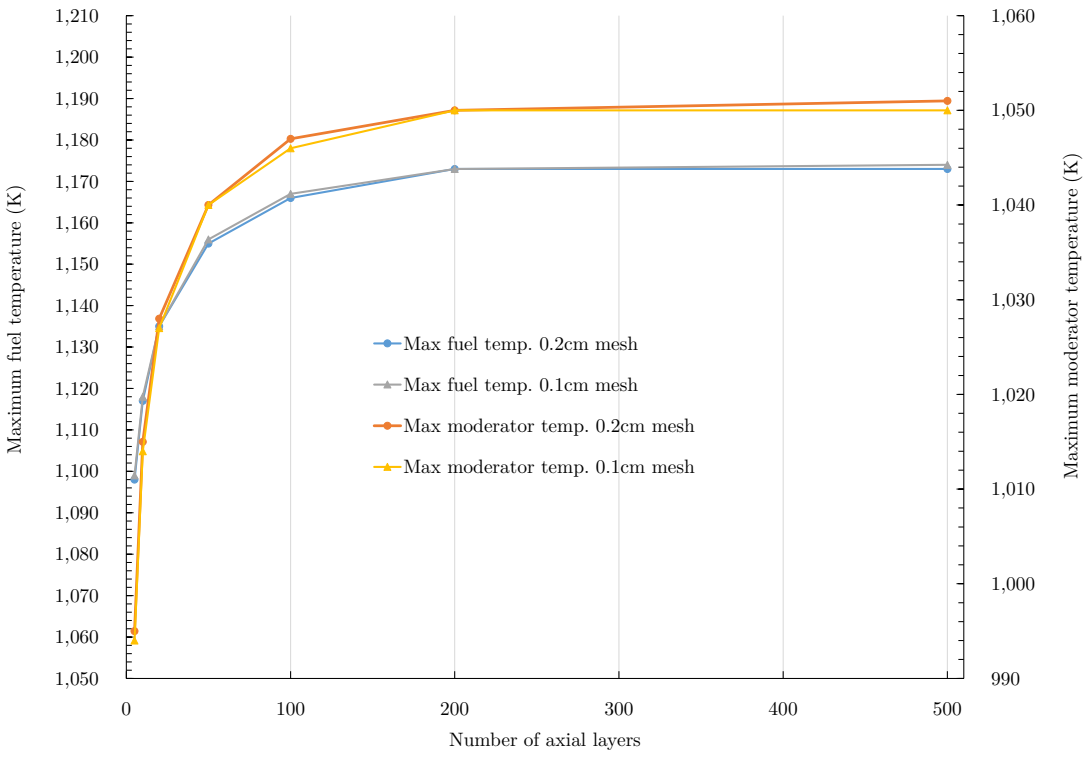

Fig. 3.15 Effect of size of finite element model mesh and number of axial layers on calculated maximum fuel and moderator temperatures in the core

3.7.2 Thermal conductivity of TRISO fuel

Modelling heat transfer within the fuel block requires some analysis of its effective thermal conductivity. As with the tungsten cermet fuel, the fuel is dispersed within a matrix, although the scale is somewhat larger. In the cermet fuel, the dispersion occurred at the micrometre level, whereas TRISO particles are approximately one millimetre in diameter. Given the greater overall level of research into TRISO-based fuels compared to tungsten cermet, far more directly-related research has been carried out into its physical properties.

One possible source of information is a report covering the theory behind PARFUME [61], a code developed at Idaho National Labs for modelling high temperature gas-cooled reactors using particulate fuel. This sets out a relatively straightforward method of calculating

the thermal conductivity of the combined graphite TRISO-particle system:

$$k(T) = f(\text{unirradiated}).f(\text{fluence}).f(\text{packing}).f(\text{matrixdensity}) \tag{3.29}$$

$$f(\text{unirradiated}) = k_{100}[1 - \alpha T' e^{\delta T}] \tag{3.30}$$

$$f(\text{fluence}) = 1 - \gamma[1 - e^{-\beta T}] - \varepsilon\Gamma \tag{3.31}$$

$$f(\text{packing}) = \frac{1-\phi}{1+\phi/2} \tag{3.32}$$

$$f(\text{matrixdensity}) = \frac{\text{matrix density}}{1.7\text{mg/m}^3} \tag{3.33}$$

where T is the temperature in °C, $T' = T - 100$ and ϕ is the packing fraction. The other parameters are:

$$\Gamma = \frac{\text{fast neutron fluence in n/m}^2 \text{ for E} > 0.18\text{MeV}}{1.52 \times 10^{25}\text{n/m}^2}$$

$$\gamma = 0.940 - 0.604 \times (T/1000)$$

$$\beta = 2.960 - 1.955 \times (T/1000)$$

$$\varepsilon = 0.043 \times (T/1000) - 0.008 \times (T/1000)^8$$

$$k_{100} = 47.4\text{W/mK}$$

$$\alpha = 9.7556 \times 10^{-4}$$

$$\delta = -6.0360 \times 10^{-4}$$

Packing

The first part of this worth interrogating is that related to 'packing' - the method used to find the effective average thermal conductivity of the heterogeneous material. The approach taken in Chapter 2 to estimating the thermal conductivity of tungsten cermet was a conservative one, using the method which gave the highest value, which was the Bruggeman method. The method used in the PARFUME model is much simpler. The starting point is Maxwell's expression [74] for the effective conductivity k_e of a continuous matrix of conductivity k_1 containing particles of conductivity k_2 which occupy a proportion ϕ of the volume, which is correct to $O(\phi)$:

$$\frac{k_e}{k_1} = \frac{1 + 2\beta_M\phi}{1 - \beta_M\phi} \tag{3.34}$$

where β_M (with a subscript to distinguish it from the coefficient in the PARFUME method) is given by:

$$\beta_M = \frac{k_2 - k_1}{k_2 + 2k_1} = \frac{\alpha_M - 1}{\alpha_M + 2} \tag{3.35}$$

where $\alpha_M = k_2/k_1$. The conservative assumption made in the PARFUME model is that the thermal conductivity of the particle, k_2, is zero. Therefore $\alpha_M = 0$, $\beta_M = -1/2$ and we arrive at the expression in Equation 3.32. The PARFUME approach is based on earlier work carried out in Germany [41], where the systems considered had a packing fraction ϕ of approximately 10%. However, it is shown in [36] that this approach can lead to an overestimation of the thermal conductivity of a graphite-TRISO system by around 20% when the packing fraction is 50%, as is assumed in the design under investigation. The approach recommended in [36] (including in preference to the Bruggeman model) is an improved form of Maxwell's equation, the Chiew & Glandt model [19]. This is correct to $O(\phi^2)$ and shows good agreement with experimental results for $0.15 < \phi < 0.85$. Using the recommended fitting parameters from [42], the Chiew & Glandt model provides the alternative expression:

$$\frac{k_e}{k_1} = \frac{1 + 2\beta_M\phi + (2\beta_M^3 - 0.1\beta_M)\phi^2 + 0.05\phi^3 \exp\{(4.5\beta_M)\}}{1 - \beta_M\phi} \tag{3.36}$$

This expression can be used as a replacement for Equation 3.32 in the PARFUME model. A question remains over what to use for the thermal conductivity of the TRISO particle. The conservative and simple approach of PARFUME to assume it is zero is one possibility. Of course, the particle does not have a single thermal conductivity, since it is composed of a fuel kernel with four surrounding layers, but a single effective value is required nonetheless in order to use a two-phase model. An analytical method was developed in [100], following Maxwell's method but with a layered particle rather than a simple sphere. This found that for the layer thermal conductivities shown in Table 3.5 and a graphite thermal conductivity of 15 W/mK, the effective thermal conductivity of the particle is 4.13W/mK. This finding was verified using a finite element analysis for a range of packing fractions by Folsom et al. [36]. It was found there that the dependence of this effective thermal conductivity depends strongly on the layer position, with the outer layers having more influence. In fact, the only layer which could conceivably have a significant impact on the effective thermal conductivity of the particle is the penultimate, silicon carbide, layer. Figure 3.16 shows the results from Folsom et al. [36] of their analysis of the dependence on the particle effective thermal conductivity on the conductivity of the various layers. The thermal conductivity of silicon carbide is given as a function of temperature in [61], as $k_{SiC} = 17885/T + 2$, for T in Kelvin. For

an expected temperature range between, say, 700K and 1400K, k_{SiC} would therefore vary between 15W/mK and 28W/mK. Consulting 3.16, one can see that over this expected range, the particle effective conductivity will still vary very little. Therefore, a figure of 4.13W/mK can reasonably be used in all relevant scenarios.

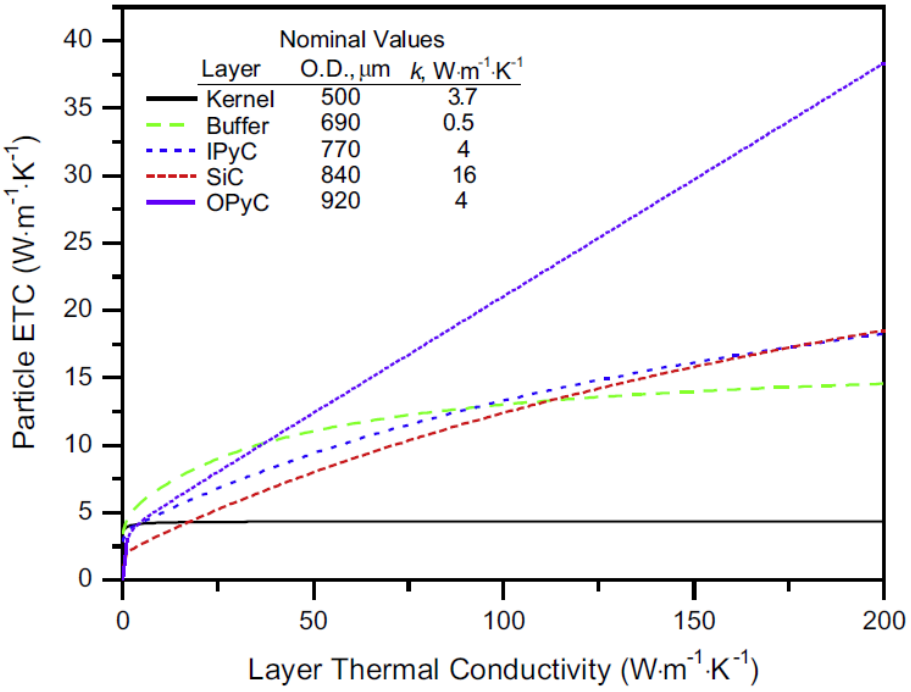

Fig. 3.16 Analysis from Folsom et al. [36] showing dependence of particle effective thermal conductivity on those of constituent layers

Table 3.5 Nominal values of thermal conductivity of TRISO particle layers in [100]

Layer	Material	Thermal conductivity (W/mK)
Kernel	Uranium dioxide	3.7
Coating 1	Porous pyrolytic carbon buffer	0.5
Coating 2	Inner pyrolytic carbon	4.0
Coating 3	Silicon carbide	16.0
Coating 4	Outer pyrolytic carbon	4.0

Graphite

Graphite is manufactured from oil or coal tar pitch coke, using either extrusion or unidirectional or isostatic compression, followed by baking and impregnation with more oil tar pitch.

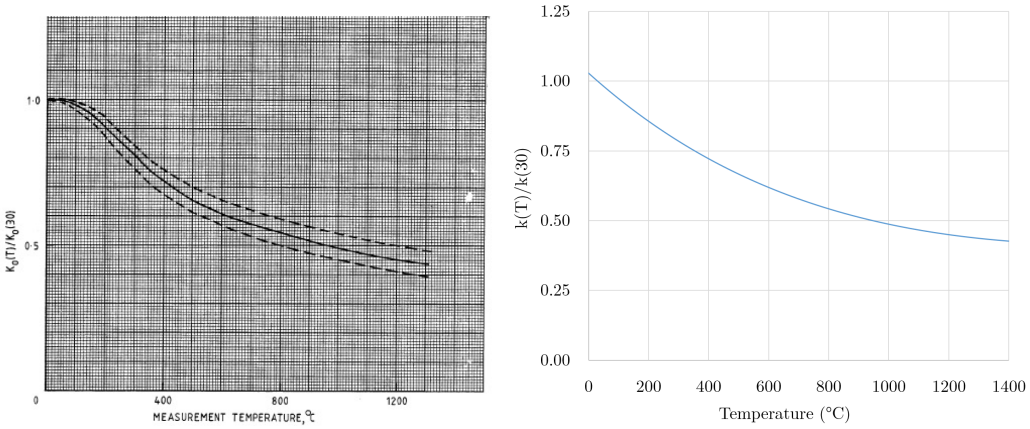

(a) Experimental data from [14] (b) Correlation used in PARFUME

Fig. 3.17 Temperature dependence of unirradiated graphite thermal conductivity normalised to value at 30°C

Finally it is heated to between 2,500°C and 3,000°C in the presence of a purifying agent to complete the graphitisation process [17]. The possible variability in this process means that there are various different grades of graphite with varying grain sizes, anisotropy levels and mechanical properties, with the naming conventions for the various grades being country-dependent. The graphite that the PARFUME correlations are based on is A3-27, a German grade. For this particular grade, Equation 3.30 gives its thermal conductivity as a function of temperature in an unirradiated state. This is compared in Figure 3.17 with experimental data from [14], both normalised to the value at 30°C. The agreement is reasonable (except at the very lowest temperatures, which are unlikely to be seen in the modelling) so Equation 3.30 appears a good choice for the heat conduction model.

Equation 3.31 gives an expression which ostensibly modifies the thermal conductivity of graphite to account for the impact of radiation damage. However, a number of problems present themselves. Firstly, the value of the exponential term $e^{-\beta T}$, is, for the temperature range of interest, effectively equal to zero and is therefore redundant. Next, one might expect that at zero fluence, $f(\text{fluence})$ should be equal to unity, which it is not: at a value of 500°C and zero fluence, $f(\text{fluence})$ is equal to 0.36. Finally, the actual dependence of $f(\text{fluence})$ on fluence is linear, which is at odds with the experimental data shown in Figure 3.18. In this data, it can be seen that thermal conductivity saturates at increasing neutron fluence, with the saturated value being *higher* for higher temperatures. It is possible that Equation 3.31 merely contains a typographical error and should be checked against the source from which it was taken. Unfortunately a copy of the source, [41], proved to be very difficult to obtain despite being widely cited.

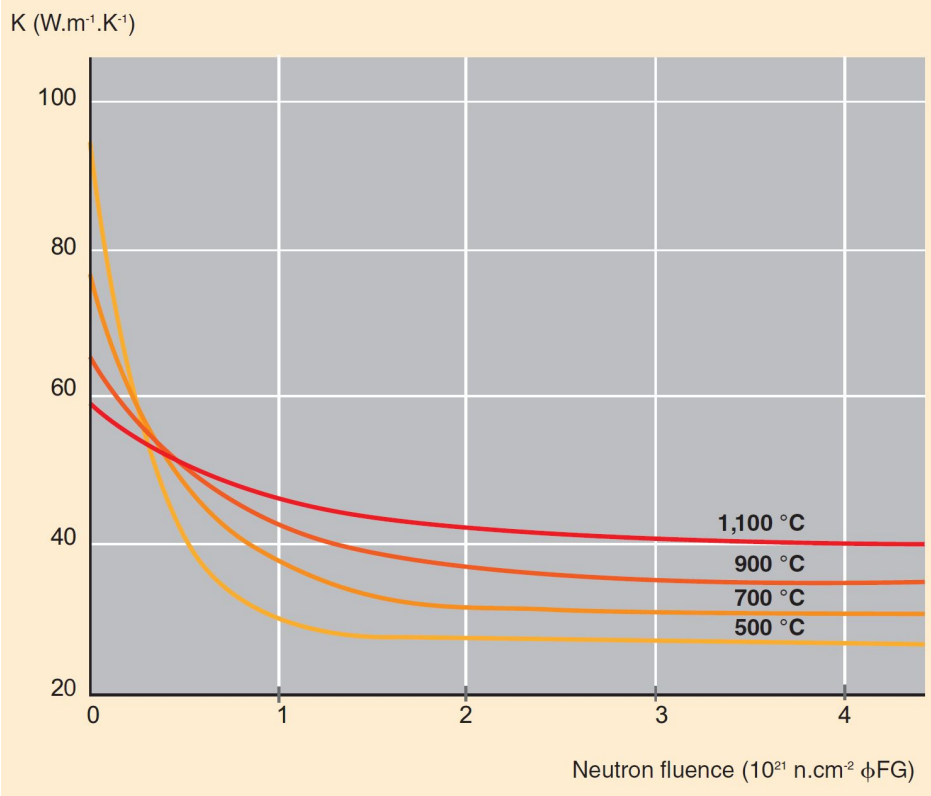

Fig. 3.18 Experimental data [17] showing impact of fast fluence (E>0.2MeV) on graphite thermal conductivity

An alternative formulation for graphite thermal conductivity can be found in [100], as follows. The reciprocal of thermal conductivity K is the thermal resistance, $1/K$. The thermal resistance of irradiated graphite at a temperature T can be expressed as the resistance of unirradiated graphite plus the additional resistance caused by irradiation:

$$\frac{1}{K(T)} = \frac{1}{K_0(T)} + \frac{1}{K_i(T)} \tag{3.37}$$

The additional thermal resistance caused by irradiation can then be separated into two parts. The first is $f(\chi, T_i)$, the fractional change in the thermal resistance (measured at 30°C) for a fast fluence of χ which occurred at an irradiation temperature of T_i:

$$f(\chi, T_i) = \frac{K_0(30)}{K_i(30)} = \frac{K_0(30)}{K(30)} - 1 \tag{3.38}$$

The second part accounts for the difference between the additional radiation damage-induced thermal resistance at a measurement temperature of T and at a measurement temperature of

30°C. Experimental data suggests that their ratio is independent of the fluence, giving:

$$\delta(T) = \frac{K_i(30)}{K_i(T)} \tag{3.39}$$

The values of $\delta(T)$ do also depend on the irradiation temperature, but the dependence was found to be weaker at irradiation temperatures of higher than 450°C [100]. Putting the two contributions together, we arrive at:

$$\frac{1}{K_i(T)} = \delta(T)\frac{f(\chi, T_i)}{K_0(30)} \tag{3.40}$$

An additional phenomenon known as 'shrinkage reversal' which occurs at very high fluences (higher than those shown in Figure 3.18) is captured by the structure factor $S(\chi, T_i)$. This phenomenon further decreases the thermal conductivity below the saturated value. This effect is not seen in Figure 3.18 which does not extend to sufficiently high fluxes, but can be seen in Figure 3.19 which covers higher fluences. Combining all of the above gives an expression for the thermal resistance for irradiated graphite:

$$\frac{1}{K(\chi, T)} = S_k(\chi, T_i)\left[\frac{1}{K_0(T)}\delta(T)\frac{f(\chi, T_i)}{K_0(30)}\right] \tag{3.41}$$

The values of $f(\chi, T_i)$, $\delta(T)$ and $S_k(\chi, T_i)$ are experimentally determined and example results are available in [100] in graph form. It would be feasible to extract these graphical data and carry out functional fits, interpolating or extrapolating where necessary.

Applying this methodology in full would introduce some degree of complexity, since there is a strong initial dependence of thermal conductivity on fast neutron fluence, which will vary across the core. It would be necessary to keep track of the fluence at different core locations throughout the burnup calculation and apply this map of fluences when calculating the graphite thermal conductivity. Reflecting the time-dependent nature of the thermal conductivity would also require carrying out a new thermal hydraulic calculation at each burnup step (or, at least, some subset of them). Before exploring this further, it is worth investigating if a reasonable assumption could be made that removes the need to account for spatially and temporally variable irradiation damage. One option is to assume that the graphite has its fluence-saturated thermal conductivity throughout the core and throughout its lifetime. This will lead to higher calculated fuel temperatures. This in turn would lead to more core designs breaching the maximum specified fuel temperature. The increased temperature would also reduce core reactivity, leading to a lower estimation of end-of-life k_{eff}. The assumption of saturated (that is, lower) thermal conductivity is therefore conservative in

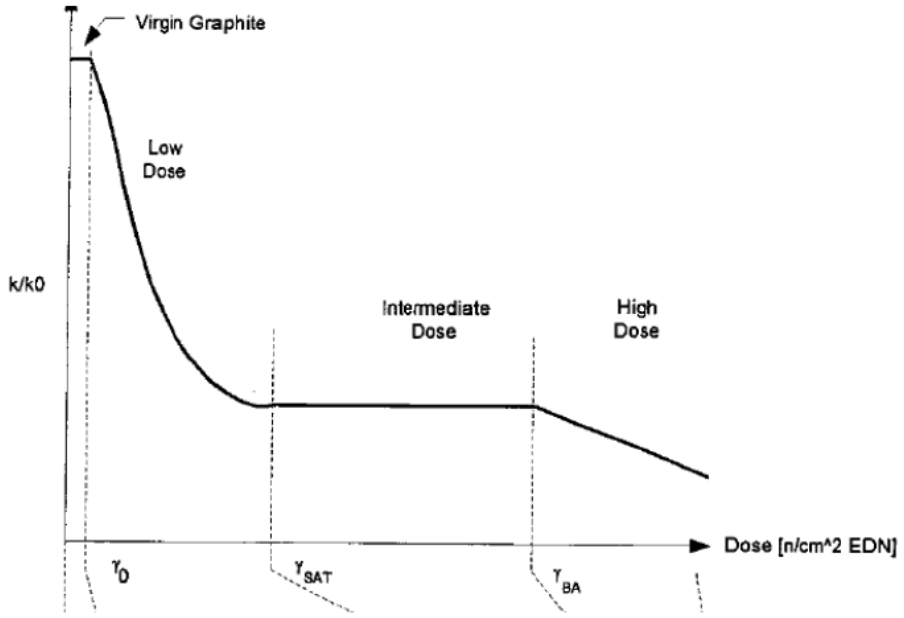

Fig. 3.19 Evolution of graphite thermal conductivity with irradiation in Pebble Bed Modular Reactor showing degradation at very high fluences. Taken from [100] but originally in [76]

both of these respects. There is a risk of introducing excessive conservatism here, however, so it is worth checking whether core designs do approach the saturation point.

To this end, three example core designs were chosen that would satisfy the required end-of-life reactivity constraint. All have ten rings of 4cm diameter fuel blocks, a fuel height of 66cm and 8cm radial and axial reflectors:

- LEU fuel with zirconium hydride moderator of 4mm around each fuel block
- LEU fuel with graphite moderator
- HEU fuel with no graphite moderator

Each of these designs was modelled in WIMS, but using 172 energy groups to allow the isolation of the 'fast' flux using the cut-off of 0.1MeV used in [17] so that the fast fluence can be compared with Figure 3.18. As usual an operating life of seven years was assumed, with a core thermal power of 4MW, which implies an optimistic conversion efficiency of 25%. The results are shown in Table 3.6. These are fairly approximate since they are based on the assumption that the flux shape and spectrum do not vary with burnup. The results also refer only to the flux at the core centre. The flux is generally highest at the core centre (and certainly is in these examples) and so one should generally be cautious using the core-centre conditions to set assumptions for the entire core. However, the thermal limits that determine

whether a core design is acceptable will almost certainly be breached first at the core centre. Therefore, the assumptions used away from the core centre are ultimately of less importance.

Table 3.6 Fast fluence at core centre for representative cores at end of life

Fuel type	**Moderator**	**End of life fast fluence (n/cm^2)**
LEU	ZrH	6.9×10^{20}
LEU	Graphite only	4.1×10^{21}
HEU	Graphite only	2.8×10^{21}

Based on the results in Table 3.6, it seems that for cases where no moderator is present it is reasonable to assume that the graphite has reached its saturation point. The first case, for moderated LEU fuel, is less clear. Referring to Figure 3.18, it can be seen that for a temperature of 700°C we might underestimate the graphite thermal conductivity by up to around 25% by adopting the assumption of saturation. This is only indicative and cores with a different power density (because of size or total power) will, of course, differ from this. For the sake of simplicity, but at the risk of unfairly penalising the moderated LEU designs, the same assumption of saturation will be applied in all cases. With regards to shrinkage reversal, this phenomenon only appears at very high fast fluences of above $12.5 \times 10^{21}\mathrm{n/cm^2}$ [100], so it is reasonable to assume that the thermal conductivity will not drop any further than its saturation value.

The actual values for graphite thermal conductivity after saturation are easily obtained from Figure 3.18 and fit to an almost linear function, fitted using the MATLAB Curve Fitting Tool with a polynomial functional form:

$$K(T) = 8.669 \times 10^{-6} \times T^2 + 0.003412 \times T + 19.42 \tag{3.42}$$

Once the temperature distribution for the bulk fuel has been determined, a relatively trivial one-dimensional heat conduction model is used to determine the fuel kernel temperature. One reason TRISO particles are valued is their ability to retain fission products at extremely high temperatures in accident scenarios, but in normal operations this is not expected to exceed 1,250°C [45], or 1,523K. This will be used as the limiting kernel temperature.

3.7.3 Moderator temperature modelling

The zirconium hydride moderator sits in a hexagonal ring around each fuel block, separated from it by a hexagonal ring of coolant, as shown in Figure 3.4. This coolant ring ensures that heat is not directly conducted from the fuel block to the moderator. Since the width

of the coolant ring can vary independently from the diameter of the main coolant channels, it will be possible to divert more coolant through the coolant ring to aid the cooling of the moderator. This is important since zirconium hydride has a significantly lower maximum temperature than the fuel kernels or their graphite matrix. Early work [110] considering ZrH as a shielding component for space suggests a 'maximum useful temperature' of 1,073K, while more recent work relating to nuclear thermal rockets [111] gives a maximum tolerable value of 1,088K. Some margin would naturally be allowed below the maximum temperature, with the latter study having a maximum moderator temperature in operation of 982K. This latter value is used as the absolute maximum in this study.

Estimating the temperature within the moderator is relatively simple compared to the fuel block due to its simple geometry. Essentially the same method is used here as was used to analyse the tungsten cermet fuel block in Chapter 2. There, the fuel surrounding each coolant channel was approximated as an annulus. The outer edge had an adiabatic boundary condition (zero temperature gradient) since this was intuitively where the maximum temperature occurred and the inner edge of the annulus had a fixed temperature boundary condition determined by analysis of convective heat transfer. The geometry of the interstitial moderator is very similar. The outer edge will also have an adiabatic boundary condition. The boundary condition for the inner surface is also a fixed value. The value it takes can be inferred by considering that the outer surface of the fuel block and the inner surface of the moderator face each other across a gap filled with a gas. It is reasonable to assume that this is transparent and that these two faces must therefore be in a radiative equilibrium. That is, the temperature of the inner face of the moderator must be equal to the outer face of the fuel block.

If no heat were generated within the moderator itself, the moderator would have a uniform temperature equal to that of its inner surface. However, the moderator does have internal heat generation, or, to put it more accurately, energy is deposited there (discussed in the next section). Once the internal heat generation rate is established, the same approach is taken as in Chapter 2: the annular domain is split into ten subdomains on which the heat transfer equation is solved, to allow the temperature variability of thermal conductivity to be captured. In fact, for zirconium hydride, the thermal conductivity varies little with temperature, as can be seen in Figure 3.20, and is assumed to be a constant 18W/mK.

Heat deposition

Each fission event releases approximately 200MeV of energy (for U-235) previously held as binding energy in the nucleus [63]. Most of the energy manifests in the form of the kinetic energy of the fission fragments, around 168MeV. They do not travel very far within

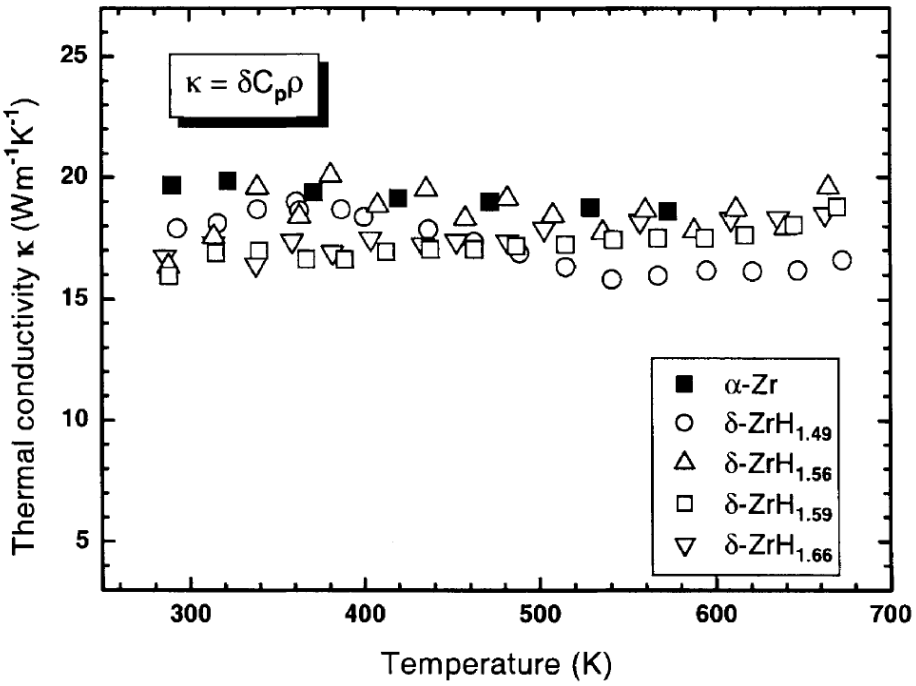

Fig. 3.20 Variation of thermal conductivity of zirconium hydride with temperature [120]

the fuel and can be assumed to deposit their energy at the site of the fission event. Prompt neutrons and prompt gammas carry around 5MeV and 7MeV respectively, travelling through the reactor and depositing their energy in a variety of core materials. Fission products subsequently produce delayed neutrons, beta particles and gammas. The delayed neutrons carry negligible energy but the beta particles carry around 8MeV. Beta decay also produces electron neutrinos which carry around 12MeV of kinetic energy but which, due to their very weak interaction with matter, can be assumed to leave the reactor. The delayed gammas carry around the same energy as the prompt gammas, around 7MeV. A further source of gammas is the radiative capture of neutrons. The proportion of neutrons that undergo radiative capture depends on the system under consideration, but one might expect that for every fission event a further 3-12MeV might appear from radiative capture. Table 3.7 summarises these figures. The most basic approach to calculating where heating occurs in a nuclear reactor is to assume that it is all deposited at the fission site. Using this approach would, of course, result in a moderator heating rate of zero since no fission occurs in the moderator. The next obvious improvement to this is to account for the heating due to neutrons which lose energy (and therefore transfer it) by elastic and inelastic scattering. Whichever method is used to calculate the neutron flux throughout the core, the rates of neutron scattering (and the energy lost in the scatters) in each spatial location and energy group should in principle be available.

Table 3.7 Emitted and recoverable energies from fission of U-235 [63]

Form	Emitted energy (MeV)	Recoverable energy (MeV)
Fission fragments	168	168
Fission product decay		
β particle	8	8
γ ray	7	7
neutrinos	12	-
Prompt γ ray	7	7
Prompt neutrons	5	5
Capture γ ray	-	3-12
Total	207	198-207

Determining accurately where photons travel and deposit their energy, however, requires a significant increase in sophistication.

Relatively recently Serpent 2 has gained a coupled neutron-photon tracking mode, which allows much more accurate calculation of spatial heat deposition [109]. In this mode, in addition to neutrons, photons are tracked from their origination sites and the energy they lose (through pair production, Compton scattering and the photoelectric effect) can be tallied in spatial bins. Since both neutrons and photons are being tracked, accurate account is taken of the creation of gammas by neutrons through radiative capture and even the creation of gammas by neutrons in (γ, n) reactions (usually a minor effect). Figure 3.21 shows, for an example design, the relative heat deposition between the fuel block and moderator for neutrons and gammas. As can be seen, neutron heating is relatively concentrated in the moderator (as one might expect, since the moderator's purpose is to remove energy from neutrons), whereas photon heating is somewhat more evenly distributed.

Some approximations remain. Beta particles are still assumed to deposit their energy at the fission site immediately. Delayed gammas are also assumed to appear immediately, in proportion to the prompt gamma source, simply scaling the prompt gamma source using the average ratio of delayed to prompt gammas. Ignoring these delays means that transient calculations are not possible but this is not a concern in the present application. The assumption that delayed gammas appear in proportion to prompt gammas (and with the same energy spectrum) is itself also an approximation. A more accurate approach involves taking account of the concentration and activity of gamma-emitting fission products and their individual spectra. The accuracy of this approximation has been examined [70] in the context of a PWR fuel assembly and it was found that the greatest impact is an overall overestimation of heat production in the control rod of just 0.6%.

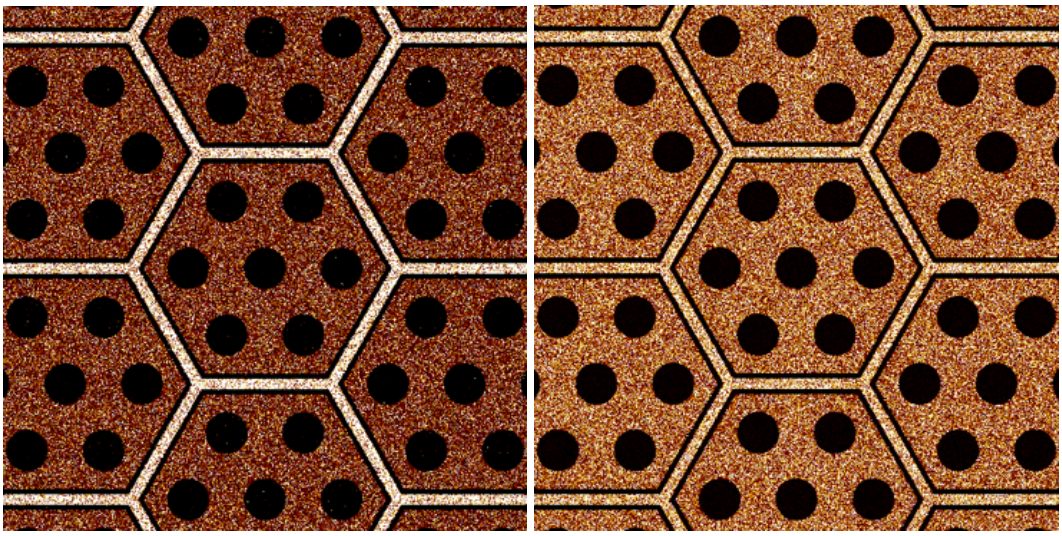

(a) Heating by elastic and inelastic neutron scattering

(b) Heating by photons

Fig. 3.21 Heat deposition maps produced by Serpent showing relative heating of fuel block and moderator by neutron scattering and photons. Brighter regions indicate a higher heating power.

Clearly it is not feasible to run the Serpent neutron-photon calculation for every core design, since this would likely represent a greater computational burden than the main neutronics calculation. A study was therefore carried out to determine if the neutron and photon heating of the moderator can be estimated for a given core design. Several two-dimensional core slices were considered. The heating rate would be expected to vary depending on the fuel to moderator ratio, so six different interstitial moderator thicknesses were tested. The thickness of the reflector and the overall size of the core might also be expected to have some influence, so the six moderator thicknesses were modelled across each of the following three core designs:

- 16 rings of assemblies with a 20cm reflector
- 10 rings of assemblies with a 20cm reflector
- 10 rings of assemblies with a 4cm reflector

First, the heat deposition in the moderator is considered across the entire reactor. In Figure 3.22 is shown the heating power in the moderator due to neutrons and photons as a proportion of the total reactor fission power. As can be seen, there is a relatively weak dependence on the size of the core and the size of the reflector for both neutron and photon heating. The dependence on the fuel to moderator ratio, on the other hand, is strong. A curve

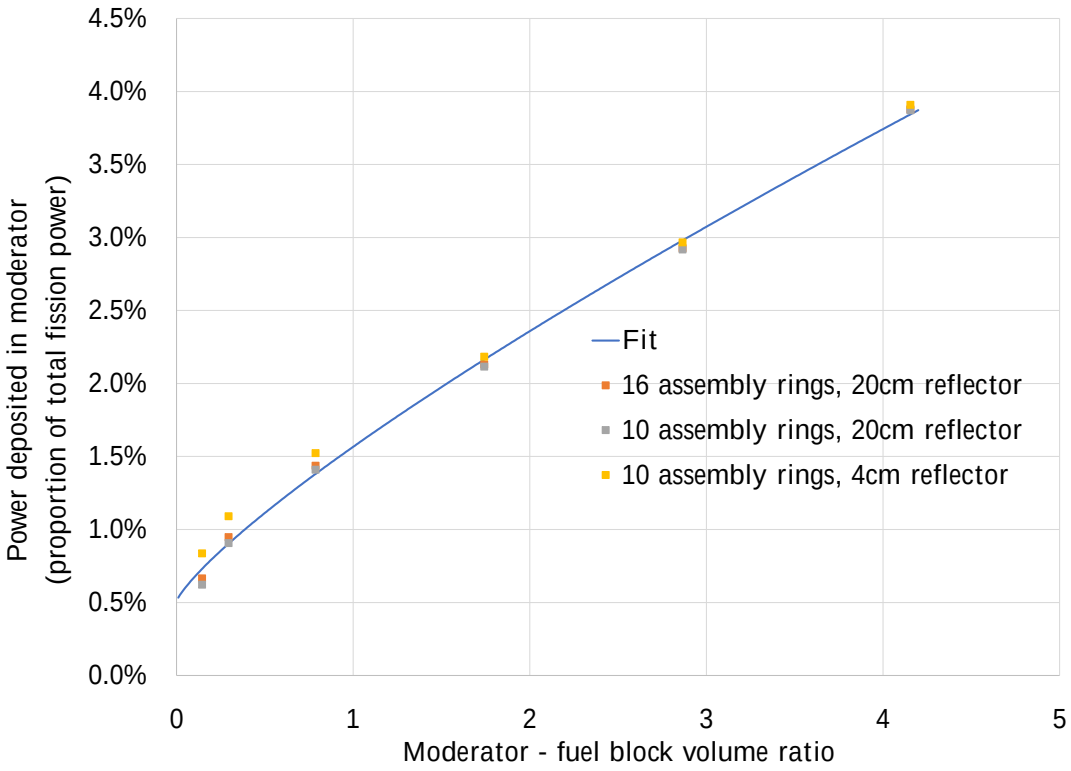

(a) Heating by elastic and inelastic neutron scattering

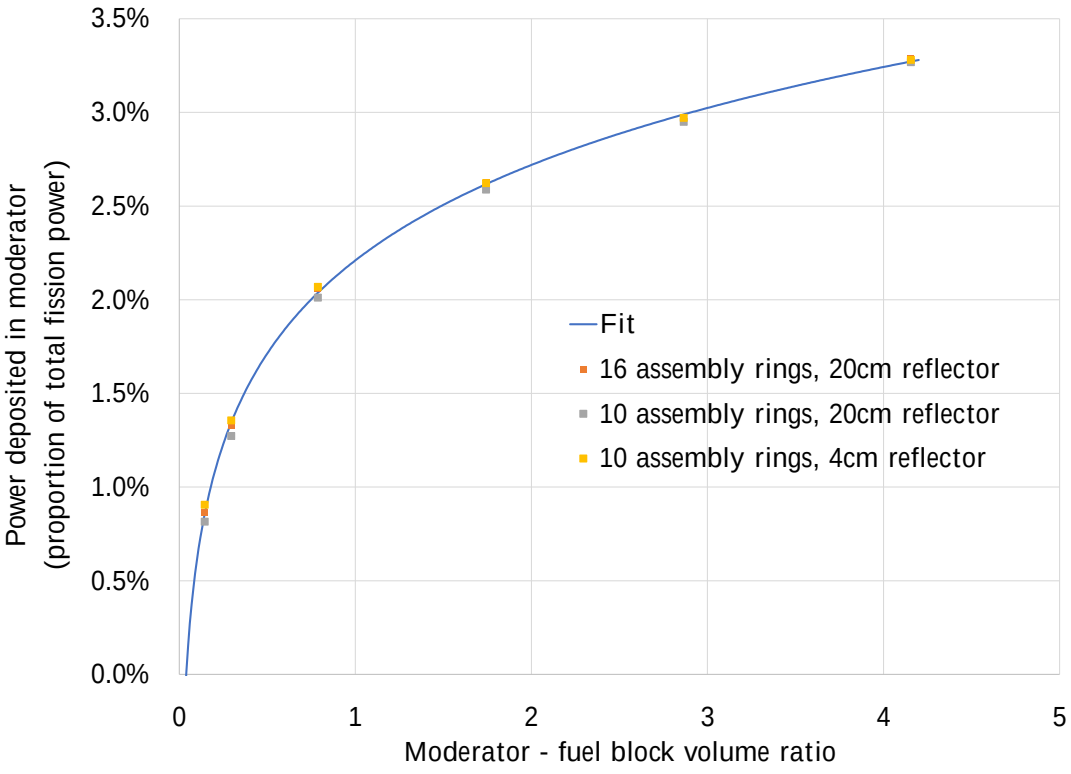

(b) Heating by photons

Fig. 3.22 Relationship between fuel/moderator ratio and moderator heating by neutrons and photons

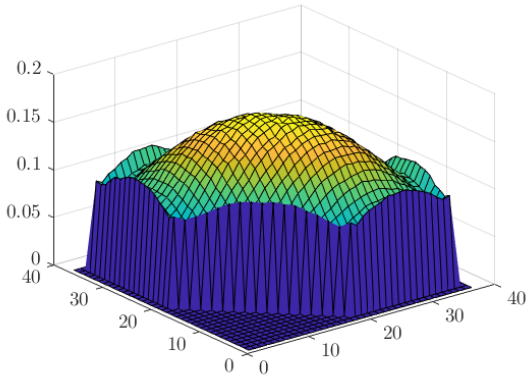

(a) Total fission power

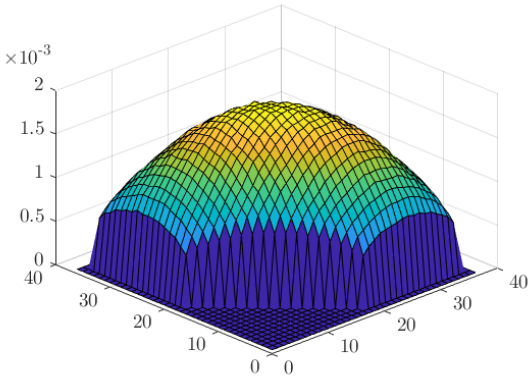

(b) Heating by neutron scattering

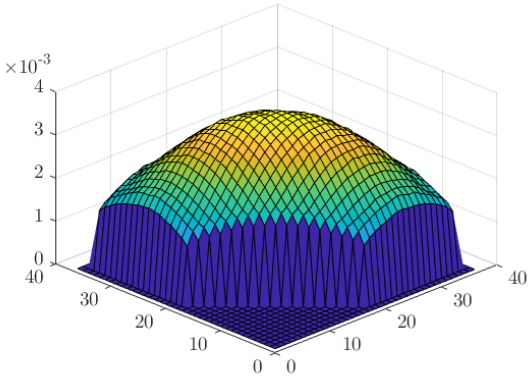

(c) Heating by photons

Fig. 3.23 Surface plots comparing distribution of fission power and heating of the moderator by neutron scattering and photons. These examples are based on a core with 16 rings of assemblies each surrounded by 5mm of moderator, with a 20cm reflector.

can be fitted to these results and used to predict the average moderator heating rate for any given fuel to moderator ratio. This was carried out using the MATLAB Curve Fitting Tool and a power law functional form. Turning now to the spatial dependence, it can be seen from Figure 3.23 that the distribution of moderator heating by both neutrons and photons very broadly follows the same shape as the total fission power, except for the peaking in a thin region next to the reflector. This suggests that a rough approximation for the shape of the moderator heating power density might be to simply use that of the total fission power, which is readily available. The power shapes shown in Figure 3.23 are only for one core design; rather than examine the distributions for all the core designs considered, the ratio of the centre peak to the average is compared in Table 3.8. It would appear from this that heating of the moderator by neutrons and photons is fairly localised. Based on these it seems

that a reasonable approach to estimating the moderator heating in any location is to simply apply the same fission power density occurring in the corresponding fuel block and scale it by the functions found in the lines of fit shown in Figure 3.22.

Table 3.8 Comparison of centre-to-average ratio for fission power and moderator heating distributions for core with 16 rings of assemblies and 20cm reflector

Moderator thickness (mm)	**1**	**2**	**5**	**10**	**15**	**20**
Fission centre-to-average ratio	1.8	2.2	2.4	2.7	2.9	3.0
Moderator heating centre-to-average ratio	2.0	2.2	2.4	2.7	2.9	3.1

3.7.4 Core flow pattern

Once coolant enters a reactor core it generally has several paths it might follow to reach the core outlet. The flow rate through each of these paths is not generally equal even in the case identical channels due to the effects of heating. Determining the flow pattern through the reactor is therefore a key part of reactor core thermal hydraulics. The key to this process is to find the flow pattern that ensures that the pressure loss along each flow path is equal, since any imbalance in pressure at the ends of the channels would drive a change in the flow pattern. One approach is to assume a flat flow profile (equal along all channels) then run the thermal hydraulics analysis code based on this flow profile to calculate the pressure loss along each channel. These pressure losses can then be used to update the flow profile by increasing flow along channels with a lower pressure loss and decreasing flow along channels with a higher pressure loss. This process iterates until convergence in the flow profile is reached. One drawback of this approach is the potentially large number of calls to the thermal hydraulics solver and the resulting burden of calculation time. Such an approach would have been usable for the simple analytical heat conduction model presented in the previous chapter, but the introduction of finite element modelling increases the run-time of the heat conduction model significantly. For each axial slice of a fuel block like that shown in Figure 3.13, the analysis typically only takes a few seconds, but must be carried out for each axial layer and for each part of the reactor core. Therefore, in order to minimise the number of calls to the thermal hydraulics solver, it is worth investing in a more sophisticated method for predicting the core flow pattern.

The first step is to introduce a ‘hydraulic resistance’. This casts the problem to be solved into a familiar form, that of electrical conduction: Ohm’s Law relates the voltage and the current to the electrical resistance by $V = IR$. Similarly, one can relate the pressure drop to

the coolant flow rate, Q, as $\Delta p = g(Q)R$, where g is some function to be determined and R is the hydraulic resistance.

As described in the previous chapter, there are two components of the pressure loss: friction and shock. It will be recalled that the friction pressure loss over a length z can be calculated as $\Delta p_{\text{fric}} = 0.5\rho v^2 z f / d_{\text{H}}$ where f is the friction factor. For turbulent flow in smooth pipes f can be approximated as $0.184\text{Re}^{-0.2}$. The Reynolds number contains a factor of v, the flow speed. It can therefore be seen that the overall dependence of the frictional pressure loss on flow speed, and therefore flow rate, will be given by $g(Q) = Q^{1.8}$ where Q is the mass flow rate. It can also be seen after rearranging that the frictional resistance R_{fric} is given by:

$$R_{\text{fric}} = 0.092 z \rho^{-1} d_{\text{H}}^{-1.2} \mu^{0.2} A^{-1.8} \tag{3.43}$$

where A is the flow area and μ is the dynamic viscosity.

If it were the case that this were the only source of hydraulic resistance and the fluid properties ρ and μ where unchanging through the channels, it would then be possible to analytically solve for the flow rate in all the channels in the system. First, the total resistance for parallel channels can be calculated using the familiar form seen in the analysis of parallel electrical resistors, but allowing for the non-linear relationship of resistance to flow:

$$\frac{1}{{R_{\text{T}}}^{1.8}} = \sum_i \frac{1}{{R_i}^{1.8}} \tag{3.44}$$

With the total resistance in hand and with a known value of the total coolant flow rate, the pressure drop can then be calculated using $\Delta p = Q_{\text{T}} {R_{\text{T}}}^{1.8}$. This pressure drop applies to all parallel channels, so the flow through each channel can then be calculated using $Q_i = \Delta p / {R_i}^{1.8}$. There is, however, a further source of pressure loss due to 'shock', or sudden geometrical changes, at the inlets and outlets of each channel. This is calculated as $\Delta p_{\text{shock}} = 0.5\rho v^2 (K_{\text{c}} + K_{\text{e}})$, as per Equation 2.11. It can be seen that the dependence of this component of the pressure loss on the flow rate will be $g(Q) = Q^2$. Overall then the pressure drop along any particular channel will be given by:

$$\Delta p = R_{\text{fric}} Q^{1.8} + R_{\text{shock}} Q^2 \tag{3.45}$$

With the mixed dependency on the flow rates it is then not possible to use the familiar 'parallel resistors' formula shown in Equation 3.44. Another method can be borrowed from analysis of electrical circuits: the application of Kirchoff's Laws, which can be applied to networks of pipes containing flowing fluids [75]. Kirchoff's current law (or first law) is that

the sum of currents flowing into a node must equal the sum of currents flowing out of that node. The reactor core is a very simple network consisting of one set of parallel channels; there are therefore only two 'nodes' at the inlet plenum, which feeds all the channels, and the outlet plenum, into which all the channels discharge. Applying Kirchoff's current law to either node gives the trivial result that the sum of the fluid flows in all channels must equal the total coolant flow rate:

$$Q_{\mathrm{T}} = \sum_i Q_i \tag{3.46}$$

Kirchoff's voltage law (or second law) states that the directed sum of voltages around any closed loop must be zero. The fluid analog of voltage here is, of course, the pressure drop Δp. For the reactor core, such loops are made by travelling from the inlet plenum along one channel to the outlet plenum, then back down to the inlet plenum along a different channel. For a core with N channels, this can produce a system of $N-1$ non-redundant equations:

$$\begin{aligned} \Delta p_1 - \Delta p_2 &= 0 \\ \Delta p_2 - \Delta p_3 &= 0 \\ &\vdots \\ \Delta p_{N-1} - \Delta p_N &= 0 \end{aligned} \tag{3.47}$$

Substituting in from Equation 3.45 above gives:

$$\begin{aligned} R_{\mathrm{fric},1} {Q_1}^{1.8} + R_{\mathrm{shock},1} {Q_1}^2 - R_{\mathrm{fric},2} {Q_2}^{1.8} - R_{\mathrm{shock},2} {Q_2}^2 &= 0 \\ R_{\mathrm{fric},2} {Q_2}^{1.8} + R_{\mathrm{shock},2} {Q_2}^2 - R_{\mathrm{fric},3} {Q_3}^{1.8} - R_{\mathrm{shock},3} {Q_3}^2 &= 0 \\ &\vdots \\ R_{\mathrm{fric},N-1} {Q_{N-1}}^{1.8} + R_{\mathrm{shock},N-1} {Q_{N-1}}^2 - R_{\mathrm{fric},N} {Q_N}^{1.8} - R_{\mathrm{shock},N} {Q_N}^2 &= 0 \end{aligned} \tag{3.48}$$

These $N-1$ equations, together with Equation 3.46, make a system of N equations with N unknowns that can in principle be solved for Q_i if the $R_{\mathrm{fric},i}$ and $R_{\mathrm{shock},i}$ are known. In fact they are not known exactly in advance since they depend on fluid properties which change due to heating. However, they can be estimated assuming that the conditions at the channel inlets persist over the entire channel. The system of equations can then be solved to obtain the Q_i. There are several methods of solving a system of non-linear equations, but the default method used by MATLAB, the 'Trust-Region-Dogleg' algorithm, is more than adequate,

resulting in a solution in less than a second even for a set of over 100 channels. For a full-core calculation, it is not in fact necessary for N to be the total number of channels in the core. An assumption is made that the core is radially symmetric such that all elements in one ring of the core are identical, so one element represents each core ring and the flow rates through its eight channels (seven interior, one annular) can be assumed to apply to all elements within that core ring.

Once the flow rates have been calculated, the main thermal hydraulics code can be executed, which calculates the core material temperatures, coolant temperatures and pressure losses along each channels. These pressure losses can be used to update the values of $R_{\text{fric},i}$ and $R_{\text{shock},i}$. The system of flow equations is solved again and the flow pattern fed to the thermal hydraulics code, and so on. This iterative process continues until a desired level of convergence in the pressure loss is reached. Defining the convergence criterion as the ratio of the highest and lowest pressure losses found across all channels, it was found that a convergence criterion of 2% is sufficient. Further iterations produce improvements in the calculated core temperatures of only a few degrees. To achieve this level of convergence usually only requires two or sometimes three calls to the main thermal hydraulics solver, illustrating the efficiency of this overall scheme.

3.8 Working fluid properties

In the analysis of both the core thermal hydraulics and the Brayton cycle energy conversion system, it is necessary to have available all relevant fluid properties such as density, heat capacity, thermal conductivity and viscosity. The initial approach taken in the previous chapter was for the thermal hydraulics code to refer to a dataset containing these temperature-dependent data, taken from the National Institute of Standards and Technology Chemistry WebBook [81]. The other working fluid of interest is a 40g/mol mixture of helium and xenon. The benefit of this mixture over pure helium is that it has approximately the same heat transfer coefficient whilst significantly decreasing the turbomachinery loading, and therefore the turbomachinery mass [29]. This will be quantified in a subsequent section. Unfortunately, no equivalent dataset is available for this mixture. Therefore these properties must be calculated as needed.

The thermophysical properties of a pure, dilute, monatomic gas are generally estimated using a perturbation technique applied to the Boltzmann equation [47]. This technique is referred to as the Chapman-Enskog approach for its independent originators. Here, ‘dilute’ refers to a gas in which the mean free path of the molecules is much larger than their size so that they can be assumed to interact only in binary collisions. However, the gas is assumed

to still be sufficiently dense that collisions between the molecules and the container walls can be neglected as relatively infrequent compared to binary collisions between molecules. Whether or not these conditions can be assumed to apply to the typical conditions in a space Brayton system operating at up to 2MPa working pressure was investigated by Tournier et al. [107]. Here it was found that for binary mixtures of helium and xenon of up to 40g/mol, the assumption of a dilute gas can be used. Specifically, for up to a molecular weight of 40g/mol, the compressibility can be assumed to be unity such that the ideal gas law can be assumed to apply and that the effect of pressure on molar heat capacity, thermal conductivity and viscosity can be neglected. The Chapman-Enskog approach can thereby be used to derive these quantities, which will now be set out [107].

Density

First, as mentioned, the density of helium-xenon binary mixtures within the range of pressures under consideration can be simply calculated using the ideal gas law:

$$\rho = \frac{P\overline{M}}{RT} \tag{3.49}$$

where P is the pressure, $\overline{M}$ is the mean gas molar mass, R is the gas constant and T is the temperature. The mean molar mass is simply calculated as $\overline{M} = x_1 M_1 + x_2 M_2$, where x_i is the proportion of the mixture that is element i and M_i is its molar mass.

Viscosity

The dynamic viscosity for pure noble gases can be calculated using the correlation:

$$\mu(T) = A_\mu (T - T_\mu)^n \tag{3.50}$$

The parameters in this equation for helium and xenon are shown in Table 3.9 below. Then,

Table 3.9 Parameters for Equation 3.50

Fluid	$A_\mu \times 10^7$	T_μ	n
Helium	3.0629	-21.33	0.7243
Xenon	7.5683	112.31	0.6555

the viscosity of the binary mixture $\bar{\mu}$ can be calculated using:

$$\bar{\mu} = \frac{\mu_1}{1+\phi_{12}x_2/x_1} + \frac{\mu_2}{1+\phi_{21}x_1/x_2} \tag{3.51}$$

where μ_i is the viscosity of gas i and the x_i are the mixture proportions as before. The ϕ_{ij} are interaction coefficients which are calculated using:

$$\phi_{12} = \frac{\mu_1}{\mu_{12}}\left[\frac{2m_1m_2}{(m_1+m_2)^2}\right] \times \left[\frac{5}{3A^*_{12}} + \frac{m_2}{m_1}\right] \tag{3.52}$$

$$\phi_{21} = \frac{\mu_2}{\mu_{12}}\left[\frac{2m_1m_2}{(m_1+m_2)^2}\right] \times \left[\frac{5}{3A^*_{12}} + \frac{m_1}{m_2}\right] \tag{3.53}$$

Here A^*_{12} can be taken as a constant, 1.10. The m_i are the molecular masses of the constituents (equal to M_i/N_A, where N_A is Avogadro's number). The quantity μ_{12} is the 'interaction viscosity', calculated using:

$$\mu_{12} = A_\mu(T - T_\mu)^n \tag{3.54}$$

Values of the parameters in this equation are tabulated for each pair of noble gases; for helium and xenon they are $A_\mu = 3.41 \times 10^{-7}$, $T_\mu = 45.89$ and $n = 0.6588$.

Thermal conductivity

The pure gas thermal conductivity can be related to the dynamic viscosity:

$$\lambda = \frac{15}{4}\frac{k_B}{m}\mu \tag{3.55}$$

where k_B is Boltzmann's constant. The thermal conductivity of a binary gas mixture is then given by:

$$\bar{\lambda} = \left[\frac{{x_1}^2}{L_{11}} - \frac{2x_1x_2L_{12}}{L_{11}L_{22}} + \frac{{x_2}^2}{L_{22}}\right] \times \left[1 - \frac{{L_{12}}^2}{L_{11}L_{22}}\right] \tag{3.56}$$

The L_{ij} factors are calculated as follows:

$$L_{11} = \frac{x_1^2}{\lambda_1} + \frac{x_1 x_2}{2\lambda_{12}} \times \frac{7.5{m_1}^2 + 6.25{m_2}^2 - 3{m_2}^2 B_{12}^* + 4m_1 m_2 A_{12}^*}{(m_1+m_2)^2 A_{12}^*} \tag{3.57}$$

$$L_{22} = \frac{x_2^2}{\lambda_2} + \frac{x_1 x_2}{2\lambda_{12}} \times \frac{7.5{m_2}^2 + 6.25{m_1}^2 - 3{m_1}^2 B_{12}^* + 4m_1 m_2 A_{12}^*}{(m_1+m_2)^2 A_{12}^*} \tag{3.58}$$

$$L_{12} = -\frac{x_1 x_2}{2\lambda_{12}} \times \frac{m_1 m_2}{(m_1+m_2)^2 A_{12}^*} \times (13.75 - 3B_{12}^* - 4A_{12}^*) \tag{3.59}$$

Here A_{12}^* and B_{12}^* can be taken as constants, both equal to 1.10. The interaction thermal conductivity λ_{12} can be related to the interaction viscosity via:

$$\lambda_{12} = \frac{15}{4}\frac{k_B}{m_{12}}\mu_{12} f_{12} \tag{3.60}$$

where $m_{12} = 2m_1 m_2/(m_1+m_2)$. The correction factor f_{12} is tabulated for each pair of noble gases; for helium and xenon it is 1.060.

Heat capacity

Since the binary mixtures under consideration can be treated as an ideal gas, the specific heat capacities at constant volume and pressure can be calculated simply using the mean molar mass $\overline{M}$:

$$C_V = \frac{3}{2}\frac{k_B}{\overline{M}u} \tag{3.61}$$

$$C_P = \frac{5}{2}\frac{k_B}{\overline{M}u} \tag{3.62}$$

where u is the atomic mass unit.

3.8.1 Validation

There are no experimental data available for properties of the exact 40g/mol helium-xenon mix often recommended for space Brayton systems. Fortunately some data are available in [59] for pairs of noble gases in other proportions. One set of data is for a 75% helium, 25% xenon mixture (by atom fraction), which is close to the 72% helium, 28% xenon mixture that gives the required molar mass of 40g/mol. These are sufficiently close that the available data are a suitable test of the model. A comparison of the outputs of the model against these data is shown in Figure 3.24.

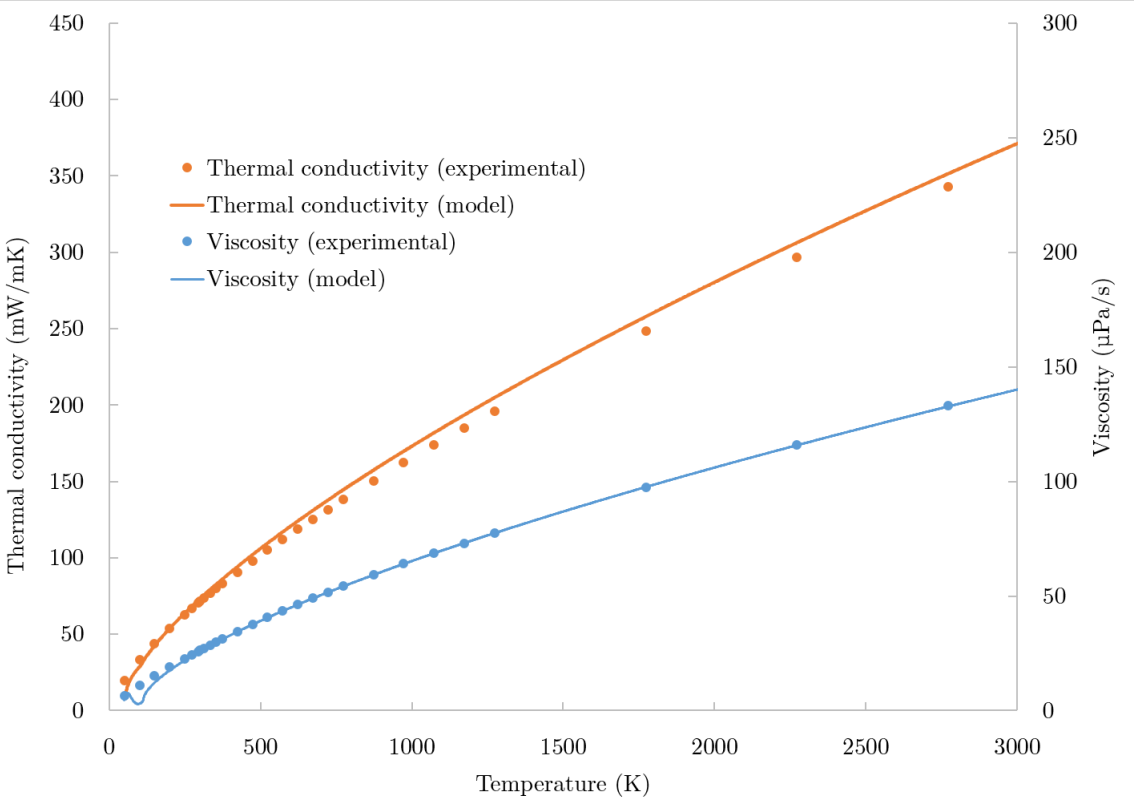

Fig. 3.24 Comparison of outputs of fluid properties model and experimental data from [59] for a 75:25 He-Xe mixture.

For viscosity, it can be seen that there is generally excellent agreement between the model and data. The model would appear to break down at very low temperatures, as can be seen for the abrupt changes in gradient, but any result below around 400K is unlikely to be relevant to the intended application of the model. In the range of interest, agreement is within 1%. The performance of the thermal conductivity model is somewhat worse, with a maximum error of around 5% near 1,000K. This is not unexpected; it is reported in [107] that this approach predicts around 87% of the low-density thermal conductivity data to within 5%, but that this is "reasonably good, considering the large scattering in thermal conductivity compared to the viscosity data".

3.8.2 Thermal hydraulic - neutronic coupling

It is possible to couple the neutronics and thermal hydraulic modules, so that the neutronics calculations take account of temperature-dependent cross sections and the thermal hydraulics calculations take account of the power distribution. Separate codes can be linked together and iterated until their results are mutually consistent.

Passing information about core temperatures from the MATLAB-based thermal hydraulics code to the routine that builds the WIMS input files is relatively simple. Coupling in the other direction is slightly more involved as the power distribution produced by MERLIN in the development version of WIMS being used is only in the form of a 'vtk' file. This type of data is commonly viewed in the program ParaView. Fortunately this has a macro-building function which allows a series of actions in the user interface to generate a Python script that can then be modified. This script extracts the power distribution information from the vtk file and saves it to a format that MATLAB can read.

Whether or not it is actually worthwhile to fully couple the neutronics and thermal hydraulics is discussed in Chapter 5.

3.9 Pressure vessel mass

The mass of piping has been generally excluded from this analysis, on the basis that when considering a single working pressure its mass should not be affected by changes in any of the design variables. However, this is not the case for the reactor pressure vessel which will need to scale with any changes in the reactor dimensions. A simple model is therefore constructed to estimate the mass of this component. The basic equation for hoop stress in a pressure vessel is given by [104]:

$$\sigma_\theta = \frac{PD_m}{2t} \tag{3.63}$$

$$\Rightarrow t = \frac{PD_m}{2\sigma_\theta} \tag{3.64}$$

where σ_θ is the hoop stress, P is the internal pressure, D_m is the mean vessel diameter and t is the vessel thickness. There is an additional longitudinal stress in a closed cylinder which is equal to half the hoop stress and perpendicular to it. For a thin-walled cylinder the radial stress is negligible and there are simply two perpendicular plane stresses in the pressure vessel wall. In such a situation there are variety of failure theories that could be applied to determine the required wall thickness from the overall stress state. The choice of theory depends in part on whether the material is brittle or ductile. For brittle materials, it is observed that failure occurs in a plane perpendicular to the direction of maximum principal stress and depends when it exceeds a certain magnitude. For two perpendicular plane stresses the maximum principal stress is simply the larger of the two stresses, which in the case of a cylindrical pressure vessel is the hoop stress. This principal stress is then compared to the allowable maximum stress for the material. For ductile materials, the situation is more

complicated, with failure theories such as the von Mises criterion generally being necessary. These take account of the fact that ductile materials generally resist stresses that change their volume (hydrostatic stresses) and fail due to stresses that change the material's shape (deviatoric stresses). In the case of perpendicular plane stresses, such a treatment will find that these stresses, to some extent, cancel out. Treating the material as brittle is therefore a more conservative (as well as simpler) approach. The hoop stress simply needs to be compared against the maximum allowable stress.

The allowable stress in such a pressure vessel is covered by the ASME Boiler and Pressure Vessel Code, within which Subsection NH covers rules for components in 'elevated temperature service' [7]. This code specifies allowable stresses at different temperatures for different durations for several metals. For high temperature gas-cooled reactors being considered for terrestrial use, one favoured material is Grade 91 steel (9Cr-1Mo-V) [77]. The highest evaluated temperature in the ASME code for Grade 91 is 650°C. The assumed lifetime of the reactor is seven years equivalent at full power, or 6.1×10^4 hours. The next highest evaluated duration time in the ASME code is 10^5 hours, which allows for additional time at partial power. Assuming that the pressure vessel does not experience more than 650°, the maximum allowable stress would therefore be 22MPa. For an example core of one metre height and diameter operating at 2MPa internal pressure limited to a vessel stress of 22MPa, Equations 3.64 and 3.65 prescribe a vessel of 4.5cm thickness and total volume of steel of 0.29m^3. With a density of 7.8g/cm^3, this vessel would have a mass of 2,205kg. However, it is noted in [77] that there is no significant experience of using Grade 91 for a reactor pressure vessel and therefore irradiation testing would be required to determine how radiation damage affects the steel's mechanical properties.

It should be noted that exceeding this stress would not necessarily result in failure; the 'expected minimum stress-to-rupture' value at this same temperature point and duration is 33MPa. Indeed, it should be borne in mind that, whilst the designers of a space mission try to minimise the probability of mission failure, they may well accept a probability considerably higher than the regulator of a terrestrial power plant would for catastrophic rupture of the main reactor pressure vessel.

The *Prometheus* project, which targeted an outlet temperature of 1,150K considered nickel-based alloys for the main pressure vessel, for their high temperature performance [118]. The preliminary target design called for a vessel which could tolerate a stress of 70MPa. A literature review of nickel-based alloys for this project [1] found that nickel-based alloys undergo significant embrittlement under irradiation, principally due to helium formation and solute segregation. This review reported various avenues of research which are attempting to ameliorate this issue, such as the replacement of some proportion of the nickel with cobalt.

However, more experimental research is required to determine whether these modifications are sufficiently effective. This outlook was confirmed in a later review in [94].

Both Grade 91 steel and nickel-based alloys suffer from a lack of data on their performance under irradiation. Additionally, Grade 91, even unirradiated, may not be able to tolerate the very high temperatures experienced in the space reactor, given that the highest temperature evaluated in the relevant ASME code [7] is 650°C (923K) but the reactor outlet temperature is likely to exceed 1000K. It is therefore assumed that some progress is made with improvements to nickel-based alloys but that the maximum allowable stress is 50MPa rather than the hoped-for 70MPa in the Prometheus programme. The density of this hypothetical alloy will be taken as that of Hastelloy X which is 8.22g/cm^3.

To calculate the mass of the pressure vessel, this density is multiplied by the volume of the alloy. The pressure vessel is assumed to be cylindrical about the core (outside the reflector), with a semi-spherical top and bottom. For a core height of h and maximum diameter D (corner-to-corner hexagon diameter) and assuming a thin-shell approximation, the volume of steel in the pressure vessel is:

$$V = \pi t(D^2 + hD) \tag{3.65}$$

3.10 Summary

The work described in this chapter had two main aims. The first was to establish a method of modelling a reactor core appropriate to the problem using deterministic methods rather than a Monte Carlo code so that the required analysis could be carried out on a timescale suitable for evaluating a large number of core designs. Trying to do this for the original tungsten cermet core design proved to be very difficult. This was due to the presence of tungsten in large amounts for which there is insufficient nuclear data in the standard WIMS library to carry out a satisfactory resonance treatment in a short time. Instead a TRISO-based core design was adopted, with the additional new design change of integrating the moderator into each assembly in the form of a wrapper whose thickness is continuously, rather than discretely, variable. An annular coolant channel separates the moderator from the fuel block to reduce the moderator temperature. Two possible routes were developed within the WIMS code suite to analyse this core: one longer route which includes a two-dimensional core slice calculation using an MoC calculation to improve material homogenisation and one quicker route which skips this step. The superior performance of the longer route is most pronounced in cores with heavy moderation. The steps required for carrying out a burnup calculation with a region-dependent resonance treatment were also set out. The accuracy of the deterministic

methods was judged on the basis of comparisons with the Monte Carlo code Serpent and deemed to be sufficiently accurate for the purpose of searching for core designs in a large design space and with a run-time compatible with this search.

The second aim was to improve on the rudimentary thermal hydraulic analysis developed in the previous chapter. Finite element analysis was used to calculate the temperature distribution in the fuel block and the resultant heating of the coolant and moderator. The relevant theory used to inform the calculation of an effective thermal conductivity for the particulate fuel form was presented. A scheme was implemented to determine a realistic coolant flow pattern across the core, ensuring that the pressure drop along all possible coolant paths is equal. In order to allow the modelling of the recommended binary mixture of helium and xenon coolant, the Chapman-Enskog method was used to estimate the relevant fluid properties, for which detailed datasets do not exist.

Chapter 4

Power conversion system

4.1 Introduction

The modelling presented so far has been limited to analysis of the reactor core. Since the purpose of the nuclear power system is not to produce heat, but, instead, electrical power for propulsion, the remainder of the power system must be analysed.

As discussed in the introductory chapter, the power system chosen is a direct cycle closed Brayton system. Aside from the reactor, the main components of this system whose mass must be calculated are the waste heat radiator, turbo-alternator, power management and distribution system (PMAD) and the recuperator, if present. Diagrams showing the flow of the working fluid through recuperated and unrecuperated systems are shown in Figure 4.1. The analysis presented in this chapter aims to find the minimum mass of this set of components for a given reactor design. The only quantities which feed through from the reactor design are the coolant inlet and outlet temperatures, the coolant mass flow rate and the pressure loss which arises in the reactor.

There are clearly many trade-offs in the configuration of the complete power system. For example, a larger waste heat radiator will provide a more effective heat sink and therefore improved thermodynamic efficiency, reducing the required reactor power and therefore its mass. Some of these trade-offs are implicitly captured in the analysis shown in this chapter while others are left for the next chapter covering the overall optimisation scheme.

Before explaining the details of how the optimal (minimum mass) power conversion system is arrived at, the basic principles of the Brayton power cycle are now presented.

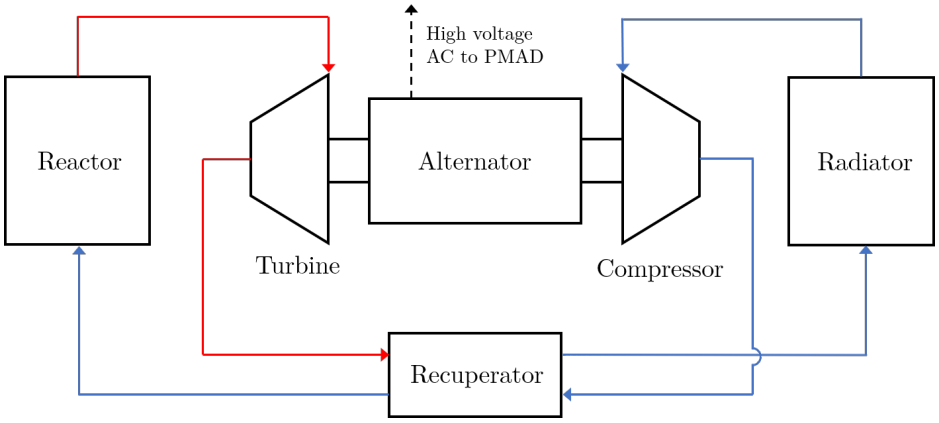

(a) Recuperated Brayton cycle

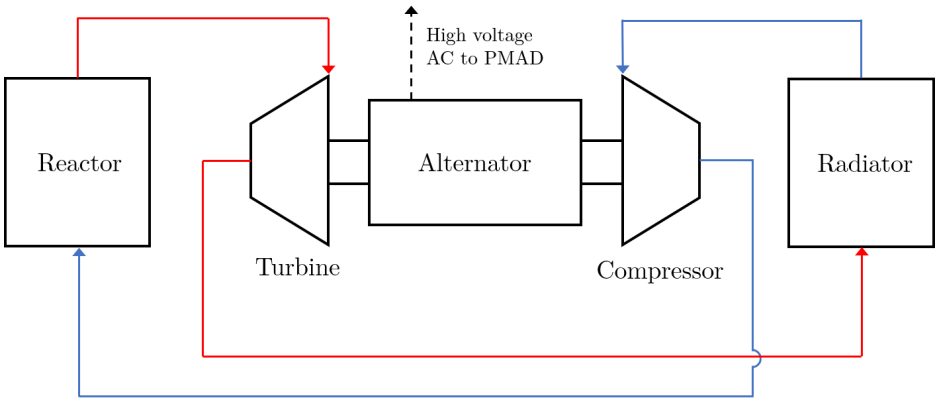

(b) Unrecuperated Brayton cycle

Fig. 4.1 Coolant flow around Brayton cycle power system, red and blue lines indicating the hot and cold sides of the cycle respectively.

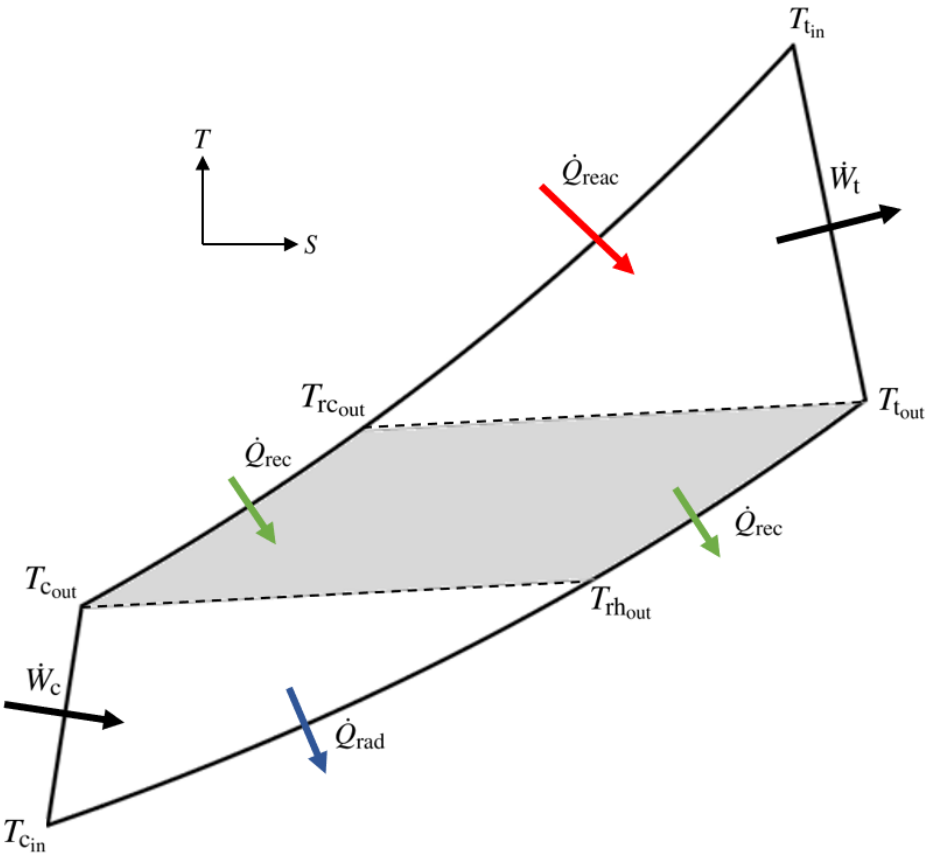

Fig. 4.2 T-S diagram of recuperated direct Brayton cycle

4.2 Direct Brayton Cycle description

In Figure 4.2 is shown an example T-S diagram of a recuperated Brayton cycle. The working fluid enters the reactor at a pressure of $P_{\mathrm{reac_{in}}}$ and temperature $T_{\mathrm{reac_{in}}}$. As it moves through the reactor core it undergoes approximately isobaric heating to $T_{\mathrm{reac_{out}}}$. The increase in temperature can be related to the thermal power of the reactor, assuming a steady state:

$$\dot{Q}_{\mathrm{reac}} = \dot{m} C_{\mathrm{P}} (T_{\mathrm{reac_{out}}} - T_{\mathrm{reac_{in}}}) \tag{4.1}$$

A pressure loss arises in the reactor and is expressed as the proportional pressure loss $\frac{\Delta P}{P}$ so that the pressure at the reactor outlet is given by:

$$P_{\mathrm{reac_{out}}} = P_{\mathrm{reac_{in}}} \left(1 - \frac{\Delta P_{\mathrm{reac}}}{P} \right) \tag{4.2}$$

There is no explicit assumption for pressure or temperature losses through the piping from the reactor outlet to the turbine inlet, so the temperature and pressure at the turbine inlet are given by:

$$T_{\mathrm{t_{in}}} = T_{\mathrm{reac_{out}}} \tag{4.3}$$

$$P_{\mathrm{t_{in}}} = P_{\mathrm{reac_{out}}} \tag{4.4}$$

The pressure decrease across the turbine is quantified by the turbine pressure ratio r_{t}:

$$P_{\mathrm{t_{out}}} = \frac{P_{\mathrm{t_{in}}}}{r_{\mathrm{t}}} \tag{4.5}$$

and the turbine outlet temperature is given by:

$$T_{\mathrm{t_{out}}} = T_{\mathrm{t_{in}}} - \eta_{\mathrm{t}} (T_{\mathrm{t_{in}}} - T_{\mathrm{it_{out}}}) \tag{4.6}$$

where η_{t} is the isentropic efficiency of the turbine and $T_{\mathrm{it_{out}}}$ is the turbine outlet temperature assuming an ideal isentropic expansion, given by:

$$T_{\mathrm{it_{out}}} = T_{\mathrm{t_{in}}} \left(\frac{1}{r_{\mathrm{t}}} \right)^{\frac{\gamma-1}{\gamma}} \tag{4.7}$$

where γ is the adiabatic ratio $C_{\mathrm{P}}/C_{\mathrm{V}}$, which is constant if we assume the fluid behaves as an ideal gas. At this stage, if the cycle is recuperated, the working fluid passes through the hot

leg of the recuperator. Again, no pressure or heat losses are assumed in the piping so that the recuperator hot leg inlet temperature and pressure are equal to those at the turbine outlet. As it passes through the hot leg, the fluid is cooled almost isobarically as it transfers heat to the fluid in the cold leg. The hot leg outlet temperature is given by:

$$T_{\mathrm{rh}_{\mathrm{out}}} = T_{\mathrm{t}_{\mathrm{out}}} - \varepsilon(T_{\mathrm{t}_{\mathrm{out}}} - T_{\mathrm{c}_{\mathrm{out}}}) \tag{4.8}$$

where ε is the recuperator effectiveness, which will be discussed in a subsequent section. There is an assumed pressure loss through the recuperator hot leg, so that the pressure at the outlet is:

$$P_{\mathrm{rh}_{\mathrm{out}}} = P_{\mathrm{t}_{\mathrm{out}}} \left(1 - \frac{\Delta P_{\mathrm{rh}}}{P}\right) \tag{4.9}$$

The fluid then passes through the waste heat radiator before reaching the compressor. If the compressor inlet temperature is known (a discussion of which parameters are chosen as the independent variables in the analysis of the power cycle and which will be calculated can be found later in this chapter), the temperature drop across the radiator is then simply given by:

$$\Delta T_{\mathrm{rad}} = T_{\mathrm{rh}_{\mathrm{out}}} - T_{\mathrm{c}_{\mathrm{in}}} \tag{4.10}$$

A pressure drop will occur across the radiator, after which the coolant arrives at the compressor, so the compressor inlet pressure will be given by:

$$P_{\mathrm{c}_{\mathrm{in}}} = P_{\mathrm{rh}_{\mathrm{out}}} \left(1 - \frac{\Delta P_{\mathrm{rad}}}{P}\right) \tag{4.11}$$

Finally, the fluid reaches the compressor. The increase in pressure is given by the compressor pressure ratio r_{c}:

$$P_{\mathrm{c}_{\mathrm{out}}} = r_{\mathrm{c}} P_{\mathrm{c}_{\mathrm{in}}} \tag{4.12}$$

and the compressor outlet temperature is given by:

$$T_{\mathrm{c}_{\mathrm{out}}} = T_{\mathrm{c}_{\mathrm{in}}} + \frac{1}{\eta_{\mathrm{c}}}(T_{\mathrm{ic}_{\mathrm{out}}} - T_{\mathrm{c}_{\mathrm{in}}}) \tag{4.13}$$

where η_c is the isentropic efficiency of the compressor and $T_{ic_{out}}$ is the compressor outlet temperature assuming an ideal isentropic compression, given by:

$$T_{ic_{out}} = T_{c_{in}} r_c^{\frac{\gamma-1}{\gamma}} \tag{4.14}$$

The compressor outlet feeds into the cold leg of the recuperator where the fluid is heated before returning to the reactor. The temperature and pressure at the recuperator cold leg outlet are given by:

$$T_{rc_{out}} = T_{c_{out}} + \varepsilon(T_{t_{out}} - T_{c_{out}}) \tag{4.15}$$

$$P_{rc_{out}} = P_{c_{out}} \left(1 - \frac{\Delta P_{rc}}{P}\right) \tag{4.16}$$

The recuperator cold leg then leads back to the reactor, therefore:

$$T_{rc_{out}} = T_{reac_{in}} \tag{4.17}$$

$$P_{rc_{out}} = P_{reac_{in}} \tag{4.18}$$

The power produced by the cycle is equal to the rate of work done by the working fluid on the turbine, $\dot{W}_t$, plus the rate of work done by the compressor on the working fluid, $\dot{W}_c$ (which will be negative). This is delivered to the common shaft of the turboset, having a power of:

$$\dot{W}_{shaft} = \dot{W}_t + \dot{W}_c \tag{4.19}$$

The values of $\dot{W}_t$ and $\dot{W}_c$ are given straightforwardly by their inlet and outlet temperatures and the common mass flow rate $\dot{m}$ through them:

$$\dot{W}_t = \dot{m} C_P (T_{t_{in}} - T_{t_{out}}) \tag{4.20}$$

$$\dot{W}_c = \dot{m} C_P (T_{c_{in}} - T_{c_{out}}) \tag{4.21}$$

where C_P is the specific heat capacity at constant pressure. Since the working fluid can be assumed to be an ideal gas, C_P is taken as a constant. Combining these three equations we arrive at the useful relation between the alternator shaft power, mass flow rate and turboset temperatures:

$$\frac{\dot{W}_{shaft}}{\dot{m} C_P} = T_{t_{in}} - T_{t_{out}} + T_{c_{in}} - T_{c_{out}} \tag{4.22}$$

4.3 Component mass models

There are two broad approaches to estimating the masses and performance of the components of the power system. The first is to find examples of similar systems that have either been used in real applications or have reached a sufficient level of development to be deemed a good approximation of the final system. No Brayton-cycle-based power systems have been used in space, but various systems have been proposed and, in places, tested. If several such systems are available, interpolation and cautious extrapolation can be carried out using this dataset. The other approach is to construct detailed physical models of the components which, for a given performance specification, produces a geometrical description which can be used to compute a mass. However, the use of real-world systems to estimate component masses is generally to be preferred over reliance on a 'first principles' model [8].

Detailed information regarding the masses of real-world, or proposed, systems is relatively sparse in the academic literature and is found mostly in NASA technical memoranda. Even here, however, details of any correlations or models used to estimate masses are not given explicitly. Such models certainly exist, contained within a "pedigreed high-fidelity" NASA code, CCEP (Closed Cycle Engine Program) [8, 9, 52]. This code makes use of empirical 'as made' component data along with models to predict component mass and performance. The CCEP code or details of its functionality are not available, so the data available in technical reports must be relied on. One additional source of information is the PhD thesis [58] of an experienced engineer at the NASA Glenn Research Centre, some parts of which were subsequently published in technical reports [54, 56]. The thesis contains an unusual level of detail on the modelling of component masses and is therefore a useful resource. It considered the mass minimisation of a nuclear space Brayton system but focussed on the conversion system, using a fairly rudimentary analysis of the reactor, calculating the mass of HEU required to sustain criticality, allowing for burnup.

4.3.1 Recuperator

The recuperator is simply a gas-gas heat exchanger. The purpose of this component is to transfer heat that would otherwise be rejected via the waste heat radiator to the working fluid before it enters the reactor core. A key performance parameter of the recuperator is its effectiveness, ε, defined as the ratio of the heat that is in fact transferred to the heat that is available to be transferred:

$$\varepsilon = \frac{\dot{Q}_{\mathrm{r}}}{\dot{Q}_{\mathrm{avail}}} \tag{4.23}$$

The rate of heat transfer across the recuperator can be given by:

$$\begin{aligned}\dot{Q}_{\mathrm{r}} &= \dot{m}_{\mathrm{c}} C_{\mathrm{Pc}} (T_{\mathrm{rc_{out}}} - T_{\mathrm{rc_{in}}}) \\ &= \dot{m}_{\mathrm{c}} C_{\mathrm{Pc}} (T_{\mathrm{rc_{out}}} - T_{\mathrm{c_{out}}})\end{aligned} \tag{4.24}$$

This can also be written in terms of the temperature change across the hot leg of the recuperator instead of the cold leg:

$$\begin{aligned}\dot{Q}_{\mathrm{r}} &= \dot{m}_{\mathrm{t}} C_{\mathrm{Pt}} (T_{\mathrm{rh_{in}}} - T_{\mathrm{rh_{out}}}) \\ &= \dot{m}_{\mathrm{t}} C_{\mathrm{Pt}} (T_{\mathrm{t_{out}}} - T_{\mathrm{rh_{out}}})\end{aligned} \tag{4.25}$$

The heating rate that is in principle available is:

$$\dot{Q}_{\mathrm{avail}} = \dot{m}_{\mathrm{t}} C_{\mathrm{Pt}} T_{\mathrm{t_{out}}} - \dot{m}_{\mathrm{c}} C_{\mathrm{Pc}} T_{\mathrm{c_{out}}} \tag{4.26}$$

Heat transfer area

Following the method of Juhasz [56], an expression is now derived for the heat transfer area of the recuperator. Starting from Fourier's Law, the rate of heat transfer per unit area is:

$$\dot{q} = U \Delta T \tag{4.27}$$

where U is the overall heat transfer coefficient (units of W/mK). Therefore the total heating rate from one side of the recuperator to the other is related to the total heat transfer area by:

$$\dot{Q}_r = UA\overline{\Delta T} \tag{4.28}$$

where $\overline{\Delta T}$ is the log mean temperature difference. This calculated quantity is typically used for heat exchangers where one can assume a steady state, constant heat transfer coefficient and constant heat capacity. The log mean temperature difference is given by:

$$\begin{aligned}\overline{\Delta T} &= \frac{(T_{\mathrm{rh_{out}}} - T_{\mathrm{rc_{in}}}) - (T_{\mathrm{rh_{in}}} - T_{\mathrm{rc_{out}}})}{\ln \frac{T_{\mathrm{rh_{out}}} - T_{\mathrm{rc_{in}}}}{T_{\mathrm{rh_{in}}} - T_{\mathrm{rc_{out}}}}} \\ &= \frac{(T_{\mathrm{rh_{out}}} - T_{\mathrm{c_{out}}}) - (T_{\mathrm{t_{out}}} - T_{\mathrm{rc_{out}}})}{\ln \frac{T_{\mathrm{rh_{out}}} - T_{\mathrm{c_{out}}}}{T_{\mathrm{t_{out}}} - T_{\mathrm{rc_{out}}}}}\end{aligned} \tag{4.29}$$

Substituting in from Equations 4.24 and 4.25 leads to:

$$\overline{\Delta T} = \frac{\frac{\dot{Q}_\mathrm{r}}{\dot{m}_\mathrm{c} C_\mathrm{Pc}} - \frac{\dot{Q}_\mathrm{r}}{\dot{m}_\mathrm{t} C_\mathrm{Pt}}}{\ln \frac{T_{\mathrm{t}_\mathrm{out}} - T_{\mathrm{c}_\mathrm{out}} - \frac{\dot{Q}_\mathrm{r}}{\dot{m}_\mathrm{t} C_\mathrm{Pt}}}{T_{\mathrm{t}_\mathrm{out}} - T_{\mathrm{c}_\mathrm{out}} - \frac{\dot{Q}_\mathrm{r}}{\dot{m}_\mathrm{c} C_\mathrm{Pc}}}} \tag{4.30}$$

Some simplifying substitutions are now made:

$$a = \frac{\dot{Q}_\mathrm{r}}{\dot{m}_\mathrm{c} C_\mathrm{Pc}} \tag{4.31}$$

$$b = \frac{\dot{m}_\mathrm{c} C_\mathrm{Pc}}{\dot{m}_\mathrm{t} C_\mathrm{Pt}} \tag{4.32}$$

$$c = T_{\mathrm{t}_\mathrm{out}} - T_{\mathrm{c}_\mathrm{out}} \tag{4.33}$$

This results in:

$$\overline{\Delta T} = \frac{(1-b)a}{\ln \frac{c-ab}{c-a}} \tag{4.34}$$

$$= \frac{(1-b)a}{\ln\left(1 + \frac{(1-b)a}{c-a}\right)} \tag{4.35}$$

The mass flow rate and the specific heat capacity around the cycle can be assumed to be unchanging, so it can be seen that $b \approx 1$. Therefore in a Taylor series expansion of the logarithm, the first term alone can be taken:

$$\ln\left(1 + \frac{(1-b)a}{c-a}\right) \approx \frac{(1-b)a}{c-a} \tag{4.36}$$

This results in:

$$\begin{aligned} \overline{\Delta T} &= \frac{(1-b)a}{\frac{(1-b)a}{c-a}} \\ &= c - a \\ &= T_{\mathrm{t}_\mathrm{out}} - T_{\mathrm{c}_\mathrm{out}} - \frac{\dot{Q}_\mathrm{r}}{\dot{m}_\mathrm{c} C_\mathrm{Pc}} \end{aligned} \tag{4.37}$$

Substituting this into Equation 4.28 gives:

$$\dot{Q}_r = UA\left(T_{\mathrm{t}_\mathrm{out}} - T_{\mathrm{c}_\mathrm{out}} - \frac{\dot{Q}_\mathrm{r}}{\dot{m}_\mathrm{c} C_\mathrm{Pc}}\right) \tag{4.38}$$

Rearranging for the heat transfer area and substituting from Equation 4.24 for $\dot{Q}_r$:

$$\begin{aligned} A &= \frac{\dot{m}_{\mathrm{c}} C_{\mathrm{Pc}} (T_{\mathrm{rc_{out}}} - T_{\mathrm{c_{out}}})}{U(T_{\mathrm{t_{out}}} - T_{\mathrm{c_{out}}} - (T_{\mathrm{rc_{out}}} - T_{\mathrm{c_{out}}}))} \\ &= \frac{\dot{m}_{\mathrm{c}} C_{\mathrm{Pc}} \frac{T_{\mathrm{rc_{out}}} - T_{\mathrm{c_{out}}}}{T_{\mathrm{t_{out}}} - T_{\mathrm{c_{out}}}}}{U\left(1 - \frac{T_{\mathrm{rc_{out}}} - T_{\mathrm{c_{out}}}}{T_{\mathrm{t_{out}}} - T_{\mathrm{c_{out}}}}\right)} \end{aligned} \tag{4.39}$$

Revisiting the definition of ε and substituting the first expression for $\dot{Q}_{\mathrm{r}}$ in Equation 4.24:

$$\varepsilon = \frac{\dot{m}_{\mathrm{c}} C_{\mathrm{Pc}} (T_{\mathrm{rc_{out}}} - T_{\mathrm{c_{out}}})}{\dot{m}_{\mathrm{t}} C_{\mathrm{Pt}} T_{\mathrm{t_{out}}} - \dot{m}_{\mathrm{c}} C_{\mathrm{Pc}} T_{\mathrm{c_{out}}}} \tag{4.40}$$

Again noting that it can be assumed that $\dot{m}_{\mathrm{c}} = \dot{m}_{\mathrm{t}}$ and $C_{\mathrm{Pc}} = C_{\mathrm{Pt}}$, this simplifies to:

$$\varepsilon = \frac{T_{\mathrm{rc_{out}}} - T_{\mathrm{c_{out}}}}{T_{\mathrm{t_{out}}} - T_{\mathrm{c_{out}}}} \tag{4.41}$$

The recuperator area in Equation 4.39 can therefore be written in terms of the recuperator effectiveness ε:

$$A = \frac{\dot{m} C_{\mathrm{P}}}{U} \left(\frac{\varepsilon}{1 - \varepsilon}\right) \tag{4.42}$$

Heat exchanger mass

With an expression for the heat transfer area in hand, an expression for the recuperator mass can now be derived. Again following Juhasz [56], the recuperator mass can be considered to be divided between the 'core', the case and ducting. The volume of the core is given by:

$$V_{\mathrm{core}} = \frac{A}{F_{\mathrm{stack}}} \tag{4.43}$$

where F_{stack} is the stacking factor which quantifies the heat exchange surface area that fits in a unit volume. The mass of the core is then simply given by:

$$M_{\mathrm{core}} = V_{\mathrm{core}} \rho_{\mathrm{core}} \tag{4.44}$$

where ρ_{core} is the mass density of the recuperator core. The mass of the recuperator casing could then given by:

$$M_{\mathrm{case}} = \alpha V_{\mathrm{core}}^{\frac{2}{3}} d_{\mathrm{case}} \rho_{\mathrm{case}} \tag{4.45}$$

Table 4.1 Power cycles examined in [10], showing electrical output, total recuperator heat transfer, mass flow rate, fluid molar mass, recuperator effectiveness and total recuperator pressure loss

Case	Power (kWe)	Q' (kWth)	$\dot{m}$	Molar mass	ε	$\beta_{\mathrm{r,tot}}$
1	2	24	0.16	83.8	0.98	0.70%
2	10	168	0.58	83.8	0.95	3.50%
3	55	261	1.72	39.9	0.9	1.90%
4	55	272	1.77	39.9	0.92	1.90%
5	105	619	3.85	39.9	0.92	2.00%
6	105	665	3.91	39.9	0.95	2.90%
7	200	927	5.99	39.9	0.92	1.90%
8	300	1353	8.93	39.9	0.9	1.90%
9	300	1380	8.91	39.9	0.92	1.90%

where α is an aspect ratio factor, d_{case} is the case thickness and ρ_{case} is the density of the case material. In the case of a cube-shaped recuperator, $\alpha = 6$. Finally, Juhasz [56] assumes that the ducting has a mass equal to 25% of that of the case.

In this method, values are therefore required for U, F_{stack}, α, d_{case}, ρ_{core} and ρ_{case}. Whilst some of these are given in [56] and [58] and others can be inferred from the example results therein, these values do not come with much justification. An alternative source of information for determining these constants is a technical note [10] considering carbon-carbon recuperators for closed Brayton cycle space power systems. This involves much more detailed modelling of the recuperator, which is itself compared with real systems and found to be in reasonable agreement. The study considers nine different cycle designs over a range of power outputs. The details of these cycles are shown in Table 4.1.

For each cycle, eight recuperator designs are considered using three possible materials: Hastelloy X, stainless steel and carbon-carbon. For a conservative mass estimate the heaviest option, Hastelloy X, is considered to determine the above parameters. There are three Hastelloy designs for each cycle design, with differing fin widths and separations. The volumes and masses of these designs are shown in Table 4.2.

Fortunately, for each recuperator design, the core volume, core mass and total mass are shown separately. This enables the required constants to be determined. In fact, not all of the constants listed need to be determined individually; for example, to calculate the recuperator core volume it is sufficient to have a value of $F_{\mathrm{stack}}U$, without knowing the values of F_{stack} and U separately.

In Table 4.3 are shown the values of $F_{\mathrm{stack}}U$ implied by the data in Table 4.2 for each fin design type. Under the simple model of the recuperator presented above, all cycles (1-9)

Table 4.2 Volumes and masses of Hastelloy X recuperators in [10]

Cycle		Fin design A	B	C
1	Core volume (m^3)	0.066	0.097	0.026
	Core mass (kg)	61	51	40
	Total mass (kg)	114	126	64
2	Core volume (m^3)	0.114	0.166	0.045
	Core mass (kg)	105	88	68
	Total mass (kg)	127	119	79
3	Core volume (m^3)	0.13	0.205	0.055
	Core mass (kg)	120	109	84
	Total mass (kg)	191	212	122
4	Core volume (m^3)	0.176	0.275	0.073
	Core mass (kg)	162	146	112
	Total mass (kg)	251	274	158
5	Core volume (m^3)	0.318	0.515	0.138
	Core mass (kg)	293	274	211
	Total mass (kg)	470	538	307
6	Core volume (m^3)	0.631	0.996	0.266
	Core mass (kg)	582	529	407
	Total mass (kg)	879	968	561
7	Core volume (m^3)	0.601	0.938	0.25
	Core mass (kg)	554	499	382
	Total mass (kg)	740	759	486
8	Core volume (m^3)	0.674	1.066	0.285
	Core mass (kg)	621	567	435
	Total mass (kg)	820	841	550
9	Core volume (m^3)	0.894	1.396	0.372
	Core mass (kg)	824	742	569
	Total mass (kg)	1065	1074	705

Table 4.3 Implied values of $F_{\text{stack}}U$ from data in Table 4.2

Fin design	A		B		C	
Cycle	$F_{\text{stack}}U$	error vs mean	$F_{\text{stack}}U$	error vs mean	$F_{\text{stack}}U$	error vs mean
1	617,222	1%	419,965	7%	1,566,794	7%
2	502,280	-18%	344,939	-12%	1,272,443	-13%
3	618,724	2%	392,361	0%	1,462,438	0%
4	600,935	-1%	384,598	-2%	1,448,830	-1%
5	723,437	19%	446,705	14%	1,667,050	14%
6	611,745	0%	387,561	-1%	1,451,169	-1%
7	595,552	-2%	381,585	-3%	1,431,706	-2%
8	619,588	2%	391,747	0%	1,465,272	0%
9	595,535	-2%	381,381	-3%	1,431,205	-2%
mean	609,446		392,316		1,466,323	

should, for a given fin design, give the same values of $F_{\text{stack}}U$ and U. With the exception of cycles 5 and 8, the calculated values are within 10% of the mean value. The mean value found for fin design A, which is the middle of the three values, is chosen as the basis of the recuperator model. Generally the principle should be to be conservative in mass estimates, but, given that the heaviest material option (Hastelloy X) has been chosen, it may be overly conservative to also adopt the heaviest fin design. It should be noted that the data used is for cycles using a working fluid with molar mass 40g/mol, with the exception of the Brayton Rotating Unit (BRU, cycles 1 and 2) designs which use 84g/mol. This study will only consider either pure helium (4g/mol), or the common choice of 40g/mol. One of the reasons why 40g/mol is an attractive design choice is that it has approximately the same heat transfer coefficient, under equivalent conditions, as pure helium, as shown in [29] (whilst giving improvements in turbomachinery loading). Therefore, it will be assumed that the recuperator heat transfer coefficient U is unaffected by the choice of 4g/mol or 40g/mol working fluid.

The next parameter to determine is the core density, ρ_{core}. This is done simply, since values of the core volume and mass are given in [10]. The average calculated densities for fin designs A, B and C are, respectively, 922, 531 and 1,528 kg/m^3. The values across the different cycles differ from the mean value by less than 1%. Again, the middle value, corresponding to fin design A, is chosen to use in the recuperator model.

Finally, the case mass must be considered. Since values of core mass and total mass are shown separately in [10], the case (and it is assumed, ducting) mass can be easily determined. Again, it is not necessary to determine all three separate parameters in Equation 4.45, namely the aspect ratio, case thickness and case density. The product of all three values can be found

Table 4.4 Implied values of $\alpha\rho_{case}d_{case}$ from data in Table 4.2

Cycle	$V^{2/3}$ (m^2)	Case mass (kg)	$\alpha\rho_{case}d_{case}$
1	0.163	53	325
2	0.235	22	94
3	0.257	71	277
4	0.314	89	283
5	0.466	177	380
6	0.736	297	404
7	0.712	186	261
8	0.769	199	259
9	0.928	241	260
mean	-	-	282

by dividing M_{case} by $V_{core}^{\frac{2}{3}}$. The scatter in the resulting data is relatively large, as can be seen in Table 4.4 which relates only to the chosen fin design, type A. The reason for this large scatter is unclear; nevertheless this dataset is the most detailed and applicable available.

Pressure losses will occur through both legs of the recuperator. Based on the worst-case designs from [10], these are set to 2.0% for the hot leg and 1.5% for the cold leg. The pressure loss ratios taken here are based on 40g/mol systems, but lower pressure losses could be assumed for pure helium systems. However, a simpler and conservative approach is taken, and these pressure loss ratios will be assumed to be independent of fluid choice.

4.3.2 Turboset

The power conversion system in a Brayton cycle consists of the compressor, turbine and alternator, mounted on a common shaft. This combined unit is often referred to as a turboalternator or turboset. As with the mass estimates for the other components, an appropriate level of modelling detail must be used, supported by as much ‘as built’ data as possible. At one extreme, the detailed modelling found in [37] extends to the detail of the number, size, shape and angle of compressor and turbine blades. From such an analysis, parameters such as the turbomachinery isentropic efficiencies can be determined, rather than assumed. However, a more high level analysis is appropriate here, where such parameters as efficiencies can be taken from representative systems. Only an expression for the mass of the turboset is required.

One expression can be found in [58], which gives the mass of the turboset as (with modified notation):

$$m_{\text{tset}} = CSP^{0.7}(1 + 0.52(\ln r_{\text{c}})/1.93) \tag{4.46}$$

where C is a constant equal to 1.8, S is a "specific weight" and P is the electrical power output. This expression has an appealing feature, in that it captures not just the dependence on the overall electrical power output of the turboset, but on the pressure ratio r_{c}. This dependence arises because the power delivered to the alternator shaft is the difference between the powers of the turbine and compressor. It is possible to have two different power cycles with the same net power output that, because of having different pressure ratios, have their turbines and compressors operating at different powers. This difference in operating power would presumably translate into a different mass. For example, it is possible to produce a shaft power of 1MW by having a turbine power of 3MW and a compressor power of 2MW. Alternatively, the same shaft power could be achieved with a turbine power of 11MW and a compressor power of 10MW. The turbine and compressor in the latter example would presumably be heavier.

Whilst this approach is appealing in principle, Equation 4.46 is presented with very little justification, either for its functional form or the values of its constants. The only guidance regarding the specific weight factor S is that the constants in the expression "can be gleaned from information on existing ground based gas turbine installations" [58, p81]. Unfortunately this analysis is not presented. Some example results are given for full system analyses in a later chapter, and it was hoped that the value of S could be determined from these results. However, different sets of results gave different values of S, suggesting that it may not in fact be a constant. The reference only to ground-based turbomachinery may at first appear odd, but it should be noted that the analysis in [58] extends well into the multi-megawatt range, whereas the 'as built' data for space Brayton systems relates only to much lower powers.

At this stage it is worth elaborating on what data exists on directly relevant systems. It should be noted again that no space Brayton systems have actually been flown, but some projects did reach as far as component fabrication and testing. Two date from the 1970s, the BRU [24], and the mini-BRU [27], with output powers of 10kW$_{\text{e}}$ and 2kW$_{\text{e}}$ respectively, intended to serve as conversion systems for either radioisotope or solar heat sources. The third system often referred to in modern literature is the Solar Dynamic system, originally intended for Space Station *Freedom* [62], but whose development and testing survived the cancellation of its intended host. This also operated at a power of 2kW$_{\text{e}}$. These three relatively low power systems are the closest any space Brayton power system came to deployment.

An alternative approach to estimating the turboset mass is presented in [115]. This prescribed specific masses for the three parts of the turboset: the turbine (0.1kg/kW), the compressor (0.15kg/kW) and the alternator (0.2kg/kW). Such an approach has the advantage that the effect of different pressure ratios discussed above is captured implicitly by specifying the masses of the turbine, compressor and alternator separately. The values were arrived at by comparison with suitable turbomachinery data available at the time, although, given the emphasis of the study was on multi-megawatt systems, this did not include the BRU systems mentioned above.

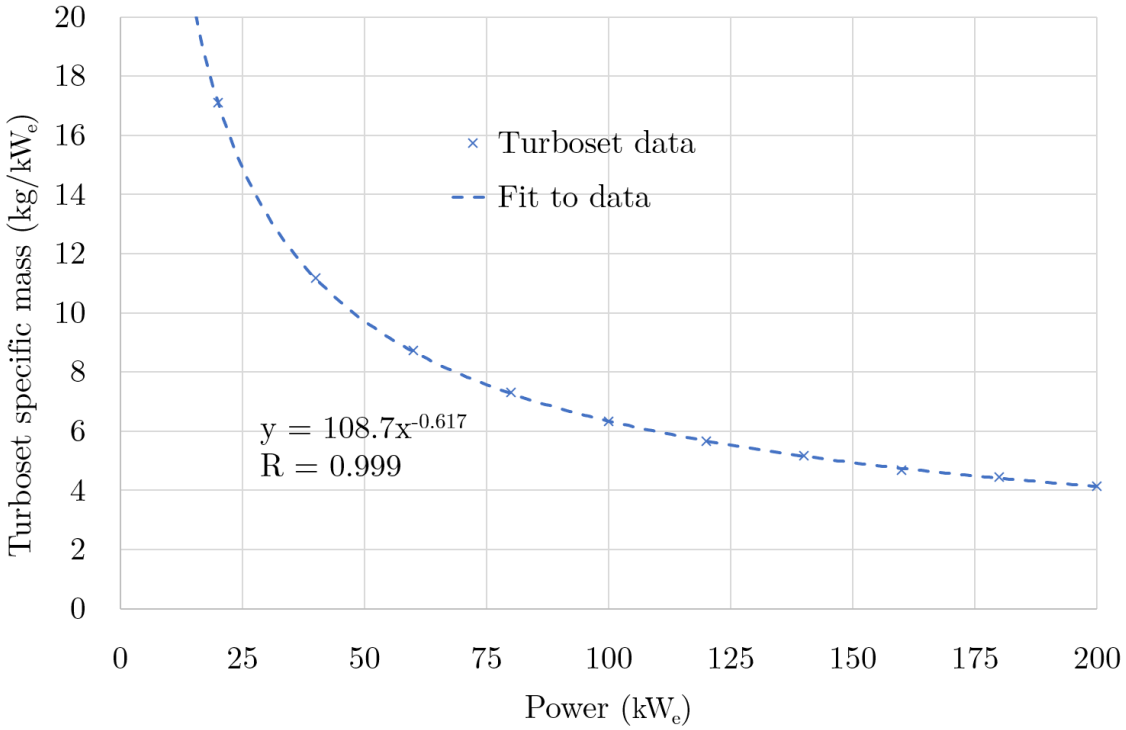

Fig. 4.3 Specific masses of turboset from [71] with line of fit

It is also worth considering studies carried out at NASA, where a great deal of data and institutional knowledge on these systems is held but not necessarily available in the literature. Such studies make use of codes such as CCEP, which is not generally available, but the outputs of which can be informative. The most useful such study is by Mason [71]. This estimates the masses of closed Brayton nuclear power systems with output powers of between 20kW$_e$ and 200kW$_e$ (noting that in all cases double-redundancy is specified for all components except the reactor core). The calculated masses are split between the reactor, shield, hot-side heat exchanger, turboset, heat rejection system and the PMAD. The specific masses for the turboset data are shown in Figure 4.3, along with a power law fit to this data. It

is noticeable that there is a strong dependence of the turboset specific mass on output power, in contrast to the fixed values given in [115]. A fit to the data finds the following relation for the specific mass of the turboset:

$$\frac{m_{\text{turboset}}}{\mathscr{P}_{\text{e}}/1000} = 108.7(\mathscr{P}_{\text{e}}/1000)^{-0.617} \tag{4.47}$$

where $\mathscr{P}_{\text{e}}$ is the electrical power (noting that the standard Roman character P is reserved for pressure). The factor of 1000 arises due to the fitting of data in kW. Rearranging for absolute mass:

$$m_{\text{turboset}} = 108.7(\mathscr{P}_{\text{e}}/1000)^{0.383} \tag{4.48}$$

Unfortunately the data in [71] relate only to the turboset as a whole and its variation with total electrical output. Therefore, the effect of differing pressure ratios is not captured. This can be overcome by combining the expression for the total turboset mass derived from [71] with the sub-component specific masses from [115]. This is under the assumption that the former dataset is the best available source for the total turboset mass, while the latter is a reasonable source for the masses of the sub-components relative to each other. First, given the pressure ratio, mass flow rate and cycle temperatures provided in [71] for the example case of a 100kW$_{\text{e}}$ system, the powers of the turbine and compressor can be inferred using Equations 4.20 and 4.21. Then, the constant specific masses from [115] are used to compute the sub-component masses. From this it can be inferred that, for a compressor pressure ratio of 2.0, the turbine, compressor and alternator make up 39.8%, 41.8% and 18.4% of the total mass, respectively. These can then be applied to Equation 4.48, resulting in three separate expressions for the turbine, compressor and alternator:

$$m_{\text{t}} = 43.3(\dot{W}_{\text{t}}/1000)^{0.383} \tag{4.49}$$

$$m_{\text{c}} = 45.5(\dot{W}_{\text{c}}/1000)^{0.383} \tag{4.50}$$

$$m_{\text{alt}} = 20.0(\mathscr{P}_{\text{e}}/1000)^{0.383} \tag{4.51}$$

This analysis has been based on turbomachinery data for the common He-Xe 40g/mol working fluid. If pure helium (4g/mol) is also to be considered, its effect on turbomachinery mass must also be investigated. As mentioned previously, the main downside of pure helium as a working fluid is that it leads to a higher aerodynamic loading on the turbomachinery.

The aerodynamic load on the compressor blades is given as [114]:

$$\lambda_c = \frac{\Delta H_c}{R_c^2 \omega^2} \tag{4.52}$$

where ΔH_c is the enthalpy rise in the compressor, R_c is the impeller radius and ω is the shaft rotational speed. It can also be shown [31] that, for the same pressure and temperature ratios and efficiency, the effect of the fluid type on the enthalpy rise is:

$$\Delta H_c \propto \frac{\hat{C}_P}{M} \tag{4.53}$$

where $\hat{C}_P$ is the molar heat capacity at constant pressure and M is the fluid molar mass. Since both pure helium and the He-Xe blend can be assumed to act as ideal gases, $\hat{C}_P$ is constant. Therefore, it can be seen that the aerodynamic load is inversely proportional to the fluid molar mass. In order not to increase the aerodynamic loading, it can be seen from Equation 4.52 that the impeller radius will need to increase. Specifically, one can see that:

$$R_c \propto \frac{1}{\sqrt{M}} \tag{4.54}$$

We are also told [31] that a larger impeller tip radius requires thicker blades, further increasing the mass gain, although the increase in thickness is not quantified. A simple assumption will therefore be made that the blades increase in cross-sectional area in proportion to their increase in length. This gives the following relation for the mass of the compressor:

$$m_c \propto R_c^3 \propto \frac{1}{M^{\frac{3}{2}}} \tag{4.55}$$

The same scaling is assumed to apply to the turbine. Therefore, revised formulae for the turboset mass components are:

$$m_t = 43.3 \left(\frac{40}{M}\right)^{\frac{3}{2}} (\dot{W}_t/1000)^{0.383} \tag{4.56}$$

$$m_c = 45.5 \left(\frac{40}{M}\right)^{\frac{3}{2}} (\dot{W}_c/1000)^{0.383} \tag{4.57}$$

$$m_{alt} = 20.0(\mathscr{P}_e/1000)^{0.383} \tag{4.58}$$

Efficiency

The efficiencies of the turbine, compressor and alternator have been taken as 90%, 85% and 90% respectively, based on relevant studies [71, 37]. It should be noted that for the turbine and compressor the stated efficiencies are isentropic. This is only strictly correct for a specified pressure ratio. If the pressure ratio is allowed to vary, a more accurate way to capture efficiencies is to use the polytropic efficiency, which does not vary with pressure ratio. One finds that, with increasing pressure ratio, the isentropic efficiency of the compressor decreases, while that of the turbine increases. One drawback of this approach is that the analytical approach taken to finding the range of allowable pressure ratios shown in Section 4.4 would have to be replaced with a numerical method.

PMAD

The alternator will produce a high voltage, high frequency alternating current (for example, $600V_{rms}$, 1.5kHz [71]). The PMAD is responsible for converting and conditioning this power into a suitable form for the various loads on the craft. This component can have a considerable mass, of the same magnitude as the turboset. The same dataset from [71] is useful here, given that the end user of the power in that study is an electric propulsion system, as is assumed for this study. The data indicates that between $20kW_e$ and $200kW_e$ the PMAD has a constant specific mass of $3.4kg/kW_e$. It is assumed that this constant specific mass persists up to $1MW_e$.

4.3.3 Waste heat radiator

For all heat engines, waste heat must somehow be rejected. For a space power system, this can only be achieved by emitting thermal radiation into the vacuum of space. In comparison to more familiar terrestrial means of disposing of waste heat, such as convective heat transfer to cooling water, radiative cooling is extremely inefficient. The waste heat rejection system is therefore typically a large component. Another challenge associated with radiative cooling is self-irradiation of the radiator. Terrestrial passive 'radiators', such as those found on some computer chips or a motorcycle engine block, feature an array of parallel fins that present a large area to the surrounding air. Such a configuration is unsuitable for purely radiative cooling because photons emitted from one fin will impinge on another. The 'view factor' is a measure of the extent to which this effect occurs. A common configuration with a very low view factor is a single static planar radiator. An example can be seen in the design for *Prometheus*. The trapezoidal profile is chosen to fit the radiator in the shadow of the reactor shield. Another common layout is that seen in the SP-100 design which resembles a

shuttlecock. Clearly this has an increased view factor to itself, but benefits from improved stowability.

The large mass of such a heat rejection system has prompted research into more exotic alternatives. The most commonly discussed of these is the liquid droplet radiator. This functions by ejecting a heated fluid as a spray of fine droplets, typically parallel to the main fuselage of the craft. These collectively have a large surface area and thereby efficiently radiate their heat into space, before being collected a point further along the craft [85]. Such a design avoids the need to stow and unfold a solid radiator and has potentially large weight savings over conventional designs. Another design worth mentioning, if only for its inventiveness, is the Curie point radiator; this operates on a similar basis to the liquid droplet radiator but using small solid ferromagnetic particles. When ejected into space, they are above their Curie point. After cooling radiatively, they fall below their Curie point and become attracted by a magnetic field produced by an electromagnet and are drawn back to a collector which can be located very close to the emitter [16]. There are several other intriguing proposed designs which are catalogued and discussed in [57].

However, based on recent literature, solid static radiators are the only design that appears deployable in the near and medium term. These generally feature heat pipes for distributing heat across the radiator area. A heat pipe is a closed tube containing a suitable fluid that can exist either as a liquid or a vapour within the operating temperature range. When heat is applied to one end (the evaporator), the operating fluid evaporates and is transported along the interior of the pipe to the cold end (the condenser). Here it condenses, releasing its latent heat, and is carried back to the evaporator via capillary action along the inner wall of the pipe, referred to as the wicking region. The capillary action is achieved by a suitable surface texture such as longitudinal grooves. Heat pipes can have very high effective thermal conductivities, as much as 500 times that of a copper cylinder of equivalent dimension [20].

As well as being highly effective heat transportation devices, heat pipes have other features that are desirable for this application. They are robust, with no moving parts. They are also independent, so that if one is damaged (micrometeorite impact being the main hazard), only its corresponding radiator section will be rendered inoperable. A typical space radiator design features a large number of heat pipes arranged perpendicular to a main coolant duct through which a pumped fluid flows. This fluid heats the evaporator ends of the heat pipes. The heat pipes do not have a condenser 'end' as such, instead the entire section of heat pipe that is not in contact with the main coolant duct radiates heat into space and acts as a condenser. The radiative cooling is enhanced by fins attached to the heat pipe.

There are two options for what flows through the main coolant duct. One is to send the main Brayton cycle working fluid through the coolant duct, a configuration known as

direct heat rejection. The alternative is to use a cold-end heat exchanger to transfer heat from the Brayton working fluid to another fluid, which is then used in the radiator main coolant duct. This latter option is referred to as indirect heat rejection. The benefit of indirect heat rejection is that a liquid coolant can be used which acts as a far more effective means of transferring heat to the heat pipe evaporators. A liquid metal is generally chosen, such as sodium-potassium eutectic [108]. The main drawback of indirect heat rejection is the additional mass of a gas-liquid heat exchanger, pumping equipment and the liquid metal coolant inventory, as well as a more complex startup procedure involving thawing the coolant. The need to pump this fluid also creates a small additional parasitic electrical load. An investigation of whether an indirect heat rejection system is, on balance, superior is not carried out here. For the purposes of this investigation, the simpler direct heat rejection method is adopted.

A radiator design is adapted from [30] and [108], which both present a stowable, shuttlecock-shaped radiator, with the difference between the two studies being the choice of fluid within the heat pipes. The former considers high temperature water heat pipes and the latter considers rubidium heat pipes for even higher temperatures. Both use a D-shaped titanium and carbon-carbon heat pipe design, surrounded by carbon-carbon armour with integrated carbon-carbon fins. Here, carbon-carbon refers to a composite material consisting of graphite reinforced with carbon fibre. The exact dimensions of the heat pipes in these studies are allowed to vary across the radiator to optimise for the temperatures in each section and to achieve a more stowable design. A simple 'average' heat pipe design is adopted for the present study to simplify modelling, with the caveat that this is not likely to lead to an optimal radiator design. This design is shown in Figure 4.4.

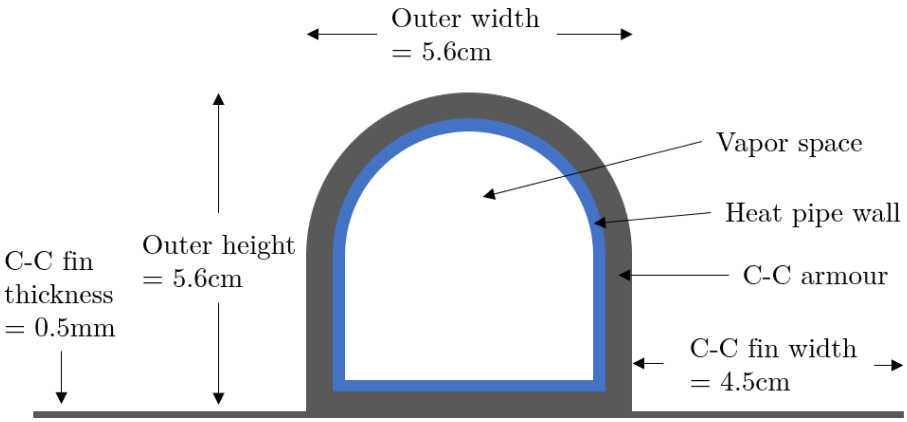

Fig. 4.4 Heat pipe cross section, adapted from [30, 108]

The way in which the finned heat pipe interfaces with the main coolant duct is also taken from [30] and [108]. This design has a flat rectangular coolant duct, with the flat base of the finned heat pipe adhered to it. The width of the rectangular duct is taken to be 20cm, and the length of the heat pipe 2m. This layout can be seen in Figure 4.5. It can also be seen that in Figure 4.5b the two sections of the radiator panel are at a slight angle to each other. This is not relevant to the subsequent radiator modelling, but is shown to illustrate how the 'shuttlecock' layout can be achieved if desired. It should be noted that, whilst there appear to be gaps between the heat pipe fins in Figure 4.5a, this is depicted to aid understanding of the layout; in reality a gap would serve no purpose and the fins of neighbouring pipes are connected.

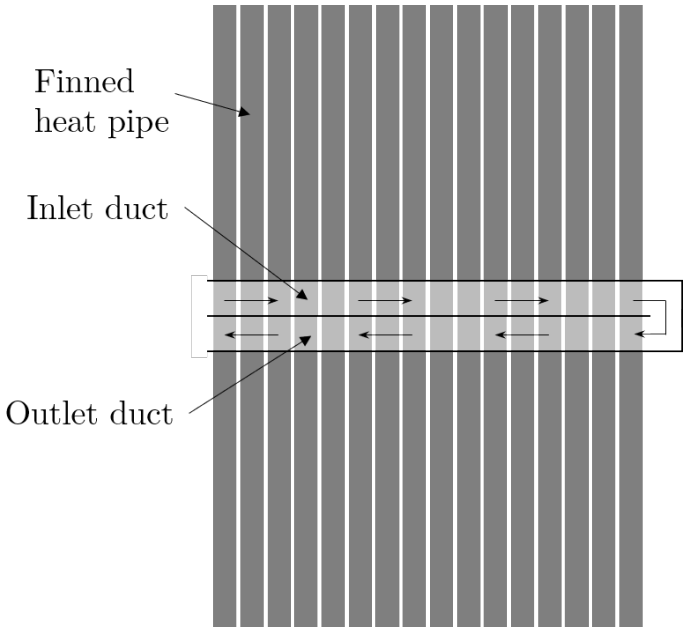

(a) Plan view of radiator panel

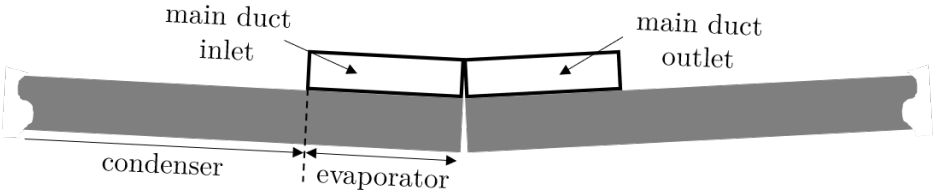

(b) Cross section of radiator panel

Fig. 4.5 Arrangement of main coolant duct and finned heat pipes in radiator panel

The methodology used to calculate the required radiator area is adapted from [58] and [54] and proceeds as follows. First, we observe that for an elemental section of the main duct in the steady state condition, the rate of heat transferred through an elemental area of

the main duct, dA_i, must be equal to the heat radiated away from the corresponding area of radiator, dA_r. Applying Fourier's Law and the Stefan-Boltzmann Law respectively, results in (according to [54]):

$$h_i(T - T_w)dA_i = \sigma\varepsilon F(T_w^4 - T_s^4)dA_r \tag{4.59}$$

where h_i is the convective heat transfer coefficient to the main duct wall, T is the temperature of the coolant, T_w is the temperature of the duct wall, σ is the Stefan-Boltzmann constant, ε is the radiator emissivity, F is the view factor to space and T_s is the effective temperature of space. Before proceeding, a few comments and alterations are made:

- Determining the view factor F is often a complex process. It is clear that the side of the panel attached to the heat pipe will have a view factor to space of less than unity, since photons emitted from the fins might impinge on the heat pipe, or vice versa. One possible approach would be to approximate the geometry as a set of rectangular planes, for each pair of which there exist expressions for the view factor with respect to each other. A simple and conservative approach is taken, ignoring the additional area provided by the heat pipe itself, and treating the radiator as a single plane so that F can be assumed to unity for both sides of the radiator.

- The elemental internal area A_i for the duct design chosen relates to only one side of the duct in contact with the finned heat pipe.

- The effective temperature of space is not, as one might hope, that of the cosmic microwave background. Since we are for now considering travel within the Solar System, solar irradiation must be considered. The effective average space temperature can be estimated for orbits around various bodies [58]. A common value used to cover a variety of mission profiles between Earth and Jovian orbits is 200K [30, 108].

- There is an assumption implicit in Equation 4.59 that the temperature of the main duct wall, T_w, is equal to the temperature of the radiating surface. One would expect that there would be temperature drops through the duct wall, carbon-carbon armour, heat pipe wall, along the heat pipe, back through the heat pipe wall and armour and finally along the fin. It is reasonable to assume that on average there is a total temperature drop between the main duct wall and the base of the fins of 50K [30, 108]. It should be noted that the losses along the heat pipe are negligible compared to the conduction losses. For the fin itself, a 'fin effectiveness' can be calculated. This is defined as the ratio of the heat emitted by the fin to the heat that would be emitted if the entire fin

had the same temperature as its base. For the fin materials and geometry chosen, a fin effectiveness of 95% is achievable [97].

- The emissivity of the carbon-carbon armour is taken to be 0.9 [30].

With the addition of a total duct-wall-to-fin-base temperature drop of ΔT and fin effectiveness α_{fin}, Equation 4.59 becomes:

$$h_{\text{i}}(T - T_{\text{w}})\text{d}A_{\text{i}} = \sigma\varepsilon(\alpha_{\text{fin}}(T_{\text{w}} - \Delta T)^4 - T_{\text{s}}^4)\text{d}A_{\text{r}} \tag{4.60}$$

A new simplifying definition is made [54], an effective heat transfer coefficient given the ratio of heat transfer areas:

$$h_{\text{r}} = h_{\text{i}}\frac{\text{d}A_{\text{i}}}{\text{d}A_{\text{r}}} \tag{4.61}$$

This ratio of areas can be calculated simply, referring to Figure 4.4 and assuming that the elemental section of radiator panel is that corresponding to a single heat pipe. As noted above, the view factor of the 'top' side of the panel is assumed to be unity and the extra surface area provided by the heat pipe is neglected. The entire top surface of the 2m long heat pipe has an effective area of 2,920cm^2. The rectangular main coolant duct is 20cm wide, exposing the remaining 180cm of the bottom face of the heat pipe to space. However, the top of the duct has the same carbon-carbon outer surface as the heat pipe and so could be considered to act as a radiating surface. The bottom radiating area is therefore also 2,920cm^2. These sum to a total radiating area for one heat pipe of 5,840cm^2, the value of $\text{d}A_{\text{r}}$. The value of $\text{d}A_{\text{i}}$ is the contact area between the coolant duct and heat pipe, which is 292cm^2. The value of $\text{d}A_{\text{i}}/\text{d}A_{\text{r}}$ is therefore 0.05. Substituting into Equation 4.60 yields an expression for the main coolant temperature at a point in the duct:

$$T = T_{\text{w}} + \frac{\sigma\varepsilon}{h_{\text{r}}}(\alpha_{\text{fin}}(T_{\text{w}} - \Delta T)^4 - T_{\text{s}}^4) \tag{4.62}$$

For a known value of the fluid temperature T, this can be readily solved for the duct wall temperature T_{w} using the Newton-Raphson iterative root-finding process. First a function $f(T_{\text{w}})$ is defined for which we seek the root $f(T_{\text{w}}) = 0$. Its derivative is also taken. These are:

$$f(T_{\text{w}}) = T_{\text{w}} + \frac{\sigma\varepsilon}{h_{\text{r}}}(\alpha_{\text{fin}}(T_{\text{w}} - \Delta T)^4 - T_{\text{s}}^4) - T \tag{4.63}$$

$$f'(T_{\text{w}}) = 1 + \frac{4\sigma\varepsilon\alpha_{\text{fin}}}{h_{\text{r}}}(T_{\text{w}} - \Delta T)^3 \tag{4.64}$$

The Newton-Raphson process proceeds on the basis that, for a given root guess x_n, a better estimate of the root is given by:

$$x_{n+1} = x_n - \frac{f(x_n)}{f'(x_n)} \tag{4.65}$$

This iterative process continues until a specified level of convergence is reached.

The total area of the radiator is calculated on a finite element basis. The radiator is required to produce a certain overall drop in the main coolant temperature, which can be divided up into small radiator segments each producing a drop in the main coolant temperature of $\mathrm{d}T$. For each of these segments, the area of radiator required is given by:

$$\mathrm{d}A_\mathrm{r} = \frac{\dot{m} C_\mathrm{P} \mathrm{d}T}{\sigma \varepsilon (\alpha_\mathrm{fin} (T_\mathrm{w} - \Delta T)^4 - T_\mathrm{s}^4)} \tag{4.66}$$

With the area in hand, the mass of the radiator can be calculated simply by multiplying by the areal density. It has been suggested [55] that this density could approach 1.0kg/m^2 using the latest carbon-carbon materials, if tolerance to launch vibrations can be demonstrated. A more conservative value of 6.0kg/m^2 [30] is chosen here.

One parameter which has not yet been given is the height of the main coolant duct. Increasing this parameter leads to a decreased heat transfer coefficient, but a lower frictional pressure loss. Decreasing the heat transfer coefficient will lead to a larger radiator, but a reduced pressure loss through the radiator will improve the cycle efficiency leading to mass savings elsewhere. The way this is handled is to assume a pressure loss in advance and iteratively find the duct height which corresponds to this pressure loss by repeated runs of the radiator analysis code. A fixed pressure loss of 5% is assumed in all cases. It would, of course, be possible to make the radiator pressure loss a variable in the overall optimisation scheme; however, this is not included in this study.

Finally, it is common to see in radiator designs several separate radiator panels, especially when they are arranged in a radial pattern like the SP-100. This has the advantage of decreasing the pressure loss, by having several parallel main ducts rather than a single (much longer) duct. This is particularly important in the direct heat-rejection design being used here due to the poorer heat transfer properties of the gas coolant compared to liquid metal. For this study, a reasonably achievable set of ten parallel main ducts is assumed.

4.4 Cycle parameters

The only parameters relating to the reactor that are relevant to the non-reactor part of the overall power system are its inlet and outlet temperatures, the mass flow rate and the reactor pressure drop. Given a set of these parameters, there are in principle multiple sets of power cycle parameters that result in the desired electrical power output of 1MW. These power cycle parameters are the pressure ratio, temperature ratio, recuperator effectiveness and the temperature drop required of the waste heat radiator. The aim is to find, for a given core design, which of these possible cycles has the lowest mass. The independent variable chosen in the search for the minimum mass power conversion system is the compressor pressure ratio.

Before proceeding, two definitions are made for the sake of readability:

$$D \equiv \frac{\dot{W}_{\text{shaft}}}{\dot{m} C_{\text{P}}}$$
$$\gamma' \equiv \frac{\gamma - 1}{\gamma} \tag{4.67}$$

First, for a given value of the compressor pressure ratio r_{c}, the turbine pressure ratio can be calculated using:

$$r_{\text{t}} = \beta_P r_{\text{c}} \tag{4.68}$$

where β_P is the proportion of pressure remaining after frictional losses arising in the components of the power cycle. In the case of the unrecuperated system, the pressure loss is assumed to arise only in the reactor and waste heat radiator:

$$\beta_P = \left(1 - \frac{\Delta P_{\text{reac}}}{P}\right)\left(1 - \frac{\Delta P_{\text{rad}}}{P}\right) \tag{4.69}$$

For a recuperated cycle, losses will also arise in the two legs of the recuperator:

$$\beta_P = \left(1 - \frac{\Delta P_{\text{reac}}}{P}\right)\left(1 - \frac{\Delta P_{\text{rad}}}{P}\right)\left(1 - \frac{\Delta P_{\text{rh}}}{P}\right)\left(1 - \frac{\Delta P_{\text{rc}}}{P}\right) \tag{4.70}$$

Using these newly defined quantities, the outlet temperatures of the turbine and compressor can be written in terms of the compressor pressure ratio:

$$T_{\text{t}_{\text{out}}} = T_{\text{t}_{\text{in}}}(1 - \eta_{\text{t}}(1 - (\beta_P r_{\text{c}})^{-\gamma'})) \tag{4.71}$$
$$T_{\text{c}_{\text{out}}} = T_{\text{c}_{\text{in}}}(1 - \eta_{\text{c}}^{-1}(1 - r_{\text{c}}^{\gamma'})) \tag{4.72}$$

These temperatures must satisfy Equation 4.22 so that the desired output power is achieved. There is potentially a range of values of r_c that accomplish this. However, there are some constraints which limit the values that r_c can take, the first of which applies to both unrecuperated and recuperated cycles.

Avoiding unphysically low temperatures: $T_{c_{in}} > T_{space}$

The lowest temperature in the cycle occurs at the radiator outlet, after heat has been transferred from the working fluid into space. In order to avoid heat being transferred *from* space *to* the working fluid, it must be the case that the lowest temperature of the working fluid is higher than the temperature of space. As mentioned in the radiator modelling section, this has been set at 200K. Noting that $T_{rad_{out}} = T_{c_{in}}$,

$$T_{c_{in}} > T_{space} \tag{4.73}$$

Using Equations 4.22 and 4.67 this becomes

$$\eta_c \frac{T_{t_{in}} - T_{t_{out}} - D}{r_c^{\gamma'} - 1} > T_{space} \tag{4.74}$$

Making the appropriate substitutions for the turbine temperatures and rearranging produces a quadratic equation in $r_c^{\gamma'}$ whose roots provide the minimum and maximum values of r_c:

$$\begin{aligned} &(-\eta_c^{-1} T_{space}) r_c^{2\gamma'} \\ +&(\eta_t T_{reac_{out}} + \eta_c^{-1} T_{space} - D) r_c^{\gamma'} \\ &-\eta_t \beta_P^{-\gamma'} T_{reac_{out}} = 0 \end{aligned} \tag{4.75}$$

4.4.1 Unrecuperated cycles

With no recuperator, the compressor feeds directly into the reactor, so that $T_{c_{out}} = T_{reac_{in}}$. Additionally, the turbine inlet temperature is simply equal to the reactor outlet, $T_{t_{in}} = T_{reac_{out}}$. Substituting these temperatures into Equation 4.22 results in:

$$\frac{\dot{W}_{shaft}}{\dot{m} C_P} = T_{reac_{out}} - T_{t_{out}} + T_{c_{in}} - T_{reac_{in}} \tag{4.76}$$

Now substituting in Equations 4.71 and 4.72 and the simplifications in 4.67

$$D = T_{\text{reac}_{\text{out}}} - T_{\text{reac}_{\text{out}}}(1-\eta_{\text{t}}(1-(\beta_P\, r_{\text{c}})^{-\gamma'}) + T_{\text{reac}_{\text{in}}}(1+\eta_{\text{c}}^{-1}(r_{\text{c}}^{\gamma'}-1))^{-1} - T_{\text{reac}_{\text{in}}} \quad (4.77)$$

This equation is quadratic in the term $r_{\text{c}}^{\gamma'}$. After rearranging it has the form:

$$\begin{aligned} &\eta_{\text{c}}^{-1}(D-\eta_{\text{t}}T_{\text{reac}_{\text{out}}}+T_{\text{reac}_{\text{in}}})r_{\text{c}}^{2\gamma'} \\ +(D(1-\eta_{\text{c}}^{-1})+\eta_{\text{t}}T_{\text{reac}_{\text{out}}}(\eta_{\text{c}}^{-1}(1+\beta_P)-1)-\eta_{\text{c}}^{-1}T_{\text{reac}_{\text{out}}})&r_{\text{c}}^{\gamma'} \\ &+\beta_P^{-\gamma'}T_{\text{reac}_{\text{out}}}\eta_{\text{t}}(1-\eta_{\text{c}}) = 0 \end{aligned} \quad (4.78)$$

The real root of this equation then provides the compressor pressure ratio which produces the required electrical power output. Once this is known, temperatures at all points in the cycle can be calculated and the system mass can be estimated.

4.4.2 Recuperated cycles

The inclusion of a recuperator, which can have an effectiveness ε between 0 and 1, means that there are, in principle, multiple compressor pressure ratios that lead to compressor and turbine temperatures that satisfy Equation 4.22. Each of these viable cases will have a different mass, so the minimum mass configuration should be sought. Since calculating the mass of the radiator involves a Newton-Raphson process to solve the quartic equation in temperature, which is itself nested inside the iterative process to find the appropriate radiator duct height, it is clear that there is no analytical solution to finding the minimum mass pressure ratio (and corresponding recuperator effectiveness). A numerical method is therefore required. Before applying any such method, the bounds of allowable pressure ratios must be determined, in addition to the constraint on the minimum cycle temperature mentioned above. There are several constraints which must be applied, which are discussed in the following sections.

Recuperable cycle: $T_{\text{t}_{\text{out}}} > T_{\text{c}_{\text{out}}}$

For a cycle to be recuperable, the hot leg of the recuperator must be hotter than the cold leg, or heat will flow in the wrong direction from the compressor outlet to the waste heat radiator. Whilst this is not an unphysical scenario, it is certainly undesirable. Avoiding this situation imposes an upper limit on the pressure ratio, the point at which $T_{\text{t}_{\text{out}}} = T_{\text{c}_{\text{out}}}$. Substituting in Equation 4.71 for $T_{\text{t}_{\text{out}}}$ and Equation 4.72 for $T_{\text{c}_{\text{out}}}$ in the expression $T_{\text{t}_{\text{out}}} = T_{\text{c}_{\text{out}}}$ results in:

$$T_{\text{t}_{\text{in}}}(1-\eta_{\text{t}}(1-(\beta_P r_{\text{c}})^{-\gamma'})) = T_{\text{c}_{\text{in}}}/(1-\eta_{\text{c}}^{-1}(1-r_{\text{c}}^{\gamma'})) \quad (4.79)$$

Using the same substitutions as before, so that this expression is in terms of reactor temperatures only, we arrive at another quadratic equation in $r_c^{\gamma'}$, the greater positive root of which is this maximum pressure ratio:

$$\begin{aligned} &\eta_c^{-1}(1-2\eta_t+D/T_{reac_{out}})r_c^{2\gamma'} \\ &+\left[(1-\eta_c^{-1})D/T_{reac_{out}}-(\eta_c^{-1}+\eta_t)+2\eta_t\eta_c^{-1}(1+\beta_P^{-\gamma'})\right]r_c^{\gamma'} \\ &+\eta_t\beta_P^{-\gamma'}(1-2\eta_c^{-1})=0 \end{aligned} \tag{4.80}$$

Recuperable cycle: $T_{c_{out}} > T_{reac_{in}}$

Searches through the space of possible pressure ratios must also be limited to cases where the compressor outlet temperature is less than the reactor inlet temperature. Otherwise this would require heat to flow in the wrong direction through the recuperator. Starting with $T_{c_{out}} = T_{reac_{in}}$, substitutions are again made from Equations 4.71, 4.72 and 4.22. This results in another quadratic equation in $r_c^{\gamma'}$:

$$\begin{aligned} &\eta_c^{-1}(D+T_{reac_{in}}-\eta_t T_{reac_{out}})r_c^{2\gamma'} \\ &+\left[\eta_t T_{reac_{out}}(\eta_c^{-1}(1+\beta_P^{-\gamma'})-1)+D(1-\eta_c^{-1})-\eta_c^{-1}T_{reac_{in}}\right]r_c^{\gamma'} \\ &+\beta_P^{-\gamma'}T_{reac_{out}}\eta_t(1-\eta_c^{-1})=0 \end{aligned} \tag{4.81}$$

Recuperator effectiveness < 1

The recuperator effectiveness was derived earlier as the ratio of the heat available to be transferred from the hot to cold leg to that which is actually transferred:

$$\varepsilon = \frac{T_{rc_{out}} - T_{rc_{in}}}{T_{t_{out}} - T_{c_{out}}} \tag{4.82}$$

As before, we note that the recuperator cold leg inlet is fed by the compressor and its outlet feeds into the reactor. Making these substitutions:

$$\varepsilon = \frac{T_{reac_{in}} - T_{c_{out}}}{T_{t_{out}} - T_{c_{out}}} \tag{4.83}$$

The pressure ratio at which $\varepsilon = 1$ therefore occurs at

$$\frac{T_{reac_{in}} - T_{c_{out}}}{T_{t_{out}} - T_{c_{out}}} = 1 \tag{4.84}$$

Substituting from Equations 4.71 and 4.72 and rearranging results in the following expression for the compressor ratio:

$$r_c = \left[\frac{\beta_P^{-\gamma'}}{1 - \eta_t^{-1}(1 - T_{\text{reac}_{\text{in}}}/T_{\text{reac}_{\text{out}}})} \right]^{\frac{1}{\gamma'}} \tag{4.85}$$

Finding the optimal pressure ratio

Now that the pressure ratio search space has been determined, the minimum mass recuperated system can be searched for. This search is carried out using a fairly simple method, taking 100 evenly-spaced sample points in the allowable range, then a further 100 points between the points neighbouring the minimum mass point, repeating this process until the minimum mass is found to within 1kg. This assumes that the total mass, as a function of the compressor pressure ratio, is smooth with a single minimum in the range considered. This has not been proved mathematically but has been observed to be so in all cases inspected. This method does fail when the minimum-mass sample point is at the boundary (the first or hundredth point). In such a case, the code reverts to using standard MATLAB functionality for finding the minimum of a constrained nonlinear function, which by default uses an interior-point method. This is more powerful than the simple method described above and is more efficient in terms of the number of function evaluations required, but is overall slower in terms of computation time.

4.4.3 Analysis flowchart

The overall scheme for finding the minimum mass Brayton cycle system is shown in a simplified form in Figure 4.6. Note that this does not include the mass of the reactor, which is calculated separately.

4.4.4 Example case

To illustrate the process of finding the minimum-mass conversion system for a given set of reactor inlet/outlet temperatures and mass flow rate, a worked example is now provided.

- Reactor inlet temperature = 700K
- Reactor outlet temperature = 1000K
- Pure helium coolant flow rate = 5kg/s

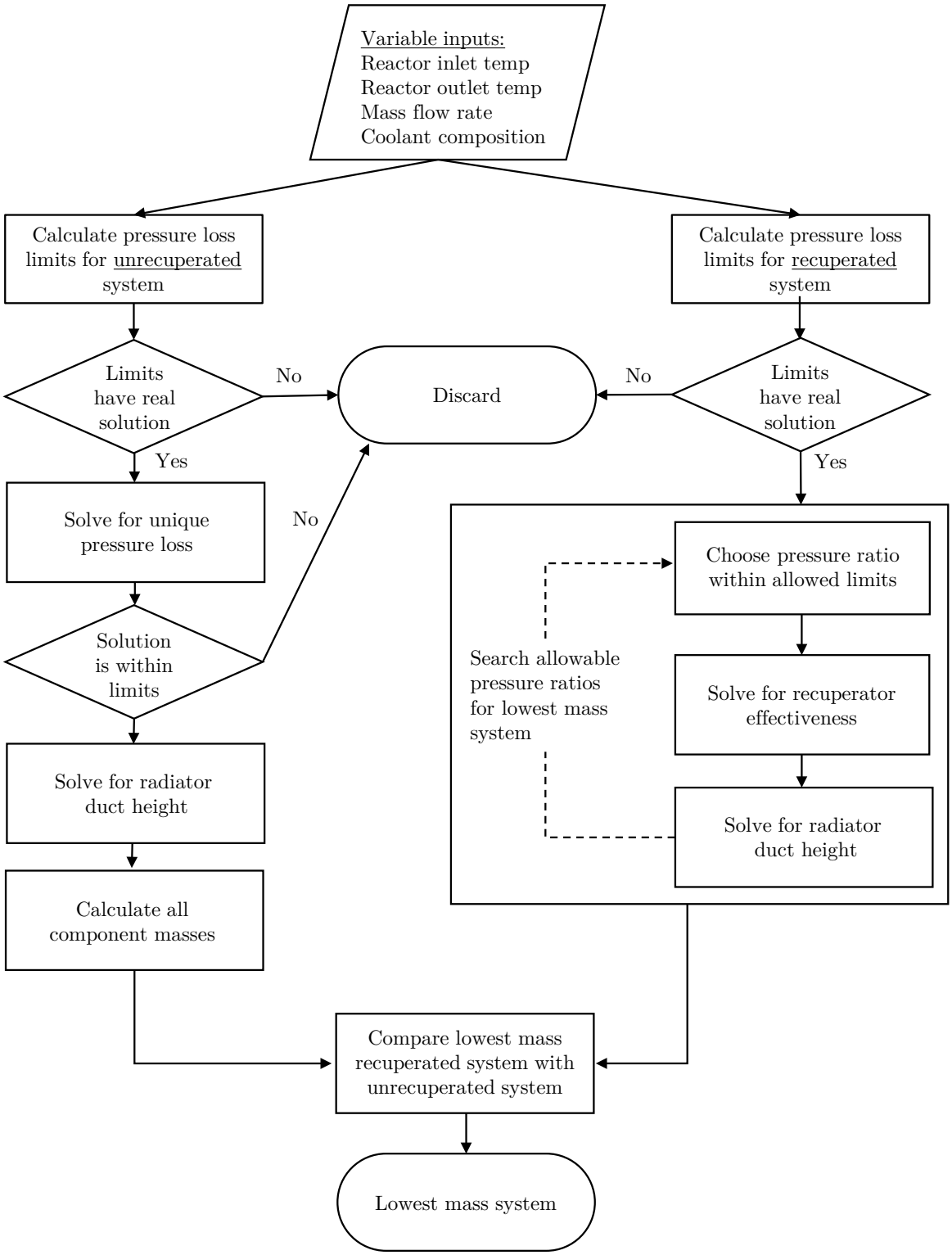

Fig. 4.6 Flowchart showing process leading to minimum mass conversion system

Table 4.5 Allowable pressure ratios in unrecuperated cycles for example case

Condition	r_c limit	
	Lower	Upper
$T_{c_{in}} > T_{space}$	1.41	10.40

Table 4.6 Allowable pressure ratios in recuperated cycles for example case

Condition	r_c limit	
	Lower	Upper
$T_{c_{in}} > T_{space}$	1.51	10.09
$T_{t_{out}} < T_{c_{out}}$	-	3.62
$T_{c_{out}} < T_{reac_{in}}$	-	4.90
$\varepsilon < 1$	-	3.10

As described above, there are several limits on allowable pressure ratios. For the case of unrecuperated cycles, only the first one of these is relevant. This is shown in Table 4.5. Then, the pressure ratio for the unrecuperated system is calculated using Equation 4.78. This results in a pressure ratio of 4.24. Since this is between the minimum and maximum shown in Table 4.5, this is an allowable system. The turbomachinery mass is calculated using Equations 4.56-4.57, the PMAD mass using the fixed specific mass of 3.4kg/kW$_e$, as explained in Section 4.3.2, and the radiator mass using the computational procedure described in Section 4.3.3. The total mass of these components is 182 tonnes.

Now we proceed to consider recuperated cycles. Table 4.6 shows the limits on the pressure ratio in this case. Note that the first condition is recalculated because the additional pressure loss arising in the recuperator slightly decreases the turbine pressure ratio and therefore the net work done in the cycle. Based on these values, the search space is therefore limited to pressure ratios between 1.51 and 3.10. It can be helpful to visualise how the various temperatures around the cycle and the recuperator effectiveness vary as a function of pressure ratio. Figure 4.7 shows this. Of particular interest is the shape of the recuperator effectiveness curve. It has an asymptote at the point at which $T_{t_{out}} = T_{c_{out}}$ where it changes sign. However, at higher pressure ratios above around 5.0 it can be seen that it returns to the acceptable range of $0 < \varepsilon < 1$. This complex shape is the main reason for choosing the compressor pressure ratio as the independent variable in the search for the lowest mass power conversion system, rather than the recuperator effectiveness. Due to the low overall computational cost of evaluating a conversion system design, the minimum mass system can be found by a simple brute-force search through the allowable pressure ratios. The minimum

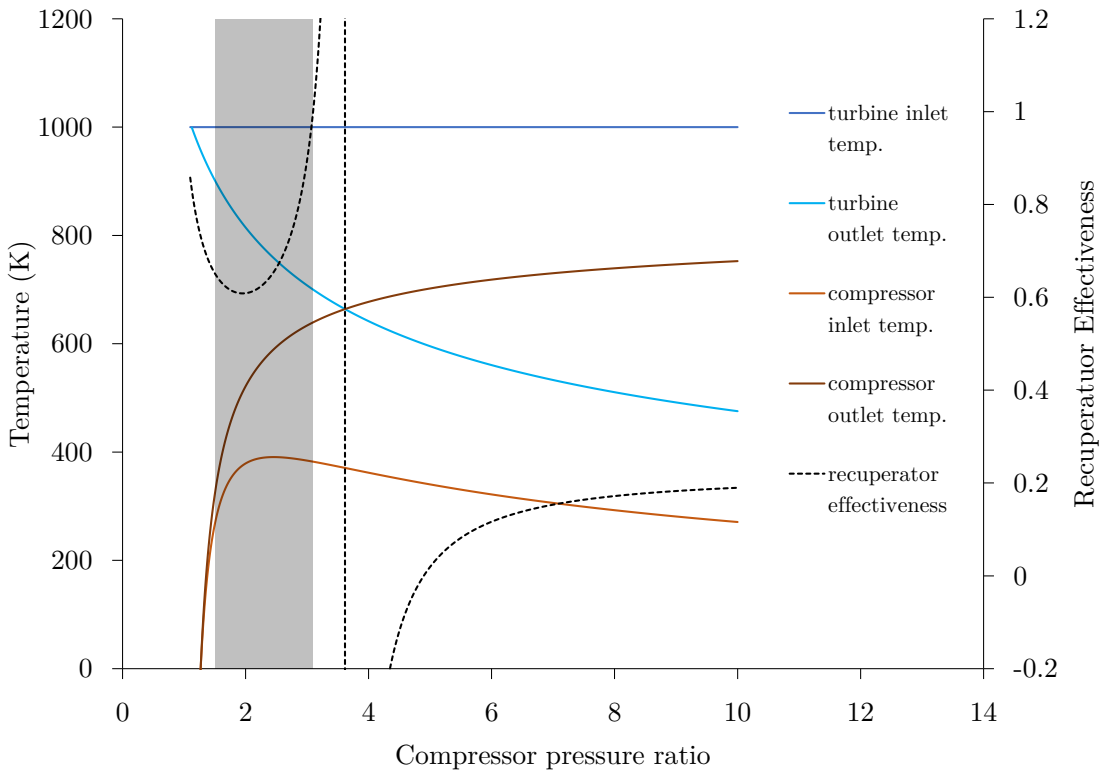

Fig. 4.7 Compressor and turbine temperatures and recuperator effectiveness for example case. Shaded area indicates region that satisfies the limits on the pressure ratio in Table 4.6

mass system in this is found to have a mass of 83 tonnes, using a compressor pressure ratio of 1.73 and a recuperator effectiveness of 0.62. In this case, the best recuperated system has a lower mass than the unrecuperated system and is therefore chosen as the overall optimum.

4.5 Summary

A conversion system based on a direct Brayton cycle with direct heat rejection and optional recuperation was chosen as the means of converting the reactor heat output to 1MW of electrical power. Approximate models were chosen to estimate the masses of the turbomachinery, alternator, recuperator and waste heat radiator, based on their required power output, temperature drop or effectiveness as appropriate. A routine was developed to find the lowest mass cycle configuration, using the compressor pressure ratio as the independent variable and carrying out an exhaustive search. This routine takes as its inputs a fixed set of reactor conditions: the inlet and outlet temperatures, the core pressure drop and working fluid mass flow rate.

Chapter 5

Minimum mass designs

5.1 Introduction

The overall purpose of this investigation is to determine the impact on the overall mass of the fission power system of the choice of an LEU fuel form over a HEU fuel form, in the limited case of a TRISO fuel form combined with a gas-cooled direct Brayton conversion system. A fair comparison between any two such system types would, of course, be between the minimum mass system from each type. The process of finding these minimum mass systems is the subject of this chapter.

The method of finding the mass of the conversion system described in the previous chapter was essentially a brute force method. This was a reasonable approach because the overall calculation time to find the minimum mass system was on the order of seconds. Once the neutronic and thermal hydraulic analyses of the core are included in this process, a simple brute force method will no longer be appropriate due to the significantly longer calculation time. Some effort will be required to intelligently choose core designs to evaluate to reduce the computational burden of seeking the minimum mass design.

This brings us to the well-established field of optimisation. Using the terminology of that discipline, the current pursuit is a multivariate, single-objective optimisation problem. That is, there are several core design parameters which feed into an 'objective function', in this case the calculation of the total system mass. Minimising this mass is the single objective. The problem is constrained, with simplest constraints being the bounds for each variable that define the design space, specifying the range of values that the inputs will be allowed to take. Some of these might be real-world limits, such as the maximum size of a coolant channel that does not touch another coolant channel. Other limits might just be sensible bounds to the search space to avoid an algorithm wasting time evaluating, for example, the reactivity of

a core with a kilometre-thick reflector. Other types of constraints might also limit the search space, but require evaluating to determine if they are breached.

For example, we might have an objective function $f(x,y)$ whose minimum value we wish to seek. We might wish to confine the search to a region between $x = 2$ and $x = 10$ - these are the simple bounds. We might also wish to further reduce the search space to the region where $x + y < 8$, which is a linear constraint, or perhaps to the region inside the circle defined by $x^2 + y^2 < 40$, a non-linear constraint. More generally, we might have a non-linear constraint relating to a non-analytical function $g(x,y)$, requiring that $g(x,y) < c$ whilst minimising $f(x,y)$. In the case of our optimisation problem, the constraints are the temperature limits (fuel, moderator and turbine inlet) and the requirement for $k_{\text{eff}} > 1$ at the end of life. Evaluating these constraint functions is in fact where all the computational burden lies in the current study. The objective function itself is actually very computationally light, since the core design parameters prescribe volumes which lead to a trivial mass calculation for the core (and a simple core vessel calculation) and the power conversion system mass minimisation presented in the previous chapter also requires only a few seconds to complete.

The problem also requires *global* optimisation, as we should assume that multiple local minima exist and we wish to seek the lowest of these minima. There are many well-established global optimisation methods. Since most of the computational infrastructure developed so far is in MATLAB, it seemed sensible to make use of the Global Optimisation Toolbox within the MATLAB framework. This provides for the use of a number of popular global optimisation methods, principally genetic algorithms, particle swarm, simulated annealing and a surrogate function method. The documentation for this toolbox provides the basic theory behind each method as implemented in MATLAB. There is little guidance as to when one might prefer one method over another except for a fairly strong recommendation that the surrogate function method is suitable for problems with a time-consuming objective function. Arguably, the current problem does have an expensive objective function with a run-time of the order of around 15-30 minutes assuming one execution of both the neutronics module, with burnup, and the thermal hydraulics code. The surrogate function method would therefore seem a sensible choice of optimisation method.

5.2 Surrogate function method

The basic principle behind the surrogate function method is to use evaluated points to construct a function by interpolation and extrapolation, which is an estimate of what the complete space of the objective function looks like. If the real objective function is 'expensive', then evaluating points on the surrogate function will be much cheaper. A minimum can therefore

be cheaply sought on the surrogate function and, once found, the real objective function can be evaluated at that point. This newly evaluated point can then be used to improve the surrogate function.

Within this basic framework there is a wide variety of possible implementations, including the mathematical form of the surrogate function and how exactly the algorithm uses it to inform where to evaluate the objective function next. What follows is a description of the method implemented in the MATLAB Global Optimisation Toolbox [73]. Note that one aspect of this algorithm is that it can not handle non-linear constraints; instead, one uses a penalty function which increases the value of the objective when constraints are breached. For example, one might add 1,000kg to the total system mass for every degree that the moderator temperature exceeds its allowable maximum. In what follows below then, when the surrogate function algorithm is said to evaluate the objective function, this includes an evaluation of the constraints and the application of penalties as appropriate.

The first stage of the algorithm is the 'construct surrogate phase'. The steps in this phase are illustrated in Figure 5.1. First, a number of random points within the bounds are generated, in this case twenty, to enable the initial construction of the surrogate function. The surrogate is constructed by interpolating radial basis functions. The radial basis function used by MATLAB is a cubic function with a linear tail, but all radial functions satisfy the general condition that their value depends only the distance from some point $\mathbf{c}$ [73]:

$$\psi(\mathbf{x}) = \psi(||\mathbf{x}-\mathbf{c}||) \tag{5.1}$$

For a set of N points, constructing the surrogate function involves solving a N-by-N system of linear equations, which for many choices of radial basis functions has a unique solution [88]. Once this is done, the 'construct surrogate phase' finishes by naming the lowest-value evaluated point as the 'incumbent'. These steps are shown graphically in Figure 5.1. Next the algorithm enters the 'search for minimum' phase. The steps in this phase are illustrated in Figure 5.2. It generates thousands of pseudorandom values of x (or in a multivariate case, of the vector $\mathbf{x}$) in a normal distribution about the incumbent point. The width of this distribution is determined by a scale factor, initially set at 0.2. For each of these trial points, a merit function $f_{\text{merit}}(x)$ is calculated, where lower values have the greater merit. The merit function is a weighted combination of two quantities: $S(x)$ which is related to the value of the surrogate function computed at x, and $D(x)$ which is related the distance from points where the objective function has already been evaluated. Greater distances lead to a lower value of $D(x)$. The algorithm therefore attempts to strike a balance between investigating areas where the surrogate function is lowest and exploring the space that is far from evaluated points where there is little information.

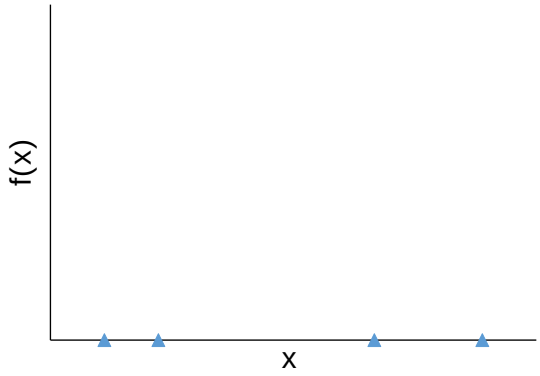

(a) Generate random points

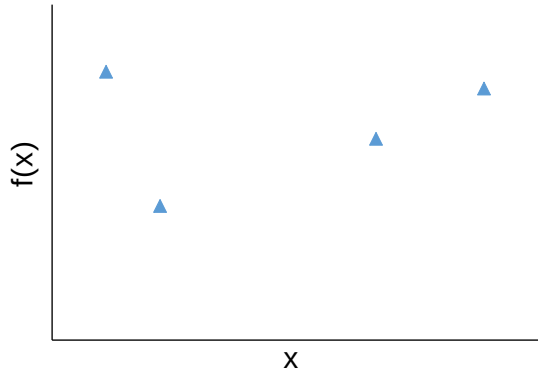

(b) Evaluate objective function

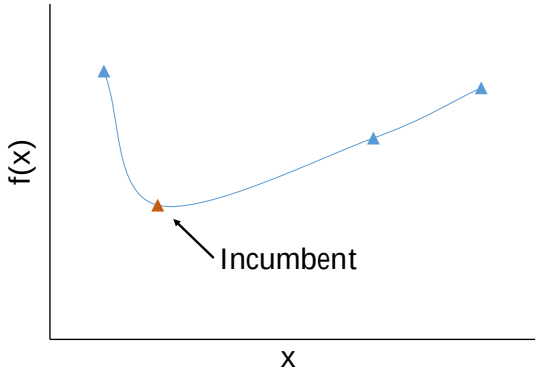

(c) Construct surrogate and assign incumbent

Fig. 5.1 Three stages in the construct surrogate phase

The function $S(x)$ is called the scaled surrogate. At each of the sample points x_i, the surrogate function is evaluated to give s_i. If the minimum of these is $s_{\min}$ and the maximum is $s_{\max}$ then the scaled surrogate for each sample point is:

$$S(x) = \frac{s(x) - s_{\min}}{s_{\max} - s_{\min}} \tag{5.2}$$

The function $D(x)$ is the scaled distance. The distances between each sample point x_i and all of the evaluated points at x_j are evaluated to give d_{ij}. Then we define $d_{\min} = \min(d_{ij})$ and $d_{\max} = \max(d_{ij})$ and calculate the scaled distance using:

$$D(x) = \frac{d_{\max} - d(x)}{d_{\max} - d_{\min}} \tag{5.3}$$

Finally, we calculate the merit function using:

$$f_{\text{merit}}(x) = wS(x) + (1-w)D(x) \tag{5.4}$$

where w is the weighting factor. Higher values of w lead to more attempts to minimise the surrogate, while lower values lead to more exploration of space where there are fewer evaluated points. The value of w is cycled through four recommended [116] values: 0.3, 0.5, 0.8 and 0.95. Once the sample point with the lowest value of the merit function has been determined, the objective function is evaluated at this point, called the *adaptive point*. The surrogate function is then updated to reflect this new information. If the adaptive point is sufficiently lower than the incumbent (the tolerance on this is unfortunately unspecified) then it becomes the new incumbent and the search is considered successful. If three successful searches occur in a row, the scale of the next search is halved, so that sample points are generated more locally. This is done by halving the scale factor, previously set at 0.2. If n_{var} (number of variables) unsuccessful searches occur, the scale is doubled. Importantly, the algorithm will not evaluate the merit function at any points that are within a certain distance from already evaluated points. This *minimum sample distance* is essentially the only parameter that the user provides to the algorithm to modify its behaviour and it can have a significant effect. If all of the sample points lie within this distance, then a *surrogate reset* is performed. This simply means that the algorithm returns to the first phase, adding a new batch of random points and reconstructing the surrogate function. The value of the minimum sample distance (MSD) therefore affects how the algorithm spends its time. A small value of the MSD will allow the algorithm to reduce the search scale to smaller sizes, spending more time minimising the surrogate function, or, put informally, attempting to find the bottom of the local minimum that it is focussed on. A large value of the MSD will lead to more frequent surrogate resets, spending more time exploring the design space to find new minima. The weight factor w also controls this behaviour between surrogate resets, but this cycles through fixed values. The MSD controls the global behaviour and is a required input by the user. It therefore requires some tuning to the specific problem being analysed. In fact, having only one parameter which requires some tuning is one of the attractive features of this surrogate function method; other common methods such as genetic algorithms have many such tuneable parameters. The process of selecting the MSD will be discussed in a subsequent section.

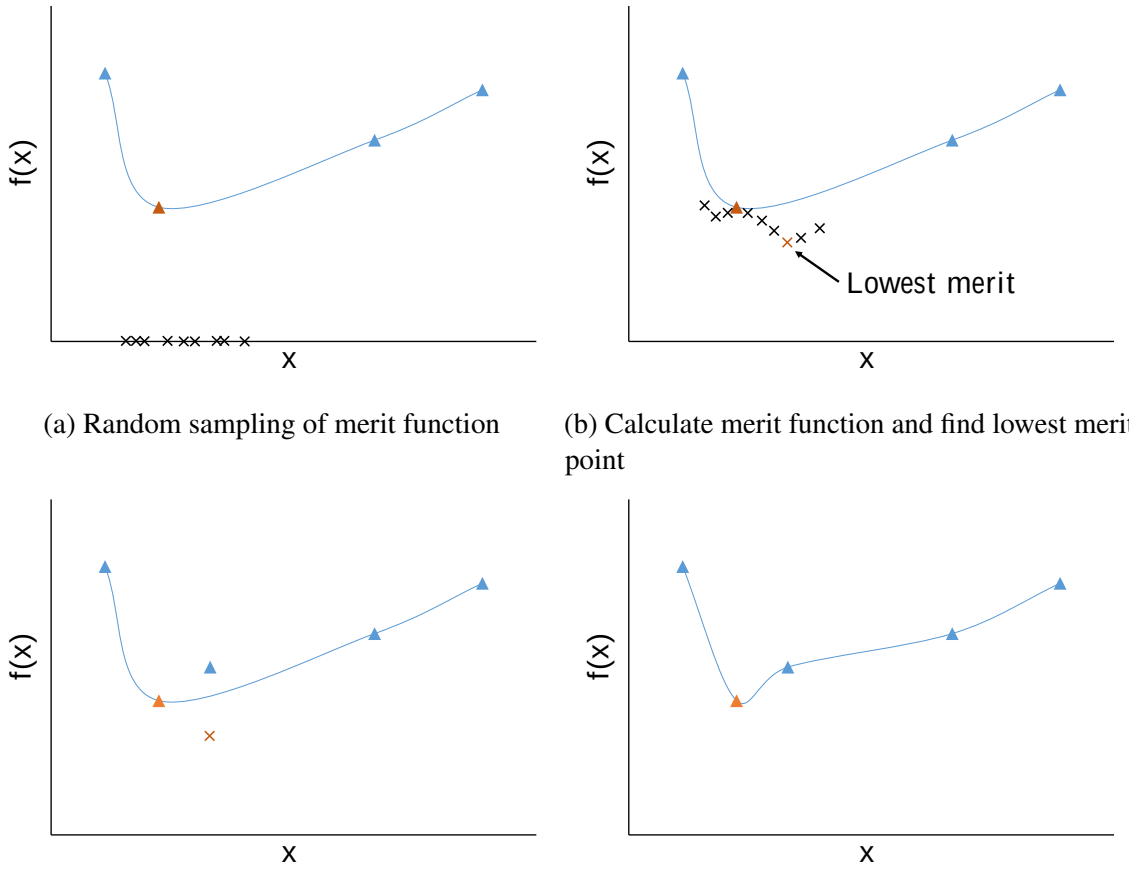

(a) Random sampling of merit function

(b) Calculate merit function and find lowest merit point

(c) Evaluate objective (adaptive point)

(d) Construct surrogate and assign incumbent

Fig. 5.2 Four stages in the search for minimum phase

5.2.1 Parallel computing

The surrogate function algorithm is compatible with parallel computing, although this could be considered an extension of its functionality and perhaps not an entirely natural one. The algorithm described above is a fairly linear one, where the algorithm uses the surrogate function as a means to determine where best to evaluate one 'adaptive' point. This new point is then used to improve the surrogate. When operating in parallel with N workers, the analysis of the surrogate can be used to inform where the next best N points to be evaluated are. Some efficiency is undoubtedly sacrificed here, as points are being evaluated that are not the best targets based on the analysis of the surrogate. This could be contrasted with a population-based method such as a genetic algorithm, where many independent evaluations can take place simultaneously. Such algorithms are more directly suited to parallel computing.

In practice, some unexpected difficulties were encountered with parallel computing. The initial intention was to use a single node of the CSD3 system which contains 32 compute

threads. On such a node a single instance of MATLAB can run which then distributes the workload amongst the 32 threads. In practice, significant instability in the surrogate function algorithm was discovered when running in parallel. The resulting crashes had the additional undesirable feature of corrupting the 'checkpoint file', which stored the algorithm's progress, so that runs could not be resumed after such a crash. Unfortunately the Mathworks support staff were unable to determine the cause of this behaviour or recommend any specific action. Such occurrences are, of course, a potential risk when using third party software over which one has no control. Fortunately it was found that running on fewer threads (16), almost entirely removed the instability albeit at the cost of performance. If this behaviour had been known in advance, it is likely that an alternative method would have been used.

5.3 Defining the objective function

In the neutronics and thermal hydraulics analyses, there are some choices which remain that affect the speed and accuracy of the calculation. In the optimisation process, we should assume that we have a fixed computational budget that we wish to make best use of. If a less accurate, but faster, analysis is used in the objective function, it will be possible to evaluate more points in the design space. But, if the analysis within the objective function has too much emphasis on speed, any minimum mass design found in the optimisation process might not reflect reality sufficiently closely to have any confidence in it.

The most computationally expensive option would be to fully couple the neutronics calculation (and using the main, rather than quick, WIMS route) at every burnup step with the thermal hydraulics calculation. This ensures that the changes in power distribution as burnup proceeds are then reflected in the temperature distribution, which then affects the nuclear cross sections and therefore the neutronics calculation. Having to converge the neutronic and thermal hydraulic calculations at every burnup step is likely to lead to an objective function that takes several hours to evaluate. It is reasonable to assume that hundreds or thousands of evaluations will be carried out, so using this maximum accuracy objective function would result in an overly computationally expensive optimisation process.

The first aspect of this that seems reasonable to relax is repeating the neutronic and thermal hydraulic coupling process with each burnup step. In the assessment of whether core temperature limits have been breached, any such breach is most likely to occur at the start of life. Broadly speaking, burnup results in a flattening of the power distribution as fissile material is depleted, so that the power in hot spots is gradually spread over the rest of the core. Therefore, there is little extra information regarding whether a core design is acceptable to be gained from repeating the analysis at every burnup step. There will, of

course, be some effect on core reactivity by the shifting in core temperatures, but this is not likely to be significant enough to justify the great increase in computational load. To give an indication of the impact on calculated core reactivity arising from temperature changes, Table 5.1 shows the temperature coefficients of reactivity for an example core.

Table 5.1 Temperature coefficients of reactivity for core materials as calculated by WIMS. Reactivity change shown in pcm per K. Based on a 10-ring core with a 0.4cm moderator wrapper and a 10cm reflector.

Material	**Temperature coefficient (pcm/K)**
UO_2	-2.06
Buffer C	-0.05
Inner PyC	-0.05
SiC	-0.03
Outer PyC	-0.09
C matrix	-0.44
ZrH	-1.87
Be	0.00

A possible simplified scheme could therefore be:

- Assume a flat temperature profile to carry out an initial fresh-core neutronics analysis (without burnup), giving a power distribution
- Use this power distribution to carry out the thermal hydraulics analysis
- Use the core materials' temperatures that arise from the thermal hydraulics analysis in the neutronics calculation that includes burnup

To estimate the impact of using this simplified scheme, one can examine the convergence progress of the fully coupled scheme to see how one iteration compares to the fully converged result. The values of k_{eff} and the maximum moderator temperature in the core are shown in Table 5.2. As can be seen, to the nearest degree, the same maximum moderator temperature is reported even when based on a power distribution with a flat (per material) temperature assumption. In addition, the value of k_{eff} only changes by a few pcm between the first and second iterations. One would expect burnup to affect the temperature coefficients of reactivity for the core materials, but probably not by the order of magnitude required to render this scheme unreliable. A fully coupled neutronics and thermal hydraulics treatment would not appear to be worth the additional computational cost. To clarify, in the proposed simplified scheme, the k_{eff} that would be used is that corresponding to Iteration 1, not Iteration 0.

Table 5.2 Values of k_{eff} and maximum moderator temperature reported in each iteration of coupled neutronics and thermal hydraulics scheme. Iteration zero uses a flat temperature assumption for each material. Based on a 10-ring core with a 0.4cm moderator wrapper and a 10cm reflector.

Iteration	$\mathbf{k_{eff}}$	**Maximum moderator temperature (K)**
0	1.33150	1,005
1	1.34338	1,005
2	1.34332	1,005

The next area of potential simplification is within the thermal hydraulics module itself. In its normal mode of operation, the thermal hydraulics code analyses an assembly for each ring of the reactor, using the approximation that assemblies within rings are identical. For each assembly, 100 vertical slices are considered, with each one of these requiring a finite element model (FEM) analysis to determine the temperature distribution within the fuel block. The first slice's FEM analysis takes around four seconds and subsequent slices take around two seconds due to having the previous slice's solution as a starting point for the FEM solver. It typically takes two or three iterations of the thermal hydraulics solver to converge the flow pattern (which does have a strong effect on calculated temperatures), so each assembly carries a calculational load of around ten minutes. For a core with ten rings, the total load will be one hundred minutes. This work can also be parallelised so that different assemblies are analysed simultaneously, but this requires the number of threads in the optimisation algorithm to be reduced accordingly.

A significant speed-up could be bought by only considering the central assembly, which is generally the hottest, although some designs with large reflectors and harder spectra can exhibit a thin edge-peaking effect. The analysis above is therefore repeated but only considering the central assembly. The results of the coupled calculation in this case are shown in Table 5.3. In this scheme, the temperatures found along the length of the central assembly are then assumed to apply to all assemblies. Interestingly, for this example core there is relatively little impact on the calculated k_{eff} as a result of only analysing the central assembly compared to the full core: an underestimation of 151pcm. The difference between the calculated maximum moderator temperatures of 8K is also acceptable. Both maximum moderator temperatures occur in the central assembly, so the only possible cause of this difference is the effect that a non-uniform radial temperature distribution has on the core-wide flow pattern. Overall, this computationally cheap approach would appear to be acceptable for the full study.

Table 5.3 Repeated analysis of example core referred to in Table 5.2 but only considering the central assembly

Iteration	k_{eff}	Maximum moderator temperature (K)
0	1.33150	997
1	1.34187	997
2	1.34175	997

Finally, for at least an initial study, the quick WIMS route should be attempted, and if designs are selected that are known to be a problem for that method (very heavily moderated) then the extra computational burden of the main route might be justified.

Whilst the computationally cheapest approach has been adopted for the main study, the functionality of higher fidelity methods has been established. A future study might refine any minimum mass designs found by reactivating the full-core thermal hydraulic analysis and the coupling with the neutronics calculation.

5.3.1 Assigning penalties

The surrogate function algorithm used has no ability to separately handle non-linear constraints. These can only be included by a penalty which is applied to the value returned as the objective function. A very simple approach is taken to this. For temperature limits, 1,000kg of mass is added to the total power system mass for every degree of breach. A reminder of the temperature limits in place can be found in Table 5.4. For end-of-life core reactivity, 1,000kg of mass is added for every pcm below criticality. It will be recalled that in the objective function, an initial fresh-core eigenvalue calculation is carried out to establish some reasonable core temperatures. This also serves as a check on initial reactivity. If the fresh core is subcritical, there is little to be gained from proceeding to the computationally more expensive thermal hydraulics and burnup calculation. A more severe penalty of 10,000kg per pcm of subcriticality is assigned and the objective function terminates early.

Table 5.4 Assumed temperature limits

Limit	Temperature (K)
Fuel kernel	1,523
ZrH moderator	982
Turbine inlet	1,300

Finally, the approach taken to finding the mass of the conversion system involved solving various quadratic equations to determine the allowable range of pressure ratios that was compatible with the reactor inlet and outlet temperatures and flow rate. When these equations had complex roots, it implied that no feasible conversion system existed. This is a purely binary outcome, so when this occurs, a fixed penalty must be applied, in this case 10^{10}kg. An improvement on this regime would include some quantification of the infeasibility of the conversion system. A scaled penalty could then be used which provides more information to the optimisation algorithm.

5.4 Algorithm parameter tuning

As mentioned previously, one of the initially attractive features of the surrogate function algorithm is that it only has one major input parameter that affects its behaviour, the minimum sample distance (MSD). If the value of the MSD is too small, the algorithm might spend too much time investigating local minima, seeking convergence there beyond the required level of accuracy. If it is too large, surrogate resets will occur too frequently, before local minima have been sufficiently converged, and the algorithm will spend too much time generating new random points. Unfortunately the MSD is a measure of distance in the space of design parameters, $(\mathbf{x})$, not the value of the objective function $f(\mathbf{x})$. If the measure of convergence was based on $f(\mathbf{x})$, one could simply provide a convergence criterion that causes a surrogate reset when the current local minimum search is giving improvements of less than, say, 1kg with each objective function evaluation. One can not say, *a priori*, what sort of distance in the $\mathbf{x}$ space might correspond to a change in $f(\mathbf{x})$ that is below the desired level of accuracy and how much this might vary between different local minima. Additionally, one would also not know the shape of the minima. There is no reason to expect that they have a radial shape, where the gradient of descent into the minimum is the same regardless of the direction from which the minimum is approached. A simple measure of the distance $||\mathbf{x}||$ will not capture any such isotropy. The best one can do is to monitor the behaviour of the algorithm using different values of the MSD and choose one that seems to converge the minima it finds to a reasonable level of accuracy. It should be noted that, within one instance of the algorithm, the MSD can not be altered mid-run.

The default value of the MSD is 0.001. It is assumed that this is a measure of distance in a scaled design space, which is a common approach in optimisation algorithms. Often the design variables are scaled onto a unit hypercube. The documentation for the surrogate function algorithm [73] does not explicitly state that this is the case, but if it were not, significant bias towards convergence in some variables would manifest. For example, the

coolant channel size is specified in centimetres whilst the power is specified in watts. The latter is therefore be around six orders of magnitude larger. Measuring a distance in this unscaled design space would problematic and it is presumed that the algorithm would not be designed in such a way.

A simple study was carried out to determine an appropriate value of the MSD. Runs of 500 total evaluations were carried out (corresponding to a total run-time of around 80 CPU hours), using MSD values spanning six orders of magnitude. In Figure 5.3 are shown three examples from this study. Note that when viewing these figures, the surrogate reset points are indicated by a vertical blue line. Due to the use of parallel computing, some objective function evaluations are partially completed at the time of a reset but are not discarded, instead being posted to the graph after the reset line.

In Figure 5.3a, it can be seen that within the 500 evaluation test, no surrogate reset occurred. Two minima are being converged separately and in the final 100 evaluations the minima found are improved on by less than 5kg. This could be considered too low a value of the MSD as this level of accuracy is not required and is spurious in the context of the approximate nature of the calculations within the objective function. Using an MSD value of 10 (shown in Figure 5.3b) causes two surrogate resets to occur. An MSD of 100 (Figure 5.3c) also leads to two resets, although sooner and a third convergence appears to be underway. In Figure 5.4 is shown the fine detail of the objective function evaluations for an MSD of 10 that is not visible in the scale used in Figure 5.3b, shown separately for the two surrogate resets. Similarly, Figure 5.5 shows the fine detail for an MSD of 100 for its two surrogate resets.

The behaviour when using an MSD of 10 appears acceptable, with resets occurring after converging within a few hundred kilograms, which is an acceptable level of accuracy for the overall study. An MSD of 100 would appear to be inadequate, with surrogate resets occurring when there is still significant spread in the previous 50 evaluations of over 1,000kg. Overall it appears that an MSD of 10 is a reasonable value with which to attempt the main study.

It is noticeable that the three runs are not consistent in which minima are explored first. This is an unfortunate feature of the surrogate function algorithm that arises when running in parallel mode. If running only on one computational thread, the optimisation process is fully reproducible. The only deliberate stochastic aspect of the algorithm is the selection of random points at the outset and at each surrogate reset. This can be reproduced by fixing the random number generator method and seed. However, the algorithm decides which point to evaluate next based on the outcomes of previous evaluations. It is therefore sensitive to the timing of the completion of objective function evaluations on different computational threads and is not in general reproducible when running in parallel. Population-based methods such

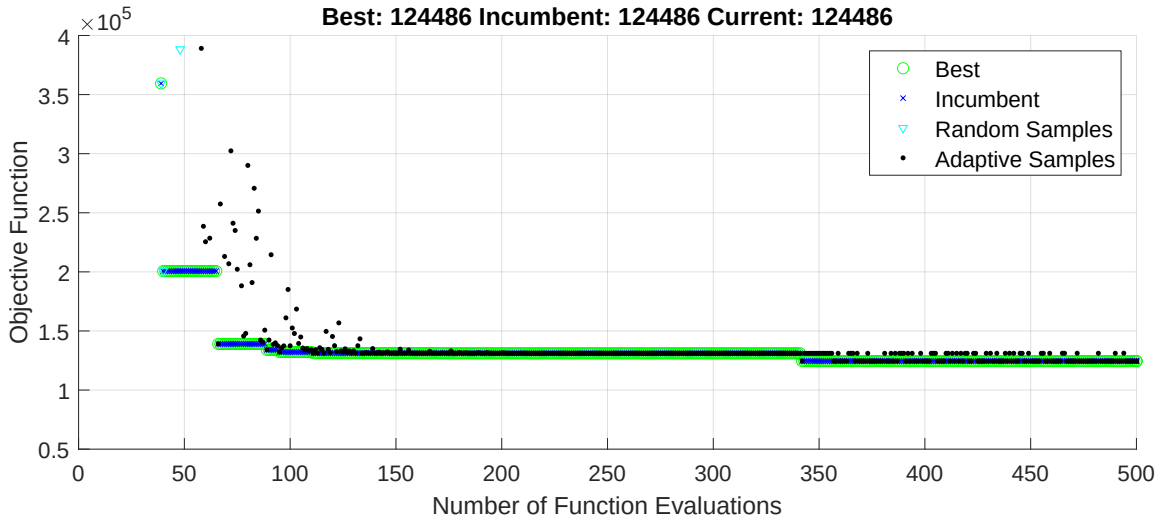

(a) MSD = 1

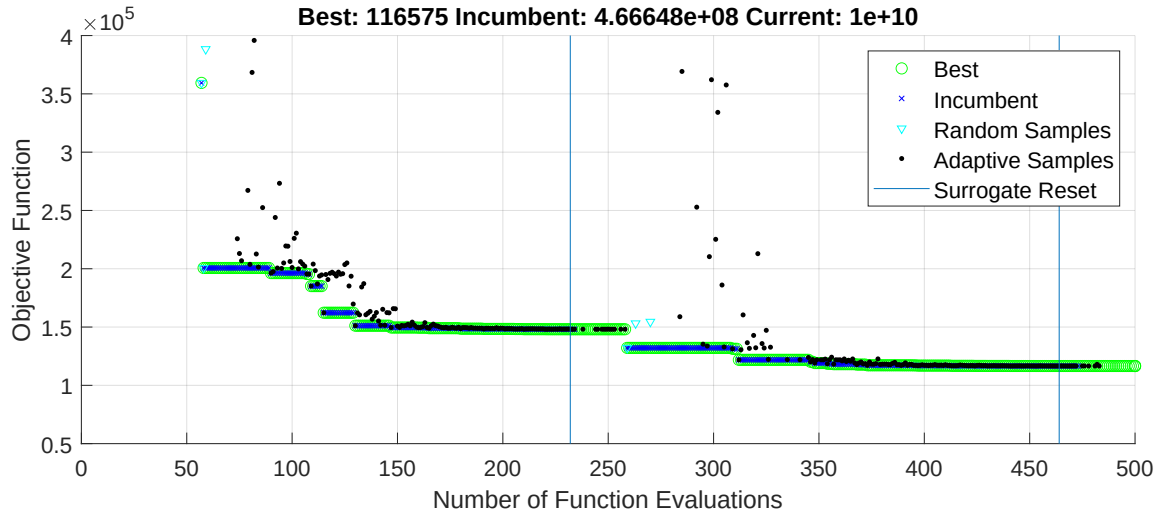

(b) MSD = 10

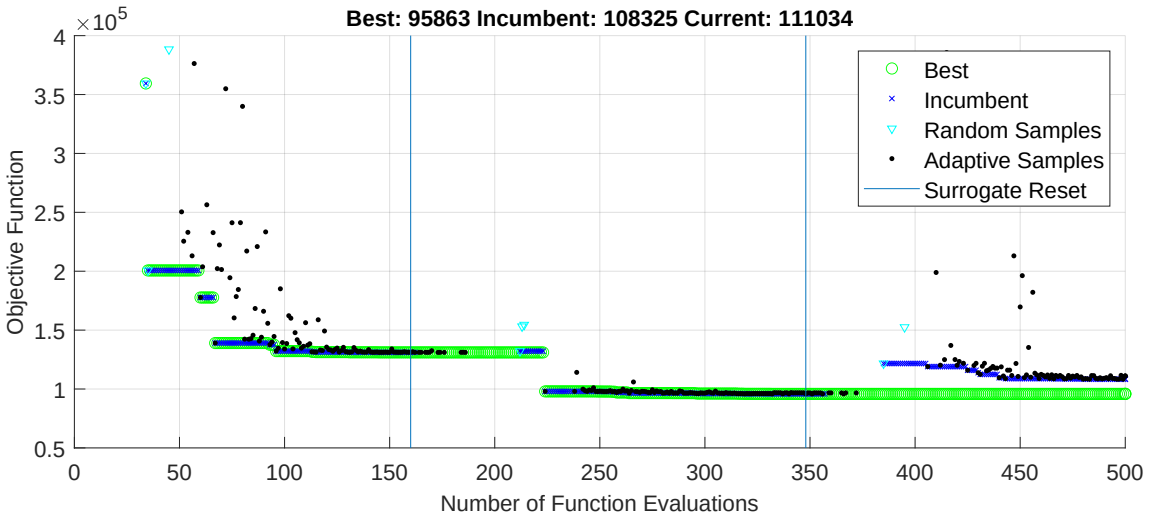

(c) MSD = 100

Fig. 5.3 Behaviour of surrogate function algorithm with different minimum sample distance (MSD)

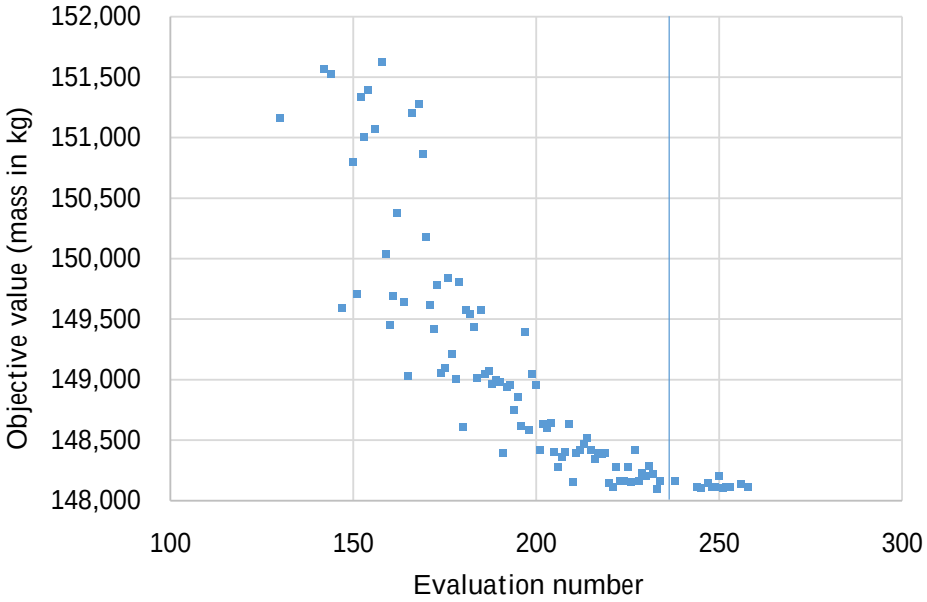

(a) First surrogate reset

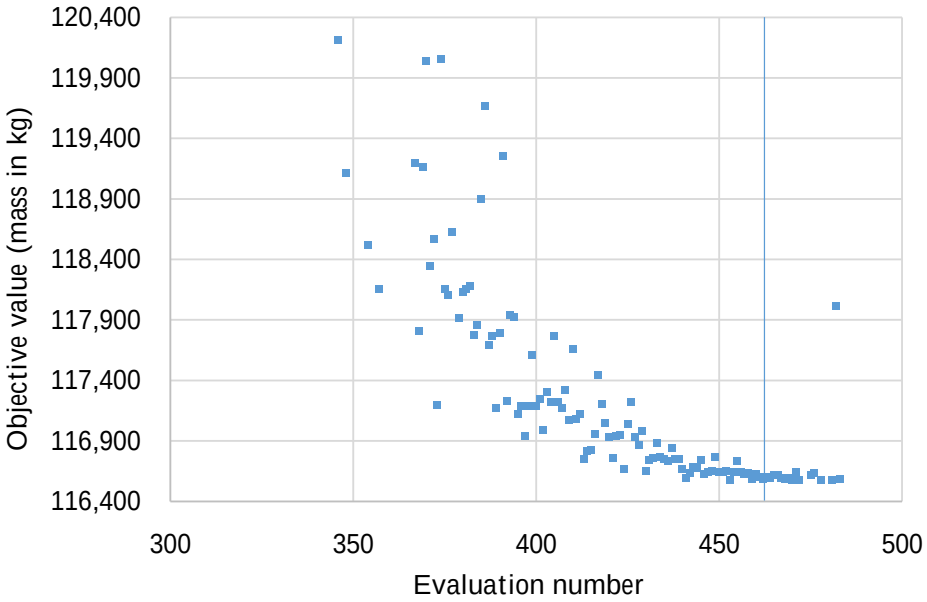

(b) Second surrogate reset

Fig. 5.4 Fine detail of objective function evaluations before surrogate reset with minimum sample distance of 10

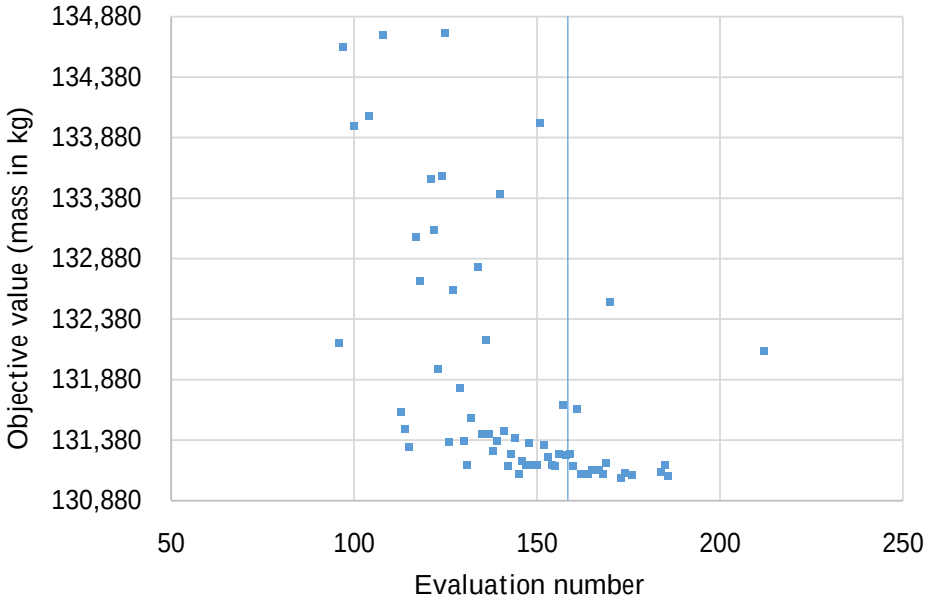

(a) First surrogate reset

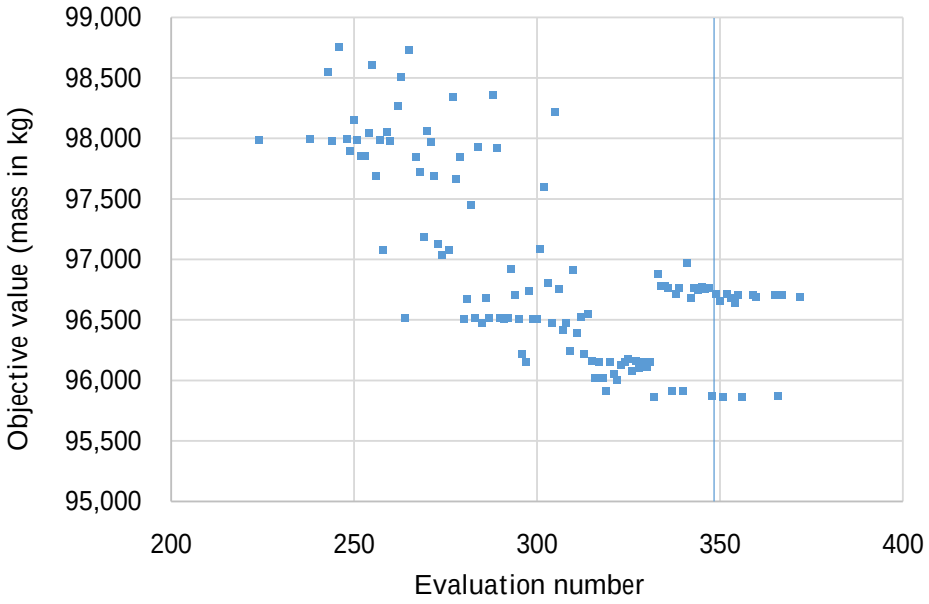

(b) Second surrogate reset

Fig. 5.5 Fine detail of objective function evaluations before surrogate reset with minimum sample distance of 100

as genetic algorithms do not suffer from this behaviour, which is a possible argument in favour of them for this application.

5.5 Defining a search space

The first decision to make is to decide what reactor types will be assessed. Clearly this must involve an LEU design and an HEU design to answer the overall question of what impact this choice has. There is also a reasonable intuition that an LEU design might require a moderator (such as zirconium hydride) to achieve a reasonable core size. However, this intuition should be tested. In particular, if the zirconium hydride is removed or replaced by graphite, the higher core temperatures that will be permissible may well buy sufficient extra thermodynamic efficiency to more than compensate in terms of overall system mass. Therefore, it seems reasonable to assess three broad reactor types: LEU with a ZrH moderator, LEU without a ZrH moderator and HEU without a ZrH moderator. There is another design choice that seems worth investigation, which is the choice of working fluid. As mentioned in Chapter 4, a HeXe mix with a molar mass of 40g/mol is often recommended as a coolant for space Brayton systems, whereas a common choice for terrestrial systems is pure helium. The key difference is that while helium has superior properties in terms of heat removal from the reactor, the addition of xenon allows for a significantly decreased turbomachinery size. It is worthwhile testing whether in every case considered this is a net advantage. Therefore a total of six design types will be considered:

- LEU fuelled with ZrH moderator using helium coolant
- LEU fuelled with ZrH moderator using 40g/mol HeXe coolant
- LEU fuelled without ZrH moderator using helium coolant
- LEU fuelled without ZrH moderator using 40g/mol HeXe coolant
- HEU fuelled without ZrH moderator using helium coolant
- HEU fuelled without ZrH moderator using 40g/mol HeXe coolant

Other core materials were assumed to be constant. For example, a beryllium reflector is assumed in all cases. Next, the design variables must be chosen, bearing in mind that the number of dimensions in the problem will strongly influence the size of the design space. The variables chosen are:

- The width of the annular coolant channel

- The radii of the internal coolant channels, which are assumed to be equal
- The reactor thermal power
- The coolant mass flow rate
- The reactor inlet temperature
- The thickness of moderator around each assembly
- The number of rings of assemblies in the core
- The thickness of the reflectors, both radial and axial

For the cases where the ZrH is not present, there are a number of possible assembly designs. One option would be to eliminate the annular moderator and the annular coolant channel so that fuel blocks are touching one another. The alternative chosen is to retain the same geometry but simply replace the ZrH moderator with graphite. This gives the opportunity to the optimisation code to add more graphite (a relatively weak moderator, but a moderator nonetheless) to the core and could potentially provide interesting results. If the extra graphite is too poor a moderator in such a small core to provide any material benefit then presumably the optimisation code will minimise it to the smallest possible amount.

5.5.1 Other possible variables

There are a number of additional variables that could be included in a future study, even for a fixed set of material choices. In order to allow the optimisation code to more fully control the relative cooling by the annular and internal fuel channels, arbitrary hydraulic resistances could be added to any channel, simulating the addition of an orifice plate or nozzle at the channel inlet. Whilst some control is possible by changing their size, changing the hydraulic diameter of the channels also affects the heat transfer coefficient. Increasing the width of the annular channel also increases the size of the overall assembly and therefore the size of the core. Changing the size of the internal channels changes the amount of fuel in the assembly, therefore affecting the specific power. Allowing flow control that is less coupled to other effects could lead to better designs. At the risk of increasing the design space to an intractable size, the control of the flow pattern could be extended to the entire core. When the assembly design is identical across the core, the flow rates through all assemblies are determined by what the hottest assembly requires. A more efficient use of pumping power is to divert more flow to the hotter regions and less flow to cooler regions.

The aspect ratio of the core could also be allowed to vary. The current 'square' aspect ratio is neutronically favourable, but, from a thermal hydraulic perspective, a flatter core is preferred. The relative sizes of the axial and radial reflectors should also be allowed to vary independently, especially in the case of a highly non-square core aspect ratio.

5.5.2 Variable bounds

Bounds are chosen for each variable, in most cases simply to limit the search space to a sensible region. If it is found that designs are selected that are at any of these limits, a further run of the optimisation algorithm could be considered that considered the previously out of bounds area. Table 5.5 shows the bounds chosen for each variable.

Table 5.5 Bounds chosen for each variable

Variable	Lower bound	Upper bound
Annular coolant channel width (mm)	1	5
Internal coolant channel radius (mm)	5	5
Reactor thermal power (MW)	3	10
Mass flow rate (kg/s)	2.0	30.0
Reactor inlet temperature (K)	400	900 if ZrH moderator, 1400 otherwise
Annular moderator thickness (mm)	0.1	20.0
Number of assembly rings in core	6	25
Reflector thickness (cm)	5	40

5.6 Results

The six core design types described above were all analysed using an approximately equal computational budget of 5,000 objective function evaluations. Strictly speaking, the computational budget should be measured in CPU time. Different design types (such as helium versus HeXe coolant) will not necessarily have a similar calculation time per objective function evaluation on average.

One issue that became clear upon examining these results is that the bounds chosen for the mass flow rate were not appropriate for both pure helium and HeXe mix cases. In particular, for the two unmoderated, helium-cooled cases, the best three designs from each appear to be at or very near the lower bound of 2kg/s. It was decided that the optimisation algorithm should be allowed to explore further below this bound. For each of those two cases, a further run using 2,000 evaluations was carried out within a narrow window of allowable

flow rates, between 0.5 and 2.0 kg/s. The results from the initial and additional runs are shown in Tables 5.6 and 5.7. It was found that in the first case (LEU fuel), the three best designs from the additional run improved slightly on all three designs from the initial run. In the second case (HEU fuel), one of the original top three designs was retained but the other two were superseded by new designs from the additional run.

It can also be seen that in the case of some of the HeXe-cooled designs, the prescribed upper bound of 30kg/s has been reached. An additional significant run that extends much further into higher flow rates would be required to establish whether improved designs exist in this new region of the design space.

For each of the six fuel/moderator/coolant combinations considered, the best three designs are shown in the results tables. Table 5.8 shows, for each of these, the design parameters and the total system mass. The subsequent tables (Tables 5.9-5.14) show more detailed results, including a mass breakdown by component and other outputs of interest. Following the results tables, Figures 5.6 to 5.13 show the progress of the surrogate function algorithm in each case, including the additional runs with modified bounds as described above.

Table 5.6 LEU fuel, no ZrH moderator, helium coolant. Results for initial run and additional run with modified mass flow rate bounds.

Annular coolant width (mm)	Internal coolant channel radius (mm)	Reactor thermal power (MW)	Mass flow rate (kg/s)	Core inlet temp. (K)	Moderator thickness (mm)	Assembly rings	Reflector thickness (cm)	MASS (kg)	Rank
Initial 5,000 evaluation run with mass flow rate between 2.0 and 30.0 kg/s									
2.3	2.3	3.97	2.2	845	12.0	12	15	73,086	4
2.8	2.3	5.41	2.0	757	9.7	12	23	73,134	5
3.9	3.6	5.80	2.0	704	13.1	11	19	73,446	6
Additional 2,000 evaluation run with mass flow rate between 0.5 and 2.0 kg/s									
3.4	2.1	3.55	1.2	742	15.4	10	19	69,837	1
1.4	1.5	6.52	1.6	480	16.5	10	23	72,456	2
2.5	3.3	5.36	1.3	481	10.6	13	19	72,793	3

Table 5.7 HEU fuel, no ZrH moderator, helium coolant. Results for initial run and additional run with modified mass flow rate bounds.

Annular coolant width (mm)	Internal coolant channel radius (mm)	Reactor thermal power (MW)	Mass flow rate (kg/s)	Core inlet temp. (K)	Moderator thickness (mm)	Assembly rings	Reflector thickness (cm)	MASS (kg)	Rank
Initial 5,000 evaluation run with mass flow rate between 2.0 and 30.0 kg/s									
2.3	2.2	3.73	2.0	875	11.8	7	16	63,944	3
3.0	3.6	3.50	2.0	884	0.7	10	24	64,934	4
2.7	2.8	5.18	2.0	698	8.8	9	10	67,417	6
Additional 2,000 evaluation run with mass flow rate between 0.5 and 2.0 kg/s									
2.3	2.2	3.12	1.8	968	2.8	9	8	59,606	1
1.4	4.1	3.65	2.0	911	0.1	13	10	62,712	2
4.1	1.6	3.01	1.3	847	0.6	14	17	65,807	5

Table 5.8 Summary of results for all six design types. Best three distinct designs shown in each case.

Annular coolant width (mm)	Internal coolant channel radius (mm)	Reactor thermal power (MW)	Mass flow rate (kg/s)	Core inlet temp. (K)	Moderator thickness (mm)	Assembly rings	Reflector thickness (cm)	MASS (kg)
LEU fuel, ZrH moderator, HeXe coolant								
1.1	1.9	5.14	29.4	654	0.1	17	22	34,572
2.1	2.2	3.18	30.0	680	2.5	11	10	38,253
5.0	4.9	4.50	25.8	618	0.1	14	34	40,045
LEU fuel, ZrH moderator, He coolant								
4.8	4.3	3.80	5.2	739	1.8	10	40	92,575
2.6	2.7	6.03	7.0	727	1.5	13	11	94,161
1.0	1.5	6.48	3.8	551	3.3	9	21	95,284
LEU fuel, no ZrH moderator, HeXe coolant								
2.1	1.5	3.31	20.0	943	0.6	13	30	20,026
3.2	4.0	3.88	26.7	987	15.9	9	20	20,026
3.1	1.5	3.15	14.6	888	9.3	13	16	23,593
LEU fuel, no ZrH moderator, He coolant								
3.4	2.1	3.55	1.2	742	15.4	10	19	69,837
1.4	1.5	6.52	1.6	480	16.5	10	23	72,456
2.5	3.3	5.36	1.3	481	10.6	13	19	72,793
HEU fuel, no ZrH moderator, HeXe coolant								
2.2	1.7	3.72	23.6	999	5.8	9	7	13,417
2.3	4.7	4.59	29.7	984	0.3	11	11	14,018
2.9	1.6	3.34	18.3	921	0.1	10	16	14,612
HEU fuel, no ZrH moderator, He coolant								
2.3	2.2	3.12	1.8	968	2.8	9	8	59,606
1.4	4.1	3.65	2.0	911	0.1	13	10	62,712
2.3	2.2	3.73	2.0	875	11.8	7	16	63,944

Table 5.9 Detailed results for LEU fuel, ZrH moderator, HeXe coolant case. Best three distinct designs.

Annular coolant width (mm)	Internal coolant channel radius (mm)	Reactor thermal power (MW)	Mass flow rate (kg/s)	Core inlet temp. (K)	Moderator thickness (mm)	Assembly rings	Reflector thickness (cm)	MASS (kg)
1.1	1.9	5.14	29.4	654	0.1	17	22	34,572
2.1	2.2	3.18	30.0	680	2.5	11	10	38,253
5.0	4.9	4.50	25.8	618	0.1	14	34	40,045

Mass breakdown (kg)

Fuel	Moderator	Reflector	Vessel	Reactor total	Turboset	PMAD	Recuperator	Radiator	Conversion total
3,870	99	5,108	1,213	10,290	2,248	3,400	70	18,563	24,281
1,247	907	1,147	407	3,708	2,081	3,400	1,562	27,502	34,546
1,699	79	8,596	1,569	11,945	2,179	3,400	69	22,452	28,099

Other outputs

Recuperator effectiveness	Compressor pressure ratio	Max kernel temp. (K)	Max moderator temp. (K)	Core outlet temp. (K)	Core pressure loss (kPa)	Initial k_{eff}	EOL k_{eff}
61%	2.44	1,018	978	987	13.24	1.076	1.022
98%	2.24	1,018	979	882	11.87	1.282	1.193
64%	2.65	1,039	973	950	0.21	1.133	1.023

Table 5.10 Detailed results for LEU fuel, ZrH moderator, He coolant case. Best three distinct designs.

Annular coolant width (mm)	Internal coolant channel radius (mm)	Reactor thermal power (MW)	Mass flow rate (kg/s)	Core inlet temp. (K)	Moderator thickness (mm)	Assembly rings	Reflector thickness (cm)	MASS (kg)
4.8	4.3	3.80	5.2	739	1.8	10	40	92,575
2.6	2.7	6.03	7.0	727	1.5	13	11	94,161
1.0	1.5	6.48	3.8	551	3.3	9	21	95,284

Mass breakdown (kg)

Fuel	Moderator	Reflector	Vessel	Reactor total	Turboset	PMAD	Recuperator	Radiator	Conversion total
792	598	7,528	1,094	10,012	59,345	3,400	1,421	18,397	82,563
1,888	869	1,718	617	5,092	64,794	3,400	463	20,412	89,069
725	641	2,170	399	3,936	60,297	3,400	50	27,601	91,348

Other outputs

Recuperator effectiveness	Compressor pressure ratio	Max kernel temp. (K)	Max moderator temp. (K)	Core outlet temp. (K)	Core pressure loss (kPa)	Initial k_{eff}	EOL k_{eff}
96%	1.69	1,048	957	879	0.43	1.352	1.209
85%	1.61	1,026	974	893	2.20	1.219	1.104
45%	2.12	1,131	974	880	27.92	1.373	1.123

Table 5.11 Detailed results for LEU fuel, no ZrH moderator, HeXe coolant case. Best three distinct designs.

Annular coolant width (mm)	Internal coolant channel radius (mm)	Reactor thermal power (MW)	Mass flow rate (kg/s)	Core inlet temp. (K)	Moderator thickness (mm)	Assembly rings	Reflector thickness (cm)	MASS (kg)
2.1	1.5	3.31	20.0	943	0.6	13	30	20,026
3.2	4.0	3.88	26.7	987	15.9	9	20	20,026
3.1	1.5	3.15	14.6	888	9.3	13	16	23,593

Mass breakdown (kg)

Fuel	Moderator	Reflector	Vessel	Reactor total	Turboset	PMAD	Recuperator	Radiator	Conversion total
1,934	89	5,471	972	8,466	2,064	3,400	336	5,759	11,560
903	2,069	4,521	1,155	8,648	2,177	3,400	386	5,416	11,379
2,783	2,566	4,689	1,561	11,599	2,002	3,400	134	6,458	11,994

Other outputs

Recuperator effectiveness	Compressor pressure ratio	Max kernel temp. (K)	Max moderator temp. (K)	Core outlet temp. (K)	Core pressure loss (kPa)	Initial k_{eff}	EOL k_{eff}
93%	2.29	1,315	1,253	1,258	5.97	1.082	1.003
93%	2.02	1,392	1,334	1,264	5.48	1.159	1.013
87%	2.82	1,412	1,382	1,300	1.63	1.062	1.012

Table 5.12 Detailed results for LEU fuel, no ZrH moderator, He coolant case. Best three distinct designs.

Annular coolant width (mm)	Internal coolant channel radius (mm)	Reactor thermal power (MW)	Mass flow rate (kg/s)	Core inlet temp. (K)	Moderator thickness (mm)	Assembly rings	Reflector thickness (cm)	MASS (kg)
3.4	2.1	3.55	1.2	742	15.4	10	19	69,837
1.4	1.5	6.52	1.6	480	16.5	10	23	72,456
2.5	3.3	5.36	1.3	481	10.6	13	19	72,793

Mass breakdown (kg)

Fuel	Moderator	Reflector	Vessel	Reactor total	Turboset	PMAD	Recuperator	Radiator	Conversion total
1,514	2,663	5,004	1,405	10,586	46,422	3,400	28	9,401	59,251
1,531	2,679	6,121	1,485	11,816	47,783	3,400	0	9,458	60,641
2,448	2,970	5,928	1,769	13,115	46,912	3,400	0	9,366	59,678

Other outputs

Recuperator effectiveness	Compressor pressure ratio	Max kernel temp. (K)	Max moderator temp. (K)	Core outlet temp. (K)	Core pressure loss (kPa)	Initial k_{eff}	EOL k_{eff}
56%	2.53	1,520	1,469	1,300	0.25	1.160	1.064
0%	2.08	1,473	1,383	1,270	3.91	1.195	1.036
0%	2.41	1,482	1,443	1,287	0.12	1.115	1.023

Table 5.13 Detailed results for HEU fuel, no ZrH moderator, HeXe coolant case. Best three distinct designs.

Annular coolant width (mm)	Internal coolant channel radius (mm)	Reactor thermal power (MW)	Mass flow rate (kg/s)	Core inlet temp. (K)	Moderator thickness (mm)	Assembly rings	Reflector thickness (cm)	MASS (kg)
2.2	1.7	3.72	23.6	999	5.8	9	7	13,417
2.3	4.7	4.59	29.7	984	0.3	11	11	14,018
2.9	1.6	3.34	18.3	921	0.1	10	16	14,612

Mass breakdown (kg)

Fuel	Moderator	Reflector	Vessel	Reactor total	Turboset	PMAD	Recuperator	Radiator	Conversion total
835	436	689	307	2,268	2,146	3,400	345	5,258	11,150
808	29	1,176	352	2,365	2,278	3,400	265	5,709	11,653
925	11	1,621	362	2,919	2,063	3,400	233	5,998	11,694

Other outputs

Recuperator effectiveness	Compressor pressure ratio	Max kernel temp. (K)	Max moderator temp. (K)	Core outlet temp. (K)	Core pressure loss (kPa)	Initial k_{eff}	EOL k_{eff}
93%	2.12	1,508	1,449	1,300	25.22	1.118	1.083
88%	2.01	1,428	1,372	1,278	2.56	1.104	1.061
91%	2.46	1,497	1,389	1,269	4.47	1.317	1.282

Table 5.14 Detailed results for HEU fuel, no ZrH moderator, He coolant case. Best three distinct designs.

Annular coolant width (mm)	Internal coolant channel radius (mm)	Reactor thermal power (MW)	Mass flow rate (kg/s)	Core inlet temp. (K)	Moderator thickness (mm)	Assembly rings	Reflector thickness (cm)	MASS (kg)
2.3	2.2	3.12	1.8	968	2.8	9	8	59,606
1.4	4.1	3.65	2.0	911	0.1	13	10	62,712
2.3	2.2	3.73	2.0	875	11.8	7	16	63,944

Mass breakdown (kg)

Fuel	Moderator	Reflector	Vessel	Reactor total	Turboset	PMAD	Recuperator	Radiator	Conversion total
722	178	651	241	1,792	46,965	3,400	129	7,320	57,815
1,414	14	1,236	439	3,104	47,859	3,400	97	8,252	59,608
480	594	1,793	414	3,282	48,387	3,400	89	8,787	60,662

Other outputs

Recuperator effectiveness	Compressor pressure ratio	Max kernel temp. (K)	Max moderator temp. (K)	Core outlet temp. (K)	Core pressure loss (kPa)	Initial k_{eff}	EOL k_{eff}
84%	1.88	1,508	1,449	1,296	1.33	1.086	1.056
78%	1.85	1,446	1,427	1,263	0.25	1.209	1.190
76%	1.90	1,513	1,360	1,234	3.67	1.272	1.192

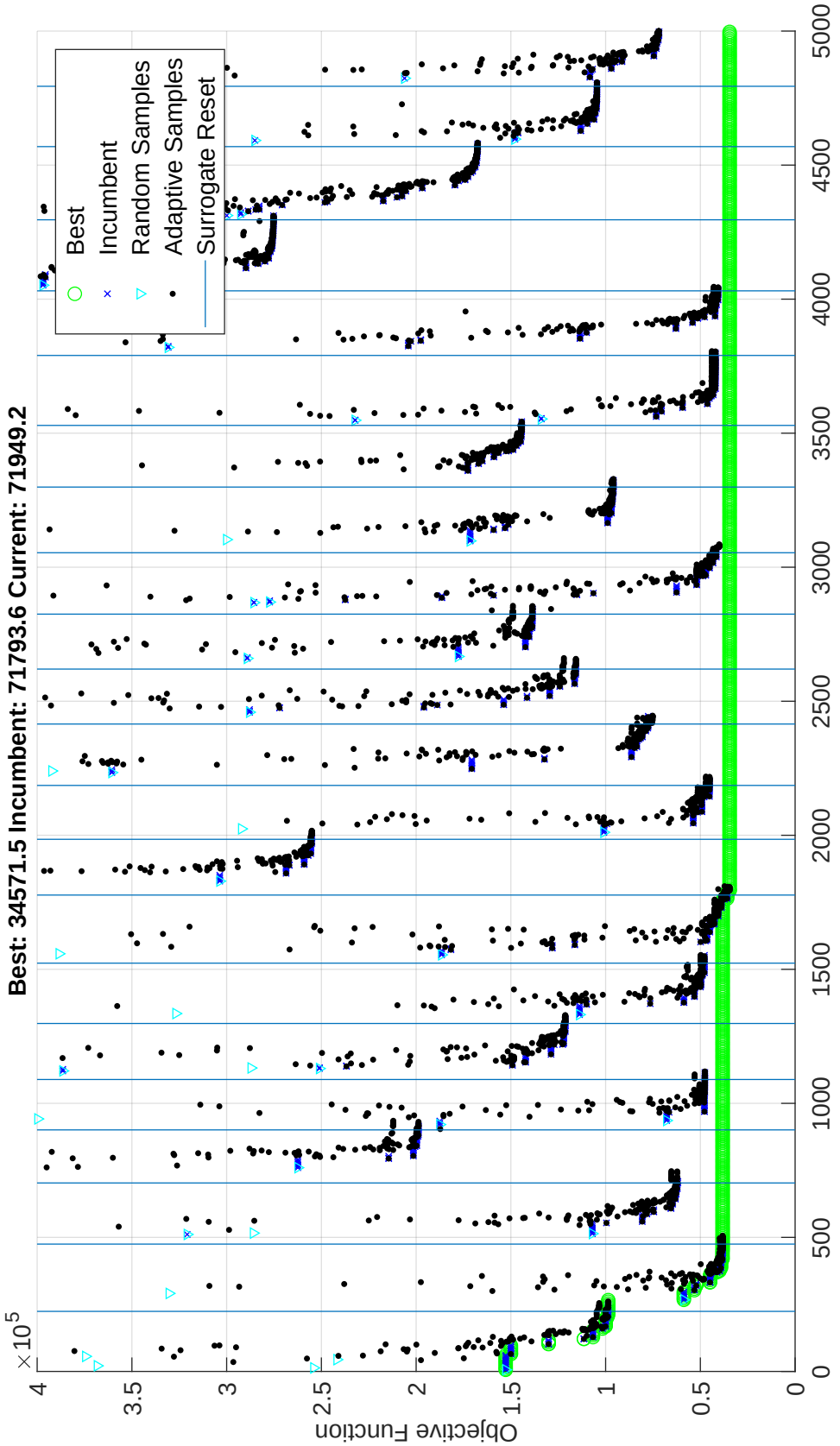

Fig. 5.6 Optimisation results for LEU fuel, ZrH moderator, HeXe coolant case.

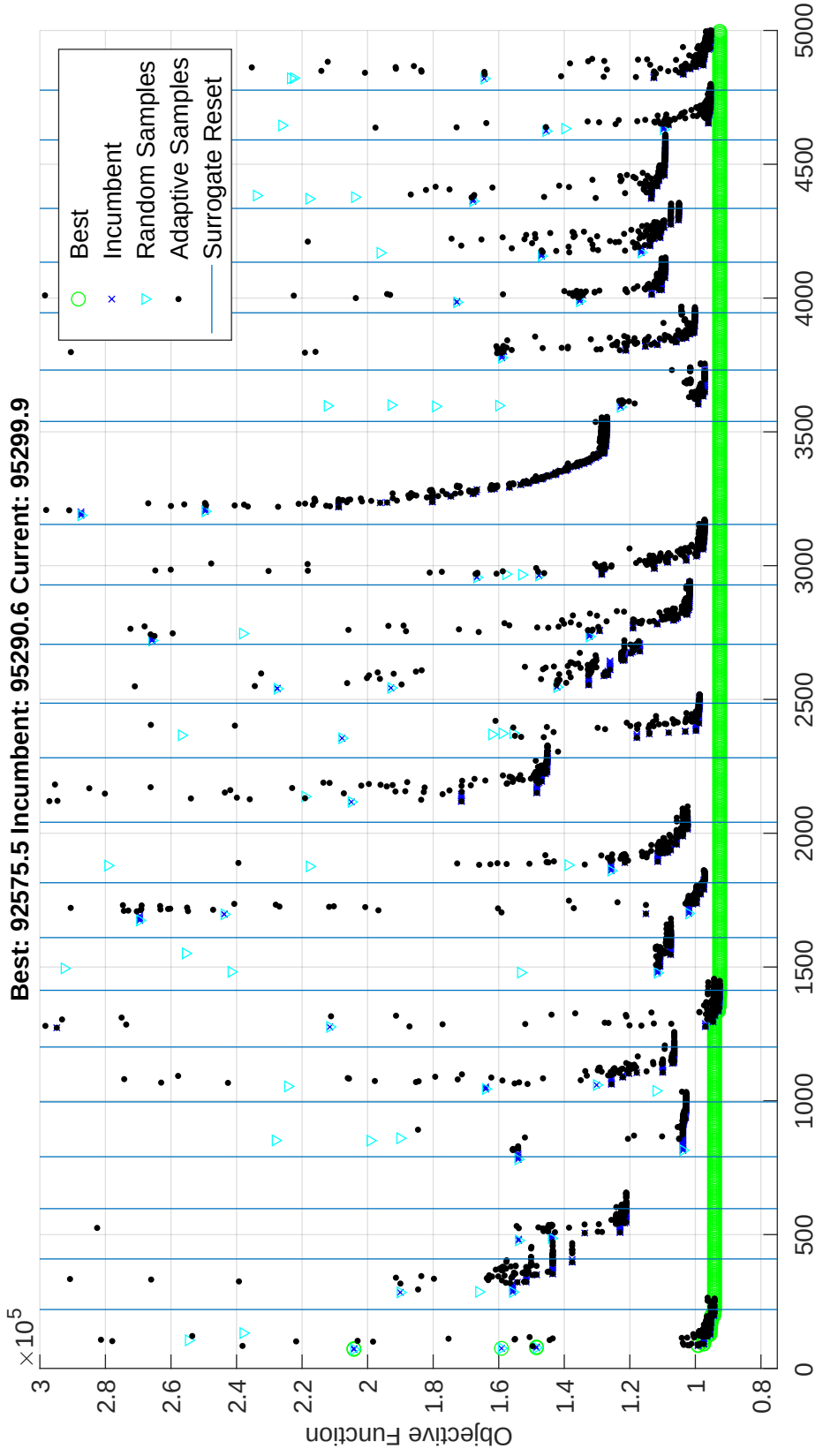

Fig. 5.7 Optimisation results for LEU fuel, ZrH moderator, He coolant case.

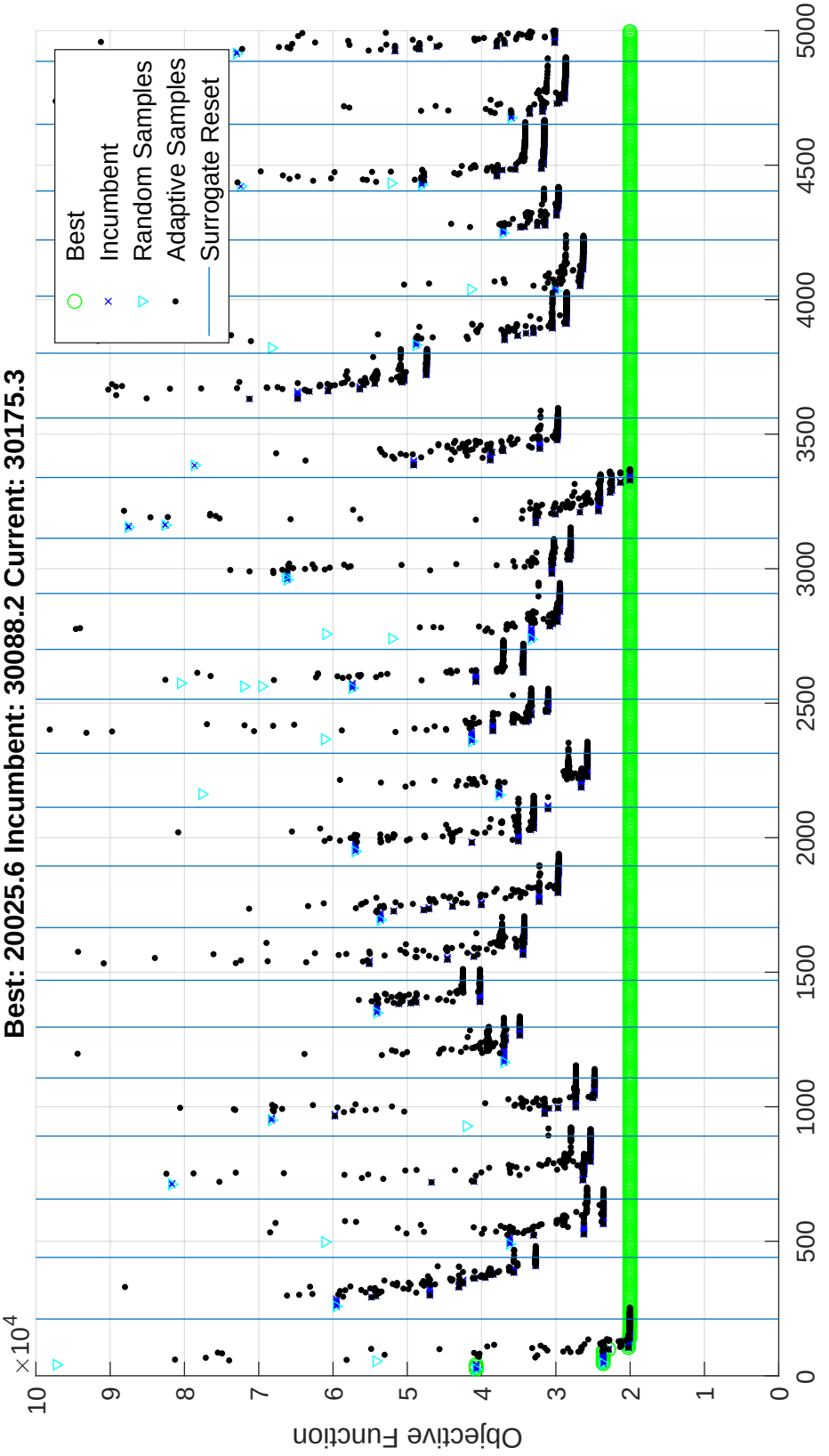

Fig. 5.8 Optimisation results for LEU fuel, no ZrH moderator, HeXe coolant case.

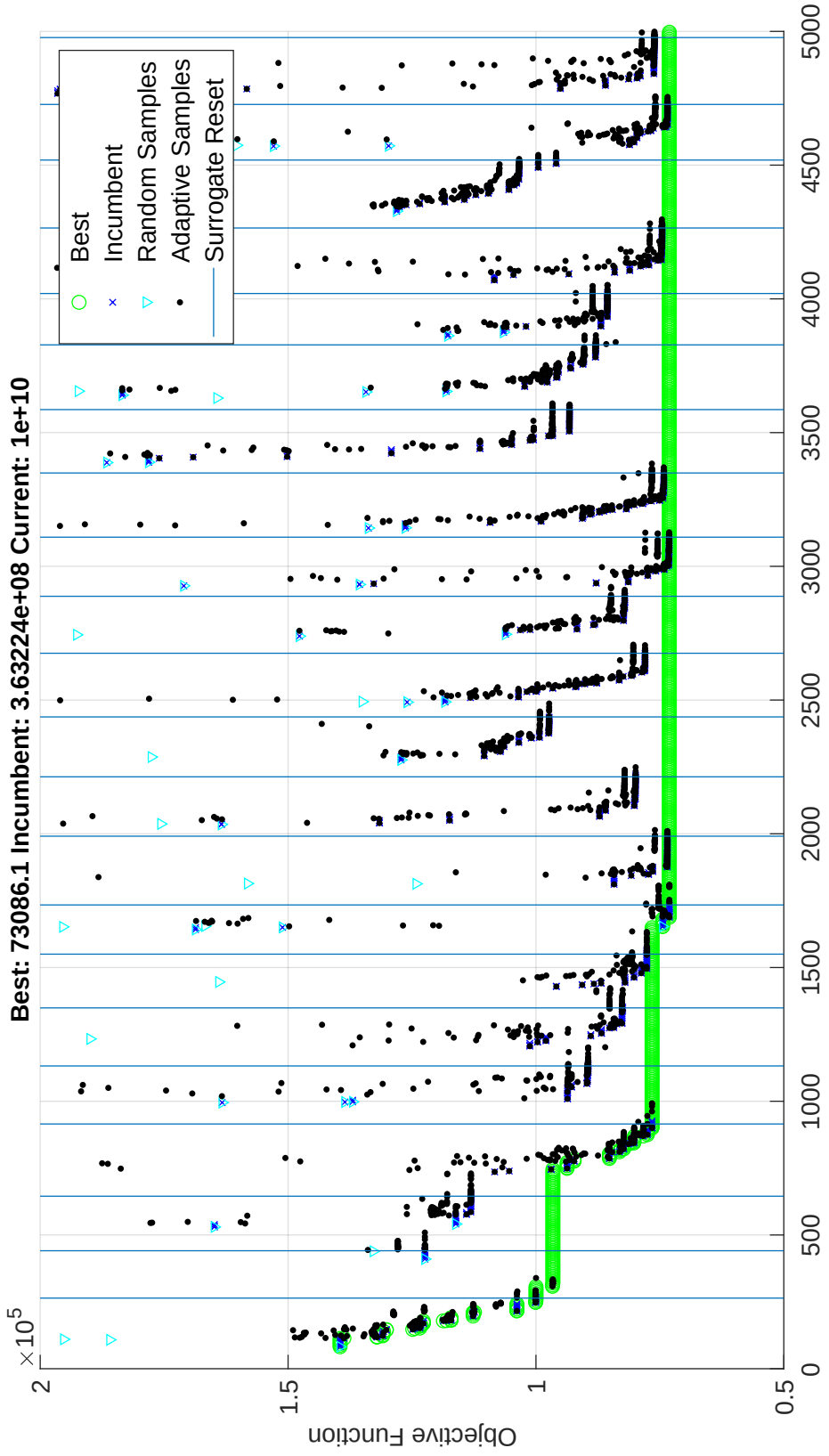

Fig. 5.9 Initial optimisation results for LEU fuel, no ZrH moderator, He coolant case.

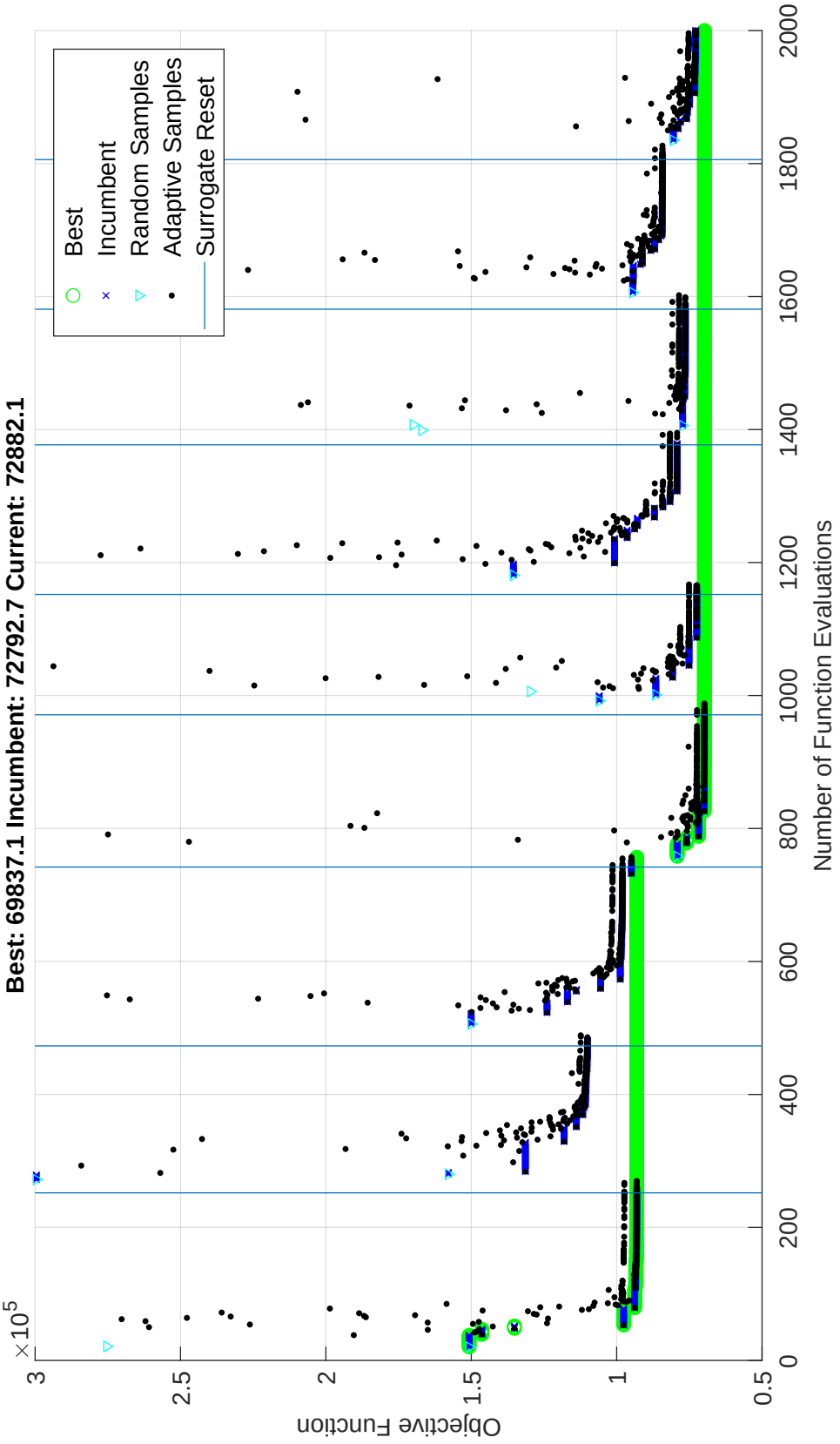

Fig. 5.10 Additional optimisation results for LEU fuel, no ZrH moderator, He coolant case with new bounds.

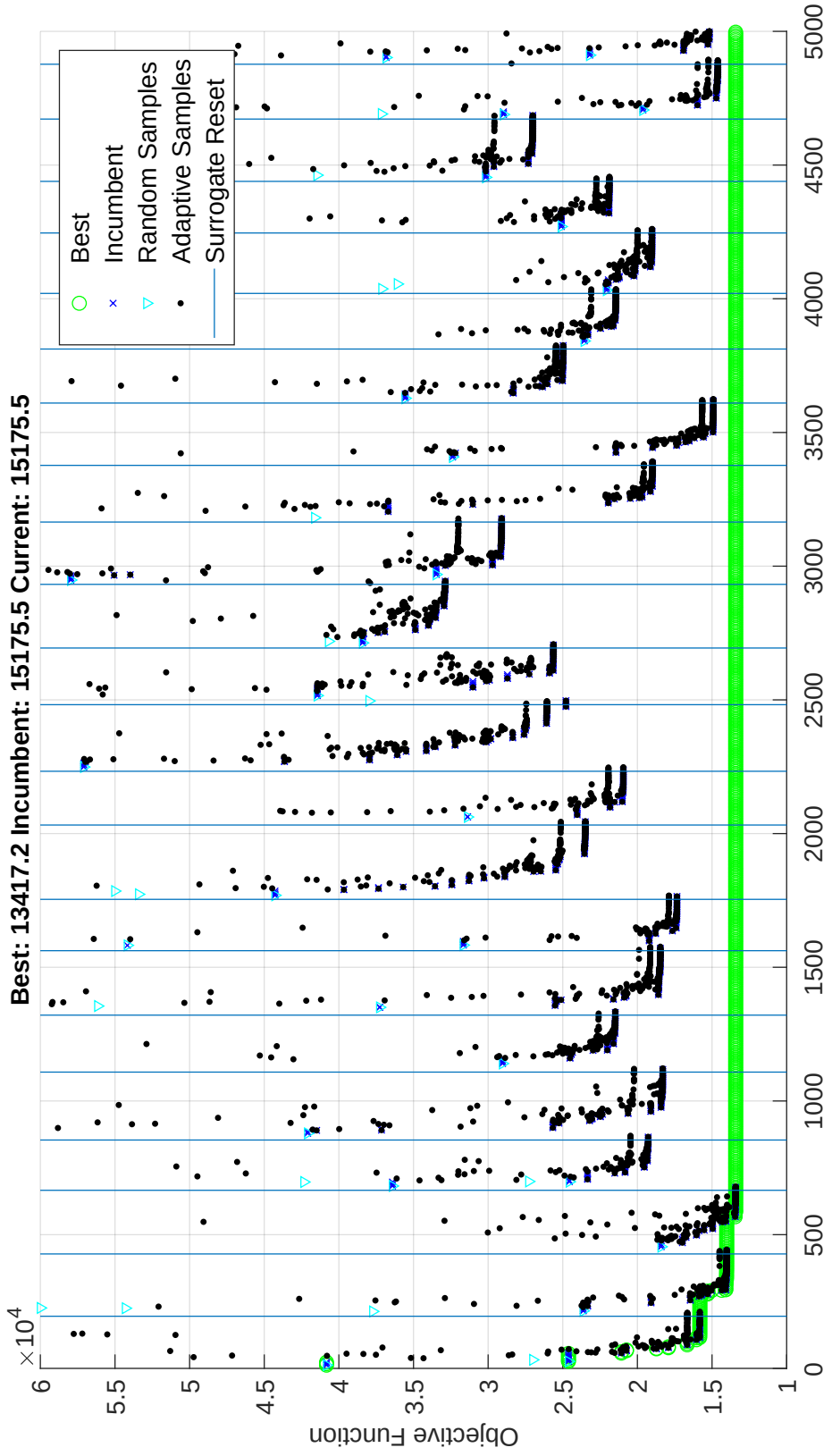

Fig. 5.11 Optimisation results for HEU fuel, no ZrH moderator, HeXe coolant case.

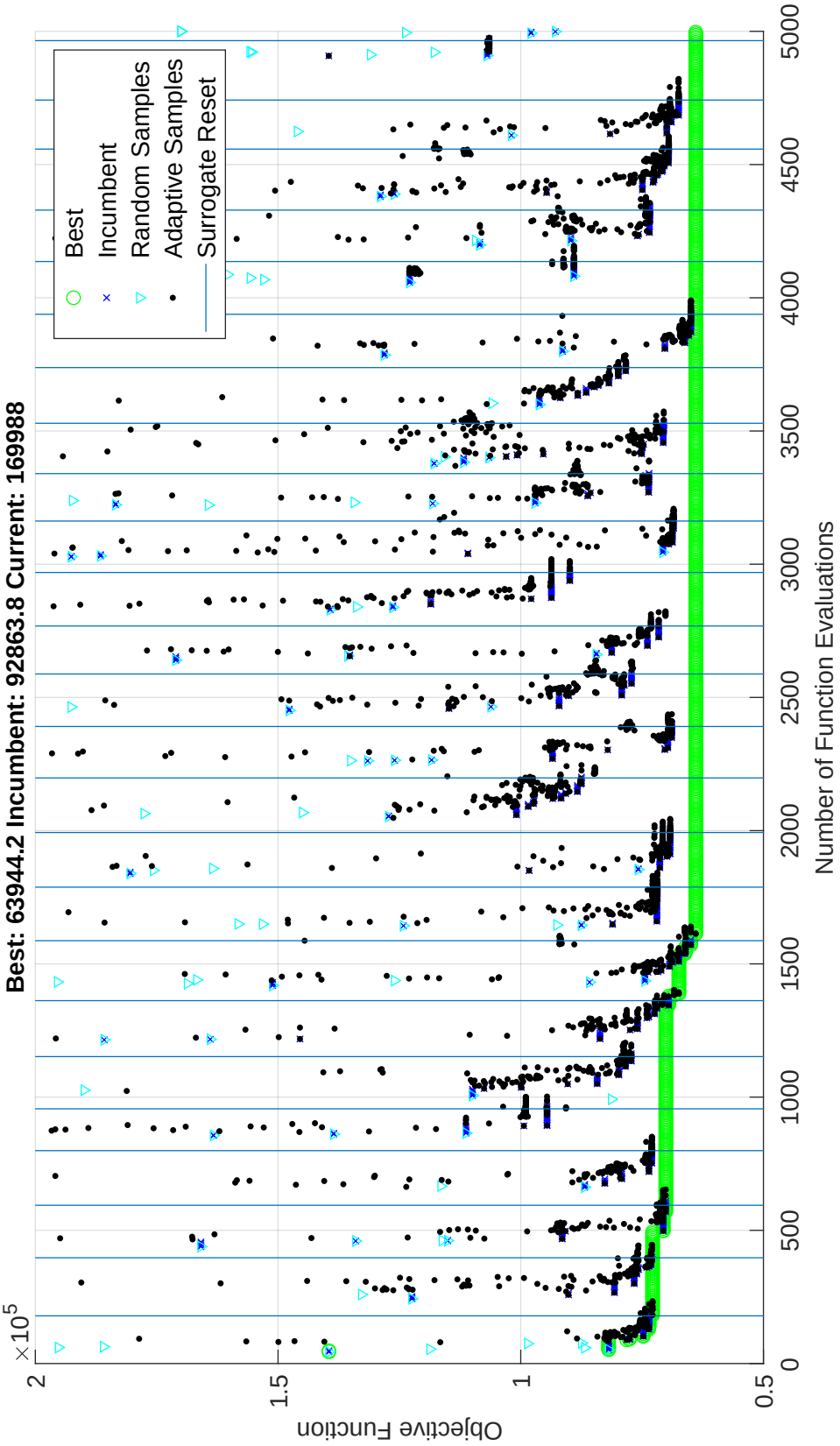

Fig. 5.12 Initial optimisation results for HEU fuel, no ZrH moderator, He coolant case.

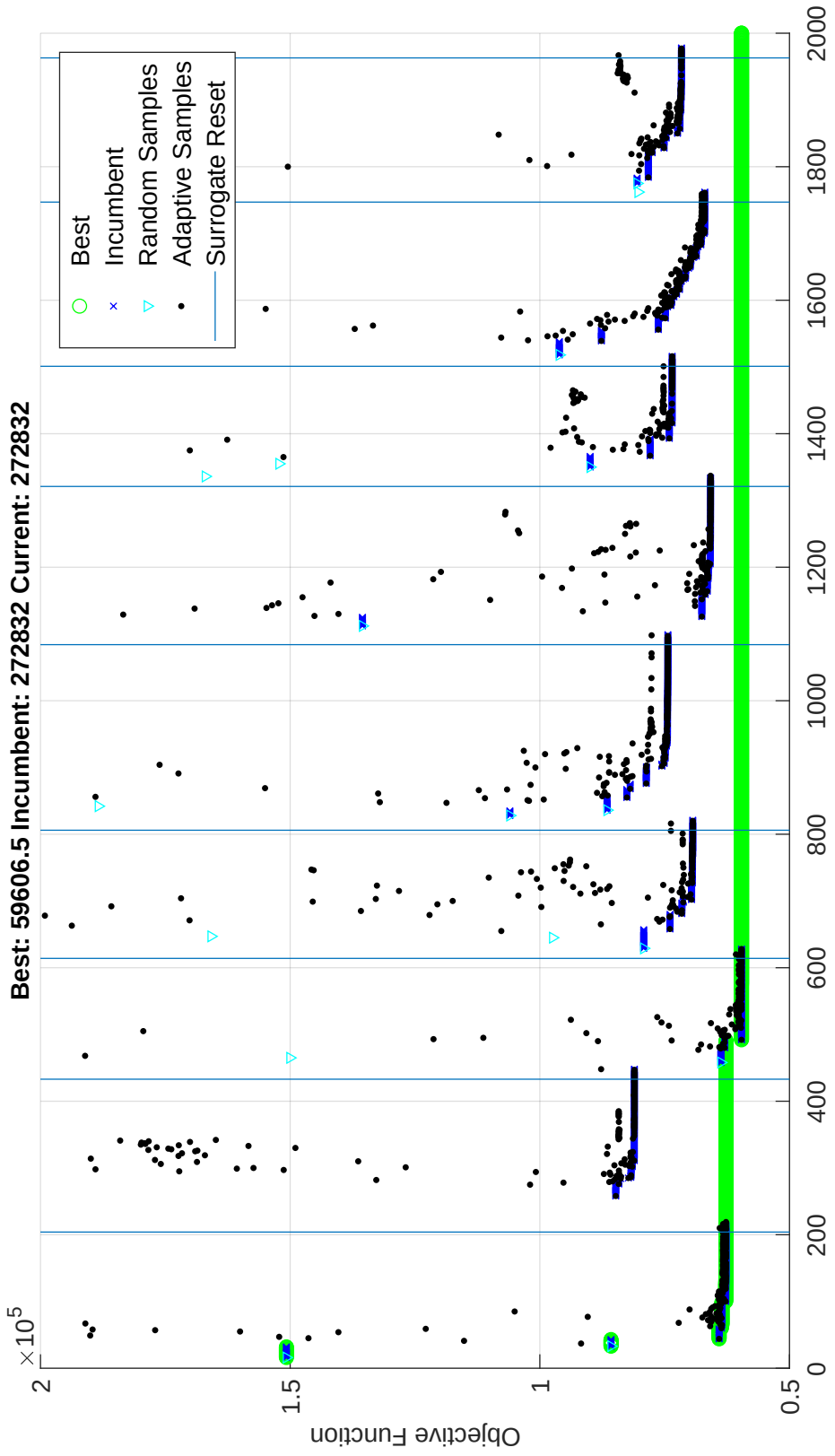

Fig. 5.13 Additional optimisation results for HEU fuel, no ZrH moderator, He coolant case with new bounds.

5.6.1 Design verification

A number of simplifications to the core modelling were adopted in order to accelerate the optimisation process. These were not expected to lead to an unacceptable loss of fidelity, as explained in Section 5.3, based on the results from an example core. In principle, however, some core designs might suffer a greater loss of fidelity than others when using these simplified models. As a reminder, the simplifications adopted were:

- Use of the 'quick' rather than 'main' neutronics analysis method.
- Use of only a single iteration of the neutronic-thermal hydraulic coupling, rather than iterating until temperatures converge.
- Restricting the thermal hydraulic analysis to the central (and assumed to be hottest) assembly.

Each of these simplifications can be removed, at the cost of a greater computation time. The three best designs presented in the results tables are therefore reassessed to check if they still satisfy the specified constraints when using higher fidelity methods. Before proceeding it should be noted that the 'main' neutronics route has the drawback that the temperature distribution and burnup are assumed to uniform in the axial direction, unlike in the quick route. It may be possible to extend the main route so that multiple core slices are analysed, enabling such axial variation, but this was not pursued. One cannot say, a priori, whether the higher fidelity neutronics or a more detailed temperature distribution is more important. Therefore, the verification exercise is carried out using both the quick and main neutronics methods, but in both cases applying full-core thermal hydraulics and with converged thermal hydraulic-neutronic coupling. If a design is still within the allowed temperature and end-of-life reactivity constraints on both measures (or with a minor breach) it is considered valid. The results of the verification exercise are shown in Table 5.15. Designs are referred to as Designs 1, 2 and 3, where relevant, based on their position in the main results tables. It can be seen that the errors in end-of-life k_{eff} arising from the use of 'quick route' neutronics are relatively small across the best designs, in line with expectations.

By far the most important simplification of the three used was found to be the restriction of thermal hydraulic analysis to the central assembly. The assumption underlying this simplification was that the peak power, and therefore temperatures, would be found in the central assembly. In fact, this simplification creates a weakness which can be exploited by the optimisation algorithm: it is possible to create reactor designs in which the highest power assemblies are actually in the outermost ring. Here, any breaches of the fuel kernel and moderator temperature limits go unnoticed. This phenomenon will be referred to as core edge

peaking (CEP). The most egregious examples of this can be found in the LEU-ZrH-HeXe class. Designs 1 and 3 both have the unexpected feature of using the smallest allowable amount of ZrH moderator (0.1mm). This seems odd because minimising the amount of moderator does nothing to remove its restrictive temperature limits, but does remove its beneficial neutronic effect. The CEP problem explains this. By minimising the amount of moderator and significantly increasing the size of the (moderating beryllium) reflector, as much as 15% of the total core power can be moved to the outer ring and extremely high core temperatures go unacknowledged. Fortunately, while designs which exploit this modelling simplification are competitive, they are not chosen exclusively. The second best design, Design 2, has a more 'expected' design, making use of the ZrH moderator and has its core power peak in the centre. A small temperature breach of 12K is found, but this is acceptable in this context. Of the three best designs in this class, Designs 1 and 3 must unfortunately be discarded.

The use of a moderating reflector might be expected to induce CEP, particularly in designs where there is relatively little moderation in the core interior. At such interfaces, where there is a sharp change in the neutron energy spectrum, this power peak can be very high but occurring in a fairly thin region. If such a design were to be pursued, an obvious remedy is to reduce the uranium enrichment in the outer ring, reducing the power there and allowing more thermal neutrons to pass from the reflector to the core interior. In many designs that exhibited CEP, it was found that such a modification could remove the CEP and bring the maximum temperatures within the specified limits, without significantly affecting end-of-life k_{eff}. For LEU-fuelled designs an enrichment of 10% or 15% was used in the outer ring, and in the case of HEU-fuelled designs, 45% or 50% enrichment. The designs for which such a remedy was found to be effective are indicated in Table 5.15. Fortunately, with the exception of the LEU-noZrH-He class, there is at least one valid design in each class so that some comparisons can be made between them.

5.6.2 Observations

The first very clear observation which can be made from the summary results in Table 5.8 is that helium is the inferior choice of working fluid for all three fuel/moderator options. In all cases, the helium-based designs are at least double the mass of their HeXe-based counterparts, being driven by the large increases in turbomachinery mass. The received wisdom that HeXe is the preferred working fluid for a space Brayton system would therefore seem to apply to the designs considered.

Next, the results shown seem to imply that for the types of system considered, a zirconium hydride moderator is not actually superior to simply using graphite. The initial presumption

Table 5.15 Summary of verification exercise results. Full-core thermal hydraulics and thermal hydraulic-neutronic coupling used in all cases. Colour-coding captures the outcome of the verification exercise. Green indicates a valid design. Amber indicates a design exhibiting mild core edge peaking (CEP) that can be remedied with an outer-ring enrichment modification. Red indicates designs that must be discarded.

	Max kernel temp. (K)	**Max moderator temp. (K)**	**EOL k_{eff}**	**Max kernel temp. (K)**	**Max moderator temp. (K)**	**EOL k_{eff}**	**Max kernel temp. (K)**	**Max moderator temp. (K)**	**EOL k_{eff}**
	LEU, ZrH moderator, HeXe coolant								
	Design 1 (mass = 34,572kg)			Design 2 (mass = 38,253kg)			Design 3 (mass = 40,045kg)		
Optimiser result	1,018	978	1.022	1,018	979	1.193	1,039	973	1.023
'Quick' neutronics	1,520	1,487	1.041	1,026	987	1.213	1,637	1,567	1.038
'Main' neutronics	1,470	1,439	1.035	1,033	995	1.228	1,616	1,547	1.032
	Severe CEP, discard			Minor temperature breach			Severe CEP, discard		
	LEU, ZrH moderator, He coolant								
	Design 1 (mass = 92,575kg)			Design 2 (mass = 94,161kg)			Design 3 (mass = 95,284kg)		
Optimiser result	1,048	957	1.209	1,026	974	1.104	1,131	975	1.123
'Quick' neutronics	1,109	1,019	1.226	1,029	978	1.124	1,135	983	1.145
'Main' neutronics	1,101	1,012	1.228	1,036	985	1.138	1,147	993	1.150
	Minor CEP, can fix with enrich			Minor temperature breach			Minor temperature breach		
	LEU, no ZrH moderator, HeXe coolant								
	Design 1 (mass = 20,026kg)			Design 2 (mass = 20,026kg)			Design 3 (mass = 23,593kg)		
Optimiser result	1,315	1,253	1.003	1,392	1,334	1.013	1,412	1,382	1.012
'Quick' neutronics	1,808	1,749	1.007	1,438	1,394	1.016	1,592	1,517	1.020
'Main' neutronics	1,777	1,720	1.001	1,424	1,382	1.020	1,548	1,527	1.024
	Minor CEP, can fix with enrich			Minor CEP but within limits			Minor CEP, can fix with enrich		
	LEU, no ZrH moderator, He coolant								
	Design 1 (mass = 69,837kg)			Design 2 (mass = 72,456kg)			Design 3 (mass = 72,793kg)		
Optimiser result	1,520	1,469	1.064	1,473	1,383	1.036	1,482	1,443	1.023
'Quick' neutronics	1,648	1,612	1.074	1,830	1,776	1.061	2,106	2,086	1.048
'Main' neutronics	1,604	1,569	1.075	1,729	1,672	1.057	1,964	1,942	1.043
	Severe CEP, discard			Severe CEP, discard			Severe CEP, discard		
	HEU, no ZrH moderator, HeXe coolant								
	Design 1 (mass = 13,417kg)			Design 2 (mass = 14,018kg)			Design 3 (mass = 14,612kg)		
Optimiser result	1,508	1,448	1.083	1,428	1,372	1.061	1,497	1,389	1.282
'Quick' neutronics	1,522	1,463	1.083	1,557	1,510	1.061	1,722	1,623	1.282
'Main' neutronics	1,535	1,477	1.118	1,478	1,460	1.231	1,565	1,441	1.204
	Minor temperature breach			Minor CEP, can fix with enrich			Severe CEP, discard		
	HEU, no ZrH moderator, He coolant								
	Design 1 (mass = 59,606kg)			Design 2 (mass = 62,712kg)			Design 3 (mass = 63,944kg)		
Optimiser result	1,508	1,449	1.056	1,446	1,427	1.190	1,513	1,360	1.192
'Quick' neutronics	1,519	1,460	1.056	1,453	1,435	1.190	1,592	1,463	1.192
'Main' neutronics	1,536	1,479	1.097	1,478	1,460	1.231	1,565	1,441	1.204
	Minor temperature breach			Within limits			Severe CEP, discard		

that using LEU fuel would necessitate the use of a strong moderator or a larger core seems to be correct, but with the latter option being overall preferable. These observations must, however, come with a strong caveat due to the aforementioned issue of the low upper bound on the mass flow rate. It is possible that a lower mass design exists in the LEU-ZrH-HeXe class at mass flow rates which are higher than 30kg/s, so one must be cautious drawing conclusions about this design type. It should also be recalled that a somewhat optimistic maximum turbine inlet temperature of 1,300K was assumed. An additional study could be carried out using a lower assumption, or perhaps even with the aim of determining what maximum turbine inlet temperature assumption nullifies the advantage of a ZrH-free design.

Another cause for caution is the apparently poor convergence of some of the designs on a final k_{eff} of unity where there would appear to be some scope for reducing the size of the reflector. Consider one of the more notable examples, which is Design 1 from the LEU-ZrH-He class. This has a reflector size of 40cm, an end-of-life k_{eff} of 1.209 and an overall mass of 92,575kg. It might be assumed that this is simply a manifestation of the CEP problem described above. This does not seem to be the case, however. A quick mini-problem was run to determine the ideal reflector size for that particular design, keeping all other design parameters the same and using the same objective function as that used in the optimisation (using the various modelling simplifications). The minimum mass system (not just core) is in fact found with a 10cm, rather than 40cm, reflector. Inspecting the fine detail of the run that found this 'optimal' point does not suggest that a premature surrogate reset occurred; the algorithm appears to have had ample opportunity to explore along this dimension in the design space but not taken it. It is possible that lower points along this dimension led to a breach of the MSD and were therefore never evaluated, but it is unclear why this should be so.

It is reasonable to speculate that, even if the CEP problem alone does not explain poor k_{eff} convergence in any particular design, it might generally reduce the effectiveness of the optimisation process. It should be recalled that the optimisation algorithm used is not directly aware of constraints; they simply manifest as penalties on the value of the objective function when breached. That is, artificial mass is added to the system to capture the violation of prescribed requirements. With this problematic, simplified thermal hydraulic modelling in place, the algorithm finds that reducing the amount of moderator and increasing the size of the reflector can, in some parts of the design space at least, lead to dramatic reductions in mass. Whilst this may not be evident in every specific system design, it must surely function as a confounding influence on the optimisation process.

The next observation that can be made relates to one of the most interesting aspects of this investigation: the many trade-offs that exist in the design space. It was not clear at the

outset of the investigation whether the best designs would cluster around a certain type of configuration or if very diverse systems could have a similar overall mass. For example, there is a clear trade-off between the thermal power of the core and the thermal efficiency of the conversion system. A higher power core is likely to be more massive (more fuel will be consumed and a lower power density might be required for effective cooling) but a high thermal power will require a less efficient conversion system, perhaps by having a smaller and less massive radiator. However, it is less clear if the resolution of such a trade-off has one solution, or if very diverse systems with similar overall masses are possible. It appears that the latter may be the case. For example, consider Designs 2 and 3 from the LEU-ZrH-He class (see Table 5.10). While they use a similar core thermal power, Design 3 has much narrower coolant channels combined with a much lower mass flow rate and core inlet temperature. Design 3 has a core that is around 1,200kg lighter, a turboset that is around 4,500kg lighter, but a radiator that is larger by around 7,200kg. The overall mass difference between the two designs is around 1,100kg. This suggests that, at least in some cases, significant diversity of similarly attractive designs is possible.

Considering the same two designs highlights another unexpected behaviour: the choice of recuperator effectiveness. For an effectiveness of less than 90%, the recuperator is a fairly light component, so it is somewhat surprising to see that Design 3 uses a relatively low effectiveness of 45%, corresponding to a very small 50kg recuperator. One might expect that increasing this effectiveness would allow an increased reactor inlet temperature and smaller radiator for very little additional mass. A detailed investigation of such a case would determine if this suspicion is correct. It should be recalled that the objective function is set up in such a way that parameters such as the recuperator effectiveness are not independent variables. The design parameters $\mathbf{x}$ that are chosen lead to a set of reactor conditions: inlet temperature, outlet temperature, mass flow rate and core pressure drop. These are then fed to a sub-problem which exhaustively searches for the lowest mass pressure ratio, with the recuperator effectiveness serving as a balancing tool to ensure that the outlet temperature of the conversion system matches the reactor inlet. This suggests that, for this particular reactor design, 45% *is* the optimal recuperator effectiveness for the design point $\mathbf{x}$. It could simply be that the optimisation algorithm might have not (yet) found the design that is otherwise identical to the one in question but with a higher inlet temperature that would lead to a higher, less suspicious, value of the recuperator effectiveness.

We now turn finally to the most important comparison, between HEU- and LEU-fuelled systems. The best LEU system, as mentioned, does not use a ZrH moderator and uses a HeXe coolant. It has an overall mass of 20,026kg. The best HEU system is also HeXe cooled and has a mass of 13,417kg. There, the LEU penalty would appear to be around

7,000kg, or around 50%, for the set of components considered. Neither of these systems is particularly close to the mass flow rate bound of 30kg/s, so the caveat mentioned in regard to the LEU-ZrH-HeXe class should not apply for this specific finding, although a further study with a higher mass flow rate upper bound should still be carried out to confirm this. One interesting feature of the best LEU and HEU designs is that their conversion systems are almost identical, operating at similar pressure ratios and with very similar masses across each component. The difference in system mass arises almost entirely from the core mass itself, which is around four times heavier for the best LEU design at 8,648kg than the best HEU design, which is 2,286kg.

5.7 Summary

In order to make a fair comparison between HEU and LEU power systems, the minimum mass design in each case should be sought. To this end a surrogate function optimisation method was chosen. Three choices of core materials were chosen: LEU fuel in combination with a zirconium hydride moderator, LEU fuel with only a graphite moderator and HEU with only a graphite moderator. This selection aimed to determine whether the presumed reduction in core size that a hydrogenous moderator might provide would offset the loss of thermodynamic efficiency caused by its restriction on core temperatures. In addition, each of these three design types was evaluated using a working fluid of both pure helium and the common choice of a 40g/mol binary mixture of helium and xenon to test whether the general recommendation for a HeXe blend applies for this design type.

The latter investigation confirmed that pure helium is the inferior coolant choice for this type of system, with significant increases in turbomachinery mass with no noticeable improvement in other system components. The main investigation found that the best LEU power system is found without using a ZrH moderator, with the larger graphite-only cores offsetting their larger mass with savings in the conversion system, namely in the waste heat radiator. Finally, the best LEU power system found had a mass 50% greater than the best HEU system found, with the difference in mass resulting almost entirely from the larger reactor. The investigation also found that it is possible in some cases to create diverse systems with significant differences in the allocation of mass across components, but which have similar overall masses. This finding, along with many of the others, may well be strongly influenced by the inclusion of other system elements, principally the core radiation shield which has not been included in this study. No allowance has been made for redundancy of components in the power conversion system, which could be very roughly accounted for by scaling the mass of the conversion system for any of the designs presented.

Chapter 6

Summary and Conclusions

Most space missions have used historically monopropellant or fuel-oxidiser propulsion systems to provide the required delta-v for orbital transfers and other in-space manoeuvres. Electric propulsion offers an alternative means of providing thrust that makes much more economical use of propellant due to its very high specific impulse. The total mass required to be moved from the ground to Low Earth Orbit to achieve the same delta-v could therefore be reduced, bringing with it lower launch costs. Equivalently, for the same overall mass, it might enable higher a higher delta-v, leading to shorter travel times, or make available wider and more frequent transfer windows. It is also a well-established technology, being routinely used by satellites for orbital adjustments and station keeping. It was also demonstrated as a suitable means of propulsion for space exploration in the very high delta-v *Dawn* mission. While in that case solar photovoltaic power was a reasonable source of electrical power for the thrusters, many mission types require significantly higher power levels. In addition, exploring further out into the solar system brings with it a reduced solar flux, reduced by 96% in a Jupiter orbit compared to Low Earth Orbit. In order to fulfil a variety of mission types, it is generally considered that at least 1MW of electrical power would be required for the thrusters. The only technology that would appear to be capable of supplying this level of power with a reasonable mass and size in the near to medium term is nuclear fission.

The use of fission power in space applications has been suggested from the beginning of the nuclear era for a variety of purposes. One design feature they almost all have in common is the use of highly enriched uranium (HEU) as fuel. From a pure engineering perspective it is the ideal fuel for such an application, allowing for a highly compact, low mass source of heat that can sustain criticality without the need for a moderator. However, there are some less technical considerations that make its use less desirable. The use of HEU, considered as weapons-grade, raises understandable concerns. Even with the recent rapid expansion of private sector launch services, space exploration remains a largely publicly funded endeavour.

Association with weapons-grade material, even if sufficient precautions have been taken, risks reducing the public's willingness to support such missions. The development and transportation of the fuel form must occur under the highest levels of security which also contributes to the cost of the mission.

An alternative fuel could be low enriched uranium (LEU), here defined to be less than 20% enriched. It is reasonable to assume that this will bring with it a penalty in terms of the system mass. For the core alone it would be expected that the core will require more fuel and/or moderator. The use of a moderator such as zirconium hydride will likely reduce the achievable core outlet temperature, reducing the thermodynamic efficiency of the energy conversion system. LEU is a much less contentious material, being used widely in civilian research reactors and proposed for some Generation IV power reactor designs. As well as alleviating the cost and perception issues mentioned above, it also allows more collaboration between space agencies and academia in developing space fission systems.

Weighing the technical disadvantages against the political advantages of choosing an LEU system is a difficult task and not one undertaken here. But whoever is required to make such a comparison will benefit from knowing what the technical disadvantages are. This project aims to address one aspect of the technical disadvantage, attempting to quantify the increase in the mass of the power system for one possible configuration. In order to make a fair comparison between LEU and HEU systems, the lowest possible mass design in each case must be sought. To reduce the scope of the investigation, only one type of power system was considered: a prismatic gas-cooled reactor configured in a direct Brayton conversion system. Both recuperated and unrecuperated systems are considered and heat rejection in the 'direct' method, where the main working fluid flows through a radiator system, transferring heat to finned heat pipes.

6.1 Core modelling

The requirements of the overall power system are that it provides 1MW of electrical power for seven years. This imposes the first requirement of the core, that it remains critical for its entire life. The core also has thermal limits on its materials, with the fuel and moderator both being considered. Therefore, both neutronic and thermal hydraulic analysis of the core is required.

6.1.1 Neutronics analysis

An initial study on the reactor alone was carried out using the Monte Carlo code Serpent, valuable for its ability to handle arbitrary geometries with ease. The first core design was based on a tungsten cermet fuel form derived from nuclear thermal rocket designs and this initial investigation found that the minimum mass LEU core was four times heavier than its HEU counterpart. It was clear, however, that analysing the large number of core designs required in a wider study would be impractical using a Monte Carlo code. Therefore, a deterministic method was pursued using the WIMS code suite. It was found that the presence of the strongly absorbing tungsten created a particular problem, requiring a fine-group resonance treatment that when included in a burnup scheme would result in an impractically long run-time. It was decided at this stage to abandon the tungsten cermet design in favour of a TRISO-based fuel form, which is much more amenable to analysis within WIMS.

Two possible routes were developed to analyse this core: one longer route which includes a two-dimensional core slice calculation using an MoC calculation to improve material homogenisation and one quicker route which skips this step. Both involve several steps, proceeding from a sub-group resonance treatment and collision probability analysis of the fuel assembly at the TRISO level of detail, through energy group condensation and material homogenisation at different scales, to a full-core calculation using the SP3 method in a simplified cylindrical geometry. Burnup calculations were carried out incorporating a spatially variable resonance treatment at each burnup step. The superior performance of the longer route was found to be most pronounced in cores with heavy moderation.

6.1.2 Thermal hydraulics analysis

The initial study for the tungsten cermet design considered a single central coolant channel using the equivalent annulus approximation for estimating the temperature distribution in an inverted hexagonal fuel array. After switching to the TRISO-based core, a finite element analysis was used to calculate the temperature distribution in the fuel block and the resultant heating of the coolant and moderator at each axial position in the core. A scheme was implemented to determine a realistic coolant flow pattern across the core, ensuring that the pressure drop along all possible coolant paths is equal. In order to allow the modelling of the recommended binary mixture of helium and xenon coolant, the Chapman-Enskog method was used to estimate the relevant fluid properties, for which detailed datasets do not exist.

6.2 Conversion system analysis

One type of conversion system was considered, a direct Brayton cycle with direct heat rejection, both with and without recuperation. The components in the system are therefore the turbine, compressor, alternator, recuperator, PMAD and waste heat radiator. It was decided that core design would function as the independent variable (in fact a set of variables) and that a routine would be developed that would find the minimum mass conversion system given the relevant outputs from the chosen core design: inlet temperature, output temperature, core pressure drop and coolant mass flow rate. A combination of information on the masses of real or proposed systems and basic physical models was used to arrive at expressions relating the masses of the components to their required performance parameter, such as power output, temperature drop or effectiveness. Given that the calculations involved are computationally quite cheap, a brute force search through the physically allowable pressure ratios was a feasible way to determine the minimum mass conversion system for any given core design.

6.3 Optimisation scheme

A surrogate function optimisation method available in MATLAB was used to seek minimum mass core designs. High speed, lower fidelity variants of the analysis tools developed were used for the main study. The quicker neutronics route within WIMS was used and the thermal hydraulics was carried out considering only the central (and generally hottest) assembly to assess thermal limit breaches. Coupling between the neutronic and thermal hydraulics calculations was limited to a single iteration. These simplifications resulted in an acceptably low change in outputs, with the exception of the core edge peaking effect, where the optimisation algorithm selected designs where the peak temperatures were at the core periphery rather than the core centre. This resulted in significant underestimations of peak core temperatures in some cases.

The study considered three system types: LEU fuel in combination with a zirconium hydride moderator, LEU fuel with only a graphite moderator and HEU with only a graphite moderator. This selection aimed to determine whether the presumed reduction in core size that a hydrogenous moderator might provide would offset the loss of thermodynamic efficiency caused by its restriction on core temperatures. In addition, each of these three design types was evaluated using a working fluid of both pure helium and the common choice of a 40g/mol binary mixture of helium and xenon to test whether the general recommendation for a HeXe blend is preferable for this design type. The computational budget for each of

these cases was limited to 5,000 evaluations of the objective function, which contained within it the neutronic and thermal hydraulic analysis of the core and the rapid iterative search for a minimum mass conversion system.

The latter investigation confirmed that pure helium is the inferior coolant choice for this type of system, with significant increases in turbomachinery mass with no noticeable improvement in other system components. The main investigation found that the best LEU power system is found without using a ZrH moderator, with the larger graphite-only cores offsetting their larger mass with savings in the conversion system, namely in the waste heat radiator. Finally, the best LEU power system found had a mass 50% greater than the best HEU system found, with the difference in mass resulting almost entirely from the larger reactor. The investigation also found that it is possible in some cases to create diverse systems with significant differences in the allocation of mass across components, but which have similar overall masses. This finding, along with many of the others, may well be strongly influenced by the inclusion of other system elements, principally the core radiation shield, which has not been included in this study, and the lack of allowance for redundancy anywhere in the system.

This study has considered how the effect of changing from HEU fuel to LEU fuel in a particular power system design could affect the mass of the overall system. The components considered form a subset of the real system that would be required; in reality, account must be taken of piping, cabling, structural elements, thruster mass, redundancy requirements and radiation shielding amongst many others. The overall system masses should therefore not be considered as estimates of a real-world system. However, some of the main findings may well persist even if significant sophistication were to be added to the power system model. In particular, it seems that the use of a zirconium hydride moderator does not offer an overall advantage over graphite as a moderator due to its restrictive effect on the core outlet temperature, assuming that the slightly optimistic maximum turbine inlet temperature of 1,300K is in fact applicable.

The main comparison of interest, between HEU and LEU resulted in a 50% weight penalty. Depending on the mass of the remainder of the vessel including the payload, this may be considered acceptable if it made a significant difference to security costs, collaboration efficiency or public perception. Increasing the scope of the analysis might even reduce this further. For example, if a 100% redundancy were required in the conversion system, a very approximate estimate of the impact of this could be made by doubling the mass of the conversion system. In this case, the overall penalty based on the best LEU and HEU designs would fall to 30%.

6.4 Recommendations for Future Work

The computational infrastructure developed for this study is very flexible and modular in nature, presenting some areas for potential future investigation with very little modification.

6.4.1 Minor extensions

With relatively little extra development the following areas could be considered:

- Extending or repeating runs carried out where the best designs occurred at or near chosen bounds on the mass flow rate to check if better designs exist beyond this boundary.
- The discovered core edge peaking problem could be addressed by analysing both the central and outermost assemblies, requiring a small modification to the analysis routine.
- Other moderator types: for example, yttrium hydride has a better temperature tolerance than zirconium hydride which should improve the allowable outlet temperature.
- Other reflector types: in particular, a non-moderating reflector such as spinel should be considered.
- Core aspect ratio: from a purely neutronic point of view the square aspect ratio considered is preferred but flatter cores with many short coolant channels would be preferred from a purely thermal hydraulic perspective. If shielding were to be considered, this might lead to a preference for a taller core.
- Higher or lower electrical powers: It might be valuable to investigate how the LEU penalty varies if we change the required power level.
- Alternative optimisation method: Given the practical problems discovered with the surrogate function method used, an alternative method such as genetic algorithms which extends more naturally to parallel computing could be utilised.
- Making use of higher fidelity options: for example, full-core thermal hydraulics. One way of using these is to see the first study as a indicator of the approximate locations of local minima, then apply the more computationally expensive methods in a local search.

6.4.2 Significant extensions

These areas of interest would require somewhat more investment to investigate than the above items:

- Shielding: This is perhaps the most obvious neglected aspect of the power system. The mass of the radiation shield will be strongly dependent on the size and power of the reactor and could potentially alter some of the main findings from this study. Developing a sufficiently fast method of finding the lowest mass shield for a given reactor design could be a fruitful area of research, and there may be an interesting dependency on the core aspect ratio.

- More sophisticated modelling of turbomachinery, the recuperator and other conversion system components.

- Reactivity control: the reflector would ordinarily contain rotating control drums which have a strong absorber on one side. These will add additional mass to the core. These alone may not be sufficient to control reactivity through the entire core lifetime and the use of burnable poisons could be investigated.

- Other cycle configurations: the direct Brayton cycle with direct heat rejection was considered, but it is possible to decouple both the hot and cold sides of the cycle with heat exchangers.

- Other core types: in particular, the effect of using a metallic coolant rather than a gas could be investigated.

- More sophisticated moderator cooling: the present design uses a one-pass flow pattern, but a two-pass coolant path in conjunction with insulating material could improve the cooling of the moderator, but will require a more complex thermal hydraulics analysis.

- Higher order neutronics: in particular, significant computational infrastructure exists for producing core geometries in CACTUSOT, the three-dimensional method of characteristics solver within WIMS. Should future development (such as the coarse mesh finite difference method on a hexagonal grid) become available this could be used as the main neutronics tool.

References

[1] Angeliu, T. M., Ward, J. T., and Witter, J. K. (2007). Assessing the effects of radiation damage on Ni-base alloys for the prometheus space reactor system. *Journal of Nuclear Materials*, 366(1):223–237.

[2] ANSWERS (2015). WIMS: User Guide for Version 10. Technical report.

[3] ANSWERS (2018a). Private correspondence.

[4] ANSWERS (2018b). Private correspondence.

[5] Ashcroft, J. M. (2006). Documentation of Naval Reactors Papers and Presentations for the Space Technology and International Forum (STAIF) 2006. Technical report, Knolls Atomic Power Laboratory (KAPL), Niskayuna, NY.

[6] Askew, J. R. (1972). A characteristics formulation of the neutron transport equation in complicated geometries. Technical report, United Kingdom Atomic Energy Authority.

[7] ASME Boiler and Pressure Vessel Committee on Nuclear Power (2010). *ASME boiler & pressure vessel code: an international code. III Division 1 - subsection NH. Class 1 components in elevated temperature service. Rules for construction of nuclear facility components / ASME Boiler and Pressure Vessel Committee on Nuclear Power.* American Society of Mechanical Engineers, New York, 2010 edition. edition.

[8] Barrett, M. and Johnson, P. (2005). Performance and Mass Modeling Subtleties in Closed-Brayton-Cycle Space Power Systems. In *3rd International Energy Conversion Engineering Conference*, San Francisco, California. American Institute of Aeronautics and Astronautics.

[9] Barrett, M. J. (2004). System Mass Variation and Entropy Generation in 100-kWe Closed-Brayton-Cycle Space Power Systems. In *AIP Conference Proceedings*, volume 699, pages 445–452, Albuquerque, New Mexico (USA). AIP.

[10] Barrett, M. J. and Johnson, P. K. (2008). Carbon-Carbon Recuperators in Closed-Brayton-Cycle Space Power Systems. *Journal of Propulsion and Power*, 24(3):609–613.

[11] Beckert, C. and Grundmann, U. (2007). A Nodal Expansion Method for Solving the Multigroup SP3 Equations in the Reactor Code DYN3D. In *Proceedings of M&C + SNA 2007*, Monterey, California.

[12] Bell, G. I. and Glasstone, S. (1970). *Nuclear Reactor Theory*. Van Nostrand Reinhold Inc.,U.S., first edition.

[13] Bennett, G. L. (1989). A look at the Soviet space nuclear power program. In *Energy Conversion Engineering Conference, 1989. IECEC-89, Proceedings of the 24th Intersociety*, pages 1187–1194. IEEE.

[14] Brocklehurst, J. (1984). Irradiation Damage in CAGR Moderator Graphite. Technical Report ND-R-1117, UKAEA.

[15] Bruggeman, D. a. G. (1935). Berechnung verschiedener physikalischer Konstanten von heterogenen Substanzen. I. Dielektrizitätskonstanten und Leitfähigkeiten der Mischkörper aus isotropen Substanzen. *Annalen der Physik*, 416(7):636–664.

[16] Carelli, M. D., Markley, R. A., Pierce, B. L., and Schmidt, J. E. (1988). The Curie point radiator. In *Transactions of the Fifth Symposium on Space Nuclear Power Systems*, Albuquerque, New Mexico.

[17] CEA, editor (2006). *Gas-cooled Nuclear Reactors*. CEA, Paris. OCLC: 123900736.

[18] Chan, J., Wood, J. G., and Schreiber, J. G. (2007). Development of Advanced Stirling Radioisotope Generator for Space Exploration. volume 880, pages 615–623. AIP.

[19] Chiew, Y. C. and Glandt, E. D. (1983). The effect of structure on the conductivity of a dispersion. *Journal of Colloid and Interface Science*, 94(1):90–104.

[20] Chisholm, D. (1971). *The Heat Pipe*. M & B technical library; TL/ME/2. Mills and Boon, London.

[21] Clayton, D. J., Lucas, G., and Radel, T. E. (2011). Resulting Source Term from the Mars Science Laboratory Safety Analysis. Technical report, Sandia National Laboratories (SNL-NM), Albuquerque, NM (United States).

[22] Cliquet, E., Rualt, J., Masson, F., Roux, J., Paris, N., Cazale, B., Manifacier, L., and Poinot-Salanon, C. (2013). Study of space reactors for space exploration missions. OCLC: 892556717.

[23] Cropp, L. O., Gallup, D. R., and Marshall, A. C. (1990). Mass and performance estimates for 5 to 1000 kW (e) nuclear reactor power systems for space applications. Technical report, Sandia National Laboratories, Albuquerque, NM (United States).

[24] Davis, J. E. (1972). Design and fabrication of the Brayton rotating unit. Technical report, Airesearch Manufacturing Company of Arizona.

[25] Demuth, S. F. (2003). SP100 space reactor design. *Progress in Nuclear Energy*, 42(3):323–359.

[26] Dirker, J. and Meyer, J. P. (2005). Convective Heat Transfer Coefficients in Concentric Annuli. *Heat Transfer Engineering*, 26(2):38–44.

[27] Dobler, F. X. e. a. (1978). Analysis, design, fabrication and testing of the mini-Brayton rotating unit (Mini-BRU). Volume 1: Text and tables. Technical report, Airesearch Manufacturing Company of Arizona.

[28] Eades, M., Reed, M., Morrison, C., Deason, W., Judd, S., Patel, V., and Venneri, P. (2019). The Pylon: Commercial LEU Nuclear Fission Power for Lunar, Martian and Deep Space Applications. In *Proceedings of NETS 2019*, Richland WA.

[29] El-Genk, M. and Tournier, J.-M. (2006). Selection of Noble Gas Binary Mixtures for Brayton Space Nuclear Power Systems. In *4th International Energy Conversion Engineering Conference and Exhibit (IECEC)*, San Diego, California. American Institute of Aeronautics and Astronautics.

[30] El-Genk, M. S. (2006). High Temperature Water Heat Pipes Radiator for a Brayton Space Reactor Power System. In *AIP Conference Proceedings*, volume 813, pages 716–729, Albuquerque, New Mexico (USA). AIP.

[31] El-Genk, M. S. and Tournier, J.-M. (2007). Noble-Gas Binary Mixtures for Closed-Brayton-Cycle Space Reactor Power Systems. *Journal of Propulsion and Power*, 23(4):863–873.

[32] European Commission (2017). MEGAHIT Final Report. Technical report.

[33] Every, A. G., Tzou, Y., Hasselman, D. P. H., and Raj, R. (1992). The effect of particle size on the thermal conductivity of ZnS/diamond composites. *Acta Metallurgica et Materialia*, 40(1):123–129.

[34] Fink, J. K. (2000). Thermophysical properties of uranium dioxide. *Journal of Nuclear Materials*, 279(1):1–18.

[35] Finseth, J. L. (1991). Overview of Rover Engine Tests Final Report. Technical report, NASA.

[36] Folsom, C., Xing, C., Jensen, C., Ban, H., and Marshall, D. W. (2015). Experimental measurement and numerical modeling of the effective thermal conductivity of TRISO fuel compacts. *Journal of Nuclear Materials*, 458:198–205.

[37] Gallo, B. M. and El-Genk, M. S. (2009). Brayton rotating units for space reactor power systems. *Energy Conversion and Management*, 50(9):2210–2232.

[38] GE (1967). 710 High Temperature Gas Reactor Program Summary Report. Technical report.

[39] Gelbard, E. M. (1960). Application of spherical harmonics method to reactor problems. *Bettis Atomic Power Laboratory, West Mifflin, PA, Technical Report No. WAPD-BT-20*.

[40] Gibson, M. A., Mason, L., Bowman, C., Poston, D. I., McClure, P. R., Creasy, J., and Robinson, C. (2014). Development of NASA's Small Fission Power System for Science and Human Exploration. In *Proceedings of Propulsion and Energy Forum 2014*, Cleveland, Ohio.

[41] Gontard, R. and Nabielek, H. (1990). Performance evaluation of modern HTR TRISO fuels. *Forschungszentrum Jülich GmbH, HTA-IB-05/90*.

[42] Gonzo, E. E. (2002). Estimating correlations for the effective thermal conductivity of granular materials. *Chemical Engineering Journal*, 90(3):299–302.

[43] Gottaut, H. and Krüger, K. (1990). Results of experiments at the AVR reactor. *Nuclear Engineering and Design*, 121(2):143–153.

[44] Gunow, G., Forget, B., and Smith, K. (2019). Full core 3D simulation of the BEAVRS benchmark with OpenMOC. *Annals of Nuclear Energy*, 134:299–304.

[45] Gülol, O. Ö., Çolak, Ü., and Yıldırım, B. (2008). Performance analysis of TRISO coated fuel particles with kernel migration. *Journal of Nuclear Materials*, 374(1):168–177.

[46] Hales, J. D., Williamson, R. L., Novascone, S. R., Perez, D. M., Spencer, B. W., and Pastore, G. (2013). Multidimensional multiphysics simulation of TRISO particle fuel. *Journal of Nuclear Materials*, 443(1):531–543.

[47] Hirshfelder, J., Curtiss, C., and Bird, R. (1954). *Molecular Theory of Gases and Liquids*. John Wiley & Sons.

[48] Ho, C. Y., Powell, R. W., and Liley, P. E. (1972). Thermal Conductivity of the Elements. *Journal of Physical and Chemical Reference Data*, 1(2):279–421.

[49] Howe, S. D., Crawford, D., Navarro, J., and Ring, T. (2013). Economical production of pu-238. Technical report, Idaho National Laboratory (INL).

[50] Howe, S. D., Travis, B., and Zerkle, D. K. (2001). Safe Testing of Nuclear Rockets. *Journal of Propulsion and Power*, 17(3):534–539.

[51] Husemeyer, P. J. M. (2016). *Design and Optimization of a Low-Enriched Uranium Nuclear Thermal Rocket Engine*. PhD thesis, University of Cambridge.

[52] Johnson, P. K. (2005). Design and Off-Design Performance of 100 kWe-Class Brayton Power Conversion Systems. In *AIP Conference Proceedings*, volume 746, pages 711–718, Albuquerque, New Mexico (USA). AIP.

[53] Johnson, R. A., Morgan, W. T., and Rocklin, S. R. (1967). Design, ground test and flight test of SNAP 10A, first reactor in space. *Nuclear Engineering and Design*, 5(1):7–21.

[54] Juhasz, A. (2007). Heat Transfer Analysis of a Closed Brayton Cycle Space Radiator. In *5th International Energy Conversion Engineering Conference and Exhibit (IECEC)*, St. Louis, Missouri. American Institute of Aeronautics and Astronautics.

[55] Juhasz, A. (2008). High Conductivity Carbon-Carbon Heat Pipes for Light Weight Space Power System Radiators. In *6th International Energy Conversion Engineering Conference (IECEC)*, Cleveland, Ohio. American Institute of Aeronautics and Astronautics.

[56] Juhasz, A. (2010). A Mass Computation Model for Light Weight Brayton Cycle Regenerator Heat Exchangers. In *8th Annual International Energy Conversion Engineering Conference*, Nashville, TN. American Institute of Aeronautics and Astronautics.

[57] Juhasz, A. J. (1994). Review of Advanced Radiator Technologies for Spacecraft Power Systems and Space. Technical Report TM 4555, NASA.

[58] Juhasz, A. J. (2005). *Analysis and Numerical Optimization of Gas Turbine Space Power Systems with Nuclear Fission Reactor Heat Sources*. PhD thesis, Cleveland State University.

[59] Kestin, J., Knierim, K., Mason, E. A., Najafi, B., Ro, S. T., and Waldman, M. (1984). Equilibrium and Transport Properties of the Noble Gases and Their Mixtures at Low Density. *Journal of Physical and Chemical Reference Data*, 13(1):229–303.

[60] Kim, Y., Park, J., and Cleveland, J. (2006). Thermophysical properties database of materials for light water and heavy water reactors. Technical Report IAEA-TECDOC-1496, International Atomic Energy Agency, Vienna.

[61] Knudson, D. L., Miller, G. K., Miller, G. K., Petti, D. A., Maki, J. T., and Knudson, D. L. (2009). PARFUME Theory and Model basis Report. Technical Report INL/EXT-08-14497, Idaho National Laboratory (INL).

[62] Labus, T. L. S. (1989). Solar dynamic power for space station freedom. In *Proceedings of International Conference on Space Power*, Cleveland, Ohio.

[63] Lamarsh, J. R. and Baratta, A. J. (2014). *Introduction to Nuclear Engineering*. Pearson, third edition.

[64] Leppänen, J. (2013). Serpent User's Manual. Technical report, VTT, Finland.

[65] Leppänen, J., Pusa, M., Viitanen, T., Valtavirta, V., and Kaltiaisenaho, T. (2015). The Serpent Monte Carlo code: Status, development and applications in 2013. *Annals of Nuclear Energy*, 82:142–150.

[66] Lide, D. R. (2003). *CRC Handbook of Chemistry and Physics*. CRC Press, 84th edition.

[67] Lindley, B. A. (2019). Private correspondence.

[68] Lindley, B. A., Hosking, J. G., Smith, P. J., Powney, D. J., Tollit, B. S., Newton, T. D., Perry, R., Ware, T. C., and Smith, P. N. (2017). Current status of the reactor physics code WIMS and recent developments. *Annals of Nuclear Energy*, 102:148–157.

[69] Lindley, B. A., Mohamed, H., Parks, G. T., Hosking, J. G., and Lillington, J. N. (2015). Double-Heterogeneity Modelling of High Temperature Reactors Containing Particulate Fuel. In *Proceedings of TopFuel 2015*, pages 287/580–296/580, Zurich, Switzerland.

[70] Liu, Y., Kochunas, B., Martin, W., and Downar, T. (2019). Delayed fission energy effect on LWR normal operation and transients. *Annals of Nuclear Energy*, 128:84–93.

[71] Mason, L. S. (2003). A Power Conversion Concept for the Jupiter Icy Moons Orbiter. In *Proceedings of First International Conversion Engineering Conference*, Portsmouth, Virginia.

[72] Mason, L. S. (2006). A Comparison of Fission Power System Options for Lunar and Mars Surface Applications. In *AIP Conference Proceedings*, volume 813, pages 270–280. AIP.

[73] Mathworks (2019). Global Optimisation Toolbox (2019b) User's Guide.

[74] Maxwell, J. C. (1873). *Electricity and Magnetism Clarendon Press*. Oxford, UK.

[75] McPherson, M. J. (1993). *Subsurface Ventilation and Environmental Engineering*. Springer, London, first edition.

[76] Mitchell, M. (2003). Graphite thermal conductivity and heat-removal paths for PBMR. In *Pro. Fourth. Int. Nuclear Graphite Specialist Meeting*, Marugame, Japan.

[77] Mizia, R. E. (2008). Next Generation Nuclear Plant Reactor Pressure Vessel Acquisition Strategy. Technical Report INL/EXT-08-13951.

[78] Morris, R. and Pappano, P. (2007). Estimation of maximum coated particle fuel compact packing fraction. *Journal of Nuclear Materials*, 361(1):18–29.

[79] NASA (2017). Space Technology: Game Changing Development, Nuclear Thermal Propulsion (NTP). Press release.

[80] NASA/JPL (2005). Prometheus Project Final Report. Technical Report 982-R120461, National Aeronautics and Space Administration.

[81] NIST (2017). NIST Chemistry WebBook.

[82] Nonbøl, E. (1996). Description of the Advanced Gas Cooled Type of Reactor (AGR). Technical Report NKS/RAK2(96)TR-C2, Risø National Laboratory.

[83] O'Brien, R. C., Ambrosi, R. M., Bannister, N. P., Howe, S. D., and Atkinson, H. V. (2008). Safe radioisotope thermoelectric generators and heat sources for space applications. *Journal of Nuclear Materials*, 377(3):506–521.

[84] O'Brien, R. C., Ambrosi, R. M., Bannister, N. P., Howe, S. D., and Atkinson, H. V. (2009). Spark Plasma Sintering of simulated radioisotope materials within tungsten cermets. *Journal of Nuclear Materials*, 393(1):108–113.

[85] Pfeiffer, S. L. (1989). Conceptual design of liquid droplet radiator shuttle-attached experiment. Technical Report NASA CR-185164, Grumman Space Systems.

[86] Pietrak, K. and Wisniewski, T. S. (2015). A review of models for effective thermal conductivity of composite materials. *Journal of Power Technologies*, 95(1):14.

[87] Poston, D. I. and Mcclure, P. R. (2017). White Paper – Use of LEU for a Space Reactor. Technical Report LA–UR-17-27226, 1375148, NASA.

[88] Powell, M. J. (1992). *The theory of radial basis function approximation in 1990, Advances in Numerical Analysis II: Wavelets, Subdivision, and Radial Functions*, volume 105. Oxford University Press.

[89] Powers, J. J. and Wirth, B. D. (2010). A review of TRISO fuel performance models. *Journal of Nuclear Materials*, 405(1):74–82.

[90] Price, M. S. T. (2012). The Dragon Project origins, achievements and legacies. *Nuclear Engineering and Design*, 251:60–68.

[91] Rayman, M. D., Chadbourne, P. A., Culwell, J. S., and Williams, S. N. (1999). Mission design for deep space 1: A low-thrust technology validation mission. *Acta Astronautica*, 45(4):381–388.

[92] Rayman, M. D., Fraschetti, T. C., Raymond, C. A., and Russell, C. T. (2006). Dawn: A mission in development for exploration of main belt asteroids Vesta and Ceres. *Acta Astronautica*, 58(11):605–616.

[93] Rimpault, G., Grimstone, M., and Tullet, J. (1990). Accurate Treatments of Fast Reactor Fuel Assembly Heterogeneity in the ECCO Cell Code. In *PHYSOR*, Marseille.

[94] Rowcliffe, A. F., Mansur, L. K., Hoelzer, D. T., and Nanstad, R. K. (2009). Perspectives on radiation effects in nickel-base alloys for applications in advanced reactors. *Journal of Nuclear Materials*, 392(2):341–352.

[95] Schmidt, G. R., Manzella, D. H., Kamhawi, H., Kremic, T., Oleson, S. R., Dankanich, J. W., and Dudzinski, L. A. (2010). Radioisotope electric propulsion (REP): A near-term approach to nuclear propulsion. *Acta Astronautica*, 66(3):501–507.

[96] Shiozawa, S., Fujikawa, S., Iyoku, T., Kunitomi, K., and Tachibana, Y. (2004). Overview of HTTR design features. *Nuclear Engineering and Design*, 233(1):11–21.

[97] Siamidis, J., Mason, L., Beach, D., and Yuko, J. (2004). Heat Rejection Concepts for Brayton Power Conversion Systems. In *2nd International Energy Conversion Engineering Conference*, Providence, Rhode Island. American Institute of Aeronautics and Astronautics.

[98] Smith, K. S. (2002). Full-core, 2-D, LWR core calculations with CASMO-4E. In *PHYSOR 2002*, Seoul, Korea.

[99] Stacey, W. M. (2018). *Nuclear Reactor Physics*. John Wiley & Sons.

[100] Stainsby, R., Grief, A., Worsley, M., and Dawson, F. (2009). Investigation of local heat transfer phenomena in a pebble bed HTGR core. *AMEC NSS Limited, London, United Kingdom*.

[101] Stanculescu, A. and International Atomic Energy Agency, editors (2005). *The role of nuclear power and nuclear propulsion in the peaceful exploration of space*. Number 1197 in STI/PUB. International Atomic Energy Agency, Vienna.

[102] Stray, B., Delaney, M., Lindley, B., Shepherd, M., Richards, S., Hosking, G., and Smith, P. (2016). Solution of the OECD/NEA SFR Neutronic Benchmark Using WIMS and MONK. In *Proceedings of PHYSOR 2016*, Sun Valley, Idaho.

[103] Tak, N.-i., Kim, M.-H., and Lee, W. J. (2008). Numerical investigation of a heat transfer within the prismatic fuel assembly of a very high temperature reactor. *Annals of Nuclear Energy*, 35(10):1892–1899.

[104] Timings, R. (2005). *Mechanical Engineer's Pocket Book*. Newnes, Oxford ; Boston, 3rd revised edition.

[105] Tobochnik, J. and Chapin, P. M. (1988). Monte Carlo simulation of hard spheres near random closest packing using spherical boundary conditions. *The Journal of Chemical Physics*, 88(9):5824–5830.

[106] Todreas, N. E. and Kazimi, M. S. (2011). *Nuclear Systems Volume 1: Thermal Hydraulic Fundamentals*. CRC Press, 2nd edition.

[107] Tournier, J.-M., El-Genk, M., and Gallo, B. (2006). Best Estimates of Binary Gas Mixtures Properties for Closed Brayton Cycle Space Applications. In *4th International Energy Conversion Engineering Conference and Exhibit (IECEC)*, San Diego, California. American Institute of Aeronautics and Astronautics.

[108] Tournier, J.-M. P. and El-Genk, M. S. (2006). Liquid Metal Loop and Heat Pipe Radiator for Space Reactor Power Systems. *Journal of Propulsion and Power*, 22(5):1117–1134.

[109] Tuominen, R., Valtavirta, V., and Leppänen, J. (2019). New energy deposition treatment in the Serpent 2 Monte Carlo transport code. *Annals of Nuclear Energy*, 129:224–232.

[110] Van Houten, R. and Baxter, W. G. (1965). Titanium, zirconium, and yttrium hydrides as space shielding materials. *Journal of Spacecraft and Rockets*, 2(3):469–472.

[111] Venneri, P. F. and Kim, Y. (2015). A feasibility study on low-enriched uranium fuel for nuclear thermal rockets – I: Reactivity potential. *Progress in Nuclear Energy*, 83:406–418.

[112] Voss, S. S. and Dix, G. P. (1984). The Pied Piper: A Historical Overview of the US Space Power Reactor Program. In *Proceedings of First Symposium on Space Nuclear Power Systems*, Albuquerque, New Mexico.

[113] Wallace, R. A. (1985). SP-100 Missions Overview. In *Proceedings of the Second Symposium on Space Nuclear Power Systems*, Albuquerque NM. Orbit Book Company.

[114] Walsh, P. P. and Fletcher, P. (2004). *Gas Turbine Performance*. John Wiley & Sons. Google-Books-ID: zxRdacCvjVsC.

[115] Walter, C. E. (1987). Gas-cooled reactor power systems for space. Technical Report UCRL–95047-REV.2, Lawrence Livermore National Lab.

[116] Wang, Y. and Shoemaker, C. A. (2014). A general stochastic algorithmic framework for minimizing expensive black box objective functions based on surrogate models and sensitivity analysis. *arXiv preprint arXiv:1410.6271*.

[117] Wertz, J. R. and Larson, W. J. (1999). *Space Mission Design and Analysis*. Microcosm Press and Kluwer Academic Publishers, 3rd edition.

[118] Wollman, M. J. and Zika, M. J. (2006). Project Prometheus Reactor Module Final Report. Technical Report SPP-67110-0008, Knolls Atomic Power Lab (NY) and Bettis Atomic Power Lab (PA).

[119] Worrall, M. J. (2013). *Feasibility study of a small, thorium-based fission power system for space and terrestrial applications*. PhD thesis, Colorado School of Mines.

[120] Yamanaka, S., Yamada, K., Kurosaki, K., Uno, M., Takeda, K., Anada, H., Matsuda, T., and Kobayashi, S. (2001). Thermal properties of zirconium hydride. *Journal of Nuclear Materials*, 294(1):94–98.

[121] Zakirov, V. and Pavshook, V. (2011). Feasibility of the recent Russian nuclear electric propulsion concept: 2010. *Nuclear Engineering and Design*, 241(5):1529–1537.